Development of Mussel-inspired Antifouling Coatings and Underwater Adhesive Materials and the Associated Surface Interaction Mechanisms

By

Mingfei Pan

A thesis submitted in partial fulfillment of the requirements for the degree of

Doctor of Philosophy

In

Materials Engineering

Department of Chemical & Materials Engineering

University of Alberta

Abstract

Nature biology like blue mussels, barnacles, and sandcastles can tightly attach to solid surfaces in the ocean, even under dynamic and turbulent environments. Exploration of these organisms has revealed the significance of catechol-enriched adhesive proteins as the unique paradigm for the development of synthetic systems for a broad range of applications. However, studies on the corresponding intermolecular interactions between the catechol-containing materials are limited which brings the challenge to realize the delicate control of catechol chemistry and the full recapitulation of the biological adhesive functions. In this thesis, three original research works regarding the molecular design and engineering of mussel-inspired antifouling coating and adhesive hydrogel materials are presented, with the assistance of drop and colloidal probe atomic force microscope (AFM) techniques to investigate the correlated surface interaction mechanisms, which hold great promises in industrial and medical applications under practical conditions.

In the first work, a mussel-inspired antifouling coating formed by polydopamine (PDA) codeposited with cationic {2-(methacryloy-loxy)ethyl}trimethylammonium chloride (MTAC) and anionic acrylic acid (AA) was demonstrated bearing adjustable surface charge property, employing tunable long-range electrostatic interaction to achieve adaptive antifouling performance in response to the varying electrical characteristic of the contaminants, i.e., emulsions. The results from surface forces measured by drop probe AFM technique indicated that modulating the surface electrical properties of the coatings through varying the solution pH could effectively alter their electrostatic interactions with emulsions from attraction to repulsion, in combination with hydrodynamic interactions, to enable emulsion repellence of the coatings. Meanwhile, by properly modulating the surface charge of a PDA-PAA-PMTAC-deposited

polyvinylidene fluoride (PVDF) membrane, an enhanced water permeability with durable antifouling property was achieved for efficient and universal water purification.

Achieving robust adhesion on wet biological tissues for hydrogels containing high water content is still challenging, as water disrupts the surface boding, thus resulting in weak adhesion strength. In the second work, mimicking the structure of the Mytilus byssal thread covered by a thin protective cuticle, a design strategy was proposed to construct a soft armour-like hydrophobic interface as the outermost adhesive layer over the hydrophilic hydrogel matrix to realize instant and robust wet adhesion. The external hydrophobic shell generates a water depletion region at the contact interface to promote rapid adhesion (within 5 s) and protect the weakening of interfacial bonds from water penetration even under high hydraulic pressure. Atomic force microscope (AFM) colloidal probe technique was also used to investigate the assembling mechanisms for the hydrophobic layer of the hydrogel. The developed hydrogel adhesives are further applied in the wet intraoral environment to facilitate the high-contrast imaging for ultrasound diagnosis, which benefits the integration of human-machine interface for biomedical applications.

Development of soft conductive materials has enabled the promising future of wearable sensors for health monitoring. However, conventional soft conductive materials typically lack robust adhesive and on-demand removable properties for a target substrate. In the third work, a novel hydrogel ionic conductor was developed composed of a cationic micelle cross-linked polymer network. The developed ionic conductor possesses a range of desirable properties including mechanical performances such as excellent stretchability (>1100%), toughness, elasticity (recovery from 1000% strain), conductivity (2.72 $S \cdot m^{-1}$), self-healing capability, and antimicrobial property, owing to multiple non-covalent supramolecular interactions (e.g.,

hydrogen bonding, hydrophobic, and π-π/cation-π interactions) present in the cross-linked network. Moreover, the ionic conductor was integrated with bridging polymers to form a motion-sensing entirety. The environment-adaptive wet adhesion of the motion sensor for various substrates (adhesion strength up to ~ 30 kPa) was achieved by the introduction of pH or temperature-responsive polymers as the bridging agent that can form a topological connection with the hydrogel network and substrate surfaces. Further, the on-demand removability can be achieved by the external stimuli of environmental pH or temperature. The resulting motion sensors possess excellent sensitivity and reliability for the detection of human motions, showing great promise for advanced health monitoring devices with enhanced performances.

This thesis work expands the application of marine mussels-derived dynamic interactions in the development of multifunctional antifouling coating and wet adhesive hydrogels and elucidates the related intermolecular interactions at nanoscale, which devises a new passage on catechol containing-synthetic systems with diverse anchoring, antifouling, adhesive, and cohesive properties for the environmental and biomedical applications.

Preface

This thesis is an original work conducted by Mingfei Pan under the supervision of Dr. Hongbo Zeng, containing published contents from the peer-reviewed journals.

Chapter 2 of this thesis has been published as Pan, M.; Gong, L.; Xiang, L.; Yang, W.; Wang, W.; Zhang, L.; Hu, W.; Han, L; Zeng, H.; Modulating surface interactions for regenerable separation of oil-in-water emulsions. *Journal of Membrane Science* 625 (2021): 119140. I was responsible for materials synthesis, data collection and analysis, as well as the manuscript composition. Dr. Lu Gong instructed the surface force measurement experiment. Wenshuai Yang helped conduct the material characterization. Dr. Li Xiang, Dr. Wenda Wang, Dr. Ling Zhang, Dr. Wenjihao Hu and Dr. Linbo Han contributed to the manuscript revision. Dr. Hongbo Zeng was the corresponding author and involved in the experimental design and manuscript composition.

Chapter 3 of this thesis has been published as Pan, M.; Nguyen, K.C.T.; Yang, W.; Liu, X.; Chen, X.Z.; Major, P.W.; Le, L.H.; Zeng, H.; Soft Armour-like Layer-Protected Hydrogels for Wet Tissue Adhesion and Biological Imaging. *Chemical Engineering Journal* 434 (2021): 134418. I was responsible for materials synthesis, data collection and analysis, as well as the manuscript composition. Kim-Cuong T Nguyen helped conduct the intraoral ultrasound imaging experiment. Wenshuai Yang helped conduct the material characterization and Dr. Xiong Liu helped the cell viability experiment. Dr. Xing-Zhen Chen, Dr. Paul W. Major, and Dr. Lawrence H. Le contributed to the manuscript revision. Dr. Hongbo Zeng was the corresponding author and involved in the experimental design and manuscript composition.

Chapter 5 has been published as Pan, M., Wu, M., Shui, T., Xiang, L., Yang, W., Wang, W., Liu, X., Wang, J., Chen, X.Z. and Zeng, H.; Highly stretchable, elastic, antimicrobial conductive hydrogels with environment-adaptive adhesive property for health monitoring. *Journal of Colloid and Interface Science* 622 (2022): 612-624. I was responsible for material synthesis, experimental design, data collection and analysis, as well as manuscript composition. Meng Wu and Dr. Tao Shui helped conduct the material characterization and Dr. Xiong Liu helped the antimicrobial experiment. Dr. Li Xiang, Wenshuai Yang, and Dr. Xing-Zhen Chen helped with the manuscript revision. Dr. Hongbo Zeng was the corresponding author and involved in the experimental design and manuscript composition.

Acknowledgements

First of all, I would like to acknowledge the guidance provided by Prof. Hongbo Zeng. Prof. Zeng has introduced me to the field of colloidal and interface science and provided valuable advice and vast knowledge in many areas, not only in academic research but also in entire career path. With the fantastic experiment facilities and free academic atmosphere provided by Prof. Zeng, I could generate very creative ideas and conduct my own research work with a high-quality criterion. I would take Prof. Zeng as a role model for my entire life.

I must express my gratitude to Dr. Lu Gong, a senior PhD student in our research group, for his constructive guidance on my surface force measurement experiment. Besides, I would like to thank all my group members and co-authors especially Wenda Wang, Li Xiang, Jingsi Chen, Meng Wu, and Wenshuai Yang for their kind support in all aspects during my PhD study.

My deep thanks go to my family, especially my parents, for pushing me towards pursuing my PhD's Degree, for never losing faith and for their unbounded support.

In conclusion, I recognize that this research would not have been possible without the financial assistance of Natural Sciences and Engineering Research Council of Canada (NSERC), Canada Foundation for Innovation (CFI), Future Energy System under the Canada First Research Excellence Fund, and the Canada Research Chairs Program (H. Zeng), the Department of Chemical and Materials Engineering at the University of Alberta, and express my gratitude to those agencies.

Table of Contents

List of Tables

List of Figures

List of Abbreviations

mfp	mussel foot protein
DOPA	amino acid 3,4- dihydroxyphenyl-L-alanine
SFA	surface force apparatus
AFM	atomic force microscopy
PDA	polydopamine
PVP	poly(N-vinyl pyrrolidone)
PP	polypropylene
PEI	polyethyleneimine
TA	tannic acid
GO	graphene oxides
Np	nanoparticles
CVD	Chemical vapor deposition
AP	atmospheric-pressure plasma
DTO	dopamine-triggered one-step
PC	polymerization and codeposition
PSBMA	poly(sulfobetaine methacrylate)
O/W	oil-in-water

ATRP	surface-initiated atomic transfer radical polymerization
DA	dopamine
MTAC	{2-(methacryloy-loxy)ethyl}trimethylammonium chloride
SDS	sodium dodecyl sulfate
CTAB	cetrimonium bromide
PVDF	polyvinylidene fluoride
UV	ultraviolet
SEM	emission scanning electron microscope
EDS	energy-dispersive X-ray spectroscopy
SEM	emission scanning electron microscope
FTIR	Fourier transform infrared
OCA	oil contact angle
DLS	dynamic laser scattering
$\theta_{W/A}$	water contact angle
DLVO	Derjaguin-Landau-Verwey-Overbeek
VDW	van der Waals
EDL	electrical double layer
C_f	fraction of the concentration

3D	three-dimensional
C_{18}	stearyl methacrylate
AM	acrylamide
CHO	Chinese hamster ovary
HEK	human embryonic kidney
DMEM	Dulbecco's Modified Eagle Medium
FBS	fetal bovine serum
PBS	phosphate-buffered saline
AF	Aquaflex
nBUA	ultrasound attenuation
WC	water content
W_i	initial weight
W_d	lyophilized weight
U_T	toughness
Hb	hydrophobic
BAC	benzalkonium chloride
CTAC	cetyltrimethylammonium chloride
PEGDA	poly(ethylene glycol) diacrylate

NaOH	sodium hydroxide
HCl	hydrogen chloride
S	electrical conductivities
L	gauge length
A	cross-sectional area
R_b	bulk resistance
$\Delta R / R_0$	variation of resistance
I_0	current at t = 0
I	measured current
CM	cationic micelle
GF	gauge factor

CHAPTER 1. Introduction

Nature not only affords us abundant natural resources but also provides us with various bionic resources for the advancement of cutting-edge technology [1-3]. The translation of the unique features developed by the nature to our synthetic systems requires a comprehensive understanding of the correlated chemical, structural, and mechanical principles. For instance, through the exploration of the structure belonging to spider silk and lotus leaf, researchers have successfully developed the tough fabrics and superhydrophobic surfaces, respectively [4-7]. Both of the cases are the huge breakthrough in the area of biomimetic materials that can be used in the demanding environment.

Achieving robust adhesion in the wet environment is always desirable for many medical and industrial applications, like the surgery on wet tissues and operations in the aqueous environment. In order to solve this insurmountable challenge, the adhesion behavior of marine mussels has raised the interest of many researchers. Marine mussel byssal plaque could rapidly and tightly attach to various solid surfaces including racks and steel plates before the next coming waves [8]. This brings new opportunities to develop advanced materials with wet adhesive properties as most of the existing adhesives suffer from the decline of adhesion performance in the wet environment.

1.1 Mussel-inspired Catechol Chemistry

1.1.1 Mussel foot proteins

Mussel attachment tenacity is enabled by a bundle of radially distributed threads, called byssus, with four parts: adhesive plaque, thread comprising distal and proximal portions, stem, and root, as shown in Figure 1.1 [9]. The entire thread is protected by a cuticle, which contains

one type of mussel foot protein (mfp) called mfp-1. Within the plaque, five major proteins with different sequences are identified to be mfp-2, mfp-3, mfp-4, mfp-5, and mfp-6, respectively. Among all these mfps, mfp-3 and mfp-5 that abundantly appear at the plaque-substrate interface are believed to play a distinct and critical role in the robust adhesion capability of mussel byssus [10]. Both mfp-3 and mfp-5 contain high content of post-translationally modified amino acid 3,4-dihydroxyphenyl-L-alanine (DOPA), which is regarded as the most important adhesive component. In order to further figure out the interaction mechanism of mfps with substrate surfaces, two unique instruments, surface force apparatus (SFA) and atomic force microscopy (AFM) are utilized to directly quantify the correlated interaction forces, which would be discussed in the next section.

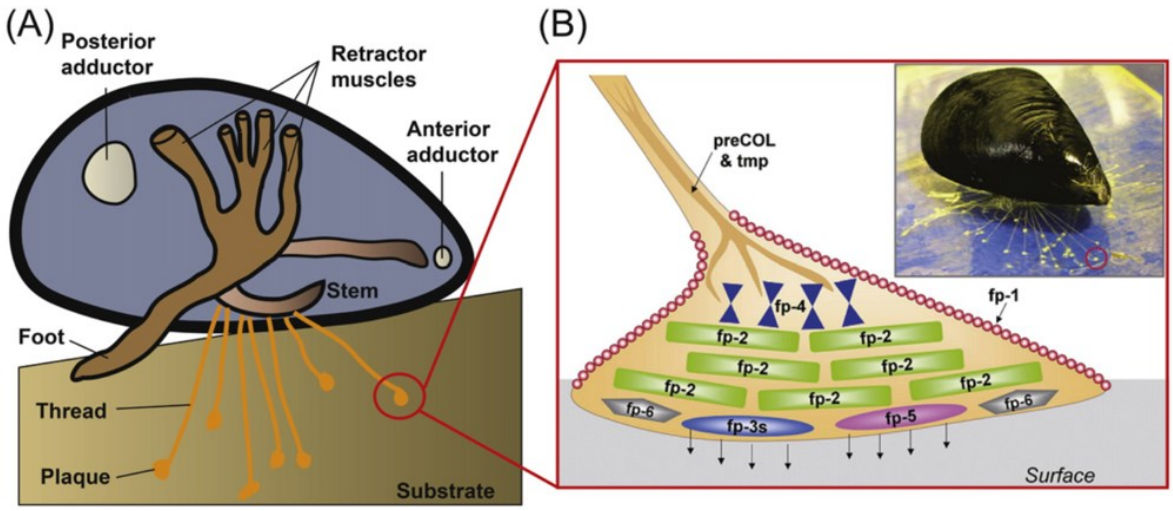

Figure 1.1 (A) Schematic showing a mussel attached to a substrate surface. One of the byssal plaques (red circle) is enlarged as a schematic (B) to illustrate the known distribution of mussel foot proteins (mfp) in the literature, with the inset showing the attachment of a mussel to a sheet of mica (Reprinted with permission from reference [9], © Elsevier).

1.1.2 Mussel-inspired covalent and non-covalent interactions

Mussel adhesion is attributed to the integration of multiple DOPA-mediated interactions and greatly affected by the targeting substrates. Figure 1.2 presents the possible covalent and non-covalent interactions that are coexisted in the marine Mussel systems [9, 11].

a) Hydrogen bonding. Catechol groups of DOPA with two neighboring hydroxyl groups can act as hydrogen donors/acceptors and provide anchoring points to the natural metal oxide surfaces like rocks. The adhesion of mfp-1, mfp-3, and mfp-5 to the fresh cleaved mica and OH-terminated surfaces was characterized using SFA, of which mfp-3 exhibited the highest adhesion due to its high content of DOPA and flexible molecular chain [12].

b) Coordination bond. Metal coordination commonly appears in the biological systems between proteins and transition metal ions like Ca^{2+}, Zn^{2+}, and Fe^{3+}. Within the byssus of marine mussel, DOPA–Fe^{3+} coordination complex was found in the cuticle, which is responsible for its high stiffness and elasticity. The metal coordination between mfp-1 and Fe^{3+} was comprehensively studied by Zeng *et al.* using SFA [13]. As shown in Figure 1.3, a strong and reversible bridging effect between two mfp-1 films was observed by injecting 10 μm Fe^{3+} while pH is also found to significantly affect the complexation of Fe^{3+}. By increasing pH from 2 to 7, the DOPA–Fe^{3+} coordination complex varied from mono-complex to tris-complex, thus resulting in the decreased interfacial adhesion and increased cohesion tendency. The above fundamental research provides a viable paradigm to develop DOPA-modified adhesive materials with tunable adhesion and cohesion strength modulated by concentration of Fe^{3+} and solution pH.

c) Schiff base reaction or Michael addition. The quinone groups generated by the oxidized catechol can react with amino and thiol groups that existed in mfps via Schiff base

reaction or Michael addition, which enhances the cohesive strength of mfps. Due to the mild reaction conditions of Schiff base reaction or Michael addition in aqueous solution (room temperature and pH>5), a serious self-assemble coating materials have been developed using natural polyphenol and amino group-enriched polymers with the enhanced deposition efficiency [14, 15].

d) Cation-π interaction. Cation–π interaction is a non-covalent interaction that exists between cations and electron-rich π orbitals. With the coexistence of protonated amino groups and benzene groups belonging to DOPA, tyrosine, and phenylalanine, cation–π interaction along with Schiff base reaction or Michael addition substantially contributes to the cohesion of mussel byssus [16, 17].

e) Hydrophobic interaction. Hydrophobic interaction is intrinsically an entropy-driven spontaneous process that widely exists between hydrophobic groups in the aqueous solution. The interaction between mfps and hydrophobic surface (i.e, CH_3-modified mica surface) was quantified by Israelachvili. Due to the high content of aromatic amino acid DOPA, mfp-3 and mfp-5 exhibit the higher adhesion strength (8.9 ± 0.2, and 6.7 ± 0.2 mJ m^{-2}) compared to that of mfp-1 (3.5 ± 1.0 mJ m^{-2}) [12]. These results indicate that the mussel byssus can interact with the hydrophobic moieties of a target substrate, thus facilitating robust adhesion.

(A) Mussel-mediated crosslinking reaction

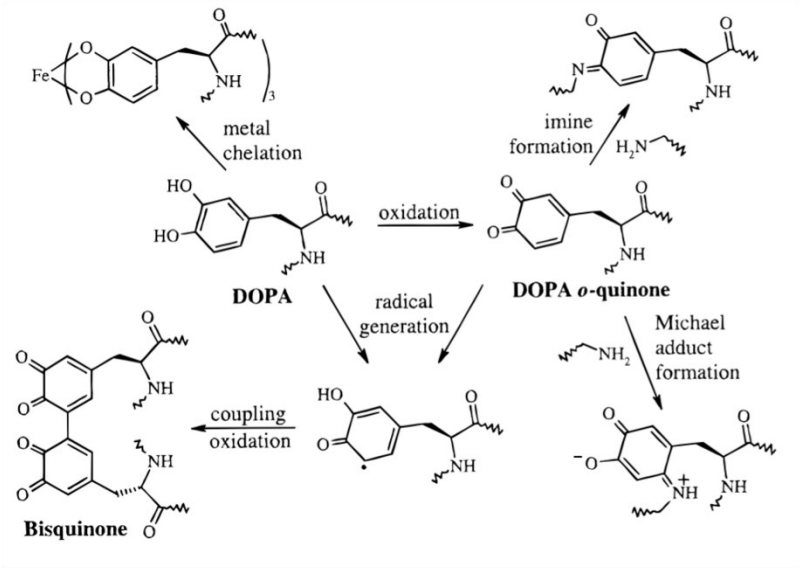

(B) Mussel-mediated adhesion to substrates

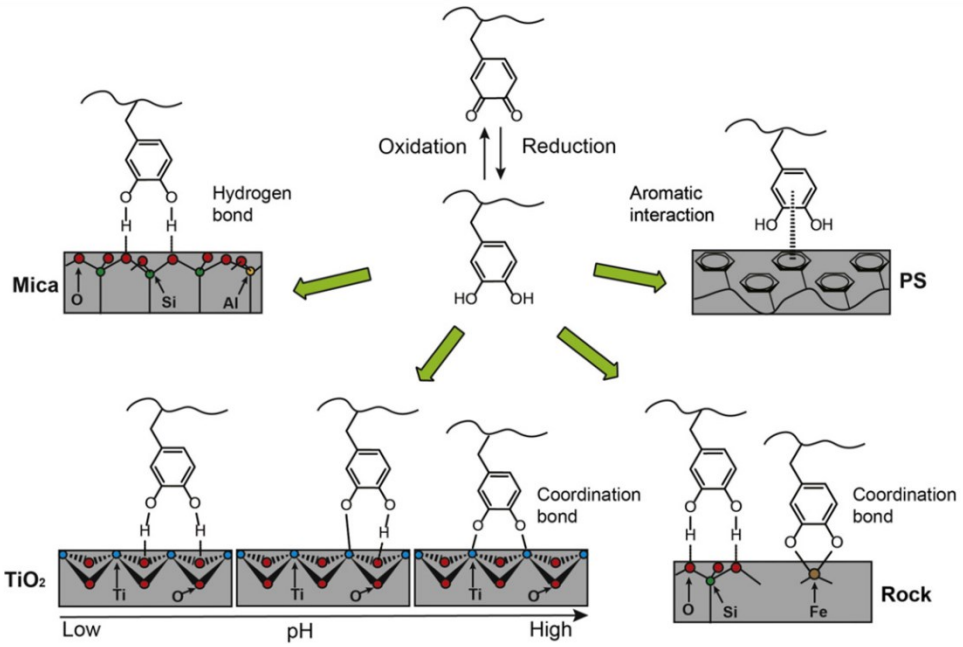

Figure 1.2 (A) Cross-linking Reaction Pathways for DOPA and DOPA o-Quinone Residues (Reprinted with permission from reference [10], © American Chemical Society); (B) Adhesion of mussel proteins to different substrates with the associated interaction mechanisms (Reprinted with permission from reference [9], © Elsevier).

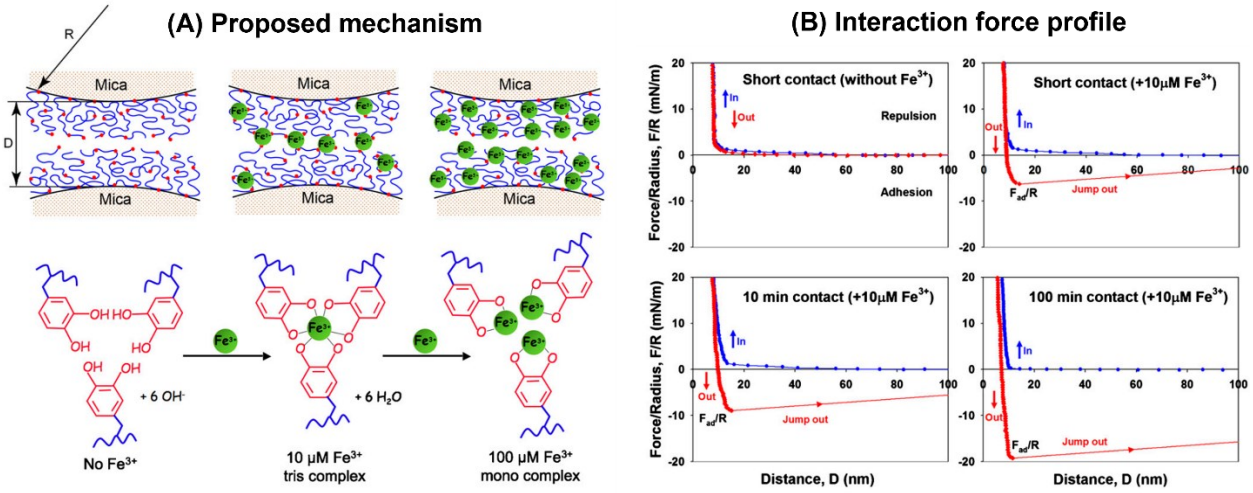

Figure 1.3 (A) SFA experiments of mfp-1 with different amount of Fe^{3+}; (B) The corresponding interaction force profiles (Reprinted with permission from reference [13], © States National Academy of Sciences).

1.2 Mussel-inspired Coating Materials

In many practical applications, engineering the desirable surface properties has always been a challenge. Conventional surface modification methods like chemical vapor deposition and polymer grafting method typically have some drawbacks such as strict operation conditions (high temperature and pressure) and complicated pre-treatment process on the substrate surfaces. Inspired by the universal adhesion behavior of marine mussels, Messersmith *et al.* first reported a universal deposition strategy using one of the catechol-based derivatives, dopamine, to form a polydopamine (PDA) coating on various substrates in a mild alkaline solution of atmospheric temperature and pressure [18]. PDA coating processes the advantage of surface independent, mild operation conditions, capable of forming strong binding with the target surfaces, and appliable for further functionality.

Based on this pioneer work, a great number of mussel-inspired coating strategies have been proposed using diverse catechol-based derivatives (dopamine, tannic acid, gallic acid, and caffeic acid) to develop multifunctional coating materials [10]. More specifically, these codeposition methods are designed based on the different mussel-inspired surface interactions. For instance, Xu *et al.* reported an antifouling and antimicrobial PDA/poly(N-vinyl pyrrolidone) (PVP) coating deposited on polypropylene (PP) membrane [19]. The modification is a two-step approach, PP membrane is first deposited with an intermediate PDA layer, followed by the coating of PVP. Due to the strong noncovalent interactions (mainly hydrogen bond) between PDA and PVP, the obtained PDA/PVP-coated PP membrane exhibited a long-term stability and durability for filtrating wastewater with antifouling peripeties against oils and proteins. Besides the noncovalent interactions, covalent interactions like Schiff base reaction/Michael addition have also been employed for the surface modification process. The codeposition of dopamine and polyethyleneimine (PEI) is a one-step process and the obtained PDA/PEI coating layer exhibited an enhanced underwater superoleophobicity and high positive surface charge [20, 21]. Therefore, the developed PDA/PEI coating could be used in applications such as the separation of negatively-charged contaminants like dyes, proteins, and oils. More recently, it was reported that the semiquinone radical species generated by the oxidation of dopamine are capable of triggering the polymerization of acrylate monomers in mild alkaline solution [22, 23]. The codeposition of dopamine with these acrylate monomers could form a dense and uniform coating layer. The obtained PDA-polyacrylate coating is interconnected by covalent bonds which endows the codeposited layer an enhanced stability. Compared to some grafting methods used to prepare polymer coating, the PDA codeposition method exhibits a high flexibility. The desired surface functionality (i.e., pH and temperature responsible surfaces) on the target substrate

surfaces can be readily realized by selecting the proper acrylate monomers (like acrylic acid and N-isopropyl acrylamide) containing the corresponding functional groups. Benefited from the mussel-related surface interaction study, numerous catechol-based coating strategies have been proposed and applied in many practical applications due to the precise modulation of both the noncovalent and covalent interaction between catechol-based derivatives and co-components to form a stable codeposition layer on the surface of the target substrates. Besides the modification of membrane substrates, catechol-based derivatives including tannic acid (TA) and PDA were also applied to modify the surface properties of some 2D materials, especially the carbon-based 2D materials like graphene oxides (GO). Recently, Zeng *et al.* reported the fabrication of Ag nanoparticle (Np)/TA-grafted magnetic GO sheets for the high-efficient reduction of organic pollutants in wastewater [24]. Due to the multiple intermolecular interactions (π-π stacking, electrostatic interaction, and hydrogen bonding), the deposition of tannic acid on the GO sheets is fast and uniform, typically within 1 min, thus providing abundant anchoring points for the loading of Ag nanoparticles (Np). The as-prepared Ag Np/TA-mGO sheets exhibited an ultrahigh catalytic rate constant of 5.4×10^{-2} s^{-1} for the reduction of methylene blue, which is around one order magnitude higher than the previously reported value in the literature.

1.3 Mussel-inspired Adhesive Materials

Although mfp-3 and mfp-5 have proven to be the primer to enable underwater adhesion, the production of mfp-3 and mfp-5 greatly relies on the extraction from mussels. It is costly and not quite feasible to achieve the large-scale production of these mfp-based adhesives. In order to figure out a more appliable approach, Waite *et. al.* first proposed a synthesis route by mimicking

the natural catechol-containing siderophores [25]. The developed Tren-Lys-Cam can reject the hydrated ions adsorbed on mica surfaces and exhibited a robust adhesion energy in saline solution under a wide range of pH (from 3.3 to 7.5), characterized by SFA. After that, several different catechol-containing adhesive polymers have been developed by incorporating DOPA moieties into the backbones, side chains, or end groups of polymers. These polymers resemble the wet adhesion behavior of mussels to some content.

Beyond the mussel-inspired adhesive polymers which mostly served as thin cell loading coating or bio-glue, mussel-inspired adhesive hydrogels have also been developed and applied for many biomedical applications [26]. Unlike the polymer materials, adhesive hydrogels are usually premolded during the preparation and have a fixed shape. The adhesive hydrogels containing catechol-derivatives can form stable fixation with the target tissue surfaces instantly and served as the scaffold for the delivery of drugs and acoustical or optical signals, which benefits the diagnosis and treatment for the clinical applications. For instance, Lu *et. al.* developed a tough and adhesive hydrogel by confining PDA between clay sheets [27]. The obtained PDA-clay-PAM hydrogel was used as the scaffold for the loading of epidermal growth factor (EGF) and served as the wound dressing for dermal regeneration. The wound area treated by EGF-loaded PDA-clay-PAM hydrogel exhibited a 15 % higher healing rate than that of the unloaded PDA-clay-PAM hydrogel.

1.4 Objectives

Despite remarkable achievement has been achieved in analyzing the mussel-inspired chemistry and advancement of catechol-containing coating and adhesive materials, it remains a challenge to integrate the desirable functionalities (e.g., tunable surface properties for mussel-inspired antifouling coating, water-repelling capability and on-demand removability for mussel-inspired adhesives, etc.) that can adapt to the varying terminal requirements in practical applications. In order to achieve these functions, drop probe and colloidal probe AFM techniques were first employed to investigate the nanomechanics of the catecholic systems which benefits the molecular engineer of the coating and adhesive materials with desired interfacial properties and optimized performance towards their functions.

The overall objective of this thesis is to design mussel-inspired polymeric systems based on mussel-correlated dynamic molecular interactions and to use these polymeric systems to help construct functional materials with potentials for environmental and biomedical applications such as antifouling coatings, underwater tissue adhesives, and couplant for acoustical imaging. Meanwhile, the corresponding molecular interaction mechanisms are also investigated. The detailed objectives are listed as follows.

(1) Develop a mussel-inspired antifouling coating bearing adjustable surface charge property, employing tunable long-range electrostatic interaction to achieve adaptive antifouling performance in response to the varying electrical characteristic of emulsions. Drop probe atomic force microscope (AFM) techniques were used to measure the surface forces between surfactant-stabilized emulsion droplets and the developed coating to unravel the fouling/antifouling mechanisms for oil/water separation.

(2) Develop an adhesive hydrogel covered by an outermost hydrophobic layer as the tissue couplant to enable the water-repelling and rapid underwater adhesion for reliable ultrasound imaging in the wet intraoral environment. Colloidal probe AFM techniques were used to investigate the interaction forces between the sulfonates and PDA-Fe^{3+} complex to unravel the assembling mechanisms for the hydrophobic layer of the hydrogel driven by metal coordination chemistry.

(3) Develop a novel hydrogel ionic conductor composed of a cationic micelle cross-linked polymer network with bridging polymers to enable the controllable wet adhesive property to various substrates. Rheological and tensile measurements were used to investigate the effect of multiple noncovalent interactions (hydrogen bonding, hydrophobic and cation-π and π-π interactions) on the mechanical properties of the developed conductive hydrogel as the strain sensor.

References

[1] A. Mahdavi, L. Ferreira, C. Sundback, J.W. Nichol, E.P. Chan, D.J. Carter, C.J. Bettinger, S. Patanavanich, L. Chignozha, E. Ben-Joseph, A biodegradable and biocompatible gecko-inspired tissue adhesive, Proceedings of the National Academy of Sciences, 105 (2008) 2307-2312.

[2] M.P. Murphy, B. Aksak, M. Sitti, Gecko - inspired directional and controllable adhesion, Small, 5 (2009) 170-175.

[3] H. Zhao, Q. Sun, X. Deng, J. Cui, Earthworm - Inspired Rough Polymer Coatings with Self - Replenishing Lubrication for Adaptive Friction - Reduction and Antifouling Surfaces, Advanced Materials, 30 (2018) 1802141.

[4] Y.-T. Cheng, D.E. Rodak, Is the lotus leaf superhydrophobic?, Applied physics letters, 86 (2005) 144101.

[5] H.J. Ensikat, P. Ditsche-Kuru, C. Neinhuis, W. Barthlott, Superhydrophobicity in perfection: the outstanding properties of the lotus leaf, Beilstein journal of nanotechnology, 2 (2011) 152-161.

[6] S.S. Latthe, C. Terashima, K. Nakata, A. Fujishima, Superhydrophobic surfaces developed by mimicking hierarchical surface morphology of lotus leaf, Molecules, 19 (2014) 4256-4283.

[7] T. Lefèvre, M. Auger, Spider silk inspired materials and sustainability: perspective, Materials Technology, 31 (2016) 384-399.

[8] J.H. Waiter, Reverse engineering of bioadhesion in marine mussels, Annals of the New York Academy of Sciences, 875 (1999) 301-309.

[9] L. Li, H. Zeng, Marine mussel adhesion and bio-inspired wet adhesives, Biotribology, 5 (2016) 44-51.

[10] B.P. Lee, P.B. Messersmith, J.N. Israelachvili, J.H. Waite, Mussel-inspired adhesives and coatings, Annual review of materials research, 41 (2011) 99-132.

[11] M. Yu, J. Hwang, T.J. Deming, Role of L-3, 4-dihydroxyphenylalanine in mussel adhesive proteins, Journal of the American Chemical Society, 121 (1999) 5825-5826.

[12] J. Yu, Y. Kan, M. Rapp, E. Danner, W. Wei, S. Das, D.R. Miller, Y. Chen, J.H. Waite, J.N. Israelachvili, Adaptive hydrophobic and hydrophilic interactions of mussel foot proteins with organic thin films, Proceedings of the National Academy of Sciences, 110 (2013) 15680-15685.

[13] H. Zeng, D.S. Hwang, J.N. Israelachvili, J.H. Waite, Strong reversible Fe3+-mediated bridging between dopa-containing protein films in water, Proceedings of the National Academy of Sciences, 107 (2010) 12850-12853.

[14] H.C. Yang, M.B. Wu, Y.J. Li, Y.F. Chen, L.S. Wan, Z.K. Xu, Effects of polyethyleneimine molecular weight and proportion on the membrane hydrophilization by codepositing with dopamine, Journal of Applied Polymer Science, 133 (2016).

[15] W.-Z. Qiu, H.-C. Yang, Z.-K. Xu, Dopamine-assisted co-deposition: an emerging and promising strategy for surface modification, Advances in colloid and interface science, 256 (2018) 111-125.

[16] Q. Lu, D.X. Oh, Y. Lee, Y. Jho, D.S. Hwang, H. Zeng, Nanomechanics of cation–π interactions in aqueous solution, Angewandte Chemie, 125 (2013) 4036-4040.

[17] L. Xiang, J. Zhang, W. Wang, L. Gong, L. Zhang, B. Yan, H. Zeng, Nanomechanics of π-cation-π interaction with implications for bio-inspired wet adhesion, Acta Biomaterialia, 117 (2020) 294-301.

[18] H. Lee, S.M. Dellatore, W.M. Miller, P.B. Messersmith, Mussel-inspired surface chemistry for multifunctional coatings, science, 318 (2007) 426-430.
[19] J. Jiang, L. Zhu, L. Zhu, H. Zhang, B. Zhu, Y. Xu, Antifouling and antimicrobial polymer membranes based on bioinspired polydopamine and strong hydrogen-bonded poly (N-vinyl pyrrolidone), ACS applied materials & interfaces, 5 (2013) 12895-12904.
[20] C. Zhao, F. Zuo, Z. Liao, Z. Qin, S. Du, Z. Zhao, Mussel‐Inspired One‐Pot Synthesis of a Fluorescent and Water‐Soluble Polydopamine–Polyethyleneimine Copolymer, Macromolecular rapid communications, 36 (2015) 909-915.
[21] W.-Z. Qiu, H.-C. Yang, L.-S. Wan, Z.-K. Xu, Co-deposition of catechol/polyethyleneimine on porous membranes for efficient decolorization of dye water, Journal of Materials Chemistry A, 3 (2015) 14438-14444.
[22] C. Zhang, M.-Q. Ma, T.-T. Chen, H. Zhang, D.-F. Hu, B.-H. Wu, J. Ji, Z.-K. Xu, Dopamine-Triggered One-Step Polymerization and Codeposition of Acrylate Monomers for Functional Coatings, ACS applied materials & interfaces, 9 (2017) 34356-34366.
[23] M. Pan, L. Gong, L. Xiang, W. Yang, W. Wang, L. Zhang, W. Hu, L. Han, H. Zeng, Modulating surface interactions for regenerable separation of oil-in-water emulsions, Journal of Membrane Science, 625 (2021) 119140.
[24] W. Yang, W. Hu, J. Zhang, W. Wang, R. Cai, M. Pan, C. Huang, X. Chen, B. Yan, H. Zeng, Tannic acid/Fe3+ functionalized magnetic graphene oxide nanocomposite with high loading of silver nanoparticles as ultra-efficient catalyst and disinfectant for wastewater treatment, Chemical Engineering Journal, 405 (2021) 126629.
[25] G.P. Maier, M.V. Rapp, J.H. Waite, J.N. Israelachvili, A. Butler, Adaptive synergy between catechol and lysine promotes wet adhesion by surface salt displacement, Science, 349 (2015) 628-632.
[26] M. Pan, K.-C.T. Nguyen, W. Yang, X. Liu, X.-Z. Chen, P.W. Major, L.H. Le, H. Zeng, Soft armour-like layer-protected hydrogels for wet tissue adhesion and biological imaging, Chemical Engineering Journal, 434 (2022) 134418.
[27] L. Han, X. Lu, K. Liu, K. Wang, L. Fang, L.-T. Weng, H. Zhang, Y. Tang, F. Ren, C. Zhao, Mussel-inspired adhesive and tough hydrogel based on nanoclay confined dopamine polymerization, ACS nano, 11 (2017) 2561-2574.

CHAPTER 2. Major Experimental Methods

2.1 Surface modification

2.1.1 Conventional surface modification strategies

In order to enhance the stability of coating materials to the target substrates, several surface modification strategies such as water plasma treatment, chemical vapor deposition, and silane self-assembly have been explored previously to generate active anchoring sites for the further deposition of coating materials. Water plasma treatment is usually employed as the primary step of surface modification by introducing -OH moieties as the reactive sites for post polymer grafting. A wide range of substrates including silicon, mica, and polymers are found to be appliable that could be etched by the OH radicals generated by the water plasma [1-3]. Chemical vapor deposition (CVD) is a one-step, solventless, and substrate-independent process that is used to deposit polymeric coatings on the target substrates [4, 5]. CVD process could also be coupled with plasma treatment, namely, atmospheric-pressure plasma-enhanced chemical vapor deposition (AP-PECVD), to enhance its productivity. With the addition of monomers and initiators in the fed into a vacuum chamber, the free radical polymerization occurred simultaneously with the deposition to generate the long-lasting surface functionalities on the material surfaces [6]. Besides the gaseous modification methods, dip coating-based strategies such as self-assembled silane-based modification also attracted significant attention due to their conveniency and no instrument requirement. Silane chemicals could form a highly ordered and well-packed monolayer on the solid substrates. However, due to the high reactivity of silane chemistry, a careful handling of operation is required, more specifically, avoiding the contact of silanes with water during the assembly process [7].

2.1.2 Dopamine-triggered one-step polymerization and codeposition strategy

Dopamine-triggered one-step polymerization and codeposition (DTO-PC) strategy is an emerging technique that was first proposed in 2008 [8]. Unlike the conventional surface modification strategies that usually suffer from complicated preparation procedures and limited density of deposited active reaction sites for post modification, DTO-PC strategy exhibited to be a fast, versatile, and universal deposition approach benefited from the comprehensive investigation of mussel-inspired catechol chemistry. The universal deposition of dopamine-based coating materials is attributed to its self-polymerization to form polydopamine (PDA) coating which is capable of forming multiple interactions with substrate surfaces such as the hydrogen bond to hydrophilic surfaces, hydrophobic and aromatic interactions to hydrophobic surfaces, and coordination bond to some of the metal and metal oxide surfaces [9]. Due to the diverse anchoring mechanisms, the deposited polydopamine coating typically shows a high coverage and stability on the substrate surfaces. Meanwhile, it is found that the oxidative polymerization of dopamine could generate semiquinone radical species, as shown in Figure 2.1 [8, 10]. The free radicals generated by the oxidation process of dopamine could be used to trigger the polymerization of acrylate monomers. Herein, this one-step coating strategy is proposed that dopamine and acrylate monomers are codeposited to form the coating materials. In this coating process, dopamine can simultaneously act as the surface anchoring agent and polymerization initiator of acrylate monomers. For instance, the PDA/poly(sulfobetaine methacrylate) (PSBMA)-coated substrates such as silicon wafers, aluminum sheets, gold, poly(ethylene terephthalate), and polyimide films exhibited a significant decrease in water contact angle compared to the bare or pure PDA-coated ones, indicating the successful incorporation of superhydrophilic zwitterionic sulfobetaine moieties into the coating materials. On the basis of

this novel coating strategy, the codeposition of dopamine with different monomers carrying opposite charges (e.g., acrylic acid and [2-(Methacryloyloxy)ethyl]trimethylammonium chloride) would be investigated in this work and the applications of the developed coating materials would also be explored.

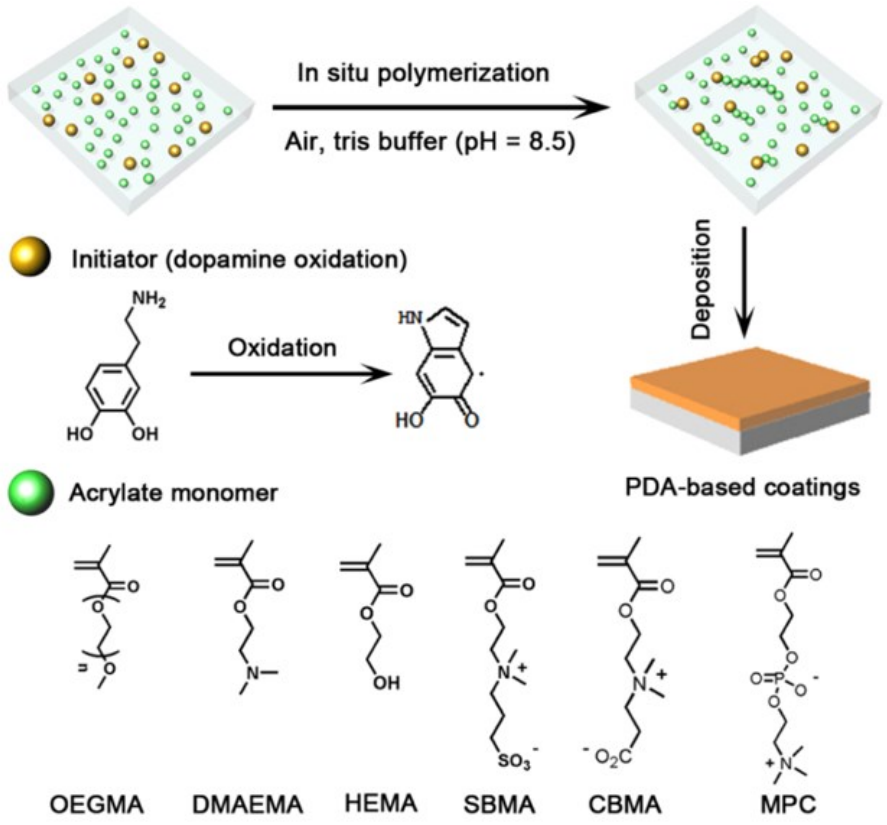

Figure 2.1 The synthesis process of PDA-based coatings using dopamine and acrylate monomers (Reprinted with permission from reference [8], © American Chemical Society).

2.2 Characterization of surface morphology using AFM imaging

In this thesis project, the morphology of the polymer film and PDA coating will be characterized by the MFP-3D AFM system (Asylum Research, Santa Barbara, CA, USA. AFM contains piezoelectric scanners, force transducers, and feedback controllers to produce a nanometre-scale resolution, which meets the requirement of this project to characterize the nano-scale morphology. Basically, the piezoelectric transducer controls the movement of the tip over the sample surface, the force transducer senses the force between the tip and the surface, and the feedback control receives the transmitted error signals from the force transducer back to the piezoelectric scanners, to maintain the setpoint for force between the tip and the sample. For AFM imaging in tapping mode, a piezoelectric transducer drives the oscillation of cantilever, as shown in Figure 2.2 [11]. The oscillating cantilever is driven to approach sample surfaces until a proper height is reached. While performing a tapping mode for imaging, tips are intermittent-contact with surfaces [12]. The interaction between tips and surfaces will certainly change the amplitude of the tips, resulting in a difference between the input and output signals for the calculation of the relative surface morphology. Considering the softness of the polymer-based materials, imaging in tapping mode is preferred to avoid the direct contact between the tip and sample surface. The silicon probe (NCHV-A, Bruker) is respectively used for tapping mode imaging in air to optimize the parameters of the coating conditions. The topography and roughness of the coating materials could be analyzed from the obtained AFM topographic images. According to the results from AFM images, the composition of the coating solution would be adjusted to improve the coverage and uniformity of the coatings which is significant to their surface and interfacial properties.

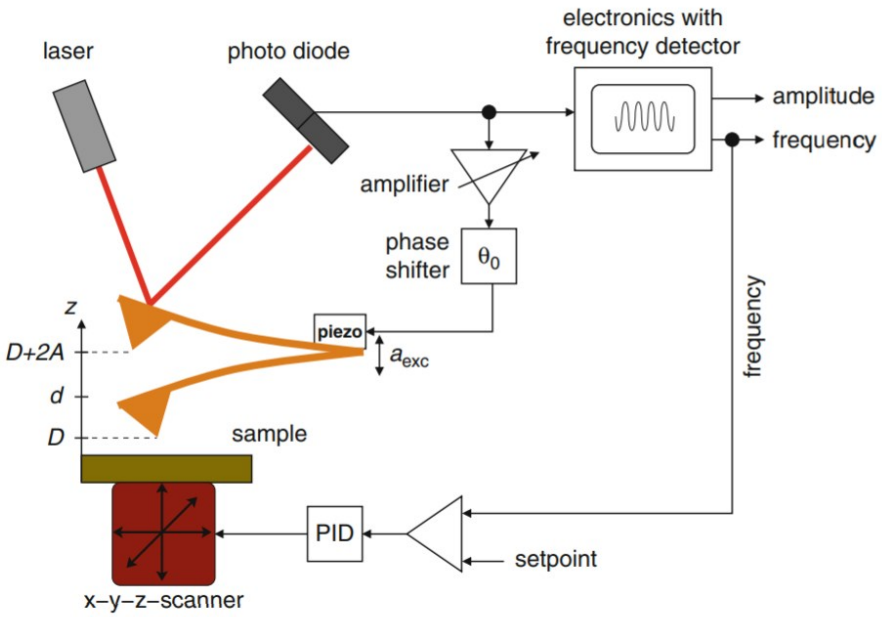

Figure 2.2 The schematic drawing of a AFM setup in tapping mode including the laser, scanning probe, detector, and feedback control system. (Reprinted with permission from reference [11], © Springer).

2.3 Drop-probe AFM techniques for force measurement

Surface force measurement is significant to characterize the interaction mechanisms between a soft oil/water interface and the surface of coating materials. The interaction forces between a surfactant-stabilized oil droplet and the coated surfaces will be measured through droplet probe AFM techniques using the force modulation of MFP-3D AFM system (Asylum Research, Santa Barbara, CA, USA). During the force measurement experiments, the oil droplets will be generated by a custom-made ultrasharp glass pipet and immobilized on a glass disk in an aqueous solution where one of the droplets will be picked up with a hydrophobized rectangular AFM cantilever as shown in Figure 2.3. Then, the cantilever-anchored droplet will be moved to the place above substrate surfaces in solutions for force measurements [13]. The force

measurements will be conducted at a constant driving velocity and the transmitted signal of interaction forces will be recorded as a function of time by the Asylum Research system [14-16].

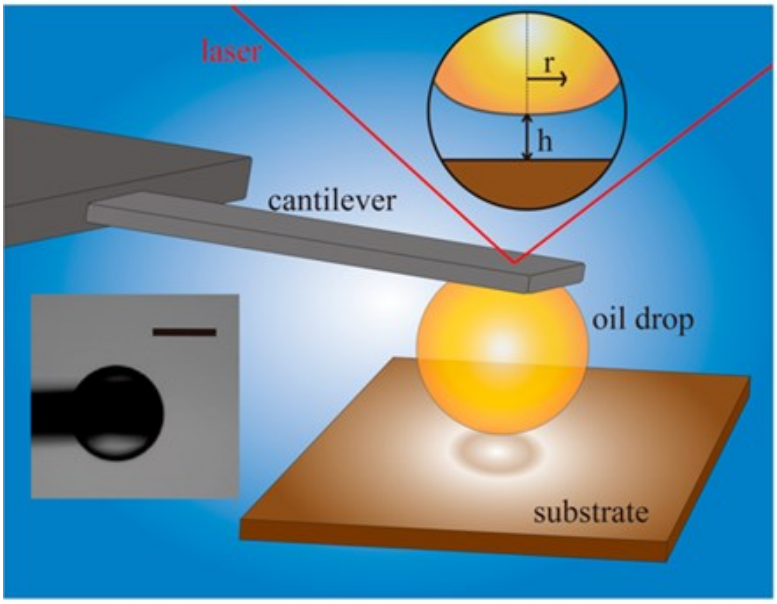

Figure 2.3 Schematic of typical experimental setup for surface force measurements between an oil drop and a substrate in aqueous solution using the drop probe AFM technique. The top inset shows the central interaction region between an oil drop and a flat substrate, and the left inset shows a microscopic image of a typical drop probe prepared (scale bar = 100 μm). (Reprinted from reference [12] with the permission, *Energy & Fuels 2018*)

References

[1] M.S. Kang, B. Chun, S.S. Kim, Surface modification of polypropylene membrane by low-temperature plasma treatment, Journal of applied polymer science, 81 (2001) 1555-1566.
[2] U. König, M. Nitschke, A. Menning, G. Eberth, M. Pilz, C. Arnhold, F. Simon, G. Adam, C. Werner, Durable surface modification of poly (tetrafluoroethylene) by low pressure H2O plasma treatment followed by acrylic acid graft polymerization, Colloids and Surfaces B: Biointerfaces, 24 (2002) 63-71.
[3] P. Luan, V.S.K. Kondeti, A.J. Knoll, P.J. Bruggeman, G.S. Oehrlein, Effect of water vapor on plasma processing at atmospheric pressure: Polymer etching and surface modification by an Ar/H2O plasma jet, Journal of Vacuum Science & Technology A: Vacuum, Surfaces, and Films, 37 (2019) 031305.
[4] M. Gupta, K.K. Gleason, Surface modification of high aspect ratio structures with fluoropolymer coatings using chemical vapor deposition, Thin Solid Films, 517 (2009) 3547-3550.
[5] N. Chen, D.H. Kim, P. Kovacik, H. Sojoudi, M. Wang, K.K. Gleason, Polymer thin films and surface modification by chemical vapor deposition: Recent progress, Annual review of chemical and biomolecular engineering, 7 (2016) 373-393.
[6] D. Lee, S. Yang, Surface modification of PDMS by atmospheric-pressure plasma-enhanced chemical vapor deposition and analysis of long-lasting surface hydrophilicity, Sensors and Actuators B: Chemical, 162 (2012) 425-434.
[7] C. Haensch, S. Hoeppener, U.S. Schubert, Chemical modification of self-assembled silane based monolayers by surface reactions, Chemical Society Reviews, 39 (2010) 2323-2334.
[8] C. Zhang, M.-Q. Ma, T.-T. Chen, H. Zhang, D.-F. Hu, B.-H. Wu, J. Ji, Z.-K. Xu, Dopamine-Triggered One-Step Polymerization and Codeposition of Acrylate Monomers for Functional Coatings, ACS applied materials & interfaces, 9 (2017) 34356-34366.
[9] C. Zhang, Y. Ou, W.X. Lei, L.S. Wan, J. Ji, Z.K. Xu, CuSO4/H2O2 - induced rapid deposition of polydopamine coatings with high uniformity and enhanced stability, Angewandte Chemie International Edition, 55 (2016) 3054-3057.
[10] M. Yu, J. Hwang, T.J. Deming, Role of L-3, 4-dihydroxyphenylalanine in mussel adhesive proteins, Journal of the American Chemical Society, 121 (1999) 5825-5826.
[11] A. Aliano, G. Cicero, H. Nili, N.G. Green, P. Garcıa-Sánchez, A. Ramos, A. Lenshof, T. Laurell, A. Qi, P. Chan, AFM, tapping mode, Encyclopedia of Nanotechnology, 99-99.
[12] Bruker, Bruker ICON3 AFM (Tapping Mode) Instruction, 2015.
[13] L. Gong, X. Qiu, L. Zhang, J. Huang, W. Hu, L. Xiang, D. Zhu, R. Sabbagh, M. Mahmoudi, V. Fattahpour, Probing the Interaction Mechanism between Oil-in-Water Emulsions and Electroless Nickel–Phosphorus Coating with Implications for Antifouling in Oil Production, Energy & Fuels, (2018).
[14] L. Zhang, L. Xie, C. Shi, J. Huang, Q. Liu, H. Zeng, Mechanistic Understanding of Asphaltene Surface Interactions in Aqueous Media, Energy & Fuels, 31 (2016) 3348-3357.
[15] C. Shi, L. Zhang, L. Xie, X. Lu, Q. Liu, J. He, C.A. Mantilla, F.G. Van den Berg, H. Zeng, Surface interaction of water-in-oil emulsion droplets with interfacially active asphaltenes, Langmuir, 33 (2017) 1265-1274.
[16] L. Xie, C. Shi, X. Cui, H. Zeng, Surface forces and interaction mechanisms of emulsion drops and gas bubbles in complex fluids, Langmuir, 33 (2017) 3911-3925.

CHAPTER 3. Modulating Surface Interactions for Regenerable Separation of Oil-in-Water Emulsions

3.1 Introduction

Oily wastewater, discharged by industrial production, such as the processing of crude oil and petrochemicals, is becoming a challenging problem due to environmental pollution and fouling issues. In general, oils in oily wastewater exist in three states, namely, floating state (oil spill), surfactant-free oil/water mixtures and surfactant-stabilized oil-in-water (O/W) emulsions according to the presence of interface-active chemicals. Compared to the surfactant-free oil/water mixtures, which are capable of autonomously coalescing and undergoing oil-water phase separation, O/W emulsions with surfactants are generally much more stable because of the interfacially adsorbed surfactants preventing the coalescence behaviors of emulsion drops, hence causing significant difficulties in the separation of dispersed oil phase from aqueous system [1-4]. Compared to the traditional separation methods such as flotation, biological and electrochemical treatment, membrane filtration possesses the advantages of high oil removal efficiency, low operation cost, and less secondary pollution. Thus, the membrane filtration method has been commonly utilized for O/W emulsion separation. However, membrane materials for filtration invariably suffer from fouling issues due to the adsorption of surfactants and oil drops on the membrane surface, resulting in the decline of permeation water flux and oil/water separation efficiency [5-9]. Therefore, it is highly desirable to develop antifouling strategies and materials for fabricating functional membranes for efficient separation of O/W emulsions.

In order to effectively inhibit the occurrence of membrane fouling, it is rational to generate strong repulsion between the potential foulants and membrane surface. In previous research,

different antifouling strategies have been developed, for example, via introducing hydrophilic components on the material surface including polyethylene glycol and titanium oxide nanoparticles as well as constructing hierarchical structure at nanoscale to trap abundant water as the physical barrier (hydration layer within several nanometers) [10-13]. Long-range surface interactions, such as electrostatic interactions allow the membranes to interact with the possible foulants at large separation distance of tens or even hundreds of nanometers, possibly preventing their attachment. Previous studies reported the effect of electrostatic repulsion on the emulsion filtration performance of separation membranes under fixed conditions [8, 14, 15]. However, studies on the dynamic adsorption behaviors and interaction mechanisms of surfactant-stabilized O/W emulsions with membrane surfaces are rather limited in the literature [16-20]. In practical cases, the interface-active chemicals from the oily wastewater are complicated which could make the oil/water interfaces carry different charges. Herein, developing antifouling materials with tunable electrostatic interactions is important to obtain the on-demand separation in response to the surface characteristics of target emulsions. Therefore, it is of both fundamental and practical importance to investigate the interaction mechanisms between emulsion drops and membrane possessing tunable surface charge property, which will provide useful implications for developing intelligent membrane materials for efficient oil/water separation.

Different methods have been reported to introduce charged functional polymers on material surfaces for modification, including photo-grafting, chemical vapor deposition, and surface-initiated atomic transfer radical polymerization (ATRP) [11, 21-23]. Recently, a mussel-inspired codeposition method of polydopamine (PDA) with functional polymers or acrylate monomers has been widely exploited for surface modification applications, for example, functionalizing nanoparticles, membranes, and sponges [24-30]. During the codeposition process,

PDA could act as both the anchoring point to the materials surface via catechol groups and the polymerization initiator due to the semiquinone-free radicals generated by the oxidation of the dopamine (DA) monomer in saline solution to trigger the polymerization of acrylate monomers. The obtained PDA-polymer composites turn to form a uniform coating layer to modulate the surface properties such as surface hydrophilicity and charge [31-33]. Compared to the conventional coating strategies, PDA codeposition-based strategy has the merit of being robust and versatile as a one-step polymerization and codeposition without extreme operating conditions which is promising for the scale-up of manufacturing functionalized materials with tunable surface charge for the practical separation of O/W emulsion.

Herein, inspired by the universal interfacial adhesion of marine mussels, we report a facile and scalable surface modification strategy to construct an adaptive antifouling coating on polyvinylidene fluoride (PVDF) membrane using PDA codeposition with cationic {2-(methacryloy-loxy)ethyl}trimethylammonium chloride (MTAC) and anionic acrylic acid (AA). The surface charge property of the obtained PDA-PAA-PMTAC coating can be tuned by adjusting the solution pH, which leads to the protonation/deprotonation of carboxylic functional groups on the surface. Zeta potential and contact angle measurements were used to characterize the surface charge property and wettability of the obtained coating. Atomic force microscope (AFM) drop probe technique was used to measure the surface forces between surfactant-stabilized emulsion droplets and the PDA-PAA-PMTAC coating under aqueous conditions with a series of pH values, aiming at unraveling the fouling/antifouling mechanisms for the membrane filtration. Vacuum filtration tests of the PDA-PAA-PMTAC-coated membrane were also conducted with O/W emulsions stabilized by different surfactants (i.e., CTAB and SDS). Particularly, the influence of solution pH on the water permeability and selectivity was

investigated. Our work provides useful insights into the fundamental interaction mechanisms associated with fouling and antifouling issues of surfactant-stabilized O/W emulsions on membrane surfaces as well as the development of functional membrane surfaces to eliminate the fouling problems.

3.2 Experimental Section

3.2.1 Materials

Dopamine hydrochloride, acrylic acid (AA), 2-methacryloyloxy ethyl trimethylammonium (MTAC), and silicon wafers were purchased from Sigma-Aldrich (Canada). Polyvinylidene fluoride (PVDF) membrane (diameter ~ 47mm, mean pore size ~ 0.22 μm), tris(hydroxymethyl)-aminomethane (Tris), sodium chloride, sodium hydroxide, ethanol, acetone, sodium dodecyl sulfate (SDS), and cetrimonium bromide (CTAB) were purchased from Fisher Scientific (Canada). Ultrafiltrated water used in all the experiments was generated by the Barnstead Smart2Pure pro water purification system (Thermo Scientific) with a resistivity of 18.2 MΩ·cm.

3.2.2 Preparation of PDA-PAA-PMTAC coating on silicon wafer and PVDF membrane

Silicon wafers were thoroughly washed repeatedly by water/ethanol and then placed in an ultraviolet (UV)/Ozone surface cleaner for 10 min. The PVDF membranes were washed by acetone overnight to remove the adsorbed impurities followed by the cleaning of ultraviolet (UV)/Ozone surface cleaner for 10 min. 2 mg/mL DA, 5 mmol/mL AA, and 10 mmol/mL MTAC monomers were all dissolved in 10 mM Tris buffer (pH 8.5) to prepare the coating solution. The cleaned silicon wafers and PVDF membranes were firstly pre-wetted by Tris buffer solution and then immersed into the coating solution at 25°C. The solutions were shaken using an oscillator and the coating time was 0.5 h and 8 h, respectively. Subsequently, the PDA-PAA-

PMTAC-coated silicon wafers and PVDF membranes were thoroughly washed by ethanol/water alternatively for 3 times and dried in a vacuum oven at 60 °C for 2 h.

3.2.3 Surface characterization

The surface morphology of as-fabricated PDA-PAA-PMATC-coated silicon wafer was characterized by imaging using an MFP-3D atomic force microscope (AFM) system (Asylum Research, Santa Barbara, CA, USA) with bare and pure PDA-coated silicon wafers as the comparison. The surface morphology and the element distribution of as-fabricated PDA-PAA-PMTAC-coated PVDF membrane substrate were characterized by a field-emission scanning electron microscope (SEM) (Zeiss Sigma 300 VP-FESEM, Germany) with an energy-dispersive X-ray spectroscopy (EDS) at the electron acceleration voltage of 10.2 keV. X-ray photoelectron spectrometer (XPS) and Fourier transform infrared (FTIR) spectrometer (Thermo Scientific Nicolet, iS50 FT-IR) were applied to identify the chemical functional groups of the coating materials on PVDF membrane. The surface charge property of the coating materials was analyzed by the zeta potential measurements of PDA-PAA-PMTAC coating on silica nanoparticles (diameter ~ 12 nm) using a Zetasizer Nano ZSP system (Malvern Panalytical, NANO, United Kingdom). The wetting property of the PDA-PAA-PMTAC coating was evaluated via the underwater oil contact angle (OCA) measurements (contact angle goniometer, Ramé-Hart instrument, NJ) in NaCl aqueous solution at different pH. Specifically, a surfactant-stabilized (CTAB or SDS) toluene droplet was generated and introduced underneath the coating surfaces using a J-shape inverted needle. The contact angle was measured after the droplet was gently attached to the surfaces and stabilized for 5 s.

3.2.4 Oil/water separation experiment

The PDA-PAA-PMTAC-coated PVDF membrane was applied in the separation performance tests of surfactant-stabilized O/W emulsions. The surfactant-stabilized toluene-in-water emulsions (containing 5 wt.% toluene and 200 ppm CTAB or SDS surfactant) and cyclohexane-in-water emulsions (containing 5 wt.% cyclohexane and 200 ppm CTAB or SDS surfactant) were obtained by using a homogenizer (IKA T-18 Ultra Turrax, Germany) at 12, 000 rpm for 10 min and used as the model emulsion solution for oil/water separation experiment. The drop size distribution and zeta potential of the as-prepared emulsions were characterized by the dynamic laser scattering (DLS) measurement using a Zetasizer Nano ZSP system (Malvern Panalytical, NANO, United Kingdom). In the separation experiment, the membrane prewetted by 1 mM NaCl solution was placed in a dead-end membrane filtration setup. The oil/water separation performance test was initiated by directly flowing emulsion solution through the membrane [34, 35]. The permeation water flux (J, $L \cdot m^{-2} \cdot h^{-1} \cdot bar^{-1}$) is calculated according to Eq. (1):

$$J = \frac{V}{S \cdot t \cdot \Delta P} \tag{1}$$

where V is the volume of permeation water, S is the effective separation area of the membrane, t is the permeation time, ΔP is the pressure difference between ambient and evacuation pressure.

The filtrates were collected and then the total organic carbon (TOC) analysis (SHIMADZU ASI-L, Japan) was conducted to calculate the oil separation efficiency (η) based on the initial (C_i) and final (C_f) oil content according to Eq. (2):

$$\eta(\%) = (1 - \frac{C_f}{C_i}) \times 100 \quad (2)$$

3.2.5 Force measurement using drop probe AFM technique

The interaction forces between oil droplets (i.e., toluene) with CTAB or SDS adsorbed at the interface and PDA-PAA-PMTAC-coated silicon surfaces in NaCl solutions were directly measured by the AFM drop probe technique using an MPF-3D AFM (Asylum Research, Santa Barbara, CA, USA). The details of the experimental setup have been reported previously [16, 36, 37]. For the preparation of the drop probe, oil droplets were generated by introducing toluene solution containing 200 ppm CTAB or SDS through a custom-made ultrasharp glass pipet on the glass substrate of AFM fluid cell, which was firstly filled with NaCl solution. Then, oil droplets on the fluid cell would stay for 20 min until the equilibrium of oil/water interface with surfactant is reached in saline solution, which was also confirmed by the interfacial tension measurement using a goniometer (Ramé-hart Instrument Company, USA). After that, one of the oil droplets with suitable size (radius ~50-100 μm) was carefully picked up by the AFM tipless rectangular cantilever with a circular gold patch on the end, which was hydrophobized by immersion in 10 mM dodecane thiol in ethanol solution overnight. Finally, the drop-anchored cantilever (drop probe) was moved and located over the PDA-PAA-PMTAC-coated silicon substrate in the fluid cell for force measurements. The spring constant of the AFM cantilever was calibrated to be 0.3-0.4 N/m using the Hutter and Bechhoefer thermal tune method [38]. During the force measurement, the drop probe was driven to approach the silicon substrate at a fixed velocity until a pre-set deflection was detected, and then retracted from the surface. The interaction force was calculated based on the spring constant and the deflection of the cantilever by the Hooke's Law.

3.2.6 Theoretical Analysis of Force Profiles

A theoretical model based on the Stokes-Reynolds-Young-Laplace equations was applied to analyze the measured force profiles between a flat PDA-PAA-PMTAC-coated silicon surface and a deformable oil drop in aqueous solutions [36, 39, 40]. The augmented Young-Laplace equation is used to describe the deformation of the oil drop surface and correlation to the external pressure, e.g. hydrodynamic pressure and disjoining pressure, given by Eq (3):

$$\frac{\gamma}{r}\frac{\partial}{\partial r}\left(r\frac{\partial h}{\partial r}\right)=\frac{2\gamma}{R}-p-\Pi \tag{3}$$

where γ is the oil/water interfacial tension at equilibrium state, r is the radical coordinate of the oil drop, h is the thickness of water film confined between the oil drop and the flat coating surface, R is the radius of the oil drop, p and Π are the hydrodynamic and disjoining pressure, respectively. The disjoining pressure Π generally includes the surface interactions such as van der Waals (VDW) interaction and electrical double layer (EDL) interaction, given by Eq. (2-4), respectively:

$$\Pi=\Pi_{VDW}+\Pi_{EDL}+... \tag{2}$$

$$\Pi_{VDW}=-\frac{A_H}{6\pi h^3} \tag{3}$$

$$\Pi_{EDL}=\frac{2\varepsilon\varepsilon_0\kappa^2\left[\left(e^{\kappa D}+e^{-\kappa D}\right)\Psi_{oil}\Psi_{surface}-\left(\Psi_{oil}^2+\Psi_{surface}^2\right)\right]}{\left(e^{\kappa D}-e^{-\kappa D}\right)^2} \tag{4}$$

where A_H is the Hamaker constant between the oil drop and substrate surface in NaCl solution; κ is the inverse of the Debye length, ε_0 is the vacuum permittivity, ε is the dielectric constant

of the aqueous solution, Ψ_{oil} and $\Psi_{surface}$ are the surface potentials of the oil drop and coating surface, respectively. $\prod_{VDW}$ and $\prod_{EDL}$ are the disjoining pressure components due to the VDW and EDL interactions, respectively. The inverse of the Debye length is given by Eq. (5):

$$\kappa = \sqrt{\frac{\sum \rho_0 e^2}{\varepsilon \varepsilon_0 k_B T}} \tag{5}$$

where ρ_0 is the number density of ions in NaCl solutions, e is the elementary electric charge, T is temperature, and k_B is the Boltzmann constant.

The drainage behavior of confined water film between the oil drop and the flat surface (oil-water-surface system) is described by the Reynolds lubrication theory:

$$\frac{\partial h}{\partial t} = \frac{\partial}{12\mu r \partial r}\left(r h^3 \frac{\partial p}{\partial r} \right) \tag{6}$$

Here, μ is the viscosity of the NaCl solutions and t is time. The overall interaction force between the oil drop and coating surface F(t) can be determined by the integration of the hydrodynamic pressure p and the disjoining pressure $\prod$ according to the Derjaguin approximation, given by Eq. (7):

$$F(t) = 2\pi \int_0^\infty \left[p(r,t) + \prod(r,t) \right] r dr \tag{7}$$

3.3 Results and discussion

3.3.1 Synthesis and characterizations of PDA-PAA-PMTAC coating

PDA-PAA-PMTAC coating materials with both negatively charged carboxylic group (-) and positively charged quaternary ammonium (+) moieties have been deposited on silicon wafer

surfaces. Figure 3.1a illustrates the fabrication process of PDA-PAA-PMTAC coating on silicon wafer surfaces. Under mild alkaline aqueous conditions of pH 8.5, DA could oxidize to generate semiquinone radical species, serving as the initiators for the polymerization of AA/MTAC monomers as well as the formation of PDA. The surface morphologies of the pure-PDA and PDA-PAA-PMTAC-coated silicon wafer surfaces were characterized by topographic AFM imaging as shown in Figure 3.1 b-d, using bare silicon wafer as the reference (Figure S1). Compared to the pure-PDA coating which exhibits relatively larger particles or aggregates on the substrate with the root mean square (RMS) roughness around 5.7 nm (Figure 3.1b), the PDA-PAA-PMTAC coating is rather smooth and homogeneous with the RMS roughness around 1.2 nm (Figure 3.1c). This AFM results could be well explained by previous studies that the copolymerization of the AA and MTAC monomers with DA could mediate the self-aggregation of PDA and enhance the uniformity of the coating layer [31]. The obtained PDA-PAA-PMTAC coating on silicon wafer with nanoscale roughness is appropriate for the surface force measurement to investigate the intrinsic interaction mechanisms of coating surface using toluene droplet (radius ~ 50-100 μm)-anchored probe. The water wettability of the pure-PDA and PDA-PAA-PMTAC coating surfaces was evaluated by water contact angle ($\theta_{W/A}$) measurement in air shown in Fig. 1d-e. The measured $\theta_{W/A}$ is less than 10° showing that the PDA-PAA-PMTAC coating could be readily wetted by water in air (Figure 3.1e), whereas the $\theta_{W/A}$ on pure-PDA coating is around 30° (Fig. 1d), which is consistent with the result for pure-PDA and PDA-polyelectrolyte coatings reported previously [32]. The chemical composition of pure-PDA and PDA-PAA-PMTAC coating was characterized by X-ray photoelectron spectroscopy (XPS) as shown in Fig. S2. The characteristic peaks associated with the N-C_2, O-C=O and N-$(CH_3)^{3+}$ indicate the successfully depositing of PDA with AA/MTAC segments into the coating materials

[41]. The surface charge property of the PDA-PAA-PMTAC coating was characterized by zeta potential measurements at different solution pH, as shown in Figure 3.1f. The zeta potential of the PDA-PAA-PMTAC coating varies from + 34 mV at pH 4 to -39 mV at pH 10 with the isoelectric point (IEP) approximately at pH 6.8, implying the feasible surface charge adjustment with pH. The alternation of the surface charge is most likely due to the protonation/deprotonation of the carboxyl groups on the AA segments in the coating materials. The above results indicate that the AA and MTAC moieties were successfully incorporated in the PDA-PAA-PMTAC coating via the co-deposition strategy.

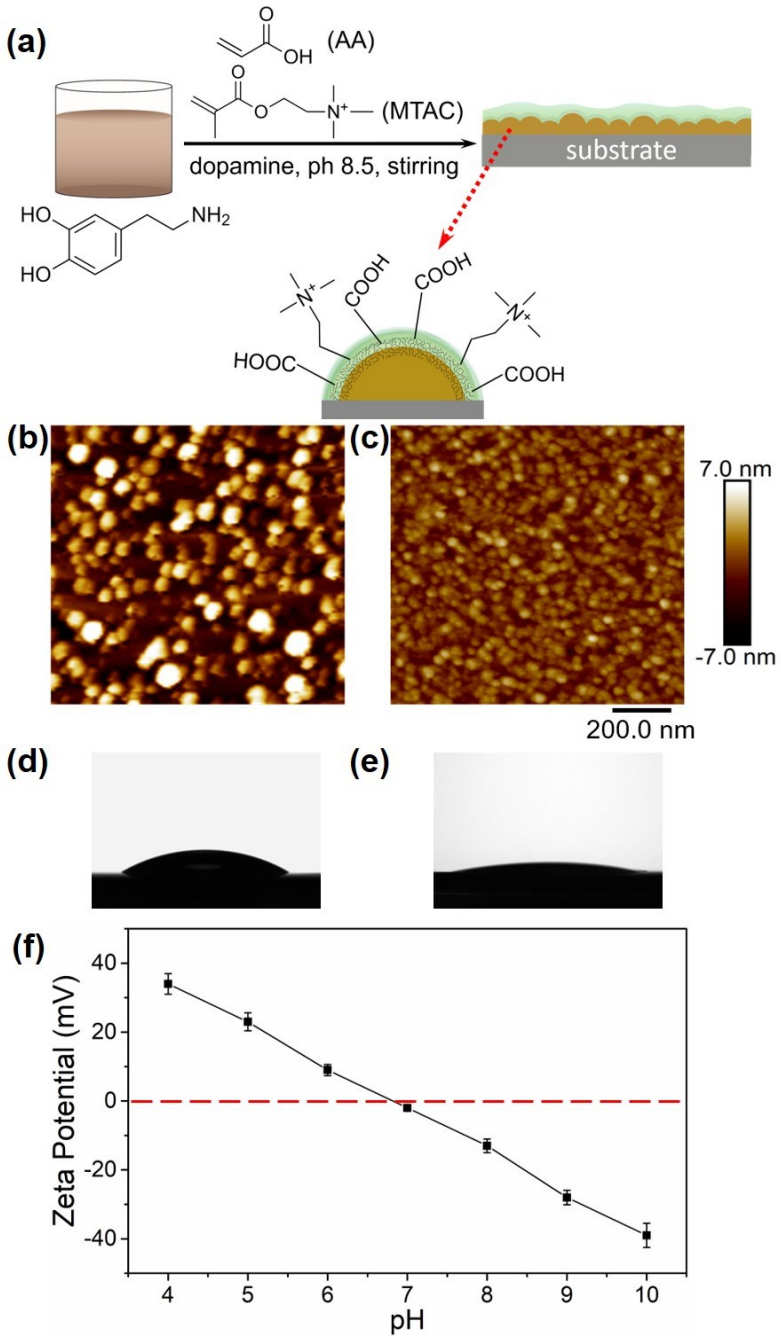

Figure 3.1 (a) Schematic of for the fabrication of PDA-PAA-PMTAC coatings on silicon wafer substrate; Topographic AFM images of (b) pure-PDA coating (RMS roughness ~ 5.7 nm) and (c) PDA-PAA-PMTAC coating (RMS roughness ~ 1.2 nm) on silicon wafer; water contact angle of (d) pure-PDA and (e) PDA-PAA-PMTAC-coated silicon wafer in air; (f) Zeta potential of PDA-

PAA-PMTAC (black) coating on the silica nanoparticles in 1 mM NaCl solution at different pH value.

3.3.2 Interaction between emulsion droplet and PDA-PAA-PMTAC coating

The interaction force between toluene droplet with 200 ppm CTAB and PDA-PAA-PMTAC-coated silicon wafer surface was firstly measured in 500 mM NaCl solution at pH 7. Figure 3.2a illustrates the schematics of the drop-surface AFM force measurement experiment with the microscopic image of a typical drop probe. As shown in Figure 3.2b, a sudden "jump-in" behavior was detected after overcoming a very weak repulsion of ~ 0.8 nN during the approaching of the toluene droplet to the coating surface, which indicated that the toluene droplet immediately detached from the AFM cantilever and attached onto the coating surface. This attachment behavior was also directly observed from the inverted microscope, as illustrated in Figure 3.2c. According to the classic Derjaguin-Landau-Verwey-Overbeek (DLVO) theory, both the VDW force and EDL force contribute to the force profile between the toluene droplet and substrate surface in aqueous solution. In 500 mM NaCl solution, the Debye length was calculated to be 0.43 nm according to Eq. (5), suggesting that the electric double layer is significantly suppressed in such high salinity (i.e., 500 mM NaCl). Thereby, the effect of electrostatic interaction was minimized and the very weak repulsion measured during approaching was due to the hydrodynamic repulsion at the moving velocity 1 μm/s. The attractive VDW force dominates the surface interaction and accounts for the attachment behavior. Varying the solution pH with high salinity will lead to the minimum influence to the interaction between emulsion droplets and the coating surface. Therefore, in this work, solutions of the low salinity with varying pH and the high salinity with natural pH have been involved. The theoretical fitting of the surface force

profile gives a Hamaker constant of 6.8×10^{-20} J for the oil-water-coating system in this work shown in Figure 3.2b.

Figure 3. 2d, 2e, and 2f show the interaction force profiles between the toluene droplet with 200 ppm CTAB and the PDA-PAA-PMTAC-coated substrate in 1 mM NaCl solutions at pH 8, 6, and 4, respectively. The force profile in Figure 3. 2d and 2e is similar to that in 500 mM NaCl solution. There was a weak repulsion of 1 nN at pH 8 and 2.3 nN at pH 6, respectively, before the toluene droplet jumped into contact with the substrate surface. However, the force profile is quite different at pH 4. The toluene droplet was pressed onto the substrate surface by the AFM cantilever till the pre-set maximum loading force of 8 nN was applied, and no attachment behavior occurred. Then the droplet was withdrawn from the surface to original position with no obvious adhesion detected. Instead of the attachment behavior occurred during the approaching process after a weak repulsion in Figure 3. 2d and 2e, the force profile during both approaching and retracing process was measured in Figure 3.2f and only pure repulsion was detected between the toluene droplet and the PDA-PAA-PMTAC coating surface. In low salinity (e.g., 1 mM NaCl solution), the Debye length κ^{-1} is ~ 9.6 nm. Thus both the VDW and EDL interactions play an important role in the drop-water-surface system. Since the alteration of the solution pH has very limited influence on the VDW force and the hydrodynamic interaction is close due to the similar droplet size and moving velocity in different measurements, it can be concluded that the EDL interaction between the toluene droplet and the coating surface becomes more repulsive when the solution pH changes from 8 to 4. The experimental force profiles were also theoretically analyzed using the Stokes-Reynolds-Young-Laplace model, and the fitting results are shown as solid curves in Figure 3.2d-f. The zeta potential values of the CTAB-stabilized emulsions under the three pH conditions were taken approximately as the surface

potentials of the drops in the theoretical calculations (Table S1). The fitted surface potentials of PDA-PAA-PMTAC-coated silicon surface are -18 mV, +16 mV, and +36 mV at pH 8, 6 and 4, respectively, which agree well with the zeta potentials of PDA-PAA-PMTAC-coated silica particles in 1 mM NaCl at the same pH (Table 1). The theoretical result indicates that decreasing the solution pH leads to more positive surface potential of the toluene droplet and the coating surface, which then attribute to the enhanced electrical double layer repulsion between the toluene droplet and the PDA-PAA-PMTAC coating surface. The toluene droplet with CTAB adsorbed at the oil/water interface carries positive surface potential due to the presence of quaternary ammonium group in the CTAB molecule, while the PDA-PAA-PMTAC coating surface has an isoelectric point of ~pH 6.8. Thus, the EDL interaction between the toluene droplet and the coating surface changed from attraction at pH 8 to repulsion at pH 6, and further to strong repulsion at pH 4. At pH 8, even though both the VDW and EDL forces are attractive, the measured force profile still exhibits slightly repulsive due to the weak hydrodynamic repulsion. The above results demonstrate that interaction forces between the toluene droplets with CTAB and the PDA-PAA-PMTAC coating can be effectively affected by surface charges, as facilely tuned by varying solution pH.

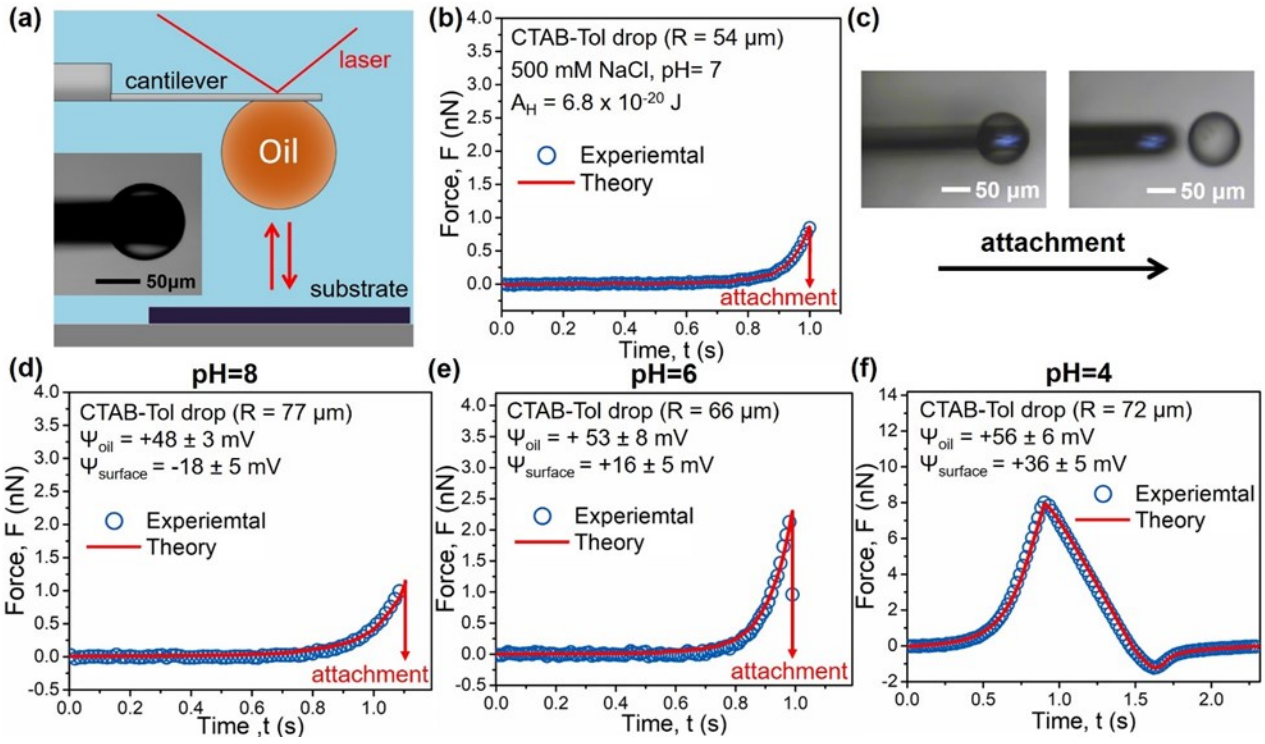

Figure 3.2 (a) Schematic of a typical drop-surface AFM force measurement using the drop probe AFM technique and microscopic image (inset) of a typical drop probe; (b) Experimentally measured interaction force profiles of a toluene droplet with 200 ppm CTAB and a PAA-PDA-PMTAC coating in 500 mM NaCl at pH 7 with (c) microscopic images of the droplet attachment; Experimentally measured interaction force profiles (open symbols) of a toluene droplet with 200 ppm CTAB and a PDA-PAA-PMTAC coating in 1 mM NaCl solutions at pH value of (d) 8, (e) 6, and (f) 4, as well as the theoretical fitting results (red solid curves).

The surface interactions between toluene droplet with 200 ppm SDS and the PDA-PAA-PMTAC-coated substrate were also investigated through force measurements at pH 6, 8 and 10 in 1 mM NaCl solution, as shown in Figure 3. Figure 3.3a and 3b show the similar force profiles with that in Figure 3.2d and 2e. A critical repulsion of 1.2 nN at pH 6 and 3.3 nN at pH 8 was overcome before the toluene droplet jumped into contact with the coating surface during the

approaching of oil drop to the coating surface in 1 mM NaCl solution. While Figure 3.3c shows that only repulsive interaction was measured until the maximum loading force of 8 nN reached during the approach and the toluene droplet retracted from the coating surface with no obvious adhesion detected. The experimental force profiles were theoretically analyzed using the Stokes-Reynolds-Young-Laplace model. The zeta potential values of the SDS-stabilized oil drops in 1 mM NaCl at different pH conditions were approximately taken as the surface potentials in the calculation (Table 3.S2). The theoretical fittings (solid curves in Figure 3.3) show that the surface potentials of the PDA-PAA-PMTAC coating are +16 mV, -18 mV, and -42 mV in 1 mM NaCl at pH 6, pH 8, and pH 10, respectively, which is also consistent with the zeta potential results measured for the PDA-PAA-PMTAC coating on silica particles in 1 mM NaCl (Table 3-1). The results in Figure 3 indicate that the SDS-stabilized oil drop-coating surface interactions during the approach process become more repulsive with increasing the aqueous pH, which was mainly due to their enhanced EDL repulsion, and that the coating surface turns from positively charged to negatively charged. At pH 10, both surfaces are strongly negatively charged, that the EDL repulsion becomes so strong that the drop could not attach to the coating. Figure 3.4 shows the contribution VDW pressure, EDL pressure, and the hydrodynamic pressure at pH 6 and 10. It is evident that the attractive VDW and EDL interaction render the attachment of toluene droplet with SDS to the PDA-PAA-PMTAC coating surface at pH 6. Then, the repulsive hydrodynamic pressure accounts for the measured weak repulsion before the attachment behavior in Figure 3.3a. At pH 10, the repulsive EDL interaction combined with the hydrodynamic repulsion is much stronger than the attractive VDW attraction, thus preventing the attachment of toluene droplet on the coating surface. In the inset of Figure 3.4a, the critical central separation before oil attachment was calculated to be 17.2 nm, where the central portion of drop surface formed a

"pimple" shape resulted from the overall attraction that exceeded the Laplace pressure inside the oil drop. For the case at pH 10, under the maximum load force applied (i.e., ~8 nN), a layer of water with minimum thickness h_{min} ~ 38 nm was still confined between the oil drop and coating surface, preventing their attachment, as illustrated in the inset of Figure 3.4b. Accordingly, measured interaction force and calculated pressure profiles of pure toluene droplet with PDA-PAA-PMTAC coating are also presented as the reference (Figure 3.S7) in low saline solution (1 mM NaCl) of pH 6 and 10 as well as high salinity (500 mM NaCl) of neutral pH, respectively. Compared to the case of charged surfactant-stabilized toluene droplet interacting with the surface coating, the electrostatic interaction between pure toluene droplet and the surface coating is reduced due to the lower surface potential. However, the drop-surface interaction could still be facilely modulated by EDL interaction via solution pH adjustment to help prevent the attachment of pure toluene droplet onto the coating surface in low salinity solution. Meanwhile, in the high salinity, the contribution of the electrostatic interaction is minimized due to the suppressed electric double layer and drop-surface interaction is determined by the attractive VDW and repulsive hydrodynamic interaction.

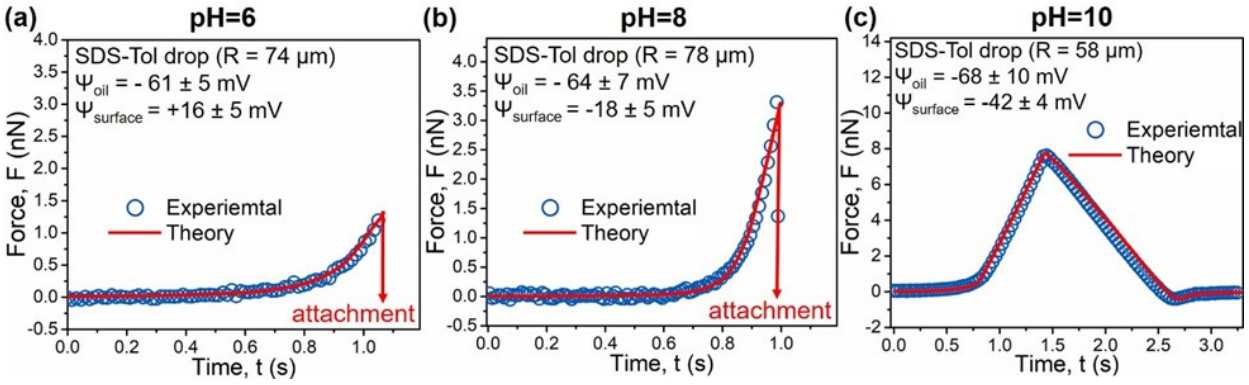

Figure 3.3 Experimentally measured interaction force profiles (open symbols) of a toluene droplet with 200 ppm SDS and a PDA-PAA-PMTAC coating in 1 mM NaCl solutions at pH value of (a) 6, (b) 8, and (c) 10, and the theoretical fitting results (red solid curves).

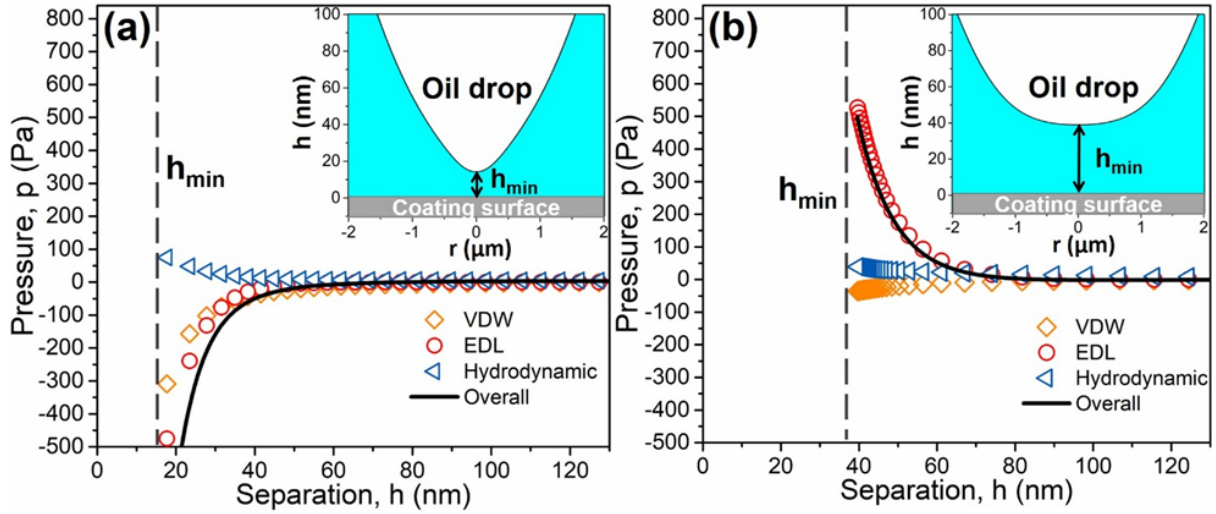

Figure 3.4 Calculated profiles of VDW disjoining pressure, EDL disjoining pressure, and hydrodynamic pressures between a toluene droplet with 200 ppm SDS interacting with a PDA-PAA-PMTAC coating surface at the central position of the droplet in 1 mM NaCl solution at pH value of (a) 6 and (b) 10, respectively. The inset illustrates the calculated drop profile at maximum force load during the approach process where a layer of water with minimum thickness h_{min} (at central point) was confined between the oil droplet and coating surface.

Table 3-1 Comparison of the theoretically fitted surface potential values of the PDA-PAA-PMTAC coating and the measured zeta potential data of silica nanoparticles coated with PDA-PAA-PMTAC in 1 mM NaCl under various pH conditions.

pH	Fitted surface potential (mV)	Zeta potential data (mV)
4	+36 ± 5	+34 ± 3
6	+16 ± 5	+10 ± 1
8	-18 ± 5	-14 ± 2
10	-42 ± 4	-39 ± 4

The effect of hydrodynamic interaction was also investigated by conducting the force measurements at different approaching velocities. Taking the case in 1 mM NaCl at pH 10 as an example, Figure 3.5a and 5b show the measured interaction force profiles (open symbols) of a toluene droplet with 200 ppm SDS and the PDA-PAA-PMTAC coating surface at both the low (0.5 μm/s) and high approaching velocity (10 μm/s), respectively and the theoretical force curves (red solid lines) calculated based on the Hamaker constant ($A_H = 6.8\times10^{-20}$ J) and surface potentials (Ψ_{oil} = -68 mV and $\Psi_{surface}$ = -42 mV), which clearly show the good agreement with each other. It is evident that the pressure contributed by the hydrodynamic repulsion is greatly strengthened at high approaching velocity of 10 μm/s and prevents the approaching of toluene droplet as shown in Figure 3.5d. For the case that the drop movement (or flow condition) is intensive, the hydrodynamic interaction acts as a "long-range repulsion" compared to EDL interaction, and the repulsive drop-surface interaction is contributed by the synergistic effect of

the hydrodynamic and EDL repulsion. It is also noted that an obvious attraction was measured during the retraction process in Figure 3.5c which is mainly due to the hydrodynamic "suction" effect at high velocity (10 μm/s). To further probe the role of hydrodynamic repulsion, the hydrodynamic pressure and the confined water film thickness at the central point between the toluene droplet with SDS and the PDA-PAA-PMTAC coating surface with varied velocities in 1 mM NaCl of pH 10 were calculated and illustrated in Figure 3.6a and 6b, respectively. With the approaching velocity increasing from 0.5 to 30 μm/s, the hydrodynamic pressure and the thickness of the confined water film are rising gradually from 18 to 950 Pa and 38 to 63 nm, respectively, under same maximum load of ~ 8 nN. Herein, the accelerated approaching velocity leads to the strengthened hydrodynamic repulsion and the thickened confined water film thickness, thus preventing the attachment of toluene drops onto coating surface.

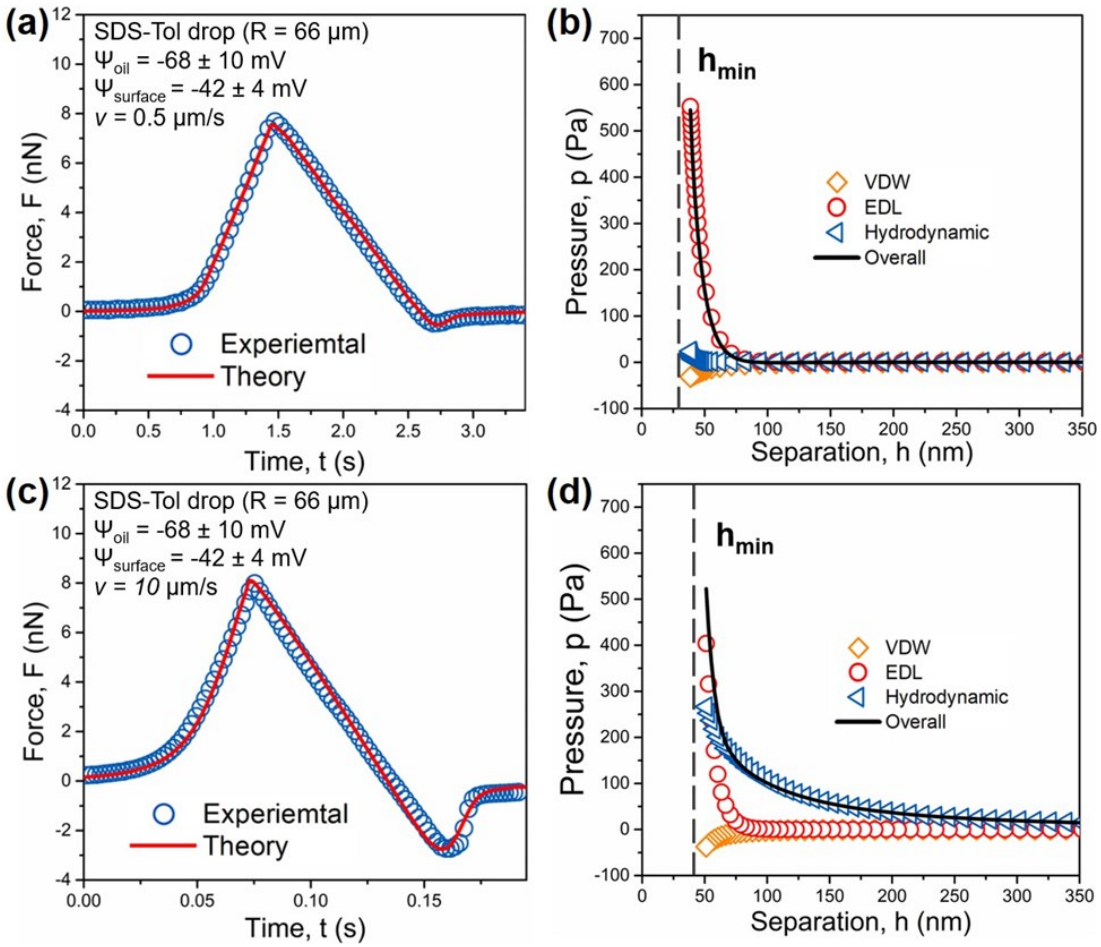

Figure 3.5 Interaction force profiles (open symbols) measured and the theoretically predicted curves (solid curves) between a toluene droplet with 200 ppm SDS and a PDA-PAA-PMTAC coating surface in 1 mM NaCl solution of pH 10 at approaching velocity of 0.5 (a) and 10 (c) μm/s with the calculated pressure profiles derived from VDW, EDL, and hydrodynamic interactions at the central points of the drops at approaching velocity of 0.5 (b) and 10 (d) μm/s, respectively.

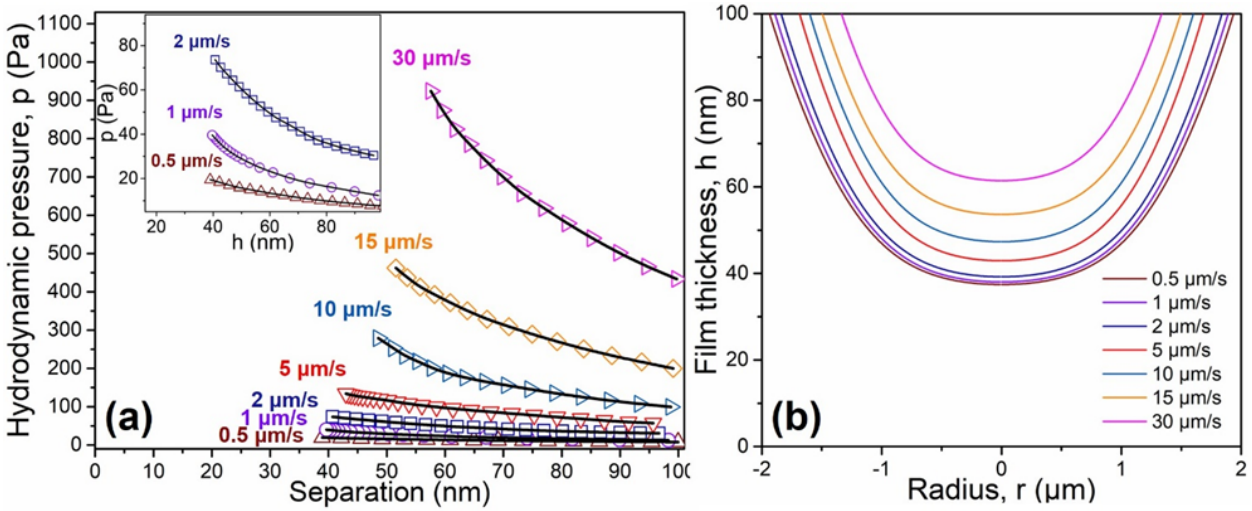

Figure 3.6 (a) Calculated profiles of hydrodynamic pressures between a toluene droplet with 200 ppm SDS interacting with a PDA-PAA-PMTAC coating surface at the central position of the drop in 1mM NaCl solution of pH 10 at different approaching velocity of 0.5, 1, 2, 5, 10, 15, and 30 μm/s; (b) the calculated drop profile at maximum force load during the approach process where a layer of water with minimum thickness h_{min} (at central point) was confined between the oil drop and coating surface.

3.3.3 Characterization of PDA-PAA-PMTAC-coated PVDF membrane

The PDA-PAA-PMTAC coating was further deposited on the PVDF membrane substrate to test its potential application in oil/water separation. The SEM images of the cross-sectional area of the pristine, pure-PDA, and PDA-PAA-PMTAC-coated PVDF membrane surface corresponded to the filtration process are shown in Figure 7. Compared to the pristine PVDF membrane shown in Figure 3.7a and 7d, PDA composites are agglomerated in large quantities on the membrane substrate surface (Figure 3.7b and 7e) which is analogous to the morphology observed on the topographic AFM images of pure PDA coating on the flat silicon wafer surface. Meanwhile, the PDA-PAA-PMTAC coating on the porous PVDF membrane surface exhibits a

high uniformity with less agglomeration (Figure 3.7c and 7f). Figure 3.7g and 7h also show the element distribution of the pure-PDA and PDA-PAA-MTAC coatings evaluated using EDS mapping at the same locations of Figure 3.7c and 7f, respectively. The mass fraction of the carbon (C), fluorine (F), oxygen (O), and nitrogen (N) was 64.3, 32.9, 1.8, and 1 wt.% on pure-PDA coating, as well as 65.8, 25.9, 4.7, and 3.7 wt.% on PDA-PAA-PMTAC coating (Table 3.S3), respectively. Compared to the EDS results of pure-PDA coating on the membrane surface, the increased mass fraction of oxygen and nitrogen and decreased fraction of fluorine could be attributed to the codeposition of AA and MTAC monomers with DA to intermediate the self-aggregation of PDA, forming a compact and homogeneous coating layer over the membrane substrate. The surface chemical functionality of the PDA-PAA-PMTAC coating on PVDF membrane surface was characterized using FTIR spectrum shown in Figure 3.7i. The transmittance peaks associated with the PDA coating (spectrum in red line) were observed at 1650 cm^{-1} for the aromatic C=C skeleton stretching vibration and 1280 cm^{-1} for the phenolic C–O–H stretching vibration, while the peaks of the PDA-PAA-PMTAC coating (spectrum in black line) at 920 cm^{-1} and 1740 cm^{-1} corresponded to the quaternary ammonium C-$N^{+}(CH_3)_3$ and carboxylic C=O stretching vibration, respectively [42-44]. From the SEM/EDS and FTIR analysis, the PDA-PAA-PMTAC coating has been successfully deposited on the membrane surfaces and still maintains the porous structure of the PVDF substrate.

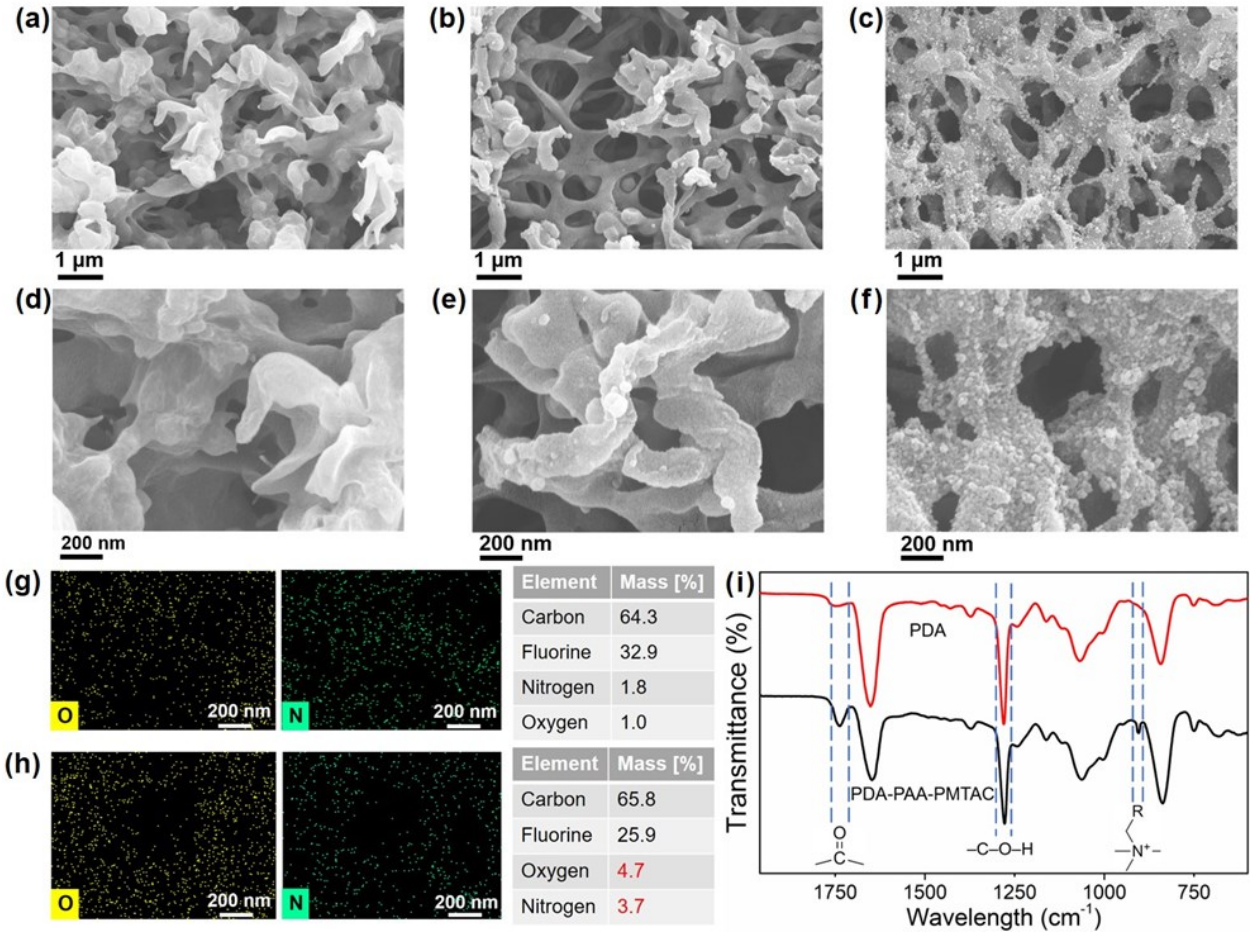

Figure 3.7 SEM images of (a) pristine (b) PDA-coated, and (c) PDA-PAA-PMTAC-coated PVDF membrane at 10k X magnification; SEM images of (d) pristine, (e) PDA coated, and (f) PDA-PAA-PMTAC-coated PVDF membrane at 50k X magnification; EDS mapping and analysis of C, F, O, and N element on (g) PDA-coated and (h) PDA-PAA-PMTAC-coated PVDF membrane at the same locations of (c) and (f) at 10 kV; (i) FTIR spectra of the PDA (red) and PDA-PAA-PMTAC (black) coating on the PVDF membrane surface.

The wettability of the surfactant-stabilized toluene droplets on the PDA-PAA-PMTAC coating was evaluated by measuring the underwater oil contact angle (OCA) measurement in 1 mM NaCl solution at different solution pH (Figure 3.8). As shown in Figure 3.8a, the underwater

OCA of toluene droplet with 200 ppm CTAB decreased from 165 ° to 97 ° with the solution pH from 4 to 8. However, for the toluene droplet with 200 ppm SDS, the underwater OCA increased from 102 ° to 166 ° with the solution pH from 6 to 10, as illustrated in Figure 3.8b. For both the CTAB and SDS toluene droplets, an impressive non-sticking phenomenon was observed when the toluene droplets with 200 ppm surfactant were ejected and brought to contact with the membrane surfaces (Video S1), indicating a superior antifouling property to the surfactant-coated emulsion drops. This phenomenon could be correlated to the strong electrostatic repulsion between the toluene droplet and PDA-PAA-PMTAC coating surface. Herein, the results from the underwater OCA measurement indicate that the wettability of the charged oil drops on PDA-PAA-PMTAC coating could be facilely tuned by adjusting the solution pH which could be mainly ascribed to the modulated electrostatic interaction between the charged oil droplets and the PDA-PAA-PMTAC coating.

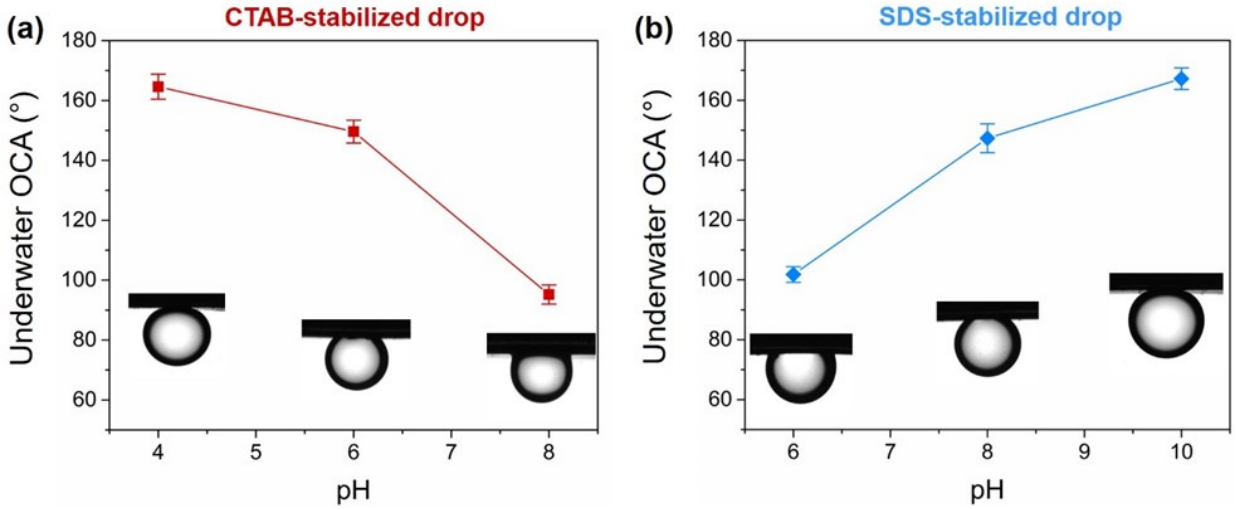

Figure 3.8 Underwater oil contact angle (OCA) of toluene droplets in 1 mM NaCl solution containing (a) 200 ppm CTAB and (b) 200 ppm SDS at different pH.

3.3.4 Oil/water separation of PDA-PAA-PMTAC-coated PVDF membrane

Figure 3.9a illustrates the schematic of the vacuum filtration setup with a piece of PDA-PAA-PMTAC-coated membrane placed at the filter holder for oil/water separation. Optical images of the pristine and PDA-PAA-PMTAC-coated PVDF membrane are also shown in Figure 3.9a. The effective separation area of the membrane is 6.15 cm^2 and the pressure difference between ambient and evacuation pressure is 0.07 MPa. Typically, the prepared toluene-in-water emulsions (containing 5 wt.% toluene and 200 ppm CTAB or SDS surfactant) before filtration remain milky and stable, and the size distribution of the toluene droplets varied from 200 nm to 1 μm with the average size of 500 nm (Figure 3.9b), which is comparable to the pore size of the PVDF membrane (average ~ 0.22 um). After filtration, the collected fluids after filtration exhibits transparent and clean, and the average size of toluene droplets decreases to 10 nm, which indicates the possible existence of the small amount of dissolved microdroplets and surfactant micelles residues. This result also suggests the excellent oil/water separation performance of the PDA-PAA-PMTAC-coated PVDF membrane. Figure 3.9c and 9d show the water permeation flux and oil removal efficiency for the oil/water separation of the CTAB and SDS-stabilized emulsions with varying solution pH, respectively. For the CTAB-stabilized emulsions, the water permeation flux decreases from 3021 $L \cdot m^{-2} \cdot h^{-1} \cdot bar^{-1}$ to 580 $L \cdot m^{-2} \cdot h^{-1} \cdot bar^{-1}$ when the solution pH increases from 4 to 8. Meanwhile, an increase in permeation flux from 702 $L \cdot m^{-2} \cdot h^{-1} \cdot bar^{-1}$ to 3340 $L \cdot m^{-2} \cdot h^{-1} \cdot bar^{-1}$ for the SDS-stabilized emulsions is observed when the solution pH increases from 6 to 10. The change of the permeation flux for membrane filtration with the solution pH could be the consequence of the altered surface forces between the toluene droplets with CTAB/SDS and PDA-PAA-PMTAC coating. The calculated oil removal efficiencies in both CTAB and SDS-stabilized emulsion cases were exceptionally high ranging

from 99.6% to 99.8%, implying that the toluene-in-water emulsions are successfully separated. The superior oil separation efficiency could be ascribed to the physical interception of the filtration membrane, also confirmed by the retention tests of the PDA-PAA-PMTAC membrane (Figure 3.S8). The optical images for the comparison of the feeding emulsion solution, the separated oil and water phases are shown in Figure 3.S10. In addition to toluene as one of the representative polar aromatic oils, the filtration test of cyclohexane-in-water emulsion using cyclohexane as one of the representative nonpolar alicyclic oils was also conducted. Both the cyclohexane-in-water emulsion stabilized by 200 ppm CTAB and SDS could form stable emulsions confirmed by IFT measurement, as shown in Figure 3.S5 and S6, respectively. The permeation water flux is increasing with the decreasing solution pH from 8 to 4 for CTAB-cyclohexane emulsion and increasing pH from 6 to 10 for SDS-cyclohexane emulsion, as illustrated in Figure 3.S9, which is in consistence with the filtration results using toluene-in-water emulsions. The above results indicate that the water permeability of the PDA-PAA-PMTAC-coated membrane for filtrating charged emulsions could be facilely tuned by solution pH, which could also be correlated to the results of measured drop-surface interaction force profiles. At the beginning of the filtrating process when the movement surfactant-stabilized toluene droplets are intensive with water flux, the hydrodynamic interaction could effectively generate a repulsive force to prevent the approaching of droplets to the membrane surface. During filtration, the surfactant-stabilized toluene droplets gradually accumulate over the membrane surface, thus confining the movement of droplets, thus the hydrodynamic repulsion would be significantly weakened. Hence, the accumulated toluene droplets could get adsorbed on the membrane surface and lead to the blockage of the porous areas and the decrease of permeation water flux [45, 46]. By tuning the solution pH from 6 to 4 for the CTAB emulsions

and pH 6 to 10 for the SDS emulsions, strong electrostatic repulsion is modulated, preventing the deposition of the emulsion droplets to the membrane surface, resulting in the increased permeation flux of water. By applying this tunable surface forces-based filtration strategy, an outstanding separation performance is achieved for treating both the CTAB and SDS-stabilized emulsions with a water permeation flux of over 3000 $L \cdot m^{-2} \cdot h^{-1} \cdot bar^{-1}$ at pH 4 and 10, respectively, which is higher than most of the reported oleophobic membrane materials [17, 46-48].

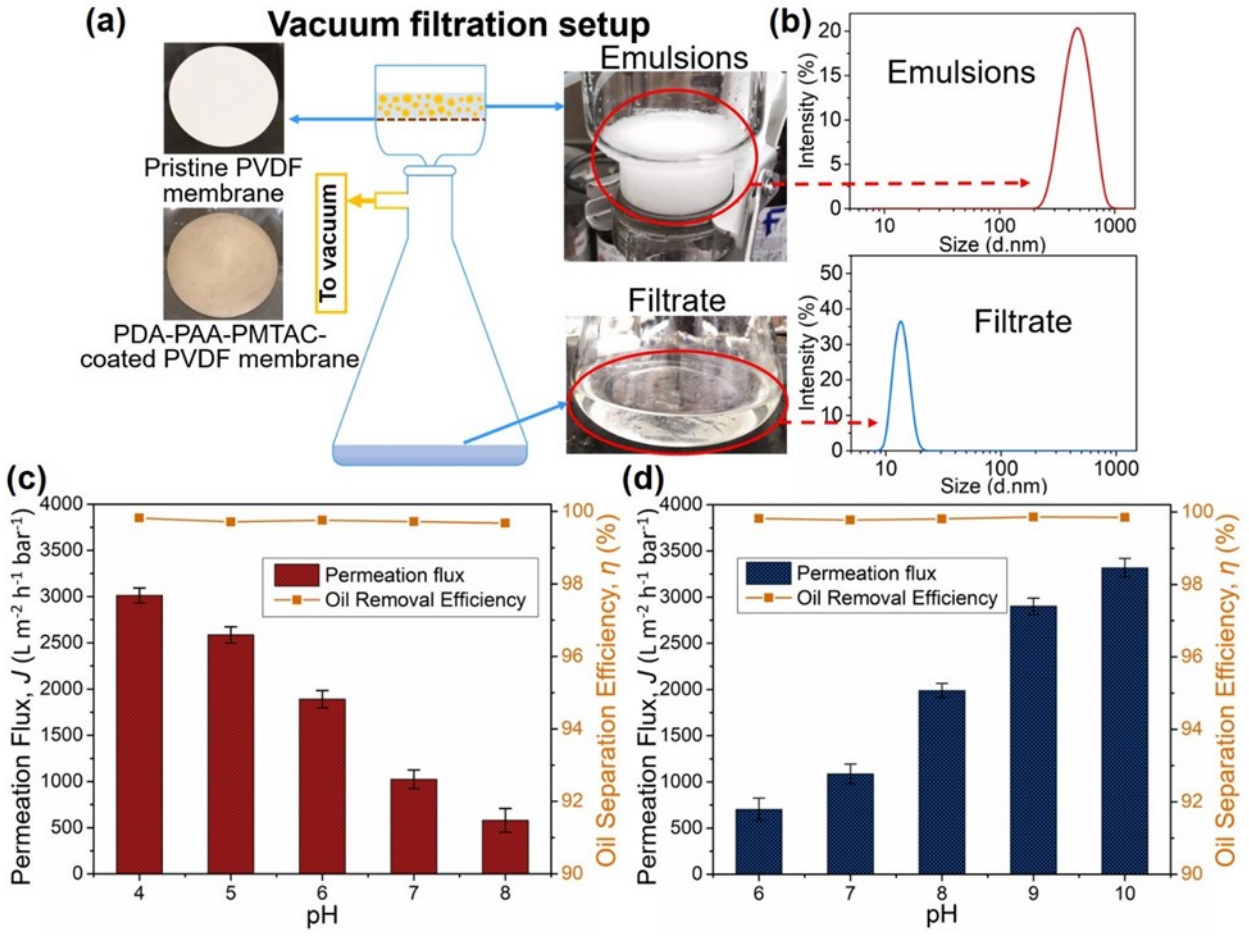

Figure 3.9 (a) Schematic of the vacuum filtration setup with photography of pristine/PDA-PAA-PMTAC-coated membrane, emulsion feed, and filtrate solution; (b) DLS size distribution of feed

emulsion and filtrate; Permeation water flux (bar chart) and oil removal efficiency (solid line) of (c) CTAB and (d) SDS emulsions at different solution pH.

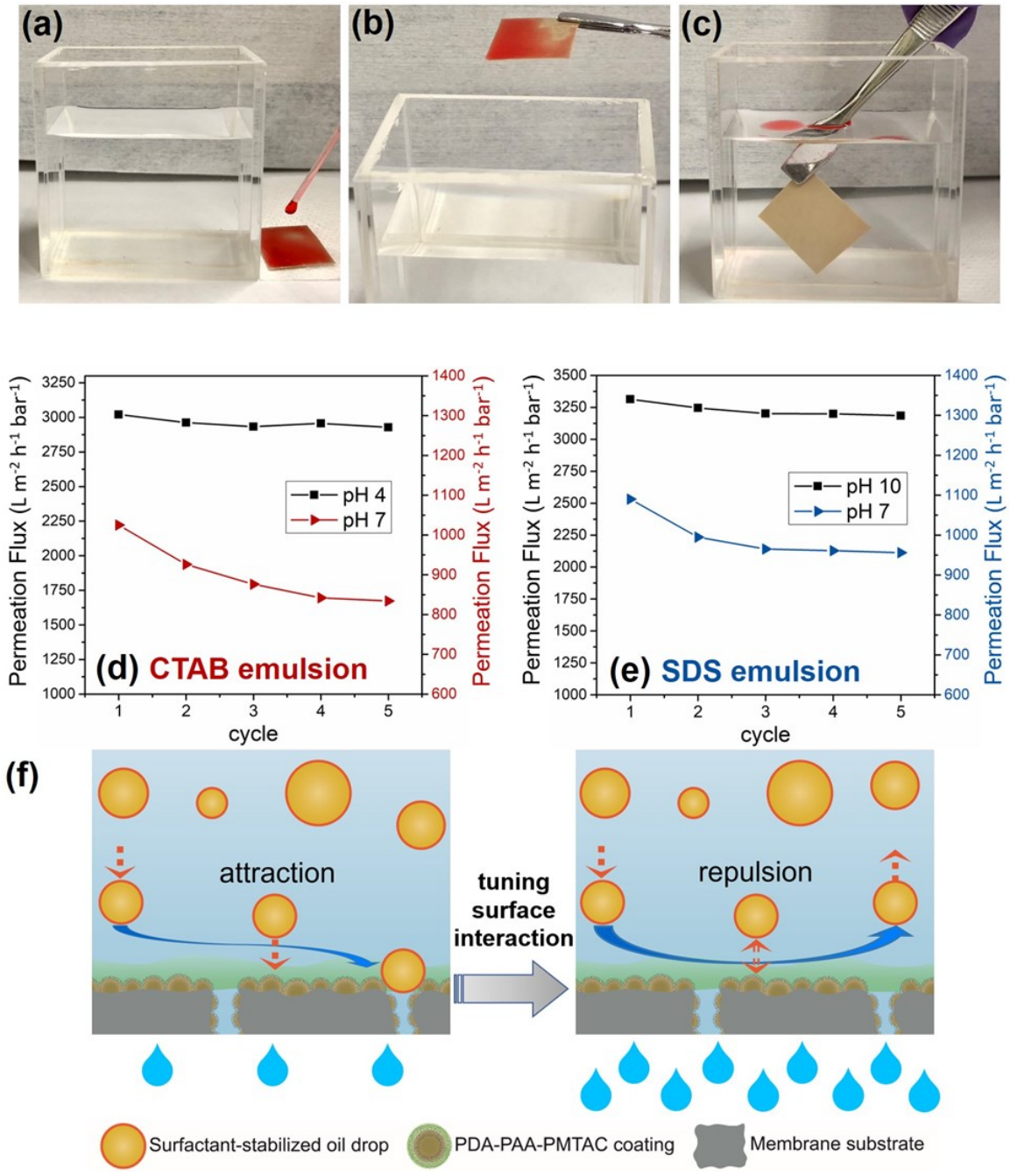

Figure 3.10 (a)-(c) Self-cleaning process of an oil-contaminated membrane; Cycling separation tests for PDA-PAA-PMTAC-coated PVDF membrane filtrating (d) CTAB emulsion (containing

5 wt.% toluene and 200 ppm CTAB) of 1 mM NaCl solution at different pH and (e) SDS emulsion (containing 5 wt.% toluene and 200 ppm SDS) of 1 mM NaCl solution at different pH; (f) Schematic showing the proposed antifouling mechanism of PDA-PAA-PMTAC coating for treating charged emulsions.

Figure 3.10 a-c shows the self-cleaning process of PDA-PAA-PMTAC-coated membrane surface contaminated by toluene with 200 ppm SDS. The coated membrane was firstly contaminated by several toluene drops (dyed by Oil red O) and then immersed in 1 mM NaCl solution at pH 10. The photographs show that toluene droplets could spontaneously detach from the membrane surface and stay at the air/water interface, probably due to the long-range attraction between water molecules and AA/MTAC moieties in the coating for self-cleaning as well as the generated electrostatic repulsion [18, 24]. Meanwhile, the self-cleaning process of PDA-PAA-PMTAC-coated membrane is also evaluated at lower pH of 4 for toluene oils containing 200 ppm SDS, some oil residues was observed on the membrane surface probably due to the weaken the electrostatic repulsion between the oils and membrane surface. The complete self-cleaning process is illustrated in video S2.

The cycling separation tests were conducted using the same vacuum filtration setup with the CTAB and SDS-stabilized emulsions at the varying solution pH. After each separation test of treating 100 mL CTAB/SDS emulsion, the membrane was rinsed by the 1 mM NaCl solution at the same pH value with the filtrating emulsion for 5 minutes and then used for the next oil/water separation cycle. As shown in Figure 3.10d and 10e, the water permeability was almost fully recovered in 1 mM NaCl solution at pH 4 for CTAB stabilized emulsion and at pH 10 for SDS-stabilized emulsion, respectively. For comparison, the cycling separation tests were also conducted in 1 mM NaCl at pH 7 for both the CTAB and SDS cases. The water permeation flux

decreases gradually after each cycle and the residual permeating flux declines to 82% and 87% of the initiated flux after only 5 cycles for CTAB and SDS cases, respectively, at pH 7. The decline of the permeation water flux with the cycling tests could be ascribed to the adsorption of toluene droplets with surfactants that block the pore area of the membrane, also confirmed by the FTIR characterization (Figure 3.S12). Thereby, on the basis of the cycling separation tests, PDA-PAA-PMTAC-coated membrane exhibits regenerable oil/water separation property for surfactant-stabilized emulsions under desired pH conditions, which also suggests its excellent antifouling property for the selective separation of the emulsions. By tuning the surface interaction through solution pH, the developed PDA-PAA-PMTAC coating could effectively resist the contamination of charged emulsions and regenerated in aqueous solution for the long-term reusability of treating practical oily wastewater. The proposed antifouling mechanism is illustrated in Figure 3.10f.

3.4 Conclusions

In this work, a facile and scalable PDA-PAA-PMTAC coating was successfully fabricated and applied for membrane filtration of O/W emulsions protected with different surfactants via a tunable surface force-based strategy. The PDA-PAA-PMTAC coating is superiorly hydrophilic and shows a remarkable uniformity on different substrates such as silicon wafer and PVDF membrane compared to the bare-PDA coating. The surface charge of the PDA-PAA-PMTAC coating could be adjusted by the solution pH mainly due to the protonation/deprotonation of carboxylic groups on the coating surface. Direct force measurements were used to investigate the nanomechanical mechanisms of the antifouling property of the coating materials to the emulsions

under the effect of solution pH and droplet moving velocity. It has been found that decreasing the solution pH leads to the positively charged coating surface, and strong electrostatic repulsion was measured between the CTAB-stabilized toluene droplets and the polymer coating. Hence, the attachment behavior of the toluene droplets will be prevented on the coating surface, suggesting good antifouling performance. On the other hand, increasing solution pH leads to negatively charged coating surface, strong electrostatic repulsion was measured between the SDS-stabilized toluene drops and polymer coating surface, contributing to the antifouling performance. Meanwhile, increasing droplet moving velocity would strengthen the hydrodynamic repulsion during the drainage process of the confined water film, strengthening the antifouling performance. The oil/water separation performance tests using the PDA-PAA-PMTAC-coated membrane demonstrate that the water permeability are significantly influenced by solution pH. An exceptional separation performance was achieved with the filtration water flux over 3000 L m^{-2} h^{-1} bar^{-1} for both the CTAB-stabilized emulsions at pH 4 and SDS-stabilized emulsion at pH 10 with the separation efficiency > 99.8 %. Moreover, the functionalized membrane contaminated by emulsion drops could be readily regenerated through immersion in 1 mM NaCl solution of suitable pH, indicating a superior reusability. This work improves the fundamental understanding of the surface interaction mechanisms associated with the fouling and antifouling issues in emulsion-related water treatment, and provides useful insights into the development of regenerable functional membrane surfaces with tunable surface interactions for various environmental applications such as oil/water separation.

3.5 Supporting Infromation

3.5.1 Surface morphology of bare silicon wafer

Figure 3.S1 shows the bare silicon wafer surface is very smooth with a root-mean-square (RMS) roughness of 0.14 nm.

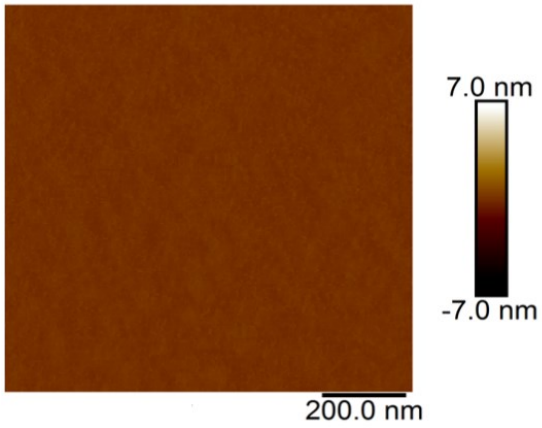

Figure 3.S1 Topographic AFM images of the bare silicon wafer (RMS roughness ~ 0.14 nm).

3.6.2 XPS spectra

The chemical composition of pure-PDA and PDA-PAA-PMTAC coating was characterized by X-ray photoelectron spectroscopy (XPS) as shown in Figure 3.S2. For pure-PDA coating, the XPS C 1s and N 1s core-level spectra (Fig. S2b and S2c) were curve-fitted into four peaks with the binding energies (BEs) at 284.6, 286.0, and 400.1 eV, which were corresponded to the C-C/C-H, C-O, and N-C_2, respectively. For PDA-PAA-PMTAC coating, the XPS C 1s and N 1s core-level spectra (Figure 3.S2e and S2f) were curve-fitted into four peaks with the binding energies (BEs) at 284.6, 286.0, 288.7, 400.1 and 402.5 eV, which were attributed to the C-C/C-H, C-O, O-C=O, N-C_2 and N-$(CH_3)_3^+$, respectively [41]. Compared to

XPS spectra of the pure-PDA coating, the signals of O-C=O and N-$(CH_3)_3^+$ were observed in that of the PDA-PAA-PMTAC coating, suggesting the depositing of AA/MTAC segments into the coating materials.

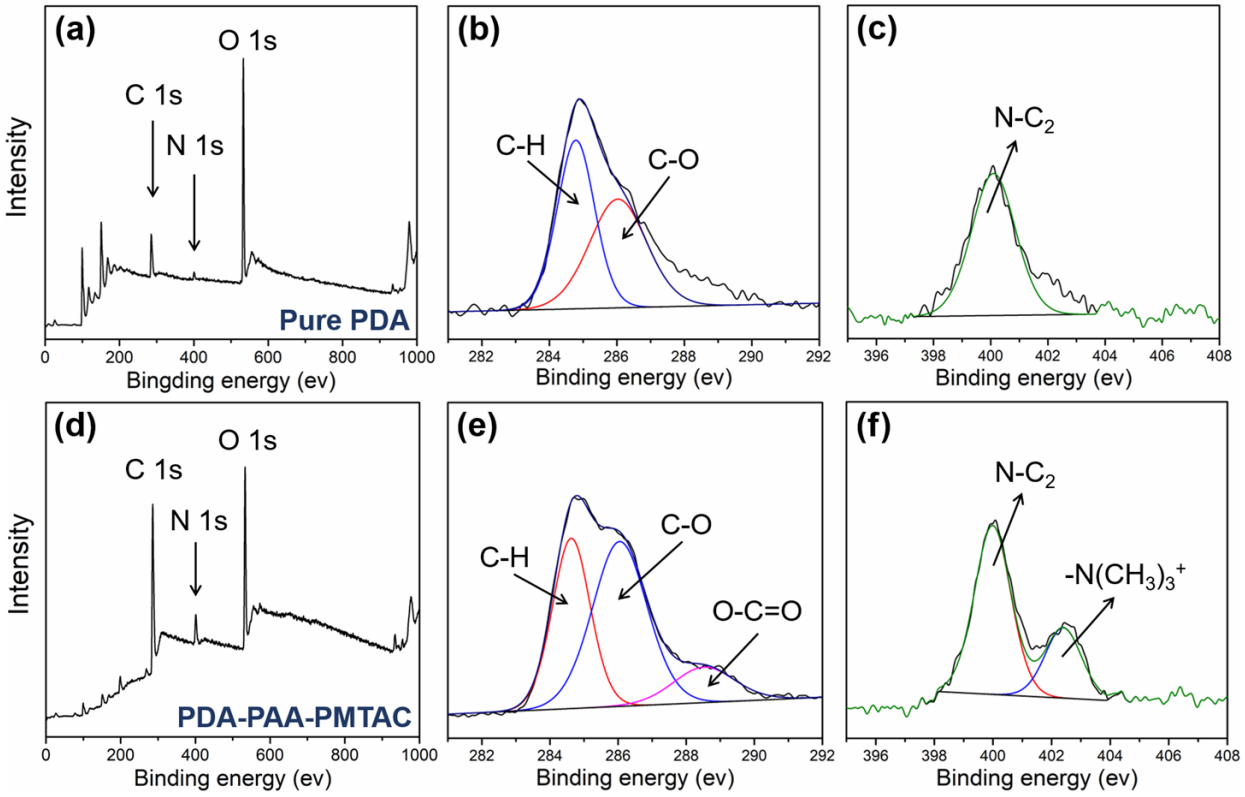

Figure 3.S2 XPS wide scan, C 1s and N 1s core-level spectra of the pure PDA (a~c) and PDA-PAA-PMTAC (d~f) coating on silicon wafer.

3.6.3 Interfacial tension (IFT) data

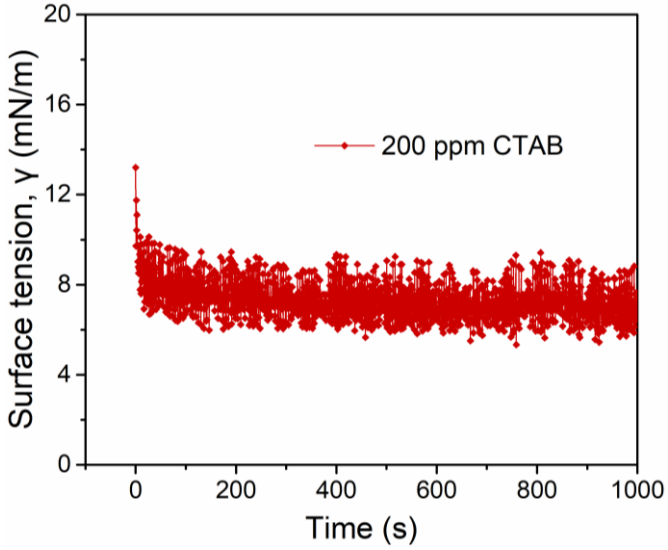

Figure 3.S3 Surface tensions of toluene droplet in 1 mM NaCl aqueous solution containing 200 ppm CTAB surfactant, measured using a pendent drop shape method.

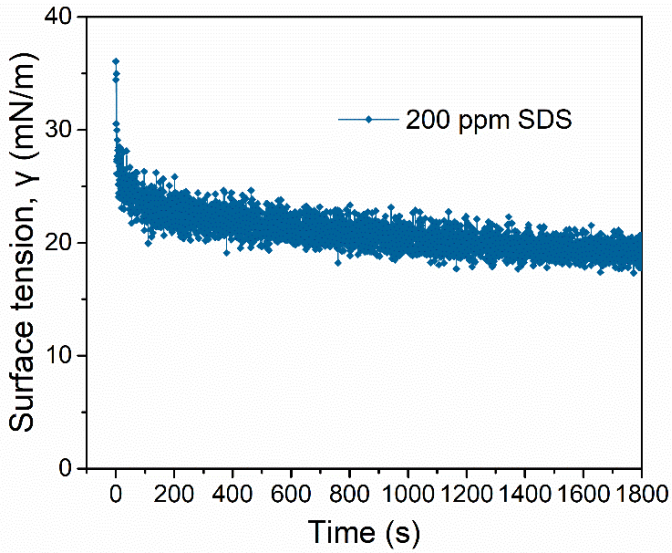

Figure 3.S4 Surface tensions of toluene droplet in 1 mM NaCl aqueous solution containing 200 ppm SDS surfactant, measured using a pendent drop shape method.

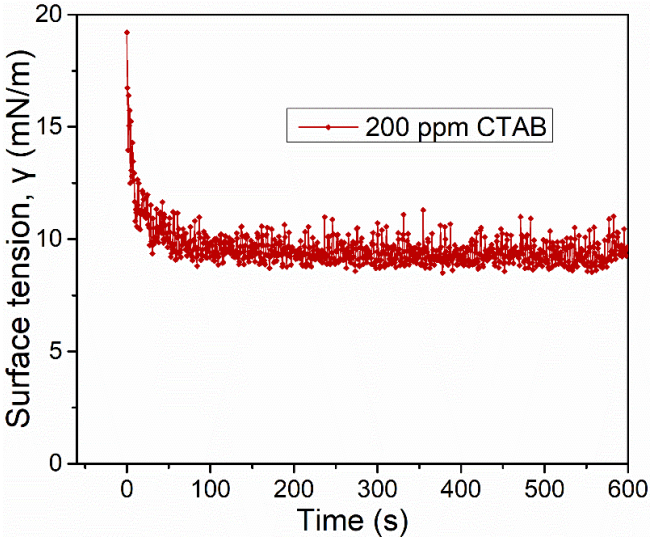

Figure 3.S5 Surface tensions of cyclohexane droplet in 1 mM NaCl aqueous solution containing 200 ppm CTAB surfactant, measured using a pendent drop shape method.

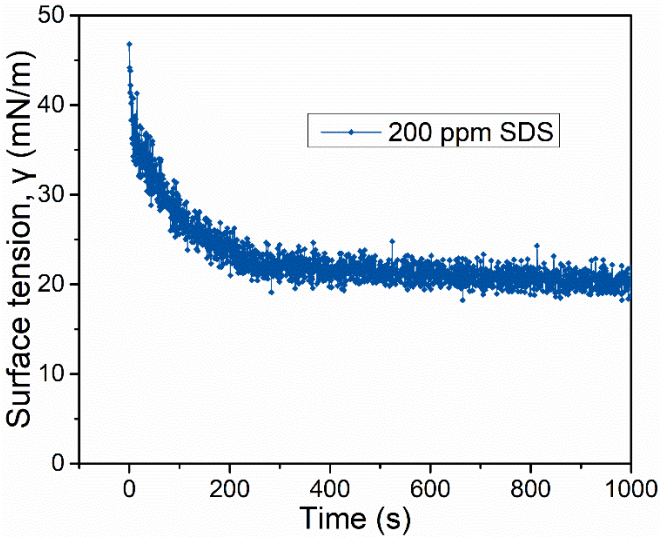

Figure 3.S6 Surface tensions of cyclohexane droplet in 1 mM NaCl aqueous solution containing 200 ppm SDS surfactant, measured using a pendent drop shape method.

3.6.4 Interaction of pure toluene droplet with PDA-PAA-PMTAC coating

Figure 3.S7 shows the measured interaction force and calculated pressure profiles in low saline solution (1 mM NaCl) of pH 6 and 10 as well as the high salinity (500 mM NaCl) of neutral pH 7. In the case of low salinity and acidic pH 6, the "jump-in" behavior was detected after overcoming a weak repulsion of ~ 1.5 nN when the pure toluene droplet was driven to approach the substrate surface by the AFM cantilever, indicating the occurrence of the attachment behavior of pure toluene droplet. However, for the case of low salinity and basic pH 10, the pre-set maximum loading force of 8 nN was reached and retracted from the coating surface to the original position during the measurement. It's noted that no attachment behavior occurred in low salinity and basic pH of 10. In high salinity solution (e.g., 500 mM NaCl), the Debye length was calculated to be 0.43 nm according to Eq. (5), which means the range and strength of the electrostatic interaction were significantly suppressed in high salinity. Thus, the van der Waals (VDW) interaction dominated the surface interaction, resulting in the attachment behavior of the droplet. Figure 3.S7b, S7d, and S7f show the each contribution of VDW pressure, EDL pressure, and hydrodynamic pressure to the overall pressure in low salinity solution of pH 6 and 10 as well as high salinity solution of neutral pH 7. The pure toluene drop is negatively charged with the calculated surface potential of -37 mV which is consistent to our previous research [16].

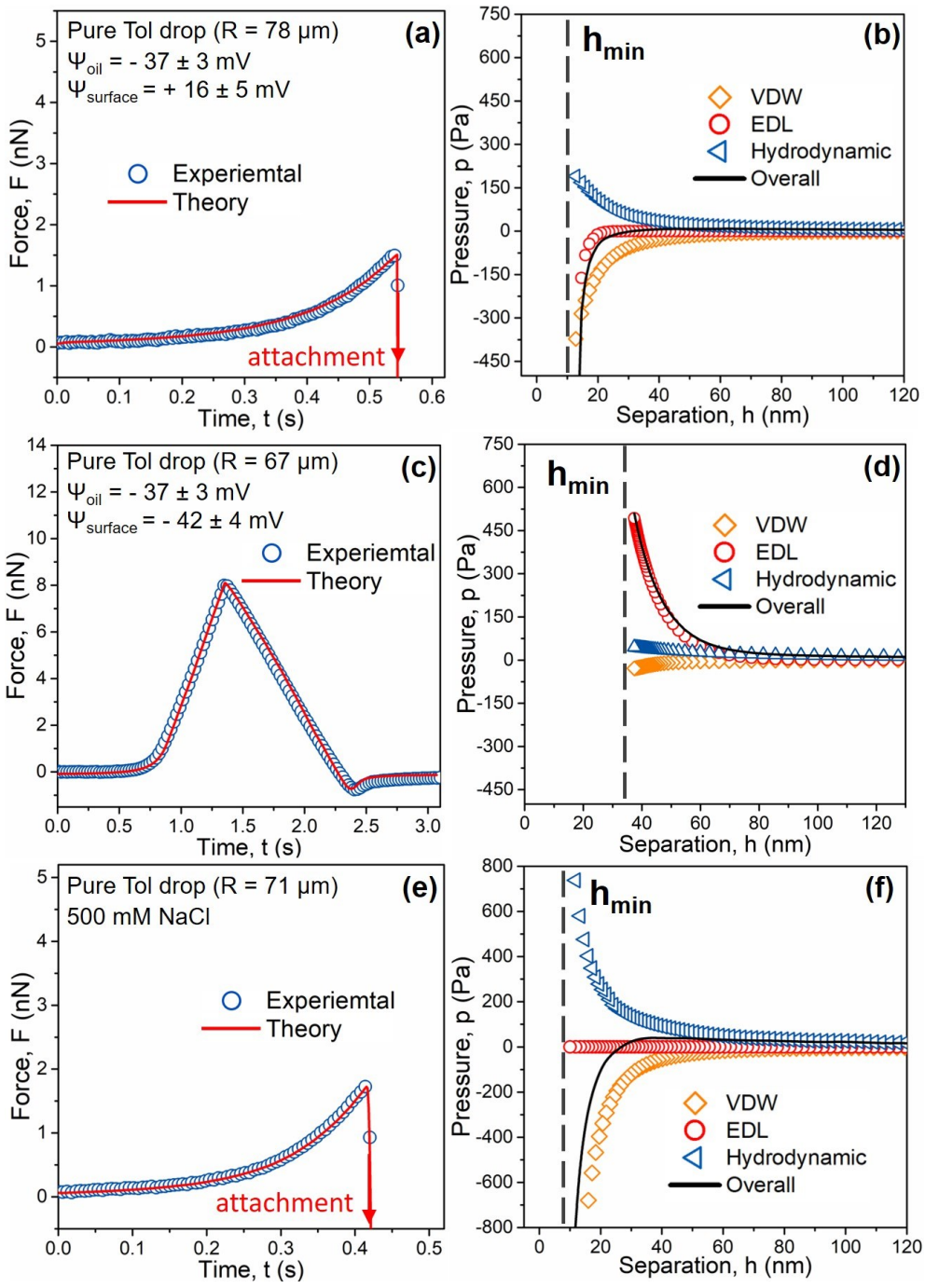

Figure 3.S7 Experimentally measured interaction force profiles (open symbols) of a pure toluene droplet and a PDA-PAA-PMTAC coating in 1 mM NaCl solutions at pH value of (a) 6 and (c) 10 as well as 500 mM NaCl of (e) pH 7, and the theoretical fitting results (red solid curves); Calculated profiles of corresponding VDW disjoining pressure, EDL disjoining pressure, and

hydrodynamic pressures between a pure toluene droplet interacting with a PDA-PAA-PMTAC coating surface at the central position of the droplet in 1 mM NaCl solution of pH (b) 6 and (d) 10 as well as 500 mM NaCl of (f) pH 7.

3.6.5 Comparison of the theoretically fitted surface potential values and the measured zeta potential data for toluene drops

Table 3.S1 Comparison of the theoretically fitted surface potential values and the measured zeta potential data for CTAB-stabilized toluene drops at different solution pH in 1 mM NaCl aqueous solution

pH	Fitted surface potential (mV)	Zeta potential data (mV)
4	**+ 56 ± 6**	**+ 62 ± 9**
6	**+ 53 ± 8**	**+ 57 ± 3**
8	**+ 48 ± 3**	**+ 51 ± 5**

Table 3.S2 Comparison of the theoretically fitted surface potential values and the measured zeta potential data for SDS-stabilized toluene drops at different solution pH in 1 mM NaCl aqueous solution

pH	Fitted surface potential (mV)	Zeta potential data (mV)
6	**- 61 ± 5**	**- 60 ± 8**
8	**- 64 ± 7**	**- 68 ± 5**
10	**- 68 ± 10**	**- 76 ± 12**

3.6.6 Retention test

The retention tests was conducted for PDA-PAA-PMTAC membrane filtrating of colloidal suspension of silica nanoparticles (NP) with different sizes. The high salinity of 500 mM NaCl aqueous solution of pH 7 is used as the solvent of silica suspension to suppress the electric double layer of the membrane and the silica NPs and minimize the effect of electrostatic interaction on the retention tests. The hydrodynamic radius of the silica nanoparticles are characterized using a Zetasizer Nano ZSP system. The concentration of the silica nanoparticles is characterized by UV–Vis spectroscopy based on lambert beer law. The retention (%) is characterized by the fraction of the concentration of silica nanoparticles in the filtrate (C_{f}) and the original suspension solution (C_{i}) using the UV-vis spectrum according to the equation:

$$retention(\%) = (1 - \frac{C_f}{C_i}) \times 100\%$$

The obtained retention curve is shown in Fig. S8. For the silica particles with hydrodynamic diameter less than 78 nm, the retention of the filtration membrane is close to 0 %, suggesting that the small silica NP could not be intercepted by the membrane with the pore size ~ 220 nm. For the silica particles with hydrodynamic diameter over 464 nm, the retention of the filtration is close to 100 %, suggesting that most of the silica NP with relatively large size could be intercepted by the membrane with the pore size ~ 220 nm. However, for the silica particles with hydrodynamic diameter of 156 nm, the retention of the filtration membrane is 68 %. This could ascribe to the size of the silica NP is close to the pore size of the membrane, only one-third of the particles re intercepted by the membrane during the filtration process.

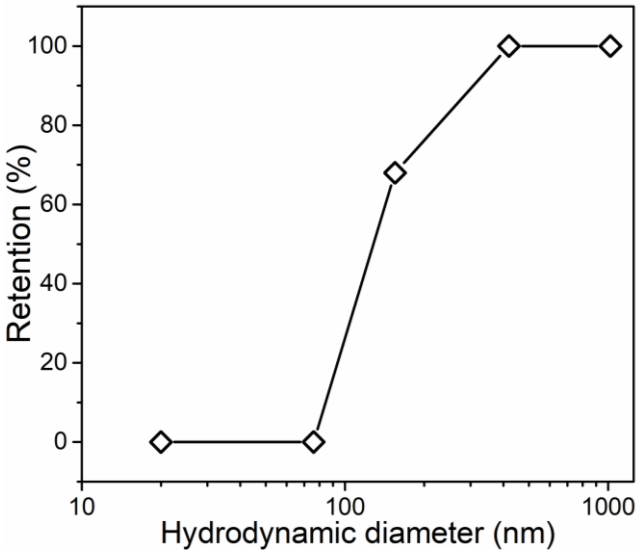

Figure 3.S8 Retention tests of PDA-PAA-PMTAC-coated PVDF membrane using silica nanoparticles of different hydrodynamic diameters.

3.6.7 Vacuum filtration of cyclohexane emulsion

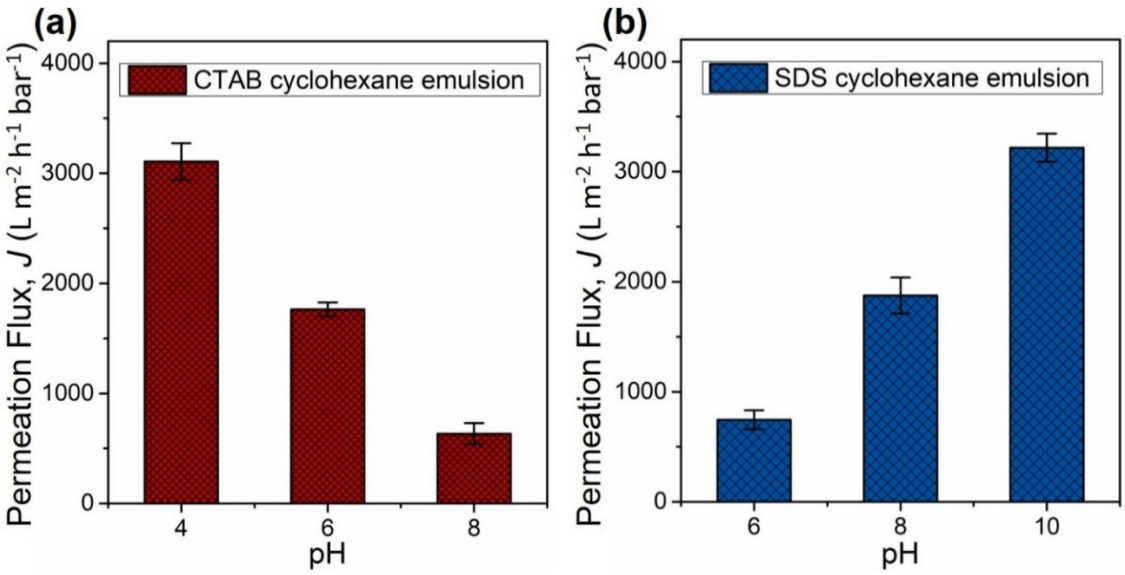

Figure 3.S9 Permeation water flux of cyclohexane-in-water emulsion with 200 ppm (a) CTAB and (b) SDS at different solution pH.

3.6.8 Optical image of separated oil phase, water phase and emulsion before filtration

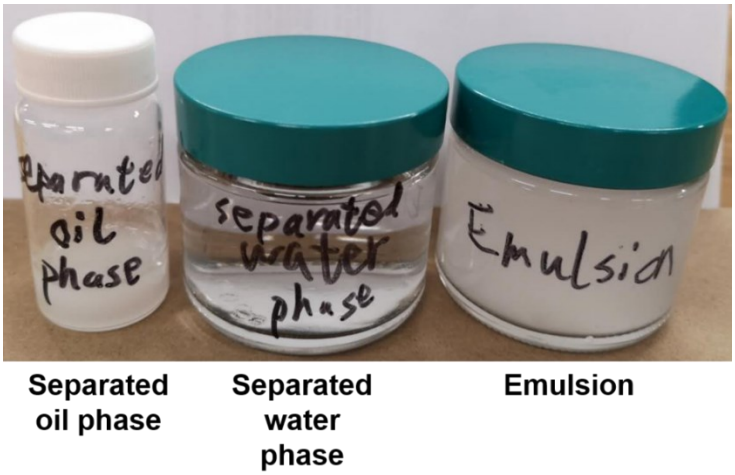

Figure 3.S10 Optical image of separated oil phase, water phase and emulsion before filtration**.**

3.6.9 Self-cleaning process of an oil-contaminated membrane

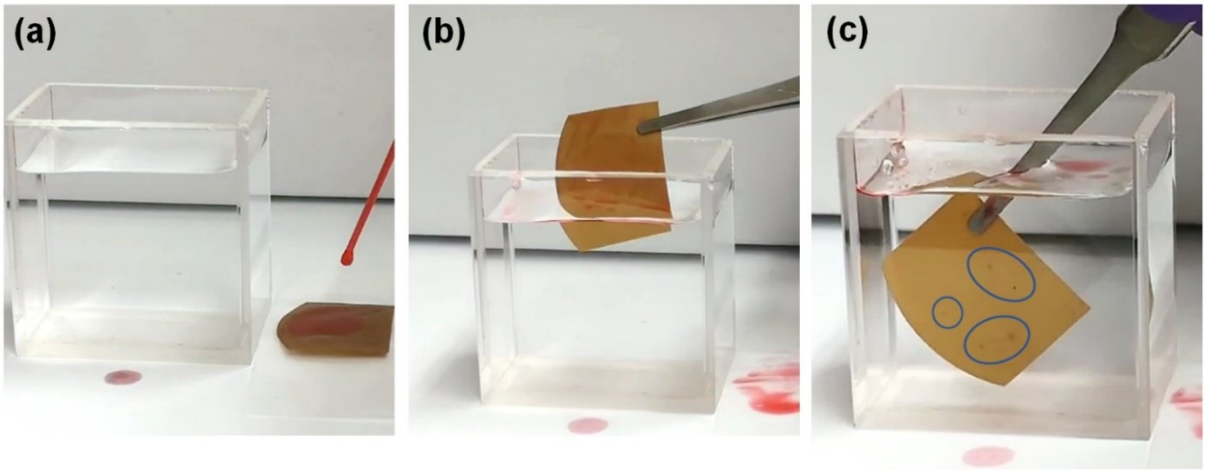

Figure 3.S11 Self-cleaning process of an oil (containing 200 ppm SDS)-contaminated membrane of PDA-PAA-PMTAC-coated PVDF membrane at pH 4.

3.6.10 FTIR spectrum of membrane after cycling tests

The FTIR spectra of the filtration membrane used for the cycling tests of SDS emulsions at two different solution pH are illustrated in Figure 3.S12. From the spectrum, the transmittance peak was observed at 1247 cm^{-1} associated with sulfonate symmetric stretching of SDS for the membrane under the cycling tests with significant water permeation flux decline at pH 7 [49]. However, for the spectrum of the membrane under the cycling tests with no significant water permeation flux decline at pH 10, there is no similar transmittance peak associated with SDS observed.

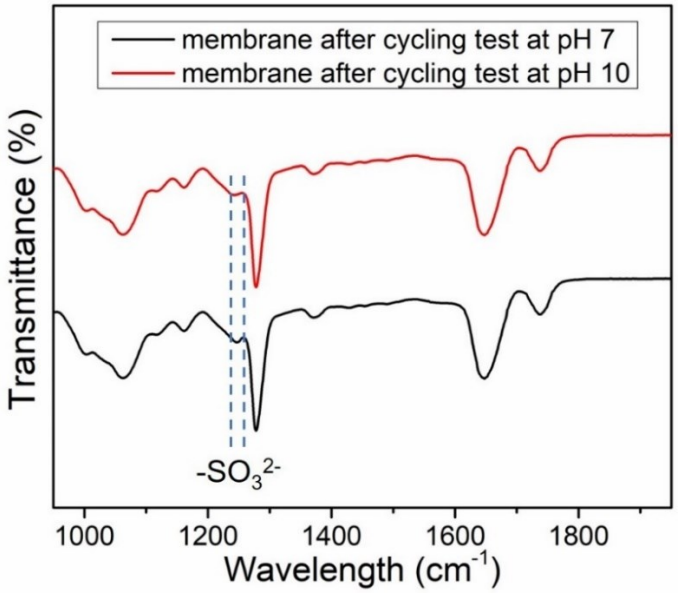

Figure 3.S12 FTIR spectra of the PDA-PAA-PMTAC-coated PVDF membrane after cycling tests at pH 7 (black) and pH 10 (red).

References

[1] J. Bibette, F. Leal-Calderon, Surfactant-stabilized emulsions, Current Opinion in Colloid & Interface Science, 1 (1996) 746-751.
[2] X. Zhu, A. Dudchenko, X. Gu, D. Jassby, Surfactant-stabilized oil separation from water using ultrafiltration and nanofiltration, Journal of membrane science, 529 (2017) 159-169.
[3] X. Su, H. Li, X. Lai, L. Zhang, X. Liao, J. Wang, Z. Chen, J. He, X. Zeng, Dual-functional superhydrophobic textiles with asymmetric roll-down/pinned states for water droplet transportation and oil–water separation, ACS applied materials & interfaces, 10 (2018) 4213-4221.
[4] L. Li, Z. Xu, W. Sun, J. Chen, C. Dai, B. Yan, H. Zeng, Bio-inspired membrane with adaptable wettability for smart oil/water separation, Journal of Membrane Science, 598 (2020) 117661.
[5] Y. Zhu, D. Wang, L. Jiang, J. Jin, Recent progress in developing advanced membranes for emulsified oil/water separation, NPG Asia materials, 6 (2014) e101.
[6] Z. Chu, Y. Feng, S. Seeger, Oil/water separation with selective superantiwetting/superwetting surface materials, Angewandte Chemie International Edition, 54 (2015) 2328-2338.
[7] C. Charcosset, Ultrafiltration, Microfiltration, Nanofiltration and Reverse Osmosis in Integrated Membrane Processes, Integrated Membrane Systems and Processes, (2015) 1.
[8] T. Jin, J. Song, J. Zhu, L.D. Nghiem, B. Zhao, X.-M. Li, T. He, The role of the surfactant sodium dodecyl sulfate to dynamically reduce mass transfer resistance of SPEEK coated membrane for oil-in-water emulsion treatment, Journal of Membrane Science, 541 (2017) 9-18.
[9] Z. Yin, R.J.E. Yeow, Y. Ma, J.W. Chew, Link between interfacial interaction and membrane fouling during organic solvent ultrafiltration of colloidal foulants, Journal of Membrane Science, 611 (2020) 118369.
[10] K. Wang, X. Liu, Y. Tan, W. Zhang, S. Zhang, J. Li, Two-dimensional membrane and three-dimensional bulk aerogel materials via top-down wood nanotechnology for multibehavioral and reusable oil/water separation, Chemical Engineering Journal, 371 (2019) 769-780.
[11] M. Ge, C. Cao, J. Huang, X. Zhang, Y. Tang, X. Zhou, K. Zhang, Z. Chen, Y. Lai, Rational design of materials interface at nanoscale towards intelligent oil–water separation, Nanoscale Horizons, 3 (2018) 235-260.
[12] L. Tan, N. Han, Y. Qian, H. Zhang, H. Gao, L. Zhang, X. Zhang, Superhydrophilic and underwater superoleophobic poly (acrylonitrile-co-methyl acrylate) membrane for highly efficient separation of oil-in-water emulsions, Journal of Membrane Science, 564 (2018) 712-721.
[13] N. Shahkaramipour, A. Jafari, T. Tran, C.M. Stafford, C. Cheng, H. Lin, Maximizing the grafting of zwitterions onto the surface of ultrafiltration membranes to improve antifouling properties, Journal of Membrane Science, 601 (2020) 117909.
[14] Y.-M. Lin, G.C. Rutledge, Separation of oil-in-water emulsions stabilized by different types of surfactants using electrospun fiber membranes, Journal of membrane science, 563 (2018) 247-258.
[15] M.B. Tanis-Kanbur, S. Velioğlu, H.J. Tanudjaja, X. Hu, J.W. Chew, Understanding membrane fouling by oil-in-water emulsion via experiments and molecular dynamics simulations, Journal of Membrane Science, 566 (2018) 140-150.

[16] L. Gong, X. Qiu, L. Zhang, J. Huang, W. Hu, L. Xiang, D. Zhu, R. Sabbagh, M. Mahmoudi, V. Fattahpour, Probing the Interaction Mechanism between Oil-in-Water Emulsions and Electroless Nickel–Phosphorus Coating with Implications for Antifouling in Oil Production, Energy & Fuels, 33 (2018) 3764-3775.
[17] W. Zhang, Y. Zhu, X. Liu, D. Wang, J. Li, L. Jiang, J. Jin, Salt-induced fabrication of superhydrophilic and underwater superoleophobic PAA-g-PVDF membranes for effective separation of oil-in-water emulsions, Angewandte Chemie International Edition, 53 (2014) 856-860.
[18] C. Shi, B. Yan, L. Xie, L. Zhang, J. Wang, A. Takahara, H. Zeng, Long-Range Hydrophilic Attraction between Water and Polyelectrolyte Surfaces in Oil, Angewandte Chemie International Edition, 55 (2016) 15017-15021.
[19] T. Wang, Y.-Q. Wang, Y.-L. Su, Z.-Y. Jiang, Antifouling ultrafiltration membrane composed of polyethersulfone and sulfobetaine copolymer, Journal of membrane science, 280 (2006) 343-350.
[20] J. Wu, W. Wei, S. Li, Q. Zhong, F. Liu, J. Zheng, J. Wang, The effect of membrane surface charges on demulsification and fouling resistance during emulsion separation, Journal of membrane science, 563 (2018) 126-133.
[21] J. Gu, P. Xiao, J. Chen, J. Zhang, Y. Huang, T. Chen, Janus polymer/carbon nanotube hybrid membranes for oil/water separation, ACS applied materials & interfaces, 6 (2014) 16204-16209.
[22] X. Chen, L. Hong, Y. Xu, Z.W. Ong, Ceramic pore channels with inducted carbon nanotubes for removing oil from water, ACS applied materials & interfaces, 4 (2012) 1909-1918.
[23] Y. Zhu, F. Zhang, D. Wang, X.F. Pei, W. Zhang, J. Jin, A novel zwitterionic polyelectrolyte grafted PVDF membrane for thoroughly separating oil from water with ultrahigh efficiency, Journal of Materials Chemistry A, 1 (2013) 5758-5765.
[24] J. Zhang, L. Zhang, X. Cui, L. Gong, L. Xiang, C. Shi, W. Hu, H. Zeng, Scalable polyzwitterion–polydopamine coating for regenerable oil/water separation and underwater self-cleaning of stubborn heavy oil fouling without pre-hydration, Chemical communications, 54 (2018) 9734-9737.
[25] C. Zhang, Y. Ou, W.X. Lei, L.S. Wan, J. Ji, Z.K. Xu, CuSO4/H2O2-induced rapid deposition of polydopamine coatings with high uniformity and enhanced stability, Angewandte Chemie International Edition, 55 (2016) 3054-3057.
[26] Y. Bie, J. Yang, X. Liu, J. Wang, Y. Nuli, W. Lu, Polydopamine wrapping silicon cross-linked with polyacrylic acid as high-performance anode for lithium-ion batteries, ACS applied materials & interfaces, 8 (2016) 2899-2904.
[27] J.-J. Li, Y.-N. Zhou, Z.-H. Luo, Mussel-inspired V-shaped copolymer coating for intelligent oil/water separation, Chemical Engineering Journal, 322 (2017) 693-701.
[28] Y. Chen, Y. Qiu, Q. Wang, D. Li, T. Hussain, H. Ke, Q. Wei, Mussel-inspired sandwich-like nanofibers/hydrogel composite with super adhesive, sustained drug release and anti-infection capacity, Chemical Engineering Journal, (2020) 125668.
[29] H.-M. Song, C. Chen, X.-X. Shui, H. Yang, L.-J. Zhu, Z.-X. Zeng, Q.-J. Xue, Asymmetric Janus membranes based on in situ mussel-inspired chemistry for efficient oil/water separation, Journal of Membrane Science, 573 (2019) 126-134.
[30] L. Zhang, M. Zhang, J. Lu, A. Tang, L. Zhu, Highly permeable thin-film nanocomposite membranes embedded with PDA/PEG nanocapsules as water transport channels, Journal of Membrane Science, 586 (2019) 115-121.

[31] L. Han, L. Xiang, J. Zhang, J. Chen, J. Liu, B. Yan, H. Zeng, Biomimetic Lubrication and Surface Interactions of Dopamine-Assisted Zwitterionic Polyelectrolyte Coatings, Langmuir, 34 (2018) 11593-11601.
[32] C. Zhang, M.-Q. Ma, T.-T. Chen, H. Zhang, D.-F. Hu, B.-H. Wu, J. Ji, Z.-K. Xu, Dopamine-Triggered One-Step Polymerization and Codeposition of Acrylate Monomers for Functional Coatings, ACS applied materials & interfaces, 9 (2017) 34356-34366.
[33] L. Han, L. Gong, J. Chen, J. Zhang, L. Xiang, L. Zhang, Q. Wang, B. Yan, H. Zeng, Universal Mussel-Inspired Ultrastable Surface-Anchoring Strategy via Adaptive Synergy of Catechol and Cations, ACS applied materials & interfaces, 10 (2018) 2166-2173.
[34] Y. Zhao, X. Yang, L. Yan, Y. Bai, S. Li, P. Sorokin, L. Shao, Biomimetic nanoparticle-engineered superwettable membranes for efficient oil/water separation, Journal of Membrane Science, 618 118525.
[35] J.-H. Jiang, L.-P. Zhu, X.-L. Li, Y.-Y. Xu, B.-K. Zhu, Surface modification of PE porous membranes based on the strong adhesion of polydopamine and covalent immobilization of heparin, Journal of Membrane Science, 364 (2010) 194-202.
[36] C. Shi, L. Xie, L. Zhang, X. Lu, H. Zeng, Probing the interaction mechanism between oil droplets with asphaltenes and solid surfaces using AFM, Journal of colloid and interface science, 558 (2019) 173-181.
[37] L. Zhang, L. Xie, X. Cui, J. Chen, H. Zeng, Intermolecular and surface forces at solid/oil/water/gas interfaces in petroleum production, Journal of colloid and interface science, 537 (2019) 505-519.
[38] J.L. Hutter, J. Bechhoefer, Calibration of atomic - force microscope tips, Review of Scientific Instruments, 64 (1993) 1868-1873.
[39] D.Y. Chan, E. Klaseboer, R. Manica, Theory of non-equilibrium force measurements involving deformable drops and bubbles, Advances in colloid and interface science, 165 (2011) 70-90.
[40] L. Xie, C. Shi, X. Cui, H. Zeng, Surface forces and interaction mechanisms of emulsion drops and gas bubbles in complex fluids, Langmuir, 33 (2017) 3911-3925.
[41] W.J. Yang, D. Pranantyo, K.-G. Neoh, E.-T. Kang, S.L.-M. Teo, D. Rittschof, Layer-by-layer click deposition of functional polymer coatings for combating marine biofouling, Biomacromolecules, 13 (2012) 2769-2780.
[42] H. Luo, C. Gu, W. Zheng, F. Dai, X. Wang, Z. Zheng, Facile synthesis of novel size-controlled antibacterial hybrid spheres using silver nanoparticles loaded with poly-dopamine spheres, RSC Advances, 5 (2015) 13470-13477.
[43] J.D. Anastassopoulou, Mass and FT-IR spectra of quaternary ammonium surfactants, in: Chemistry and Properties of Biomolecular Systems, Springer, 1991, pp. 1-9.
[44] Y. Maréchal, IR spectra of carboxylic acids in the gas phase: A quantitative reinvestigation, The Journal of chemical physics, 87 (1987) 6344-6353.
[45] M. Schmitt, H. Stark, Active Brownian motion of emulsion droplets: Coarsening dynamics at the interface and rotational diffusion, The European Physical Journal E, 39 (2016) 80.
[46] J. Ge, D. Zong, Q. Jin, J. Yu, B. Ding, Biomimetic and Superwettable Nanofibrous Skins for Highly Efficient Separation of Oil - in - Water Emulsions, Advanced Functional Materials, 28 (2018) 1705051.
[47] H. Shi, Y. He, Y. Pan, H. Di, G. Zeng, L. Zhang, C. Zhang, A modified mussel-inspired method to fabricate TiO2 decorated superhydrophilic PVDF membrane for oil/water separation, Journal of membrane science, 506 (2016) 60-70.

[48] Y. Zhu, J. Wang, F. Zhang, S. Gao, A. Wang, W. Fang, J. Jin, Zwitterionic Nanohydrogel Grafted PVDF Membranes with Comprehensive Antifouling Property and Superior Cycle Stability for Oil - in - Water Emulsion Separation, Advanced Functional Materials, 28 (2018) 1804121.
[49] R.B. Viana, A.B. da Silva, A.S. Pimentel, Infrared spectroscopy of anionic, cationic, and zwitterionic surfactants, Advances in physical chemistry, 2012 (2012).

CHAPTER 4. Soft Armour-like Layer-Protected Hydrogels for Wet Tissue Adhesion and Biological Imaging

4.1 Introduction

The emerging medical techniques for diagnosis and treatment have posed a considerable challenge: lack of soft materials as the bridging interface connecting the operation probe of the medical apparatus and human tissues. Hydrogels as a three-dimensional (3D) hydrophilic polymer matrix typically possess a high water content of over 80 wt.%, which is analogous to human tissues and applicable for biomedical use [1-11]. In the past decades, hydrogels have been widely applied to applications including tissue adhesive [12-14], wound closure [15, 16], health sensing [17, 18], and drug delivery [19-22] with tremendous progress. However, most of the existing hydrogels with the water content over 80 wt.% cannot tightly attach to the wet and dynamic tissue surfaces due to the existence of surrounding water at the contact interfaces, weakening the molecular interactions between hydrogels and tissues, thus restricting their reliable functions under practical conditions [23-26]. Although some of the curing agents like cyanoacrylate or silane-based chemicals have been explored to bridge the hydrogel with tissue surfaces, which help promote a stable adhesion under physiological conditions [27, 28]. It is noted that most of these chemicals are cytotoxic and suffer from slow adhesion formation under wet conditions, incompatibility with soft tissues, and/or lack of on-demand detachment for recyclable use [27, 29-33]. To address these issues, it is desirable to develop biocompatible hydrogels as soft adhesives to achieve instant, tough, and reversible adhesion to various wet tissues for medical practices.

In recent years, the strong and universal wet adhesion capability of some marine organisms like mussel, barnacle, and sandcastle worm has raised great attentions [34-41]. The investigation of the corresponding catechol chemistry and its interfacial interactions such as hydrogen bonding, metal coordination, π-π/cation-π interactions provided significant biomimetic resources for fabricating biopolymeric adhesives [42-48]. Different methods have been applied to incorporate catechol-based derivatives into polymer network of hydrogels to improve their adhesive and cohesive strength including being covalent grafted to the polymer chain and confined between the layer spacing of the 2D materials to form nanocomposite hydrogels [49, 50]. However, compared to the natural marine organisms, most of the reported catechol-based adhesive hydrogels still suffer from the inadequate stability of their adhesion performance in wet or underwater conditions. The discrepancy between natural marine organisms and the artificial catechol-based hydrogels here mainly originates from the limitation of water-removing and water-shielding capability of hydrogels at the contact interface with substrates and lack of dynamic bonds in the internal hydrogel network for energy dissipation [27, 51-57]. Herein, inspired by the structure of the Mytilus byssal thread covered by a thin protective cuticle [34, 42, 58-61]. A new underwater adhesive strategy was proposed via engineering a soft armour-like hydrophobic adhesive layer outside the hydrophilic polymer matrix by tuning metal coordination chemistry. We use this design principle to promote the formation of a water depletion region at the hydrogel-substrate interface and their stable attachment for the desired underwater adhesive property.

Following this strategy, we also developed our dopamine (DA)-iron-sodium dodecyl sulfate-complexation (DISC) hydrogel as the bioadhesives. The hydrogel is prepared by copolymerization of acrylamide with sodium dodecyl sulfate (SDS)/stearyl methacrylate (C_{18})

micelle consisting of a soft armour-like hydrophobic interface as the outermost adhesive layer over the hydrogel matrix. The external hydrophobic layer of the hydrogel (water contact angle in air > 110°) is triggered by the occurrence of Fe^{3+}, resulting in the formation of DA-iron-SDS complexes and recombination of the structure at hydrogel surface to realize fast repelling of the surrounding water, thus promoting a water depletion region upon contact with the target surfaces. After that, the hydrophobic layer interlinks the hydrogel matrix and target surfaces with the assistance of polydopamine moieties via diverse intermolecular interactions i.e., hydrogen bonding, π-π stacking, cation-π, and hydrophobic interactions [38, 43, 46, 62]. Atomic force microscope (AFM) colloidal probe technique was also employed to investigate the assembling mechanisms for the hydrophobic layer of DISC hydrogel. Moreover, the mechanical properties of the obtained DISC hydrogel were characterized by tensile/compression tests, while the adhesion performance of DISC hydrogel to various substrates was evaluated by the lap-shear tests. The DISC hydrogel was further employed as the tissue couplant to test its potential as the bridging interface to enhance the reliable functionality of ultrasonic imaging in the wet intraoral environment [63-65]. Owing to the precise design of the internal nanostructure via tuning molecular interaction, the as-prepared DISC hydrogel possesses instant, stable, and universal adhesive properties to various wet substrates and capability for in vivo ultrasound imaging, which benefits the tissue–device integration for biomedical applications in practical use.

4.2 Materials and Methods

4.2.1 Materials

Acrylamide (AM), stearylmethacrylate (C_{18}), dopamine hydrochloride, Irgacure UV Photo-initiator, poly(ethylene glycol) diacrylate crosslinker (Mn=700), membrane-permeant nucleic

acid stain (Syto 13), and membrane-impermeant stain (propidium iodide) were purchased from Sigma-Aldrich (Canada). Iron(III) chloride, sodium chloride, hydrogen chloride, sodium dodecyl sulfate (SDS), and were purchased from Fisher Scientific (Canada). Chicken breast, porcine skin, and heart were obtained from the local grocery store. Ultrafiltrated water used in all the experiments was generated by the Barnstead Smart2Pure pro water purification system (Thermo Scientific) with a resistivity of 18.2 MΩ·cm.

4.2.2 Synthesis of the prehydrogel

PAM-DA and PAM-SDS-C_{18}-DA prehydrogels were synthesized to investigate the effect of hydrophobic association on the adhesive strength. Precursor solution for PAM-DA prehydrogel was prepared by dispersing 1.6 g AM hydrophilic monomer, 0.04g PEGDA crosslinker, 0.015g DA, and 0.1g Irgacure UV photo-initiator in 20 mL of 0.7 M NaCl saline solution at pH 4.6. Micro micelle solutions for PAM-SDS-C_{18}-DA prehydrogel were first prepared by dispersing 1.4 g SDS in 20 mL of 0.7 M NaCl saline solution at pH 4.6. Then hydrophobic monomer C_{18} of 0.22 g was dissolved in the micro micelle solution and the mixtures were stirred at 50°C in an oil bath for 30 min until a clear precursor solution was obtained. After that, 1.3g AM hydrophilic monomer, 0.04g PEGDA crosslinker, 0.015g DA, and 0.1g Irgacure UV photo-initiator were added into the precursor solution and degassed for 20 min. Finally, the hydrogels were prepared in the rectangular degas mold under UV crosslinker for 20 min.

4.2.3 Formation of the surface hydrophobic layer

The prehydrogel then post-treated by immersing into 0.08 M $FeCl_3$ solution for different immersion time, to trigger the metal coordination-induced surface hydrophobilization process, denoted as DISC-x (x represent the number for the immersion time), respectively. The hydrogel

was then washed by water to remove the unassociated residues and gently dried under the blowing of nitrogen to remove the residual water on the surface. The water contact angle in air on the hydrophobic surface of the DISC hydrogel was measured to investigate the effect of immersing time using a contact angle goniometer (Ramé-Hart instrument, NJ).

4.2.4 Characterization of the hydrogel

The internal morphology and the corresponding element distribution of hydrogels were characterized using a field-emission scanning electron microscope (FE-SEM) (Zeiss Sigma 300 VP-FESEM, Germany) with energy-dispersive X-ray spectroscopy (EDS) at the electron acceleration voltage of 10.2 keV. Fourier transform infrared (FTIR) spectrometer (Thermo Scientific Nicolet, iS50 FT-IR) was applied to identify the chemical composition of the freeze-dried hydrogel samples. The hydrogel samples for characterization were first quenched in liquid nitrogen and freeze-dried. After that, the samples were sectioned by a blade cutter for FTIR and SEM/EDS analysis. Before SEM imaging, the sectioned samples were sputter-coated by a thin layer of gold metal.

The rheological property was characterized by an AR-G2 stress-controlled rheometer (TA Instruments) using a 20 mm cone-plate (2^{o}) configuration and 53 μm gap. Oscillatory frequency sweep tests for hydrogels containing different amount Hb segments (from 0% to 3% molar ratio of C_{18}/acrylamide) were conducted from 0.1 to 100 rad/s, at a fixed strain of 10%. The tensile and compression tests were performed using an AGS-X universal tensile testing machine (Shimadzu, Japan) equipped with the corresponding load cell (maximum load 50 N and 200 N, respectively). For the tensile tests, the rectangular hydrogel specimens were prepared with the dimension of 15.5 mm (Length) x 6.2 mm (Width) x 1.8 mm (Thickness) and stretched at a constant rate of 10 mm/min. For the compression tests, the cylinder hydrogel specimens were

prepared with the dimension of 16.2 mm (Height) and 12.5 mm (Diameter) and compressed at a constant rate of 10 mm/min. Meanwhile, 5 cycles of loading-unloading tensile and compressive tests were performed on rectangular and cylinder samples at the tensile strain of 200 % and compressive strain of 80% to investigate their recoverability after stretch and compression, respectively.

4.2.5 Force measurement using colloidal probe AFM technique

The lab-made silica probe for AFM force measurement was prepared by attaching a silica sphere of ~5 μm diameter to the top end of the tipless cantilever (NP-O10, Bruker, Santa Barbara, CA) via a two-component epoxy adhesive (EP21D-1, Mater bond, USA). After that, the silica probe was sputter-coated by gold and then both the gold-coated and gold wafer were immersed in sodium 3-mercapto-1-propanesulfonate (10 mM)/ethanol solution to obtain the sulfonate-grafted silica probe and substrate for AFM force measurement. The spring constant of the sulfonate-grafted silica probe was calculated to be 0.15~0.20 N/m using the Hutter and Bechhoefer thermal tune method. During the force measurement experiment, the sulfonate grafted-silica probe was driven to approach the sulfonate-grated substrate at a fixed velocity of 1 μm/s in different aqueous solutions. When a pre-set deflection was reached, the probe was retracted from the substrate surface. The correlated surface force was then calculated by Hooke's Law according to the spring constant obtained from the calibration and the deflection of the cantilever recorded by the photodiode.

4.2.6 Lap shear tests for tissue adhesive

The adhesion strength of the developed hydrogels was investigated via the lap shear test using the same AGS-X universal tensile testing machine (Shimadzu, Japan). The adherends used in

this work include glass, resin, wood, chicken breast, porcine skin and heart. The size of the hydrogel samples is fixed at 12 mm (Length) x 5 mm (Width) x 2 mm (Thickness). For adherends of glass, resin, and wood, the rectangular substrate was directly connected by the hydrogel adhesive samples. For animal tissues of chicken breast, porcine skin, and heart, the tissues are first glued to the rectangular wood substrates using a super glue then connected by the hydrogel adhesive samples. All the lap shear tests were performed at a constant separation rate of 2 mm/min. The wet adhesion strength was collected by spreading the water at the contact interface of adherends and hydrogel adhesives. The preload pressure of 20 kPa was applied for a short contact time of 2 min before the lap shear tests.

4.2.7 Biocompatibility test

Chinese hamster ovary (CHO) and human embryonic kidney (HEK) 293 were used as the model cells to evaluate the cell toxicity of DISC hydrogel. CHO cells were first cultured in Dulbecco's Modified Eagle Medium (DMEM)/Nutrient Mixture F-12 supplemented with L-glutamine, penicillin-streptomycin, and 10% fetal bovine serum (FBS). For 2D cell culture, a DMEM culture medium containing CHO cells at a density of $1x10^6$ was then added on the top of the hydrogel and a Petri dish plate (as the reference). After 12 h and 72 h incubation at 37 °C, cells were stained by a cell membrane integrity stain [1 μM Syto 13 and 0.5 μM propidium iodide mixed in phosphate-buffered saline (PBS)] and imaged by a laser scanning confocal fluorescent microscope for 3 samples [66]. The dead cells with destructive cell membranes would be stained by the cell-impermeant nucleic acid stain of propidium iodide. The cell viability was then quantified by Image J software.

4.2.8 Ultrasound characterization and imaging

The ultrasound speed and attenuation of the DISC-40 samples were characterized by the transmission-through technique in water. For comparison, a sample of Aquaflex ultrasound gel pad (Parker Laboratories, Inc.) was also measured for ultrasound properties. During the experiment, the gel pad samples were fixed on a gel pad holder and placed between two coaxially mounted 20 MHz transducers (Olympus V317-N-SU, Waltham, MA), that were 20 cm apart. The gel pad holder was positioned 14 cm from the emitter with the ultrasound beam perpendicular to the sample's surface. Signals were collected without (water signal) and with the sample (sample signal) at five different locations on the sample with each approximately 5 mm from the neighboring location. The group velocity (V) and phase velocity ($c(\omega)$) of the sample are determined by Eq (1-2)[67, 68]:

$$V = \frac{h}{h/V_{water} - \Delta t} \ , \tag{1}$$

$$c(\omega) = \frac{\omega h}{\omega h/V_{water} - \Delta\phi} \tag{2}$$

where h is the sample thickness, V_{water} is the water velocity (~1480 m/s), Δt is the time difference of the chosen reference point on the time series, $\Delta\varphi$ is the difference of the unwrapped phase shift of the corresponding spectra, and ω is the angular frequency. The slope of the linearly best-fitted line to the phase velocity spectrum bounded between ± 6 dB determines the dispersion. The attenuation coefficient, α (in dB/cm) of the sample can be calculated with the corresponding amplitude spectra (A) of the signals:

$$\alpha(\omega) = \frac{20}{h}\log_{10}\frac{A_{water}(\omega)}{A_{sample}(\omega)} \quad . \tag{3}$$

Similar to the dispersion computation, the slope of the linearly best-fitted line to the attenuation spectrum within the ± 6 dB frequency range determines the normalized broadband attenuation (nBUA) in dB/cm·MHz.

Ultrasound imaging was done on a porcine molar with a 5 mm thick DISC-40 hydrogel and AF gel pad as the couplings, respectively. The portable SonixTablet ultrasound system with the L40-8/12 transducer (Analogic, Vancouver, Canada) was employed for scanning. Some ultrasound gel (Parker Laboratories, USA) was used occasionally to fill the contact gap to ensure a strong ultrasonic transmission.

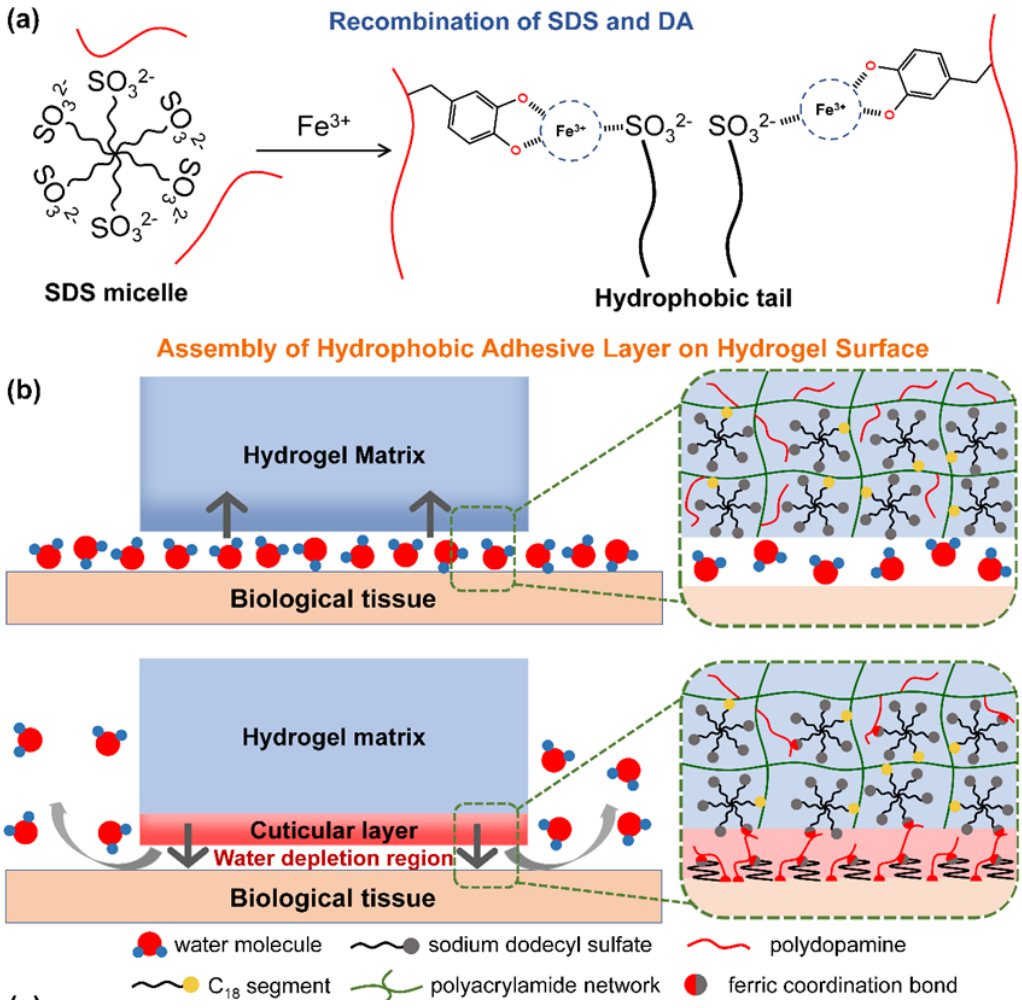

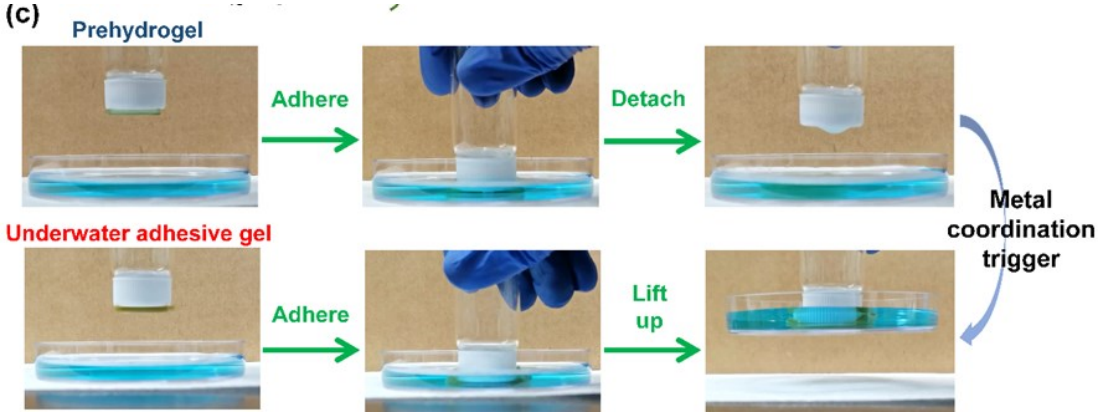

Figure 4.1 Schematic illustration of (A) iron triggered recombination of SDS micelle; (B) Constructing soft armour-like hydrophobic adhesive layer on the surface of PAM-SDS-C_{18}-DA prehydrogel; (C) Demonstration of underwater adhesion test of DISC adhesive hydrogel.

4.3 Results and discussion

4.3.1 Design and molecular engineering of DSIC hydrogels

Unlike the traditional hydrogels containing water in the entire polymer network, DISC hydrogel forms a soft armour-like hydrophobic layer over the hydrophilic polymer network by mimicking the structure of the Mytilus byssal thread covered by a thin protective cuticle. The formation and operation mechanisms of the hydrophobic shell are illustrated in Figure 4.1. The polyacrylamide (PAM)-SDS-C_{18} prehydrogel is prepared by direct photoinitiation to copolymerize the hydrophilic monomers acrylamide, hydrophobic (Hb) monomers C_{18} preserved in SDS micelles, dopamine, and a small amount of poly(ethylene glycol) diacrylate as the crosslinker under 365 nm UV irradiation [69, 70]. The DISC hydrogel was then fabricated by immersing the PAM-SDS-C_{18}-DA prehydrogel in 0.08 M $FeCl_3$ solution to trigger the metal coordination of PDA and SDS, followed by aqueous solution wash to remove the unbonded

residuals. In this process, the PAM-SDS-C_{18}-DA prehydrogel could self-regulate and assemble an outermost hydrophobic layer over the polymer network in $FeCl_3$ solution, most probably due to the metal binding of Fe^{3+} with the sulfonate groups of SDS and catechol groups of PDA [71-73], as illustrated in Figure 4.1A. In the aqueous medium, upon approaching a target surface (i.e. tissue surface), the hydrophobic layer could effectively repel the surrounding water and promote the formation of the water depletion region. The absence of water at the contact interface favors the formation of stable connections of adhesives to the adherend surfaces, realizing the desired underwater adhesion. Figure 4.1C demonstrated the comparison of adhesion tests in low saline water (10 mM NaCl) dyed by basic blue. The PAM-SDS-C_{18}-DA prehydrogel could adhere to the bottom of the Petri dish but detach from the cap of the glass bottle when being lifted up. Conversely, the Fe^{3+}-treated DISC hydrogel could instantly and tightly adhere to the bottom of the Petri dish (contact time ~ 5s) and lift up the whole Petri dish filled with water.

We then investigated the interfacial and rheological properties of the obtained DISC hydrogels. The morphology and element distribution of the obtained DISC hydrogels were characterized by field emission scanning electron microscopy (FE-SEM) and energy-dispersive X-ray spectroscopy (EDS), respectively. Figure 4.2A shows the morphology of the sectional area of a lyophilized DISC hydrogel sample. Unlike the interior of the DISC hydrogel showing a highly porous honeycomb-like structure, the surface layer of the DISC hydrogel exhibits a dense and nonporous structure, which confirmed that the DISC hydrogel has a distinctive soft armour-like cuticular structure. Moreover, the result of Fe, C and S element mapping shown in Figure 4.2A and 4.S1 also indicates the difference of the cuticular and internal region of the DISC hydrogel. Figure 4.2B illustrates the element mass fraction of the cuticular and internal layers, respectively. The mass fraction of element C, O, S, and Fe increases while the mass fraction of

element N decreases from the cuticular to the internal layer of DISC hydrogel. The difference of the element mass fraction from the cuticular to the internal layer could be attributed to the formation of the dense cuticular structure triggered by the metal coordination of Fe^{3+} with SDS and dopamine. The stability of the hydrogel is characterized by swelling tests, as shown in Figure 4.S2. The lyophilized DISC hydrogel could swell in 700 mM saline water and reached its equilibrium of ~ 87 wt.% water content at a swelling time of 240 min, which is close to its original water content of 86.7 wt.%. The hydrophobicity of the hydrogel surface was characterized by water contact angle (WCA) measurement in air to investigate the effect of immersing time in $FeCl_3$ solution. As illustrated in Figure 4.2C, the WCA in air on PAM-SDS-C_{18}-DA prehydrogel surface before Fe^{3+} treatment is around 20°. The prehydrogel turns to be hydrophilic with water being the majority and polymers being the minority in its network. After being treated with $FeCl_3$ solution, the WCA on the surface of DISC hydrogels increases with the immersion time, reaching the maximum value of 110° at the immersion time of 40 min. The hydrophobilization of hydrogel surface here could be attributed to the disassembly and recombinant of SDS micelles on the surface of the hydrogel in the presence of Fe^{3+} through metal coordination.[73] The chemical functionality of DISC hydrogel section surfaces was characterized using the Fourier-transform infrared (FTIR) spectroscopy, as shown in Figure 4.2D. The characteristic peaks located at 1247 and 1650 cm^{-1} are corresponded to sulfate symmetric stretching of SDS and the aromatic C=C skeleton stretching of PDA, respectively, while the two peaks located at 2850 and 2920 cm^{-1} are associated to antisymmetric and symmetric stretching of the long alkyl chain belong to the SDS/C_{18} moieties of the polymer network [74, 75]. The viscoelastic behaviors of the DISC hydrogels were evaluated by rheological measurement, as shown in Figure 4.2E. By introducing Hb monomer C_{18} (from 0% to 3% molar ratio of

C_{18}/acrylamide), both the storage modulus (G′) and the loss modulus (G″) of the DISC hydrogel are enhanced significantly, suggesting an increased cross-linking density of SDS/C_{18} micelle to PAM network.

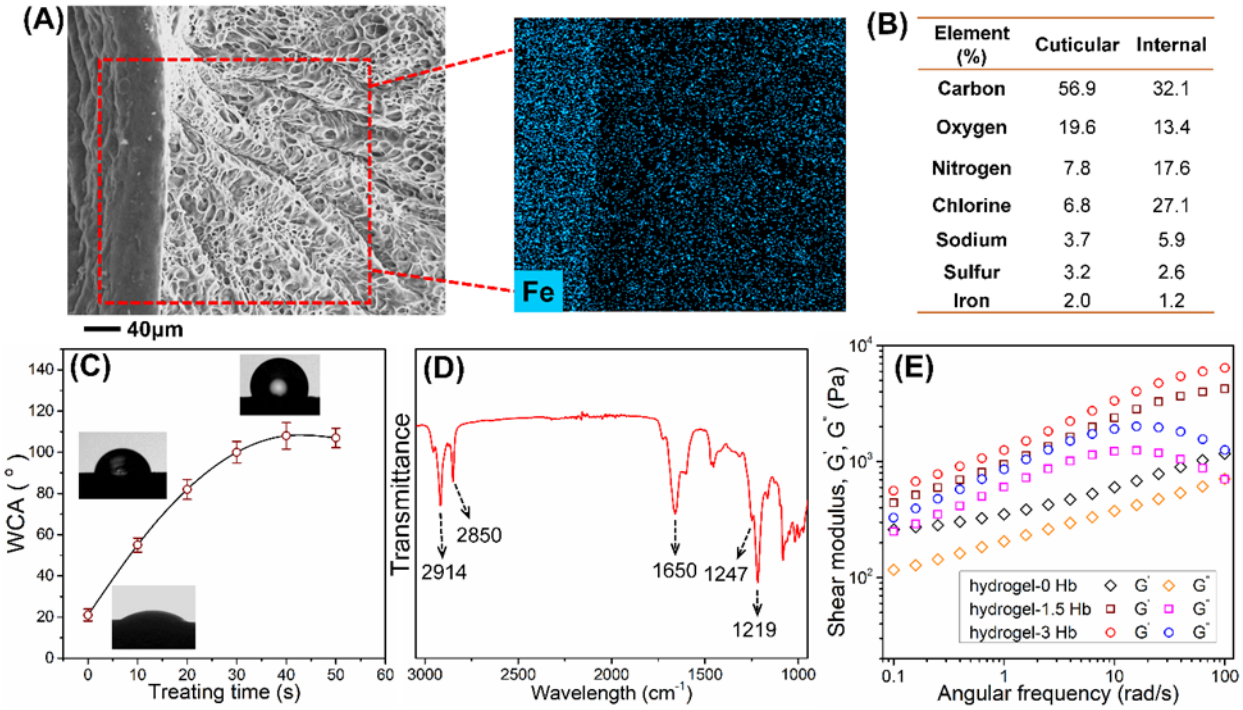

Element (%)	Cuticular	Internal
Carbon	56.9	32.1
Oxygen	19.6	13.4
Nitrogen	7.8	17.6
Chlorine	6.8	27.1
Sodium	3.7	5.9
Sulfur	3.2	2.6
Iron	2.0	1.2

Figure 4.2 (A) SEM image of DISC hydrogel regarding to the cuticular layer and internal polymer network with EDS mapping of Fe; (B) EDS analysis at the cuticular layer and internal polymer network, respectively; (C) Water contact angle in air on the hydrogel surface with different treating time of $FeCl_3$ solution; (D) FTIR spectrum of DISC hydrogel; (E) Frequency-dependent rheological measurements of DISC hydrogels with different amounts of hydrophobic/hydrophilic monomer C_{18}/acrylamide at 25 °C.

4.3.2 Nanomechanics of the hydrophobic shell assembling process

The DISC hydrogels are designed based on metal coordination chemistry to modulate the intermolecular interactions and internal structure of the DSIC hydrogels. To probe the contribution of metal coordination in the complex system with the coexistence of dopamine and

SDS, colloidal probe atomic force microscope (AFM) technique was employed to directly measure the correlated interaction forces. The details of the method for the preparation of AFM silica probe have been reported previously [76, 77]. Figure 4.S3 illustrates the schematics of colloidal probe-surface AFM force measurement experiment with the SEM image of a typical silica probe. The viscosity of solution used for force measurement was also measured by an AR-G2 stress-controlled rheometer (TA Instruments) under velocity sweep, as shown in Figure 4.S4. After adding 500 μM $FeCl_3$ and 500 mg/L dopamine in 700 mM NaCl saline, the viscosity of the solution stays almost unchanged which would bring negligible effect to the trace-retrace process during the force measurement. Figure 4.3A and 3B show the measured force profiles between SO_3^{2-}-coated silica probe and gold wafer in the absence and presence of Fe^{3+} in saline solution of 700 mM NaCl and pH 4.6. There is no obvious attraction or repulsion detected during the approach process and a minuscule adhesion of F/R ~ 0.16 mN/m measured with the retraction process when the SO_3^{2-}-coated silica probe and gold wafer were brought into contact and separate. In contrast, with the presence of 500 μM Fe^{3+}, a significant adhesion (F/R ~ 0.6 mN/m) was measured during the retraction process, suggesting the iron binding tendency of sulfonates [78, 79]. Figure 4.3C shows the measured force profiles between SO_3^{2-}-coated silica probe and gold wafer in the presence of Fe^{3+} and polydopamine (PDA) in saline solution of 700 mM NaCl and pH 4.6. Unlike the measured force in Figure 4.3A and 3B, a significant attraction was detected during the approaching process and an increased adhesion of F/R ~ 1.1 mN/m was measured during the retraction process. In 700 mM NaCl solution, the Debye length was calculated to be 0.36 nm according to DLVO theory [39], suggesting that the electric double layer is significantly suppressed. Thereby, the effect of electrostatic interaction was minimized during the approach process and the attraction observed in Figure 4.3C is mainly due to the

strong cohesive bridging effect between confined PDA-Fe^{3+} complex and SO_3^{2-}-coated surfaces. To further verify the hypothesis that Fe^{3+} and PDA could provide a cohesive bridge between adjacent sulfonates through metal coordination bonds, UV-vis spectrum and dynamic light scattering size measurement were employed to give additional evidence. As shown in Figure 4.3D, the peaks at 330 and 430 nm^{-1} in the UV-vis spectra are associated with SDS-Fe and PDA-Fe complexes, respectively, indicating the metal coordination of Fe^{3+} with sulfonate groups of SDS and catechol groups of PDA [80, 81]. Figure 4.S5 shows the size distribution of pure dopamine, pure SDS, and the mixture of dopamine, SDS, and Fe^{3+}. Compared with the pure dopamine and SDS with the narrow size peaks at 122 and 531 nm, respectively, the peak for the size distribution of the mixture containing dopamine, SDS, and Fe^{3+} shifts to 1718 nm with a more broad size distribution. The appearance of Fe^{3+} intermediates the micellar assembly and leads to the recombination of SDS and dopamine with ferric ion, which could also be correlated to the assembling of hydrophobic layer over PAM-SDS-C_{18}-DA hydrogel with the assistance of Fe^{3+}. The above force measurement and characterization data demonstrate that Fe^{3+} could provide metal binding for the adjacent sulfonates and the appearance of PDA could form PDA-Fe complex to further enhance the strong cohesive bridging for sulfonates which provides a new paradigm for constructing adhesive layer of hydrogels.

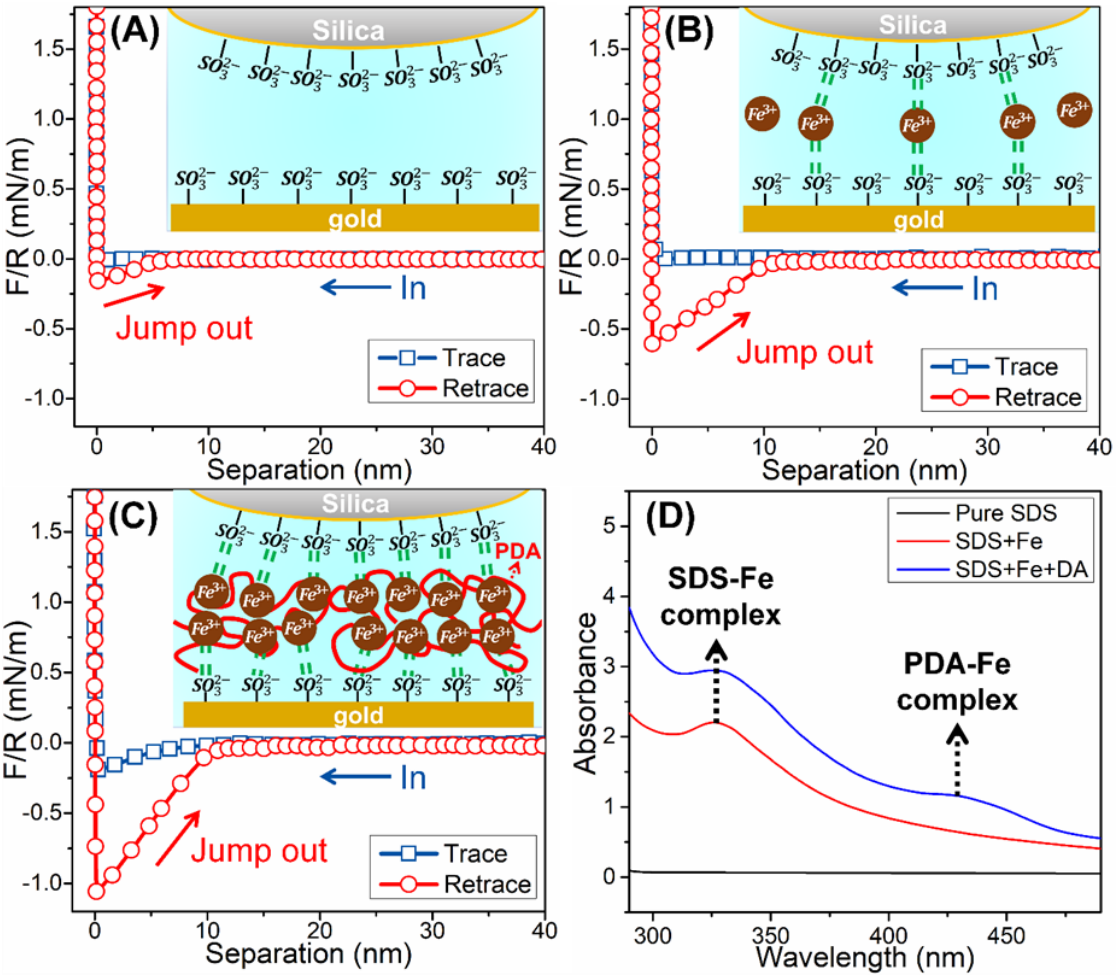

Figure 4.3 Force–distance profiles relative to interaction between SO_3^{2-}-coated silica probe and gold wafer in (A) pure saline solution, (B) 500 μM $FeCl_3$ solution, and (C) 500 μM $FeCl_3$ with 500 mg/L dopamine solution, under 700 mM NaCl condition of pH 4.6; (D) UV-vis spectrum of pure SDS, SDS-Fe, and SDS-Fe-dopamine solution.

4.3.3 Mechanical properties of DISC hydrogel

The stretchability and elasticity of the developed DISC hydrogels were characterized by the tensile and compression tests. Figure 4.4A illustrates the stress−strain curves of hydrogels with different compositions. Without the Hb monomers C_{18} and SDS, the PAM-DA hydrogel shows good stretchability with a fracture strain of more than 500%, but the strength of the PAM-

SDS hydrogel is relatively low (<14 kPa); In the presence of C_{18} monomers embedded in the SDS micelle and copolymerized in the PAM network, the obtained pam-SDS-C_{18}-DA prehydrogel hydrogel is strengthened and the fracture stress is increased to 24 kPa at the strain of 420 %. This could be attributed to the incorporation of hydrophobic association formed by SDS/C_{18} into the covalently crosslinked network, thus acting as the noncovalent cross-links to increase the tensile strength of pam-SDS-C_{18}-DA prehydrogel hydrogel. After being treated with $FeCl_3$ solution, the stretchability and strength of the obtained DISC hydrogel are further improved. The fracture stress of the DISC-20 and DISC-40 hydrogel (treated with $FeCl_3$ for 20 and 40 min) reach 34 and 45 kPa at the strain of 490 and 570 %, respectively. The toughness of the pam-DA, pam-SDS-C_{18}-DA, DISC-20, and DISC-40 are calculated as 33, 55, 90, and 138 kJ/m^3, respectively, as shown in Figure 4.S6. Introducing Fe^{3+} to the pam-SDS-C_{18}-DA prehydrogel hydrogel could endow effective mechanical reinforcement to the composites hydrogel which is mainly due to the formation of dynamic metal coordination bond that dissipates energy upon hydrogel being stretched. The strain-stress curves for the 5 loading−unloading cycling tensile tests are shown in Figure 4.S7 and the DISC-40 hydrogel exhibits a good reversibility at the tensile strain of 200 %. Figure 4.4C shows the compressive strain-stress curves during the loading−unloading process of compression tests while Figure 4.4D shows the time-stress curves of cycling compression tests with DISC hydrogels. The DISC-40 hydrogel exhibits a high compressive strength ~ 370 KPa with a good reversibility during the 5 loading-unloading cycling tests at the compression strain of 80%. Additionally, from the photos in Figure 4.4B and 4C, there are no apparent cracks formed at the surface of the DISC hydrogels when stretched to the strain of 570% and compressed to the strain of 80%. The above results of the mechanical tests indicated that the DISC-40 hydrogels possess a good stretchability

and elasticity which is able to maintain the structural integrity under the external force and conformal contact with the contact interface like rough tissue surfaces when applied as adhesives.

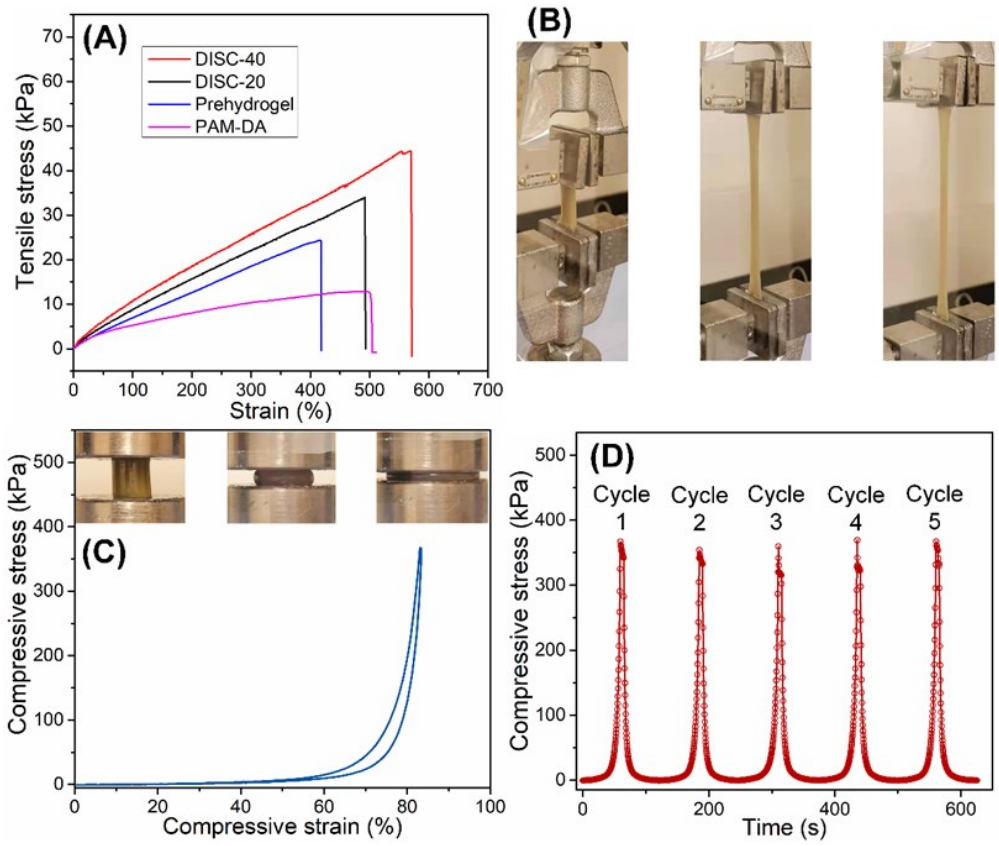

Figure 4.4 (A) Tensile stress-strain curves of pam-DA, pam-SDS-C_{18}-DA prehydrogel, DISC-20, and DISC-40; (B) Optical image of DISC hydrogel extended to strain of 570%; (C) Compressive stress-strain curves of DISC-40; (D) 5 cycles compressive stress-time curves of DISC-40.

4.3.4 Adhesive performance of DISC hydrogel

As shown in Figure 4.5A, the DISC hydrogel shows universal adhesion towards different types of biological tissues including skin, muscle, and organ under both the wet and underwater conditions. The contact interfaces of the DISC hydrogels with the tissues (chicken breast, porcine skin, and heart) could resist the intense shaking in PBS solution (Video S2), suggesting that the hydrophobic surface of the hydrogel forms a robust and universal connection with tissue

surfaces and shields contact interface against water penetration. We then conducted the lap shear test to investigate the adhesion strength of DISC hydrogels on diverse substrates varying from hard to soft, including glass, resin, wood, chicken breast, porcine skin and heart. The pam-SDS-C_{18}-DA prehydrogel, DISC-20, and DISC-40 hydrogels are listed to probe the role of modulating metal coordination chemistry to the adhesion performance. Figure 4.5B shows the adhesion strength-extension curves of lap-shear tests in air using porcine heart as the adherend. Compared to the prehydrogel with the debonding peaks of 11 kPa at the extension of 4 mm, the Fe^{3+}-treated DISC hydrogels exhibit a much greater adhesion strength with the debonding peaks of 45 kPa at the extension of 6 mm for DISC-20 and 62 kPa at the extension of 7.2 mm for DISC-40. The strengthened adhesion after the Fe^{3+} treatment could be ascribed to the introduction of dynamic metal coordination bonds which increased the dissipated energy during the debonding process (the area under adhesion strength-extension curves). The adhesion strength of DISC hydrogels attached to different substrates under both the dry and wet conditions are illustrated in Figure 4.5D and 5E, respectively. The wet adhesion strength was collected by spreading the water at the contact interface of hydrogel adhesives and the substrates. Generally, the adhesion strength of DISC-20 and DISC-40 hydrogels is higher than that of prehydrogel. Further increasing the immersion time of DISC hydrogel in $FeCl_3$ solution didn't render a significant increase of the wet adhesion strength, as illustrated in Figure 4.S8A. Meanwhile, adhesion of prehydrogel with the tissue surfaces (chicken breast, porcine skin, and heart) decline from dry to wet conditions with about ~ 30 % loss of adhesion strength, suggesting that the presence of water weakens the stability of the prehydrogel. However, there is no significant decrease observed for the adhesion strength of DISC-20 and DISC-40 to various substrates. This could be resulted from the increased hydrophobicity of the DISC hydrogel surface, which promotes the formation of a water

depletion region at the contact interface, thus preventing water penetration and achieving stable adhesion under wet conditions.[82] Compared to DISC-20, the DISC-40 exhibits better adhesive property with a higher wet adhesion strength of over 60 kPa for porcine heart (under a 20 kPa preload and short contact of 2 min). The effect of Fe^{3+} concentration to the wet adhesion performance has also been investigated, as illustrated in Figure 4.S8B. Among all the substrates, the adhesion strength of hydrogel to soft tissues are much higher than that to hard substrates (glass, resin, and wood), which could be correlated to the contact mechanics considering the elasticity [83]. Interestingly, for hydrophobic resin substrates, the adhesion strength of both the DISC-20 and DISC-40 increase from dry to wet conditions, mainly due to the formed hydrophobic interaction between two hydrophobic surfaces (hydrogel and resin substrate) in wet conditions. Due to the appearance of catechol moieties and alkyl chains on its surface layer, DISC hydrogel could form multiple interfacial interactions with different target substrates, such as hydrogen bonding with glass, hydrophobic interaction with resin, Schiff base/Michael addition with biological tissues, etc., which endows the developed adhesive hydrogel with the capability of universal adhesion [42-48]. The stability of the DISC hydrogel attached to wet tissues has then been evaluated in both 1x PBS solution and bovine blood, as shown in Figure 4.S9A. The DISC-40 hydrogel could retain 82 and 70 % of its adhesion strength after 12 h immersion in PBS and bovine blood, respectively. The stable connection of DISC-40 hydrogel with the heart tissues was maintained after the 12h stability test that was capable of lifting up a 200 g weight with a 1cm x1cm contact area, as illustrated in Figure 4.S9B. The developed DISC hydrogels were further applied as the sealant attached to the broken tissue to resist the hydraulic pressure. The correlated burst pressure was measured by pumping 1x PBS solution to the breakage of the porcine heart (2 cm x 2 cm) repaired by the adhesive hydrogel, as shown in

Figure 4.S10. The burst pressures of the prehydrogel, DISC-20, and DISC-40 are 87.4, 577, and 975 mmHg, respectively, which are much higher than the human arterial blood pressure (typically 80-140 mmHg) and many of the reported bioadhesives used for sealing broken tissues, as shown in Table 4-1. This could be ascribed to the hydrophobic surface of the DISC hydrogel preventing the water penetration, thus significantly increasing its resistance to the hydraulic pressure of PBS solution. The superior sealing property could promote its tolerance to the extreme environment for the potential use in biological applications [84-87]. Meanwhile, the adhesion behavior of DISC-40 hydrogel could be modulated by 240 nm UV curing to realize the triggerable detachment. As shown in Figure 4.5F, after 240 nm UV irradiation of 5 min, the burst pressure of DISC-40 decreases from 975 to 630 mmHg. The adhesive hydrogel then could be gently removed from the surface of the porcine heart without causing damage to the adhesive hydrogel or the tissue surfaces. The adhesion strength of the DISC hydrogel could be restored by immersing in Fe^{3+}-dopamine solution with about 25 % loss of burst pressure after 5 cycles of UV curing-Fe^{3+}/dopamine solution immersion process shown in Figure 4.S11. The weakened burst pressure after UV curing most probably results from the reduction of Fe^{3+} to Fe^{2+}, which modulates the metal coordination bond for the decreased cohesive strength of the hydrogel matrix to achieve the controllable detachment [88, 89]. When applied as the tissue sealant, the developed DISC hydrogel exhibits a good reversibility which possesses the potential for the recyclable use. By modulating metal coordination chemistry, the DISC hydrogel is endowed with superior underwater adhesive property to form an instant and stable attachment to various wet biological tissues as well as triggerable detachment capability for the reversible bonding/debonding process.

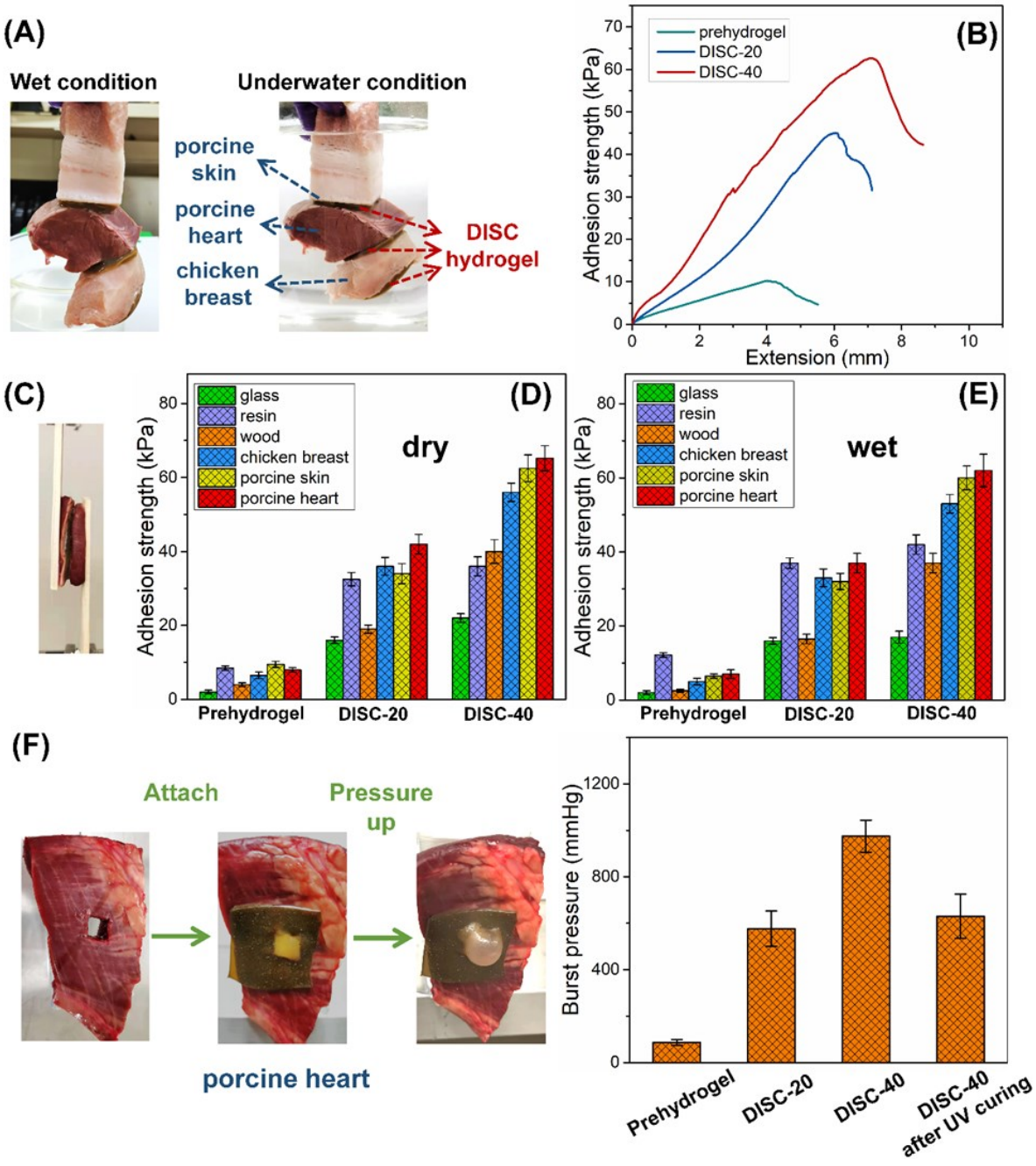

Figure 4.5 (A) Adhesive performance of DISC hydrogel to chicken breast, porcine skin and heart under wet and underwater condition; (B) Typical adhesion strength-extension curve of prehydrogel, DISC-20, and DISC-40, measured by lap shear adhesion test using porcine heart with (C) an optical image; The adhesion strength of prehydrogel, DISC-20, and DISC-40 to different substrates under (D) dry and (E) wet conditions; (F) Demonstration of DISC-40

hydrogel served as a sealant on porcine heart to resist the hydraulic pressure of PBS buffer and the measured burst pressure of different hydrogel samples.

Table 4-1 Summary of bioadhesives with measured burst pressure for biomedical use.[62, 90-93]

Materials used	Target substrate	Burst pressure (mmHg)	Adhesive Strength (kPa)	Ref.
PLGA/PEG	Porcine intestinal tissue	59	~50	[90]
GelMA	Porcine lung	112.5	49	[91]
Epigallocatechin-gallates-tyramine	Mouse dorsal skin	167.9	3	[62]
DOPA-PEG-Laponite	Collagen casing	320	N/A	[92]
Tetra-armed poly(ethylene glycol) thiol	Pig abdominal aorta vein	294	20	[93]
DISC hydrogel	Porcine heart	975	65.2	This work

The biocompatibility of the developed DISC-40 hydrogel was investigated by 2D culture of Chinese hamster ovary (CHO) and human embryonic kidney (HEK) 293 cells. After 12 h or 72 h incubation of in DMEM medium, the live cells (green color) accounted for the majority of the population which was also composed of a low proportion of dead cells (red color) (Figure 4.6A, Figure 4.S12). The cell viability was determined to be over 90% for both incubation times (Figure 4.6B), suggesting the low cytotoxicity of the DISC-40 hydrogel to both CHO and HEK-293 cell lines and its great potential for *in vivo* biomedical applications. It is noted that, before being applied to practical biomedical applications in the future, the DISC-40 hydrogel should undergo some sorts of *in vivo* tests to allow a comprehensive biosafety evaluation.

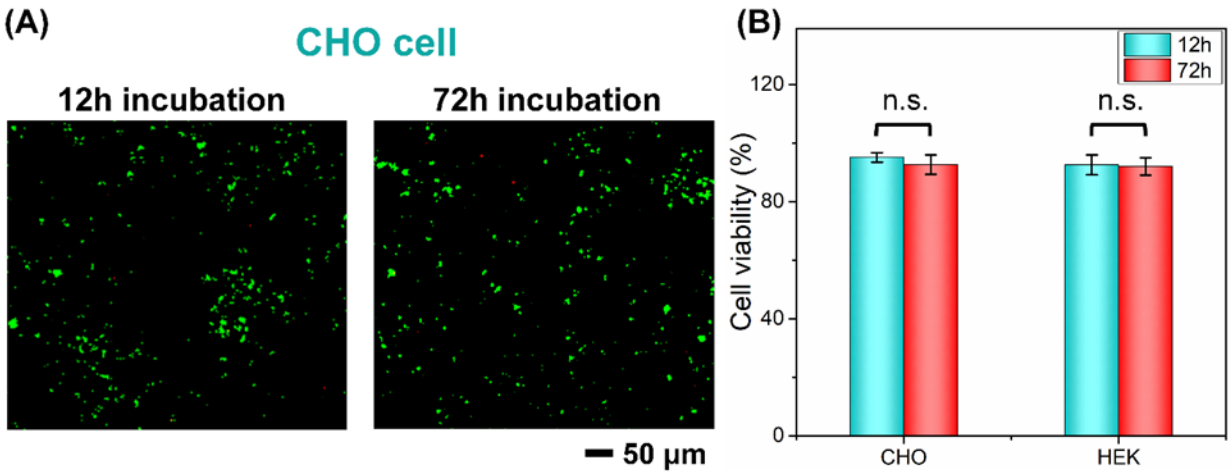

Figure 4.6 Effect of the DISC-40 hydrogel on viability of CHO and HEK-293 cells. (A) Representative confocal microscopy images of 2D culture of CHO cells on the DISC-40 hydrogel after 12 h or 72 h incubation; (B) Viability of CHO and HEK-293 cells after 12 h or 72 h incubation with the DISC-40 hydrogel (n=3 replicates per condition, n.s. represents $P > 0.05$).

4.5 Ultrasound imaging under wet intraoral environment

Due to the developed DISC hydrogel possess high water content (~ 87 w.t.%) and underwater adhesion capability, we also tested its potential application as the tissue couplant to transmit ultrasound signal for imaging in wet intraoral environment. The ultrasonic properties of the DISC hydrogel including group/phase velocities and attenuation were first characterized by the transmission-through experiment. The schematics of the experimental setup are shown in Figure 4.7A. The commercial Aquaflex (AF) gel pad for in vitro ultrasound imaging with low attenuation and good imaging quality is used as the reference here, which has been characterized in our previous work [64]. Figure 4.7B and 7C show the measured phase velocity and attenuation of ultrasound signal transmission inside the AF and DISC-40 under a frequency span from 7.3 to 22.4 MHz, within the ± 6 dB frequency range, respectively. The phase velocities and attenuation of the DISC-40 and AF increase slightly with the frequency and the fitted results of the slopes

and intercepts are included in Table 4.S1. The average transmission speed of ultrasound inside DISC-40 (1509 m/s) is close to that of AF gel (1587 m/s), both higher than the speed of ultrasound in water (1480 m/s). Meanwhile, the attenuation of ultrasound increases from 0.5 to 4 dB/cm for DISC-40 and 1.0 to 3.8 dB/cm for AF with the frequency span from 7.3 to 22.4 MHz. The normalized broadband ultrasound attenuation (nBUA) of DISC-40 and AF are calculated to be 0.17 ± 0.02 and 0.22 ± 0.03 dB/cm·MHz. To further evaluate the effect of developed DISC-40 on the ultrasound image quality, a porcine molar (Figure 4.7D) was scanned with the couplant placed between the transducer and the molar (Figure 4.7E). Figure 4.7F shows the corresponding ultrasonograms. Both images show similar echo intensity and image clarity with clear visualization of the major structures of the tooth periodontium. The reflection intensity is affected by the acoustic impedance contrast of the interface, and the acoustic impedance value is given by the product of density and velocity. The densities of AF and DISC-40 hydrogel are 1030 kg/m^3 and 1075 kg/m^3, respectively. Using their group velocities, the acoustic impedance of the hydrogel and AF are 1.62×10^6 and 1.64×10^6 rayls, respectively, very close to the acoustic impedance of human tissues (1.45 - 1.7×10^6 rayls). The impedance match of DISC-40 hydrogel with tissues avoids the significant transmission loss of ultrasound signals and ensures the enahnced echo intensity of ultrasound images. Although both couplants have comparable ultrasound quality and image clarity, the DISC-40 is more suitable for intra-oral imaging, as it has a lower attenuation for frequency higher than 20 MHz and a much stronger adhesive property compared to the commercial couplant AF (adhesion strength ~ 0.5 kPa on porcine skin) and other synthesized biocompatible gel pads in the literature (burst pressure ~ 294-320 mmHg on tissues) [63, 92, 93], which will avoid slipping across the transducer surface during scanning in the wet intraoral environment.

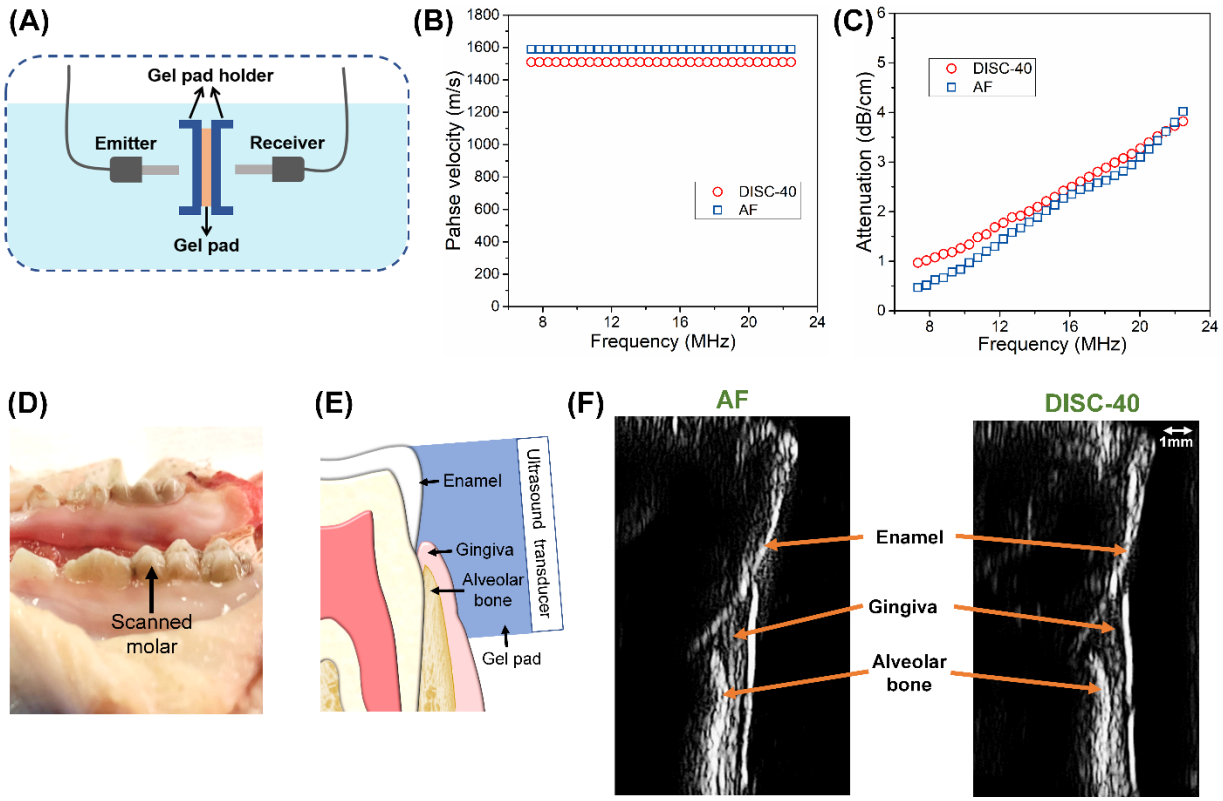

Figure 4.7 Ultrasound characterization for the gel pads. (A) Schematics of the experimental setup for ultrasound property measurement; (B) The phase velocities of DISC-40 and AF versus frequency; (C) The attenuation of DISC-40 and AF versus frequency; (D) Porcine molar used for ultrasound imaging with the arrow pointing to the scanned tooth; (E) Schematic diagram of a tooth-periodontium structures in which the couplant sits between the ultrasound transducer and the tissues; (F) The ultrasound image with DISC-40 and AF couplant.

4.4 Conclusions

In summary, we have developed a novel underwater adhesive hydrogel by mimicking the structure of mussel byssus cuticle. The hydrogel is engineered with a soft armour-like hydrophobic adhesive layer outside the hydrophilic hydrogel matrix by iron-chelation of polydopamine (PDA) and sodium dodecyl sulfate (SDS). By leveraging this unique soft armor-

like architecture, the developed hydrogels exhibited instant and robust adhesion to various biological tissues via hydrophobic shell-induced rapid drainage as well as on-demand detachment via UV curing to trigger the transition of Fe^{3+}/Fe^{2+}. When applied as the sealant materials to the broken tissue, the developed DISC-40 exhibited a great resistance to the water penetration, even under high hydraulic pressure of ~ 975 mmHg. Meanwhile, the underwater adhesive hydrogel with high water content of 86.7 wt.% and exceptional biocompatibility could perform as the tissue couplant for ultrasound imaging, showing great impedance match with biological tissues and superior imaging quality for diagnosis in the wet intraoral environment. Taken together, the results demonstrated the remarkable merits of the as-prepared underwater adhesive hydrogel for practical applications as the bridging interface connecting human and medical apparatuses to support the in-vivo diagnosis and related clinical applications.

4.5 Supporting Infromation

4.5.1 EDS mapping and swelling test of DISC hydrogels

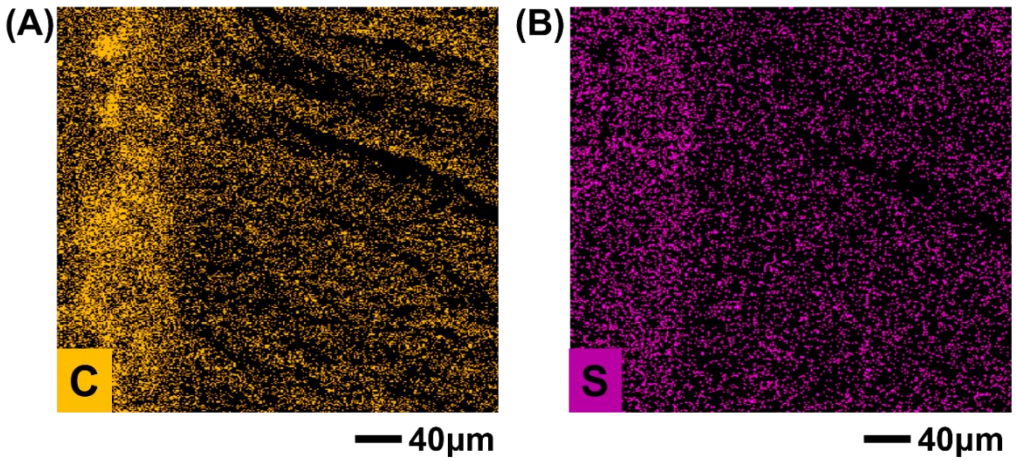

Figure 4.S1 EDS mapping of element (A) carbon and (B) oxygen at the same location of Fig. 2A.

The water content (WC) was characterized by the initial weights (W_i) and the lyophilized weights (W_d) of the hydrogel according to Eqn (1):

$$WC(\%) = \frac{W_i - W_d}{W_i} \times 100\% \quad (1)$$

The swelling ratio (R_S) of hydrogel was evaluated according to the weight of swelling (W_s) and dry (W_d) sample Eqn (2):

$$R_S = \frac{W_s - W_d}{W_d} \quad (2)$$

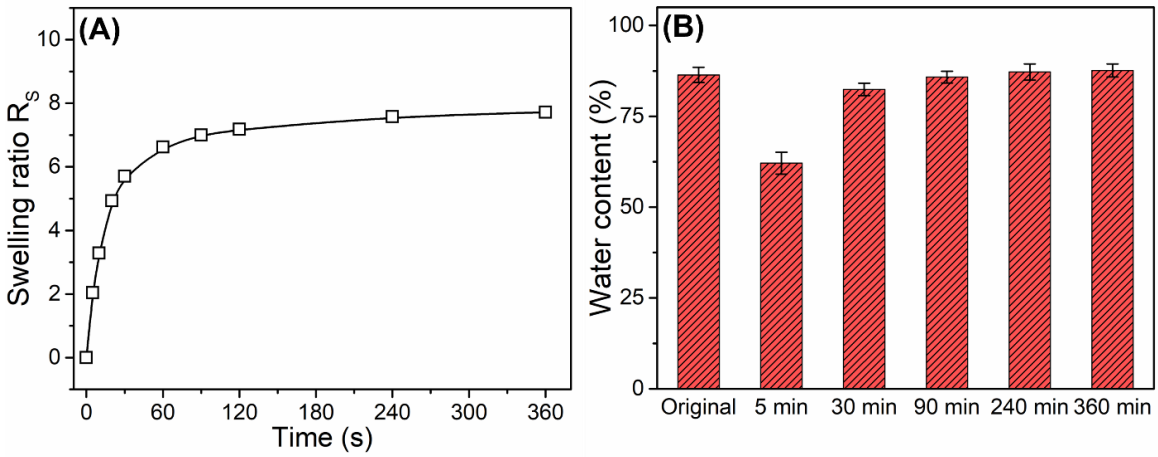

Figure 4.S2 (A) Swelling ratio of DISC-40 hydrogel; (B) Water content of original and lyophilized DISC-40 hydrogel in swelling tests.

4.5.2 AFM force measurement experiment

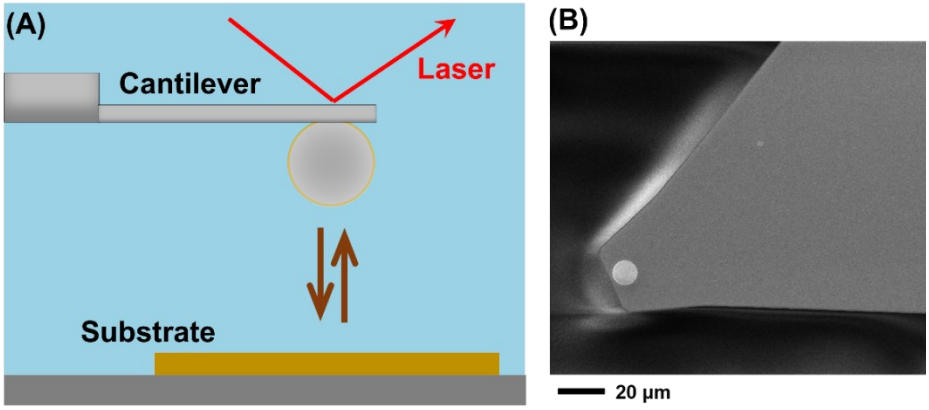

Figure 4.S3 (A) Schematic of a typical colloidal probe AFM force measurement using the silica probe and (B) SEM image of a typical silica sphere probe.

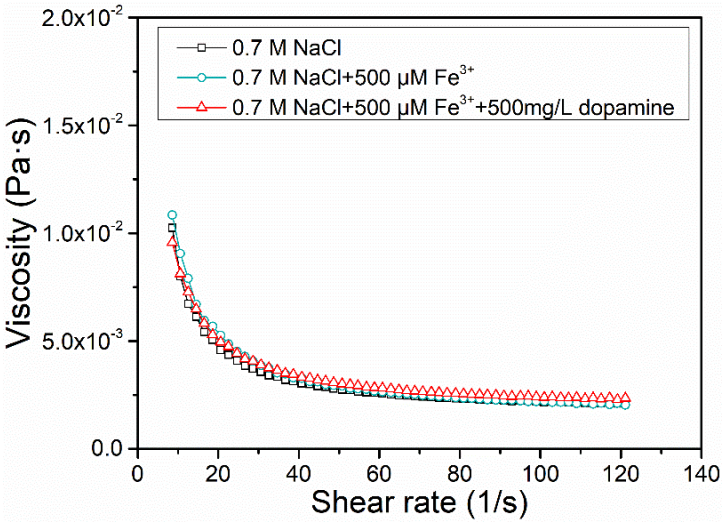

Figure 4.S4 Viscosity versus shear rate for different saline solutions.

4.5.3 Size distribution

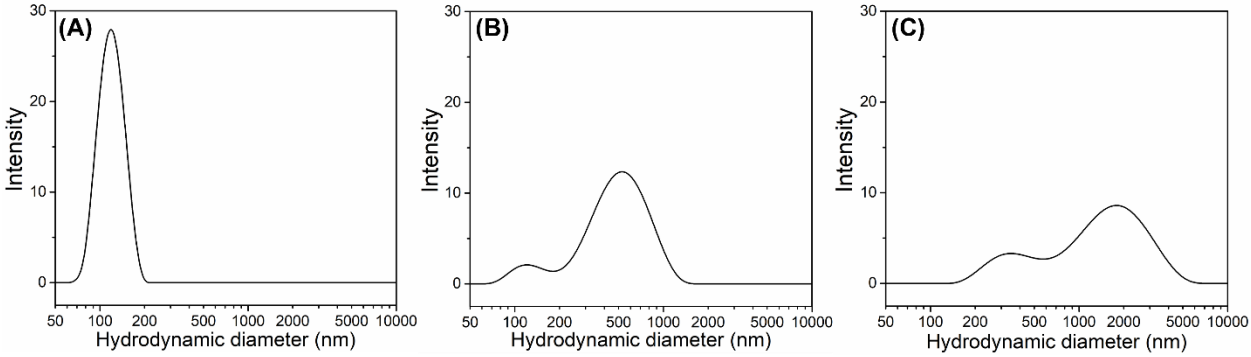

Figure 4.S5 DLS size distribution of (A) 200 ppm dopamine, (B) 2000 ppm SDS, (C) 200 ppm dopamine, 2000 ppm SDS, and 10 mM $FeCl_3$ solution in 700 mM NaCl saline solution.

4.5.4 Toughness of developed hydrogels

The toughness U_T of the hydrogel samples is defined as the area under the tensile stress–strain curve:

$$U_T = \int_0^{\varepsilon_f} \sigma d\varepsilon$$

where ε is the tensile strain, ε_f is the strain at the failure of the gel samples, σ is the tensile stress.

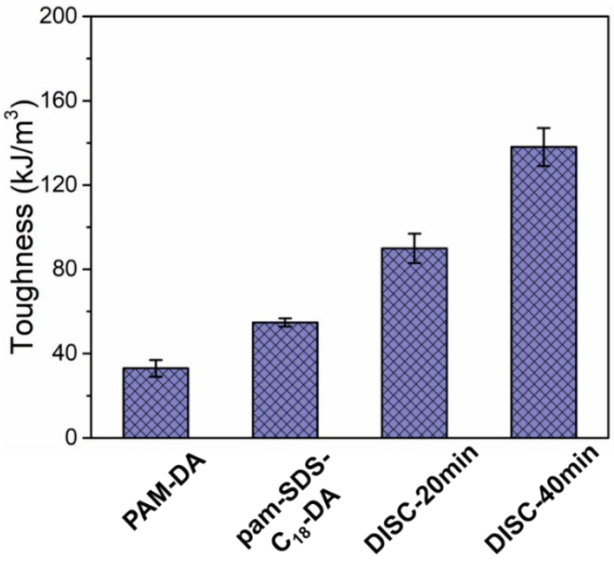

Figure 4.S6 The toughness calculated from the nominal strain-stress curves of different hydrogels.

4.5.5 Cycle tensile test of DIS-40min hydrogel

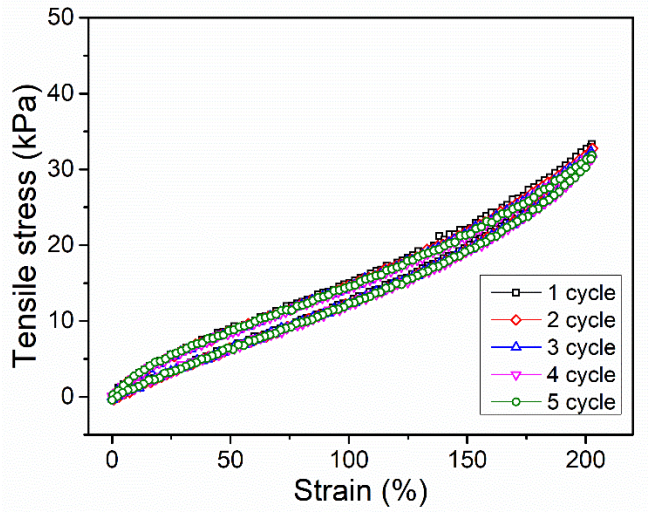

Figure 4.S7 Tensile test of 5 loading-unloading cycles operating at 30 mm/min velocity.

4.5.6 Adhesion tests

The effect of immersion time of DISC hydrogel in $FeCl_3$ solution on its wet adhesion strength has been characterized. As shown in Fig. S8A, the wet adhesion strength of DISC hydrogel on porcine skin increased from 6.5 to 61.2 kPa with the immersion time from 0 to 60 min while a slight decrease for the adhesion strength from 61.2 to 54.5 kPa was observed by further increasing the immersion time from 60 to 80 min.

The effect of Fe^{3+} to the wet adhesion performance has also been investigated. As shown in Fig S8B, the wet adhesion strength of DISC-40 hydrogel on porcine skin increased from 6.5 to 59.6 kPa with the increasing concentration of $FeCl_3$ solution from 0 to 80 mM while further increasing Fe^{3+} concentration leads to a great decline in adhesion strength. This could be correlated to the increased Fe^{3+} concentration that generates a greater possibility of forming mono complex instead of tris complex which would decrease the cohesive strength of the hydrogel network [34]. Hence, 80 mM FeCl3 solution is used for the preparation of DISC hydrogel with the optimal wet adhesion strength.

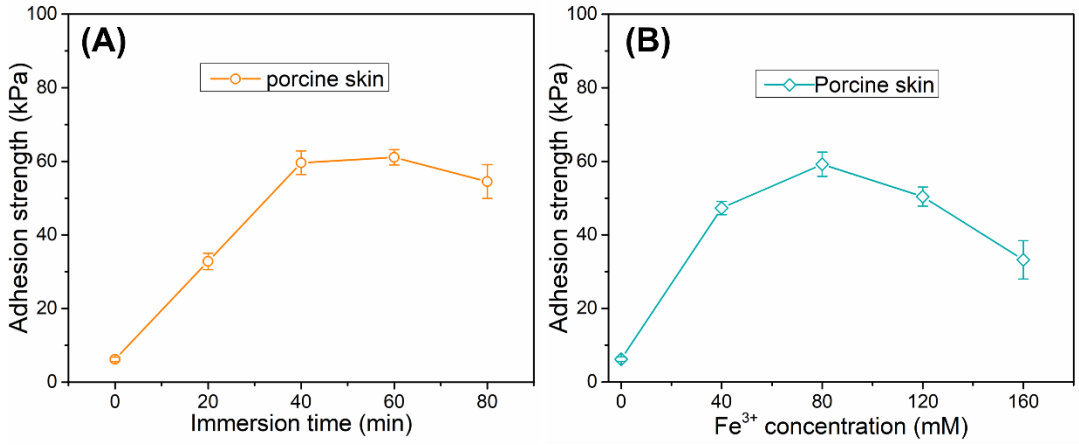

Figure 4.S8 (A) Wet adhesion strength of DISC hydrogel versus immersion time in in $FeCl_3$ solution; (B) Wet adhesion strength of DISC hydrogel versus concentration of $FeCl_3$ solution.

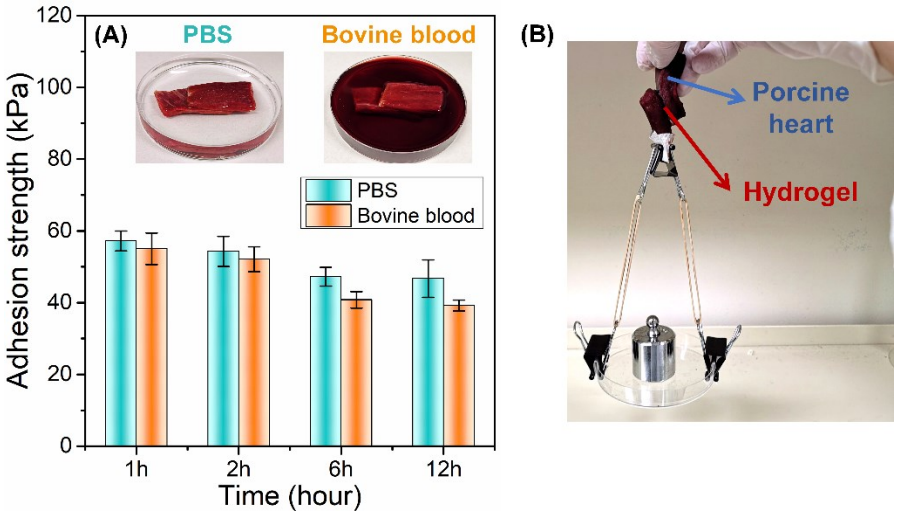

Figure 4.S9 (A) Stability tests of the adhesion performance of DISC hydrogel in PBS and bovine blood; (B) Demonstration of hydrogel attached heart tissues after the stability test.

4.5.7 Setup for burst pressure test

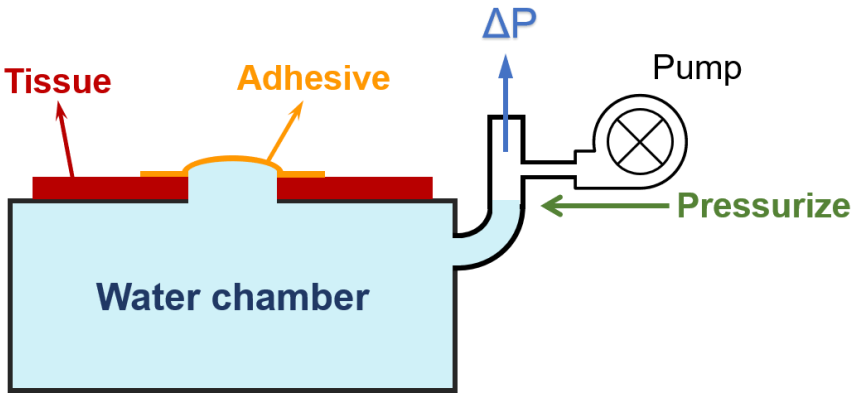

Figure 4.S10 Schematics of the experimental setup for burst pressure measurement.

4.5.8 DISC hydrogel treated by UV curing

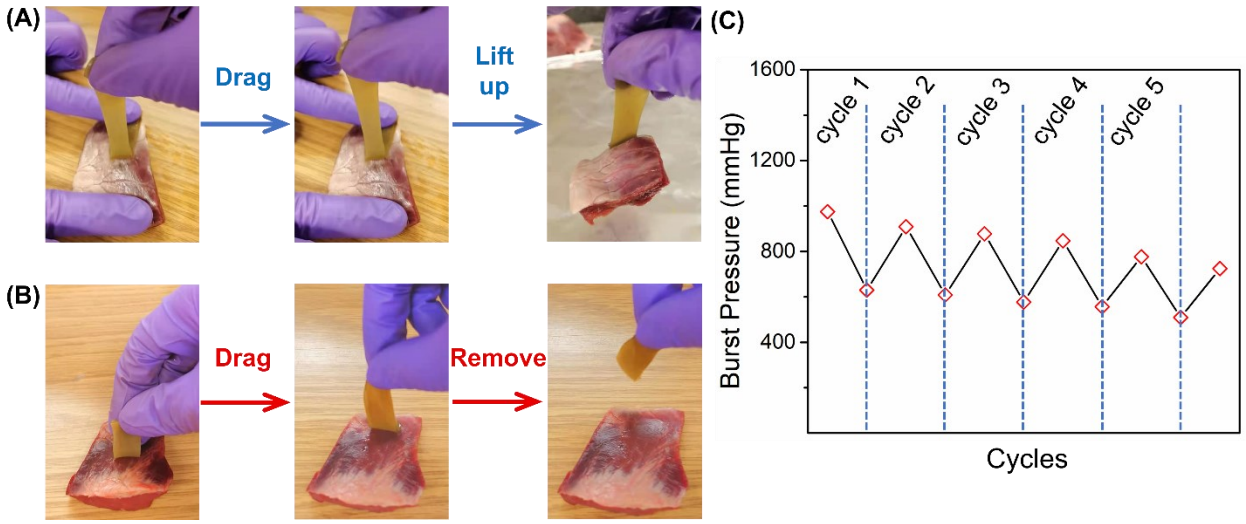

Figure 4.S11 Optical image of DISC-40 hydrogel attached to porcine heart (A) without UV curing and (B) with UV curing; (C) cycle burst pressure test of DISC-40 after UV-curing and restore with 60 mM $FeCl_3$ and 1 mg/mL dopamine solution.

4.5.9 Cell viability

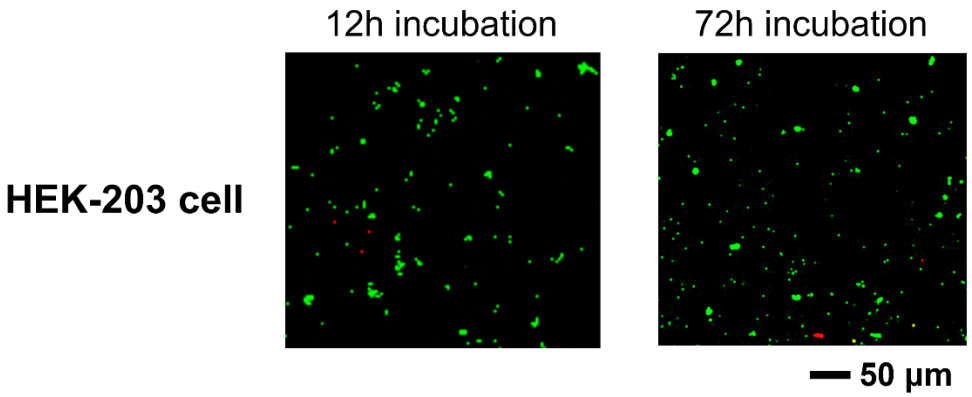

Figure 4.S12 Representative confocal microscopy images of 2D culture of HEK 293 cells on the DISC-40 hydrogel after 12 h and 72 h incubation.

4.5.10 Ultrasound imaging

Table 4.S1: Ultrasound velocities, dispersion, and nBUA of AF and the hydrogel. The dagger indicates that the quantity is determined at the spectral peak of 18.5 MHz.

Sample	**Nominal Frequency** (MHz)	**Group Velocity** (m/s)	**Phase Velocity** (m/s)	**Dispersion (7.3 – 22.4 MHz)**		$\alpha^{\dagger}$ (dB/cm)	**nBUA (7.3 – 22.4 MHz)** (dB/cm·MHz)
				Slope (m/s·MHz)	Intercept (m/s)		
Aquaflex	20	1589 ± 7	1587 ± 7	0.010 ± 0	1587 ± 0	2.94 ± 0.21	0.22 ± 0.03
DISC-40	20	1509 ± 0	1509 ± 0	0.031 ± 0	1508 ± 0	2.97 ± 0.33	0.17 ± 0.02

References

[1] L. Li, B. Yan, J. Yang, L. Chen, H. Zeng, Novel mussel-inspired injectable self-healing hydrogel with anti-biofouling property, Advanced Materials, 27 (2015) 1294-1299.

[2] C. Wang, C. Lin, R. Ming, X. Li, P. Jonkheijm, M. Cheng, F. Shi, Macroscopic Supramolecular Assembly Strategy to Construct 3D Biocompatible Microenvironments with Site-Selective Cell Adhesion, ACS Applied Materials & Interfaces, (2021).

[3] Y. Gao, K. Peng, S. Mitragotri, Covalently Crosslinked Hydrogels via Step-Growth Reactions: Crosslinking Chemistries, Polymers, and Clinical Impact, Advanced Materials, (2021) 2006362.

[4] X. Yu, X. Wang, D. Li, R. Sheng, Y. Qian, R. Zhu, X. Wang, K. Lin, Mechanically reinforced injectable bioactive nanocomposite hydrogels for in-situ bone regeneration, Chemical Engineering Journal, (2021) 132799.

[5] X. Zhang, Y. Li, D. He, Z. Ma, K. Liu, K. Xue, H. Li, An effective strategy for preparing macroporous and self-healing bioactive hydrogels for cell delivery and wound healing, Chemical Engineering Journal, (2021) 130677.

[6] B. Kong, L. Sun, R. Liu, Y. Chen, Y. Shang, H. Tan, Y. Zhao, L. Sun, Recombinant human collagen hydrogels with hierarchically ordered microstructures for corneal stroma regeneration, Chemical Engineering Journal, 428 (2022) 131012.

[7] Y. Liu, R. Guo, T. Wu, Y. Lyu, M. Xiao, B. He, G. Fan, J. Yang, W. Liu, One zwitterionic injectable hydrogel with ion conductivity enables efficient restoration of cardiac function after myocardial infarction, Chemical Engineering Journal, 418 (2021) 129352.

[8] L. Zhang, L. Chen, Y. Xiang, Z. Liu, X. Mao, L. Zhang, L. Deng, Y. Zhang, L. Cheng, X. Sun, Multifunctional integrally-medicalized hydrogel system with internal synergy for efficient tissue regeneration, Chemical Engineering Journal, 406 (2021) 126839.

[9] P. Liu, Y. Xiong, L. Chen, C. Lin, Y. Yang, Z. Lin, Y. Yu, B. Mi, G. Liu, X. Xiao, Angiogenesis-Based Diabetic Skin Reconstruction through Multifunctional Hydrogel with Sustained Releasing of M2 Macrophage-derived Exosome, Chemical Engineering Journal, (2021) 132413.

[10] J. Zhang, W. Xin, Y. Qin, Y. Hong, Z. Xiahou, K. Zhang, P. Fu, J. Yin, "All-in-one" Zwitterionic Granular Hydrogel Bioink for Stem Cell Spheroids Production and 3D Bioprinting, Chemical Engineering Journal, (2021) 132713.

[11] F. Xu, A. Lam, Z. Pan, G. Randhawa, M. Lamb, H. Sheardown, T. Hoare, Fast Thermoresponsive Poly (oligoethylene glycol methacrylate)(POEGMA)-Based Nanostructured Hydrogels for Reversible Tuning of Cell Interactions, ACS Biomaterials Science & Engineering, (2021).

[12] K. Yamagishi, I. Kirino, I. Takahashi, H. Amano, S. Takeoka, Y. Morimoto, T. Fujie, Tissue-adhesive wirelessly powered optoelectronic device for metronomic photodynamic cancer therapy, Nature biomedical engineering, 3 (2019) 27-36.

[13] S. Zhu, Y. Ying, Q. Wu, Z. Ni, Z. Huang, P. Cai, Y. Tu, W. Ying, J. Ye, R. Zhang, Alginate self-adhesive hydrogel combined with dental pulp stem cells and FGF21 repairs hemisection spinal cord injury via apoptosis and autophagy mechanisms, Chemical Engineering Journal, (2021) 130827.

[14] J.S. Lee, Y.S. Choi, J.S. Lee, E.J. Jeon, S. An, M.S. Lee, H.S. Yang, S.-W. Cho, Mechanically-reinforced and highly adhesive decellularized tissue-derived hydrogel for efficient tissue repair, Chemical Engineering Journal, 427 (2022) 130926.
[15] M. Li, Y. Liang, Y. Liang, G. Pan, B. Guo, Injectable stretchable self-healing dual dynamic network hydrogel as adhesive anti-oxidant wound dressing for photothermal clearance of bacteria and promoting wound healing of MRSA infected motion wounds, Chemical Engineering Journal, 427 (2022) 132039.
[16] K.-a. Johnson, N. Muzzin, S. Toufanian, R.A. Slick, M.W. Lawlor, B. Seifried, P. Moquin, D. Latulippe, T. Hoare, Drug-impregnated, pressurized gas expanded liquid-processed alginate hydrogel scaffolds for accelerated burn wound healing, Acta Biomaterialia, 112 (2020) 101-111.
[17] J. Liu, H. Wang, R. Ou, X. Yi, T. Liu, Z. Liu, Q. Wang, Anti-bacterial silk-based hydrogels for multifunctional electrical skin with mechanical-thermal dual sensitive integration, Chemical Engineering Journal, (2021) 130722.
[18] X. Zhang, Y. Zhang, W. Zhang, Y. Dai, F. Xia, Gold nanoparticles-deranged double network for Janus adhesive-tough hydrogel as strain sensor, Chemical Engineering Journal, (2021) 130447.
[19] J. Li, D.J. Mooney, Designing hydrogels for controlled drug delivery, Nature Reviews Materials, 1 (2016) 1-17.
[20] G. Zhang, Y. Chen, Y. Deng, T. Ngai, C. Wang, Dynamic supramolecular hydrogels: regulating hydrogel properties through self-complementary quadruple hydrogen bonds and thermo-switch, ACS Macro Letters, 6 (2017) 641-646.
[21] A. Yu, Y. Hu, X. Ma, L. Mo, M. Pan, X. Bi, Y. Wu, J. Wang, X. Li, Sequential drug release of co-assembled supramolecular hydrogel as synergistic therapy against Staphylococcus aureus endophthalmitis, Chemical Engineering Journal, 427 (2022) 130979.
[22] Y. Gao, Y. Hao, W. Zhang, Y. Wei, Y. Shu, J. Wang, Microwave-triggered ionic liquid-based hydrogel dressing with excellent hyperthermia and transdermal drug delivery performance, Chemical Engineering Journal, 429 (2022) 131590.
[23] J. Yang, R. Bai, Z. Suo, Topological adhesion of wet materials, Advanced Materials, 30 (2018) 1800671.
[24] H. Cui, W. Wang, L. Shi, W. Song, S. Wang, Superwettable Surface Engineering in Controlling Cell Adhesion for Emerging Bioapplications, Small Methods, 4 (2020) 2000573.
[25] S.H. Hong, M. Shin, E. Park, J.H. Ryu, J.A. Burdick, H. Lee, Alginate‐boronic acid: pH‐triggered bioinspired glue for hydrogel assembly, Advanced Functional Materials, 30 (2020) 1908497.
[26] S.-H. Lin, C.M. Papadakis, J.-J. Kang, J.-M. Lin, S.-h. Hsu, Injectable Phenolic-Chitosan Self-Healing Hydrogel with Hierarchical Micelle Architectures and Fast Adhesiveness, Chemistry of Materials, (2021).
[27] J. Li, A. Celiz, J. Yang, Q. Yang, I. Wamala, W. Whyte, B. Seo, N. Vasilyev, J. Vlassak, Z. Suo, Tough adhesives for diverse wet surfaces, Science, 357 (2017) 378-381.
[28] X. Wan, Z. Gu, F. Zhang, D. Hao, X. Liu, B. Dai, Y. Song, S. Wang, Asymmetric Janus adhesive tape prepared by interfacial hydrosilylation for wet/dry amphibious adhesion, NPG Asia Materials, 11 (2019) 1-9.
[29] D.H. Sierra, Fibrin sealant adhesive systems: a review of their chemistry, material properties and clinical applications, Journal of biomaterials applications, 7 (1993) 309-352.

[30] J. Jiao, F. Zhang, T. Jiao, Z. Gu, S. Wang, Bioinspired Superdurable Pestle‐Loop Mechanical Interlocker with Tunable Peeling Force, Strong Shear Adhesion, and Low Noise, Advanced Science, 5 (2018) 1700787.
[31] X. Chen, H. Yuk, J. Wu, C.S. Nabzdyk, X. Zhao, Instant tough bioadhesive with triggerable benign detachment, Proceedings of the National Academy of Sciences, 117 (2020) 15497-15503.
[32] Y. Chen, J. Meng, Z. Gu, X. Wan, L. Jiang, S. Wang, Bioinspired multiscale wet adhesive surfaces: structures and controlled adhesion, Advanced Functional Materials, 30 (2020) 1905287.
[33] Y. Zhang, S. Ma, B. Li, B. Yu, H. Lee, M. Cai, S.N. Gorb, F. Zhou, W. Liu, Gecko's Feet-Inspired Self-Peeling Switchable Dry/Wet Adhesive, Chemistry of Materials, 33 (2021) 2785-2795.
[34] H. Zeng, D.S. Hwang, J.N. Israelachvili, J.H. Waite, Strong reversible Fe3+-mediated bridging between dopa-containing protein films in water, Proceedings of the National Academy of Sciences, 107 (2010) 12850-12853.
[35] G.P. Maier, M.V. Rapp, J.H. Waite, J.N. Israelachvili, A. Butler, Adaptive synergy between catechol and lysine promotes wet adhesion by surface salt displacement, Science, 349 (2015) 628-632.
[36] B.K. Ahn, S. Das, R. Linstadt, Y. Kaufman, N.R. Martinez-Rodriguez, R. Mirshafian, E. Kesselman, Y. Talmon, B.H. Lipshutz, J.N. Israelachvili, High-performance mussel-inspired adhesives of reduced complexity, Nature communications, 6 (2015) 1-7.
[37] M.A. Gebbie, W. Wei, A.M. Schrader, T.R. Cristiani, H.A. Dobbs, M. Idso, B.F. Chmelka, J.H. Waite, J.N. Israelachvili, Tuning underwater adhesion with cation–π interactions, Nature chemistry, 9 (2017) 473-479.
[38] J. Zhang, L. Xiang, B. Yan, H. Zeng, Nanomechanics of Anion− Π Interaction in Aqueous Solution, Journal of the American Chemical Society, 142 (2020) 1710-1714.
[39] M. Pan, L. Gong, L. Xiang, W. Yang, W. Wang, L. Zhang, W. Hu, L. Han, H. Zeng, Modulating surface interactions for regenerable separation of oil-in-water emulsions, Journal of Membrane Science, 625 (2021) 119140.
[40] S. Lu, X. Zhang, Z. Tang, H. Xiao, M. Zhang, K. Liu, L. Chen, L. Huang, Y. Ni, H. Wu, Mussel-inspired blue-light-activated cellulose-based adhesive hydrogel with fast gelation, rapid haemostasis and antibacterial property for wound healing, Chemical Engineering Journal, 417 (2021) 129329.
[41] M. Suneetha, O.S. Moo, S.M. Choi, S. Zo, K.M. Rao, S.S. Han, Tissue-adhesive, stretchable, and self-healable hydrogels based on carboxymethyl cellulose-dopamine/PEDOT: PSS via mussel-inspired chemistry for bioelectronic applications, Chemical Engineering Journal, (2021) 130847.
[42] Q. Lu, D.S. Hwang, Y. Liu, H. Zeng, Molecular interactions of mussel protective coating protein, mcfp-1, from Mytilus californianus, Biomaterials, 33 (2012) 1903-1911.
[43] Q. Lu, D.X. Oh, Y. Lee, Y. Jho, D.S. Hwang, H. Zeng, Nanomechanics of cation–π interactions in aqueous solution, Angewandte Chemie, 125 (2013) 4036-4040.
[44] S. Kim, J. Huang, Y. Lee, S. Dutta, H.Y. Yoo, Y.M. Jung, Y. Jho, H. Zeng, D.S. Hwang, Complexation and coacervation of like-charged polyelectrolytes inspired by mussels, Proceedings of the National Academy of Sciences, 113 (2016) E847-E853.
[45] B. Yan, J. Huang, L. Han, L. Gong, L. Li, J.N. Israelachvili, H. Zeng, Duplicating dynamic strain-stiffening behavior and nanomechanics of biological tissues in a synthetic self-healing flexible network hydrogel, ACS nano, 11 (2017) 11074-11081.

[46] W. Zhang, R. Wang, Z. Sun, X. Zhu, Q. Zhao, T. Zhang, A. Cholewinski, F.K. Yang, B. Zhao, R. Pinnaratip, Catechol-functionalized hydrogels: biomimetic design, adhesion mechanism, and biomedical applications, Chemical Society Reviews, 49 (2020) 433-464.
[47] R. Xu, Y. Wu, Y. Ma, Y. Zhang, S. Ma, M. Cai, F. Zhou, W. Liu, Synthesis of novel copolymer/Mn+ biomimetic adhesives based on temperature strengthened coacervation effect, Chemical Engineering Journal, 425 (2021) 127249.
[48] Y. Ma, B. Zhang, I. Frenkel, Z. Zhang, X. Pei, F. Zhou, X. He, Mussel-Inspired Underwater Adhesives-from Adhesion Mechanisms to Engineering Applications: A Critical Review, Reviews of Adhesion and Adhesives, 9 (2021) 167-188.
[49] M. Shan, C. Gong, B. Li, G. Wu, A pH, glucose, and dopamine triple-responsive, self-healable adhesive hydrogel formed by phenylborate–catechol complexation, Polymer Chemistry, 8 (2017) 2997-3005.
[50] L. Han, X. Lu, K. Liu, K. Wang, L. Fang, L.-T. Weng, H. Zhang, Y. Tang, F. Ren, C. Zhao, Mussel-inspired adhesive and tough hydrogel based on nanoclay confined dopamine polymerization, ACS nano, 11 (2017) 2561-2574.
[51] P. Zhu, M. Hu, Y. Deng, C. Wang, One - pot fabrication of a novel agar - polyacrylamide/graphene oxide nanocomposite double network hydrogel with high mechanical properties, Advanced Engineering Materials, 18 (2016) 1799-1807.
[52] Y. Wang, K. Jia, C. Xiang, J. Yang, X. Yao, Z. Suo, Instant, tough, noncovalent adhesion, ACS applied materials & interfaces, 11 (2019) 40749-40757.
[53] J. Steck, J. Kim, J. Yang, S. Hassan, Z. Suo, Topological adhesion. I. Rapid and strong topohesives, Extreme Mechanics Letters, 39 (2020) 100803.
[54] J. Yang, R. Bai, B. Chen, Z. Suo, Hydrogel adhesion: A supramolecular synergy of chemistry, topology, and mechanics, Advanced Functional Materials, 30 (2020) 1901693.
[55] Z. Wang, L. Guo, H. Xiao, H. Cong, S. Wang, A reversible underwater glue based on photo-and thermo-responsive dynamic covalent bonds, Materials Horizons, 7 (2020) 282-288.
[56] H. Yuk, C.E. Varela, C.S. Nabzdyk, X. Mao, R.F. Padera, E.T. Roche, X. Zhao, Dry double-sided tape for adhesion of wet tissues and devices, Nature, 575 (2019) 169-174.
[57] H. Yuk, J. Wu, T.L. Sarrafian, X. Mao, C.E. Varela, E.T. Roche, L.G. Griffiths, C.S. Nabzdyk, X. Zhao, Rapid and coagulation-independent haemostatic sealing by a paste inspired by barnacle glue, Nature biomedical engineering, 5 (2021) 1131-+.
[58] L. Li, H. Zeng, Marine mussel adhesion and bio-inspired wet adhesives, Biotribology, 5 (2016) 44-51.
[59] Q. Liu, X. Lu, L. Li, H. Zhang, G. Liu, H. Zhong, H. Zeng, Probing the reversible Fe3+–DOPA-mediated bridging interaction in mussel foot protein-1, The Journal of Physical Chemistry C, 120 (2016) 21670-21677.
[60] F. Jehle, E. Macías-Sánchez, S. Sviben, P. Fratzl, L. Bertinetti, M.J. Harrington, Hierarchically-structured metalloprotein composite coatings biofabricated from co-existing condensed liquid phases, Nature communications, 11 (2020) 1-9.
[61] S. Hu, X. Pei, L. Duan, Z. Zhu, Y. Liu, J. Chen, T. Chen, P. Ji, Q. Wan, J. Wang, A mussel-inspired film for adhesion to wet buccal tissue and efficient buccal drug delivery, Nature communications, 12 (2021) 1-17.
[62] S.-H. Kim, K. Kim, B.S. Kim, Y.-H. An, U.-J. Lee, S.-H. Lee, S.L. Kim, B.-G. Kim, N.S. Hwang, Fabrication of polyphenol-incorporated anti-inflammatory hydrogel via high-affinity enzymatic crosslinking for wet tissue adhesion, Biomaterials, 242 (2020) 119905.

[63] L. Chen, G. Zeng, D. Guo, J. Liu, X. Zhang, S. Lin, K. Zhang, Soft elastic hydrogel couplants for ultrasonography, Materials Science and Engineering: C, 119 (2021) 111609.
[64] J. Yi, K.-C.T. Nguyen, W. Wang, W. Yang, M. Pan, E. Lou, P.W. Major, L.H. Le, H. Zeng, Polyacrylamide/Alginate double-network tough hydrogels for intraoral ultrasound imaging, Journal of colloid and interface science, 578 (2020) 598-607.
[65] S. Mitragotri, Sonophoresis: ultrasound-mediated transdermal drug delivery, in: Percutaneous Penetration Enhancers Physical Methods in Penetration Enhancement, Springer, 2017, pp. 3-14.
[66] K. Wu, N. Shardt, L. Laouar, J.A. Elliott, N.M. Jomha, Vitrification of particulated articular cartilage via calculated protocols, NPJ Regenerative medicine, 6 (2021) 1-13.
[67] L.H. Le, An investigation of pulse-timing techniques for broadband ultrasonic velocity determination in cancellous bone: a simulation study, Physics in Medicine & Biology, 43 (1998) 2295.
[68] C. Zhang, L.H. Le, R. Zheng, D. Ta, E. Lou, Measurements of ultrasonic phase velocities and attenuation of slow waves in cellular aluminum foams as cancellous bone-mimicking phantoms, The Journal of the Acoustical Society of America, 129 (2011) 3317-3326.
[69] X. Zhang, R. Zhang, S. Wu, Y. Sun, H. Yang, B. Lin, Physically and chemically dual-crosslinked hydrogels with superior mechanical properties and self-healing behavior, New Journal of Chemistry, 44 (2020) 9903-9911.
[70] Z. Jing, X. Dai, X. Xian, X. Du, M. Liao, P. Hong, Y. Li, Tough, stretchable and compressive alginate-based hydrogels achieved by non-covalent interactions, RSC Advances, 10 (2020) 23592-23606.
[71] L. Burlamacchi, A. Lai, M. Monduzzi, G. Saba, NMR, EPR, and INDO Studies on the Complexes of Dopamine with Cu2+, Mn2+, and Fe3+ in Aqueous Solution, Journal of Magnetic Resonance (1969), 55 (1983) 39-50.
[72] F. Talens-Alesson, S. Hall, N. Hankins, B. Azzopardi, Flocculation of SDS micelles with Fe3+, Colloids and Surfaces A: Physicochemical and Engineering Aspects, 204 (2002) 85-91.
[73] N. Anitha, M. Palaniandavar, Mononuclear iron (III) complexes of 3N ligands in organized assemblies: spectral and redox properties and attainment of regioselective extradiol dioxygenase activity, Dalton Transactions, 40 (2011) 1888-1901.
[74] R.B. Viana, A.B. da Silva, A.S. Pimentel, Infrared spectroscopy of anionic, cationic, and zwitterionic surfactants, Advances in physical chemistry, 2012 (2012).
[75] P.-G. De Gennes, Wetting: statics and dynamics, Reviews of modern physics, 57 (1985) 827.
[76] L. Gong, J. Wang, L. Zhang, V. Fattahpour, M. Mamoudi, M. Roostaei, B. Fermaniuk, J.-L. Luo, H. Zeng, Fouling mechanisms of asphaltenes and fine solids on bare and electroless nickel-phosphorus coated carbon steel, Fuel, 252 (2019) 188-199.
[77] L. Gong, J. Wang, L. Xiang, J. Huang, V. Fattahpour, M. Roostaei, M. Mamoudi, B. Fermaniuk, J.-L. Luo, H. Zeng, Characterizing foulants on slotted liner and probing the surface interaction mechanisms in organic media with implication for an antifouling strategy in oil production, Fuel, 290 (2021) 120008.
[78] Y. Murakami, K. Nakamura, The chelating behavior of catechol-4-sulfonate with iron (III) ion, Bulletin of the Chemical Society of Japan, 36 (1963) 1408-1411.
[79] J.S. Haynes, J.R. Sams, R.C. Thompson, Synthesis and structural studies of iron (II) and iron (III) sulfonates, Canadian Journal of Chemistry, 59 (1981) 669-678.
[80] Z. Khan, S.A. AL-Thabaiti, S. Hussain, Nanoscale water soluble self-assembled zero-valent iron: role of stabilizers in their morphology, RSC advances, 6 (2016) 7267-7278.

[81] S. Zhuo, Y. Guan, H. Li, J. Fang, P. Zhang, J. Du, C. Zhu, Facile fabrication of fluorescent Fe-doped carbon quantum dots for dopamine sensing and bioimaging application, Analyst, 144 (2019) 656-662.
[82] H. Fan, J. Wang, Z. Tao, J. Huang, P. Rao, T. Kurokawa, J.P. Gong, Adjacent cationic–aromatic sequences yield strong electrostatic adhesion of hydrogels in seawater, Nature communications, 10 (2019) 1-8.
[83] J.N. Israelachvili, Intermolecular and surface forces, Academic press, 2015.
[84] L. Han, K. Liu, M. Wang, K. Wang, L. Fang, H. Chen, J. Zhou, X. Lu, Mussel-inspired adhesive and conductive hydrogel with long-lasting moisture and extreme temperature tolerance, Advanced Functional Materials, 28 (2018) 1704195.
[85] D. Gan, W. Xing, L. Jiang, J. Fang, C. Zhao, F. Ren, L. Fang, K. Wang, X. Lu, Plant-inspired adhesive and tough hydrogel based on Ag-Lignin nanoparticles-triggered dynamic redox catechol chemistry, Nature communications, 10 (2019) 1-10.
[86] C. Xie, X. Wang, H. He, Y. Ding, X. Lu, Mussel-inspired hydrogels for self-adhesive bioelectronics, Advanced Functional Materials, 30 (2020) 1909954.
[87] Z. Jia, J. Gong, Y. Zeng, J. Ran, J. Liu, K. Wang, C. Xie, X. Lu, J. Wang, Bioinspired Conductive Silk Microfiber Integrated Bioelectronic for Diagnosis and Wound Healing in Diabetes, Advanced Functional Materials, 31 (2021) 2010461.
[88] J.-P. Laulhère, A.-M. Labouré, J. Briat, Photoreduction and incorporation of iron into ferritins, Biochemical Journal, 269 (1990) 79-84.
[89] A. De Luca, R.F. Dantas, S. Esplugas, Study of Fe (III)-NTA chelates stability for applicability in photo-Fenton at neutral pH, Applied Catalysis B: Environmental, 179 (2015) 372-379.
[90] J.L. Daristotle, S.T. Zaki, L.W. Lau, L. Torres Jr, A. Zografos, P. Srinivasan, O.B. Ayyub, A.D. Sandler, P. Kofinas, Improving the adhesion, flexibility, and hemostatic efficacy of a sprayable polymer blend surgical sealant by incorporating silica particles, Acta biomaterialia, 90 (2019) 205-216.
[91] A. Assmann, A. Vegh, M. Ghasemi-Rad, S. Bagherifard, G. Cheng, E.S. Sani, G.U. Ruiz-Esparza, I. Noshadi, A.D. Lassaletta, S. Gangadharan, A highly adhesive and naturally derived sealant, Biomaterials, 140 (2017) 115-127.
[92] Y. Liu, H. Meng, Z. Qian, N. Fan, W. Choi, F. Zhao, B.P. Lee, A moldable nanocomposite hydrogel composed of a Mussel-inspired polymer and a nanosilicate as a fit-to-shape tissue sealant, Angewandte Chemie International Edition, 56 (2017) 4224-4228.
[93] Y. Bu, L. Zhang, G. Sun, F. Sun, J. Liu, F. Yang, P. Tang, D. Wu, Tetra-PEG based hydrogel sealants for in vivo visceral hemostasis, Advanced Materials, 31 (2019) 1901580.

CHPATER 5. Highly Stretchable, Elastic, Antimicrobial Conductive Hydrogels with Environment-adaptive Adhesive Property for Health Monitoring

5.1 Introduction

The recent thrust towards soft electronics has raised considerable attention due to its flexibility, stretchability, and multi-functionality, which fits the requirement of wearable devices for the non-invasive monitoring of body signals [1-7]. Compared to other soft electronics like carbon- or metal-based thin films [8, 9], hydrogel-based electronics exhibit a similar water content (70-80 wt.%) and good mechanical match with soft tissues [10], thus helps maintain a comfortable and conformal contact with the human body in motion and avoids the discomfort to the users. Among the ways to mount wearable hydrogel electronics onto the human body, using hydrogels with the adhesive property that can adhere to skins, tissues or other targeted surfaces is of great interest, due to their tight fit, conformable contact, and ease of operation. Although tremendous progress has been achieved in the aspects of sensitivity and cyclicity using conductive hydrogels as soft sensors, the reliable health monitoring in practical conditions still remains a challenge. For instance, the moisture or water and vigorous exercise would cause the detachment of hydrogels from the human body [11, 12]. Therefore, it is highly desirable to develop conductive and adhesive hydrogels with the proper adhesive property that is capable of being stably affixed to the substrates when applied as wearable electronics, withstanding wet conditions, and being removed mildly on demand.

Hydrogel is a three-dimensional (3D) network, consisting of water as the majority and polymer as the minority. The abundant water in a hydrogel poses a significant challenge to settle

the stable connection with other surfaces [13]. Inspired by the adhesive strategy of some natural organisms like marine mussels, barnacles, and sandcastle worms, hydrogels have been advanced with the instant, universal, and robust adhesive properties to both the dry and wet substrates based on the catechol-related chemistry [14-20]. Despite the exciting progress that has been achieved in the recapitulation of the marine organisms-based adhesive strategy, the catechol-derivatives-modified hydrogels with the self-adhesive property are usually limited by the complicated preparation method, material cost, and stability exposed to oxygen. Another disadvantage of self-adhesive hydrogel with double side adhesion for motion sensing applications is that the hydrogel sensor could indiscriminately stick to other undesired substrates instead of the target substrates upon contact. To achieve the wet adhesion in a more applicable way and an on-demand manner, an alternative strategy has been proposed by coupling hydrogels with an external adhesive layer using bridging polymers, thus endowing hydrogels with adhesion property only on the side facing to the target substrates [21-23]. The robust adhesion achieved by this strategy is originated from the synergy of both the bridging polymers and hydrogels: the bridging polymers should form connections via reversible interactions (e.g., hydrogen bonds and electrostatic interaction) with the hydrogels and target surfaces while hydrogels should contain dynamic bonds to dissipate energy when the hydrogel is stressed [24]. On the basis of this strategy, we applied the bridging polymers with stimuli-responsive property on the surface of conductive hydrogels to realize the environment-adaptive adhesion, specifically triggerable attachment and controllable benign detachment on diverse substrates in response to the environmental stimulus.

Herein, we report a new class of conductive hydrogels not only showing outstanding elasticity, stretchability, self-healing, and antimicrobial properties which are favorable for

advanced soft electronics with improved reliability and lifespan, but also demonstrating stimuli-responsive adhesion capability. The hydrogel is prepared by the copolymerization of hydrophilic monomer acrylamide (AM) and hydrophobic (Hb) monomer C_{18} preserved in cationic micelles (CM) consisting of benzalkonium chloride (BAC) and cetyltrimethylammonium chloride (CTAC) under 0.8 M NaCl saline conditions. The polyacrylamide is selected as the primary network of the hydrogel in this work due to its low cytotoxicity, stability, and elasticity with the dynamic crosslinking agents The obtained P(AM-Hb/CM) hydrogel contains dynamic non-covalent supramolecular interactions (hydrogen bond, hydrophobic, π-π, and cation-π interactions) [25-27], resulting in the excellent mechanical properties for energy dissipation under stress. The pH-responsive polymers (Alginate and PAA) as well as temperature-responsive polymers (F-127 and F-68) are applied on the surface of the hydrogel motion sensor to help connect the hydrogel with the target surface. The transition from stable attachment to on-demand detachment is realized via modulating the topological connection state of the stimuli-response polymers with hydrogels and substrates, specifically, adjusting pH from acidic to basic for Alginate/PAA or lowering down the temperature for F-127/F-68. Moreover, the antimicrobial property of the hydrogel is originated from the quaternary ammonium groups of the BAC/CTAC micelles in the hydrogel which is also evaluated by the microbial growth inhibition assay. All these desired traits make the conductive hydrogel-polymer system a smart motion sensing entirety for the detection of body motion signals as well as sealing tissue breakages and measuring hydraulic pressure with the reliable and repeatable response, which benefits the advances of non-invasive health monitoring.

5.2 Experimental methods

5.2.1 Materials

Acrylamide (AM, ⩾ 99 wt.%), stearylmethacrylate (C18, ⩾ 99 wt.%), benzalkonium chloride (BAC, 50 wt.% in H2O), cetyltrimethylammonium chloride (CTAC, 25 wt.% in H2O), Irgacure 2959 UV Photo-initiator (⩾98 wt.%), poly(ethylene glycol) diacrylate crosslinker (PEGDA, Mn=700, ⩾99 wt.%), sodium alginate (⩾99 wt.%), poly(acrylic acid) (PAA, Mw ~100,000, 35 wt.% in H2O), Pluronic® F-127 and F-68 (powder, BioReagent) were purchased from Sigma-Aldrich (Canada). Sodium chloride (powder), hydrogen chloride (HCl, 37 wt.% in H2O), and sodium hydroxide (NaOH, 50 wt.% in H2O) were purchased from Fisher Scientific (Canada). Porcine skin and heart were obtained from the local grocery store. Water used in all the experiments was generated by the Barnstead Smart2Pure pro water purification system (Thermo Scientific) with a resistivity of 18.2 MΩ·cm.

5.2.2 Preparation of the Hydrogels

In a typical process, 1.9g CTAC, 1.9g BAC, and hydrophobic (Hb) monomer C_{18} were firstly added in 20 mL of 0.8M NaCl solution at 50 ºC under magnetic stir until a clear solution was obtained. A series of conductive hydrogels were prepared by varying the Hb monomer to C_{18} (0.144, 0.288, and 0.432 g, denoted as Hb1, Hb2, and Hb3, respectively) to investigate the effect of micelle crosslinking on the mechanical properties of the developed hydrogel, donated as Hb-1, Hb-2, Hb-3, respectively. After that, the CTAC/BAC-C_{18}-NaCl solution was cooled down to room temperature followed by adding 2g AM, 0.06g PEGDA, 0.08g Irgacure UV Photo-initiator under nitrogen purge for 30 min. Finally, the obtained precursor solution was transferred

to a degas mold and placed in a UV-crosslinker for 20 min for the gelation of the P(AM-Hb/CM) hydrogel.

5.2.3 Characterization of the Hydrogels

Before characterization, the hydrogel samples were firstly quenched in liquid nitrogen and freeze-dried at -55 ºC. After that, the samples were cut by a blade cutter and the obtained section was used for Fourier transform infrared (FTIR) spectrometer and scanning electron microscope (SEM) analysis. The internal morphologies and the corresponding element distribution of the hydrogels were investigated using a field-emission scanning electron microscope (FE-SEM) (Zeiss Sigma 300 VP-FESEM, Germany) with energy-dispersive X-ray spectroscopy (EDS) operated at 7.5 keV acceleration voltage. Before SEM/EDS characterization, the hydrogel samples were gold-sputtered for 2 min with a thin layer of gold metal (~ 14 nm). FTIR spectrometer (Thermo Scientific Nicolet, iS50 FT-IR) was applied to identify the chemical composition of the freeze-dried hydrogel samples.

5.2.4 Mechanical and Self-healing Properties of the Hydrogels

The mechanical properties of the developed hydrogels are characterized by rheology measurement as well as tensile/compression tests at room temperature. All the rheology measurements were performed using a 2° cone configuration (20 mm-diameter) with a gap of 53 μm. The viscoelastic behavior of the hydrogel was evaluated by oscillatory frequency sweep tests with the shear rates ranging from 0.1 to 100 rad/s, at a 10 % strain. Both the tensile and compression tests were performed using an AGS-X universal tensile tester (Shimadzu, Japan). Rectangular hydrogel samples with a fixed dimension of 25 mm (length) × 5 mm (width) × 1.2 mm (thickness) were used for tensile tests at a constant stretching rate of 20 mm/s. Cylinder

hydrogel samples with a fixed dimension of 12.4 mm (diameter) × 15 mm (height) were prepared for compression tests at a constant stretching rate of 20 mm/s.

The self-healing property of the hydrogel is characterized by both the rheological and tensile tests. The strain amplitude sweep was first conducted with the strain varying from 0.1 to 1200%, at a frequency of 10 rad/s, to generate hydrogen network failure. After that, the strain was immediately switched from 1200% to 1% and kept for 60 s, at the same frequency of 10 rad/s, to investigate the restoration of the hydrogel network. The self-healing capability of the hydrogel was also evaluated by measuring the tensile strength of the repaired samples. The original hydrogel samples were firstly cut into two halves with a scissor and the two separated interfaces were then brought into contact without the applied stress for 30 min and 12h at room temperature. After the healing process for a certain time, the healing efficiency was evaluated by the uniaxial tensile tests.

5.2.5 Adhesive Property of the Hydrogels

The adhesion property of the as-prepared hydrogels was characterized via the lap shear test using the same tensile test machine (AGS-X universal tensile tester, Shimadzu, Japan). The substrates used in this work include glass, wood, porcine skin and heart. The porcine skin and heart are mounted on the wood plate using the superglue (Gorilla Glue, Ohio, United States). The size of the hydrogel samples is kept at 20 mm (Length) x 5 mm (Width) x 1.2 mm (Thickness). The pH-responsive polymers (Alginate and PAA) solutions with a pH value of 8 and thermo-responsive polymers (F-127 and F-68) solution at room temperature were first spread on the substrates. Then the hydrogel samples with specific pH and temperature conditions were placed between the substrates. After that, a preload of 25 kPa (weights on the contact interface of hydrogel with substrates) was applied for 30 min, followed by the adhesion tests. All the lap

shear tests were conducted at a constant extension velocity of 10 mm/min. The wet adhesion strength was collected by spreading the water at the contact interface of adherends and the hydrogel.

5.2.6 Electrical and Sensing Performances of the Hydrogels

The electrical conductivities (S) of hydrogels were first characterized by the electrochemical impedance spectroscopy using an electrochemical workstation (CHI920, CH Instruments, USA) [28]. The values of S is obtained via the following equation:

$$S = \frac{L}{R_b \cdot A} \tag{1}$$

where L is the gauge length, A refers to the cross-sectional area of the hydrogel sample and R_b is the bulk resistance obtained from the electrochemical impedance spectroscopy via frequency span from 10^{-1} to 10^{6} Hz (intercept at Z′ axis) with an amplitude of 5 mV at open circuit voltage.

The response of the hydrogel to the stretching and compression were characterized by monitoring its variation of resistance ($\Delta R / R_0$) during the tensile and compression tests. The real-time current-time (I-t) curves of the hydrogel were recorded on an electrochemical workstation with a constant voltage of 1.5 V. Then $\Delta R / R_0$ was calculated according to the following equation:

$$\frac{\Delta R}{R_0} = \frac{I_0}{I} - 1 \tag{2}$$

where I_0 represents the current at t = 0, I is the measured current.

5.2.7 Antimicrobial Assay

Inhibition of microbial growth by the developed hydrogel against microbial was evaluated by the disc-diffusion method [29, 30]. Briefly, 150 μL *E. coli* in suspension at 10^6 colony forming units (CFU)/mL was spread on Luria-Bertain (LB) agar plates. The P(AM-Hb/CM) hydrogel was placed on the plates with pure PAM hydrogel serving as the control.[31] The plates were then incubated at 37 °C overnight. Zones of inhibition around each hydrogel disc were assessed to determine the antibacterial effect.

To further evaluate the antimicrobial effect of the P(AM-Hb/CM) hydrogel, the hydrogel was incubated with 1 mL *E. coli* in suspension at 10^6 CFU/mL in a 12-well plate at 37 °C, followed by mild shaking for 4 h. The suspension was then evenly spread on the LB agar plates and incubated at 37 °C for 14h. Pure PAM hydrogel was used as the control. Colonies on each plate were counted by Image J software.

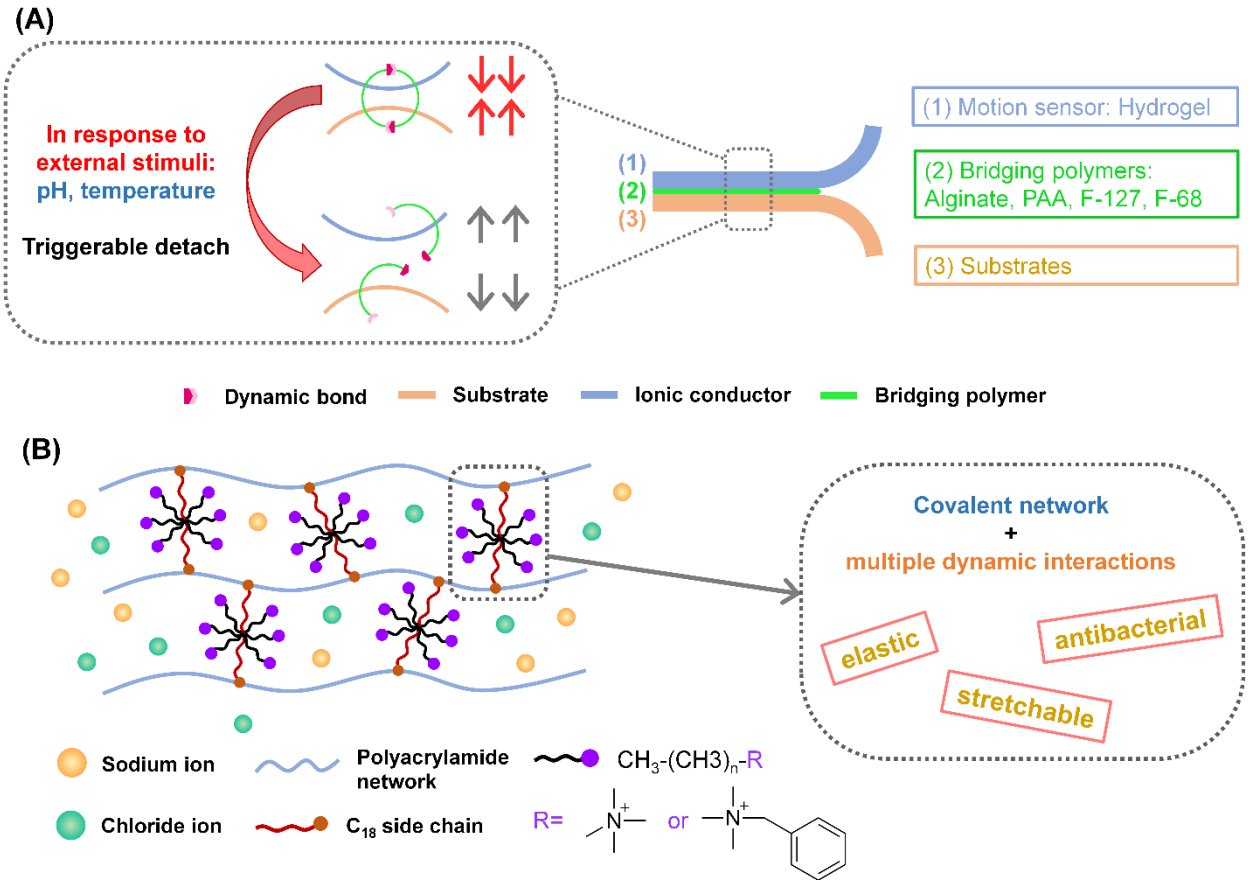

Figure 5.1 (A) Schematic illustration of the strategy to engineer adhesive soft sensor consisting of conductive hydrogel and stimuli response polymers; (B) Schematic illustration of the formation of P(AM-Hb/CM) hydrogel.

5.3 Results and discussion

5.3.1 Design and Molecular Engineering of Conductive Hydrogels with Environmental-adaptive Adhesive Property

As presented in Figure 5.1A, in order to functionalize the soft sensor with environment-adaptive adhesive property, the conductive hydrogel is engineered with an adhesive layer consisting of different types of interpenetrating polymers including the pH-responsive polymers

(Alginate/PAA) and thermo-responsive polymers (F-127/F-68). More specifically, the bridging polymers solution is first prepared in their soluble range of pH or temperature while the hydrogel and the target surface are pre-set to the conditions (pH or temperature) that would result in the decreased solubility of the bridging polymers [32, 33].

Following this design principle, the stable attachment of the hydrogel sensor to the target substrates is achieved via placing Alginate/PAA or F-127/F-68 between the hydrogel and target surfaces, which promotes the formation of bridging polymers being in topological connection state with the polymer network of the hydrogel and the target surfaces at acidic pH and body temperature, respectively. Meanwhile, the controllable detachment is triggered by changing the pH and temperature back to the soluble range of the bridging polymers (mildly basic pH of 8 and room temperature) at the contact interface of hydrogel with adherend substrates. Figure 5.1B illustrates the design of the conductive hydrogels consisting of a primary covalent network via the copolymerization of hydrophilic monomer acrylamide with Hb monomer C_{18} preserved in BAC/CTAC/C_{18} micelles. Two types of cationic surfactants (BAC and CTAC) were selected for the formation of micellar structures with C_{18} to involve multiple dynamic non-covalent interactions (i.e., hydrophobic, π-π and cation-π interactions) into the hydrogel matrix for better energy dissipation upon stretched which would enhance the stretchability of the hydrogels when served as the strain sensor. Also, the micellar structure could endow the hydrogels with excellent elasticity due to the fast and reversible reassembly of the micelles upon deformation, thus improving the fatigue resistance of the sensor [28, 34, 35]. Introducing ions into the hydrogel system can facilitate the micellar growth and solubilization of the Hb segment C_{18} in the cationic BAC/CTAC micelles, which leads to the incorporation of the hydrophobic monomer copolymerized in the PAM chain to form a crosslinking network [36].

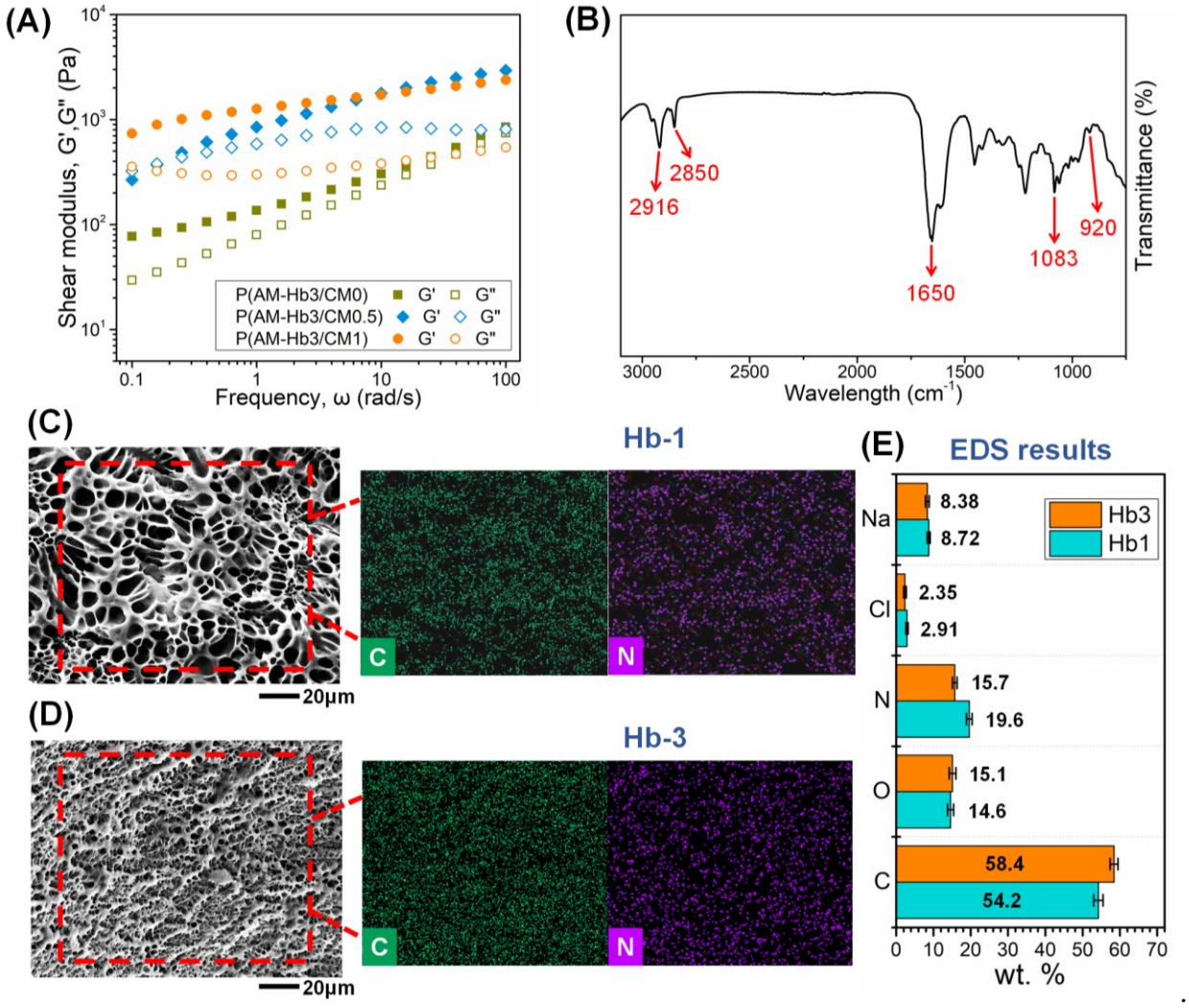

Figure 5.2 (A) Frequency-dependent rheological measurements of P(AM-Hb3/CMx) hydrogels with different amounts of BAC in the cationic micelles, where x refers to the weight ratio of BAC to CTAC; (B) FTIR spectrum of P(AM-Hb3/CM0.5) hydrogel; (C) SEM images of the cross-sections of P(AM-Hb1/CM0.5) and P(AM-Hb3/CM0.5) hydrogels with EDS mapping of C and N; (D) EDS results of P(AM-Hb1/CM0.5) and P(AM-Hb3/CM0.5) hydrogels (data reported as means ± standard deviation (SD) for n = 10 for scanning times).

The viscoelastic behaviors of the developed P(AM-Hb/CM) hydrogels were first evaluated by rheological measurements. Figure 5.2A shows the storage modulus G′ and loss modulus G″ with the angular frequency ranging from 0.1 to 100 rad/s. For P(AM-Hb3/CM0) with pure CTAC micelles, a cross-over point of G′= G″ was found during the frequency sweep, indicating its solid-like behavior at low frequency (G′ > G″) and quasi-liquid behavior (G′ < G″) at high frequency. However, the values of G′ were always higher than G″ during the frequency sweep for P(AM-Hb3/CM0.5) and P(AM-Hb3/CM1) hydrogels with 0.5 and 1 weight ratio of BAC in total cationic micelles, respectively, suggesting a permanent elastic network was formed in both the hydrogel samples with a solid-like behavior [37]. This could be attributed to the alkyl-benzyl groups adjacent to the quaternary ammonium moieties of BAC in the micelles, forming π-π and cation-π interactions, which leads to a higher cross-linking density of the hydrogels [38]. The chemical composition of the P(AM-Hb3/CM0.5) hydrogel was characterized using FTIR spectrum shown in Figure 5.2B. The transmittance peaks located at 920, 1217 and 1650 cm^{-1} were ascribed to the asymmetric bending the quaternary ammonium C-N^{+}-R_3, stretching of -C-O-, and the aromatic C=C skeleton stretching vibration respectively, while the two peaks located at 2850 and 2916 cm^{-1} corresponded to the antisymmetric and symmetric stretching of the long alkyl chain belonging to the micelles, confirming the presence of BAC-CTAC/ C_{18} micelles in the hydrogel [39-42]. The internal morphologies of P(AM-Hb/CM0.5) hydrogels with different amount of hydrophobic monomer C_{18} were examined by SEM (Figure 2C). Compared with the loosely porous structure of P(AM-Hb1/CM0.5) with larger pore size around 10 μm, the P(AM-Hb3/CM0.5) exhibited a denser network with a relatively smaller pore size around 2 μm. With the increase of hydrophobic monomer C_{18} during the hydrogel preparation, the cationic micelle forms more crosslinks with the PAM network, which leads to a denser microstructure with

smaller pore size. Figure 5.2C and 2D also show the EDS mapping of the P(AM-Hb1/CM0.5) and P(AM-Hb3/CM0.5) hydrogels, with the element mass fraction (Figure 5.2E). Compared to the EDS results of P(AM-Hb1/CM0.5) hydrogel, the increased mass fraction of carbon and decreased fraction of nitrogen detected on P(AM-Hb3/CM0.5) hydrogel surface further confirmed that the hydrophobic monomer C_{18} with long alkyl chain was incorporated into the PAM network and formed a dense network.

5.3.2 Mechanical and Self-Healing Properties of the Hydrogels

The mechanical properties of the obtained P(AM-Hb/CM) hydrogels were evaluated by both the tensile and compression tests using an AGS-X universal tensile testing machine. Figure 5.3A illustrated the normalized tensile stress-strain curves of P(AM-Hb/CM) hydrogels with different compositions. With the increase of Hb segments C_{18} in the hydrogel, the tensile strength and the fractured strain are significantly increased from 9.2 kPa and 470 % for P(AM-Hb1/CM0.5) to 85 kPa and 1130 % for P(AM-Hb3/CM0.5), respectively. Meanwhile, the hydrogels containing only CTAC or BAC were also investigated. Compared to the P(AM-Hb3/CM0.5) with 0.5 weight ratio of BAC in total cationic micelles, the tensile strength and fractured strain of P(AM-Hb3/CM0) are relatively low (26 kPa at 710 %), while the P(AM-Hb3/CM1) exhibits the highest tensile strength among all the samples but fractured early at 820 % strain. As shown in Figure 5.3B, the toughness was then calculated to be 82.0, 212, 28.0, 109, and 339 kJ/m^3 for P(AM-Hb3/CM0), P(AM-Hb3/CM1), P(AM-Hb1/CM0.5), P(AM-Hb2/CM0.5), and P(AM-Hb3/CM0.5), respectively. The elastic modulus of the obtained hydrogels were calculated from the linear region of the stress-strain curves, as shown in Figure 5.S1. According to the above results, P(AM-Hb3/CM0.5) with the highest stretchability and toughness is selected as the conductive hydrogel for sensing experiments. Figure 5.S2 shows the

elasticity of P(AM-Hb3/CM0.5) at a tensile strain of 1000 %. The PAAFC-L hydrogel restored 83 % of its original tensile strength when a relatively high strain of 1000% was applied, which demonstrated its good elasticity under large deformation. Figure 5.3C shows the successive loading–unloading tests of 100, 300, 600, and 1000 % strain cycles with a 2 min time interval between each cycle. The area between the loading-unloading curves here represents the dissipated energy, as shown in Figure 5.3D. The dissipated energy increased significantly with the stretch strain from 100 to 1000 %, which makes the hydrogel feasible as the energy dissipative matrix to delay the interfacial detachment when applied as the adhesive hydrogels [38]. Figure 5.3E and 3F show the compressive stress-strain and cycling stress-time curves, respectively. The P(AM-Hb3/CM0.5) hydrogel exhibits a compressive stress of 250 kPa at 80% strain and maintains almost unchanged after 7 loading-unloading cycles. The nearly identical loading and unloading curves indicate the excellent elasticity of the hydrogel. The above results indicated that the developed P(AM-Hb3/CM0.5) shows good mechanical properties to resist the external force when being stretched or compressed.

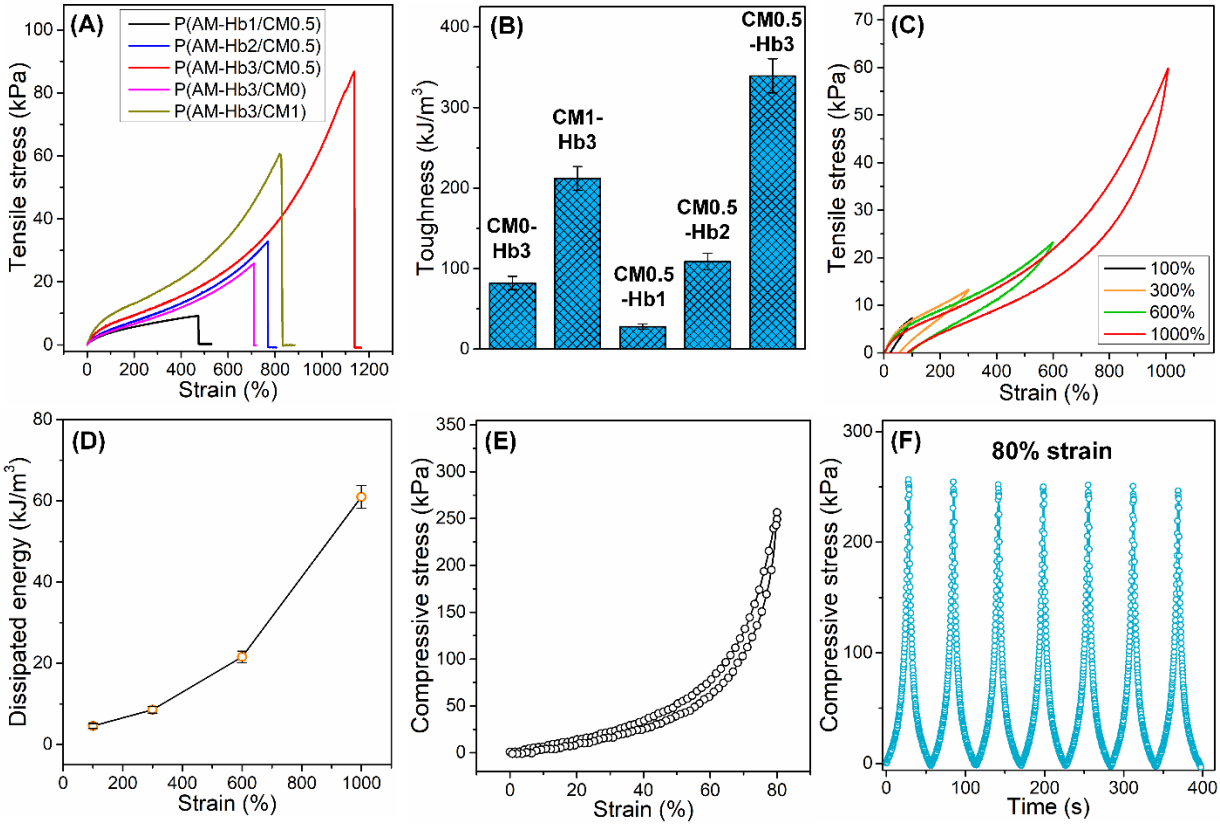

Figure 5.3 (A) Typical stress−strain curves of P(AM-Hb/CM) hydrogel with various content of Hb segments and composition of cationic micelles; (B) toughness of P(AM-Hb/CM) hydrogels (data reported as means ± SD for n = 3 samples per group); (C) representative cyclic tensile loading–unloading curves with a gradual strain increase for the P(AM-Hb3/CM0.5) hydrogel and (D) the dissipated energy under different strain; (E) representative compressive stress-strain curve for P(AM-Hb3/CM0.5) hydrogel with (F) cycling compressive stress-time curve.

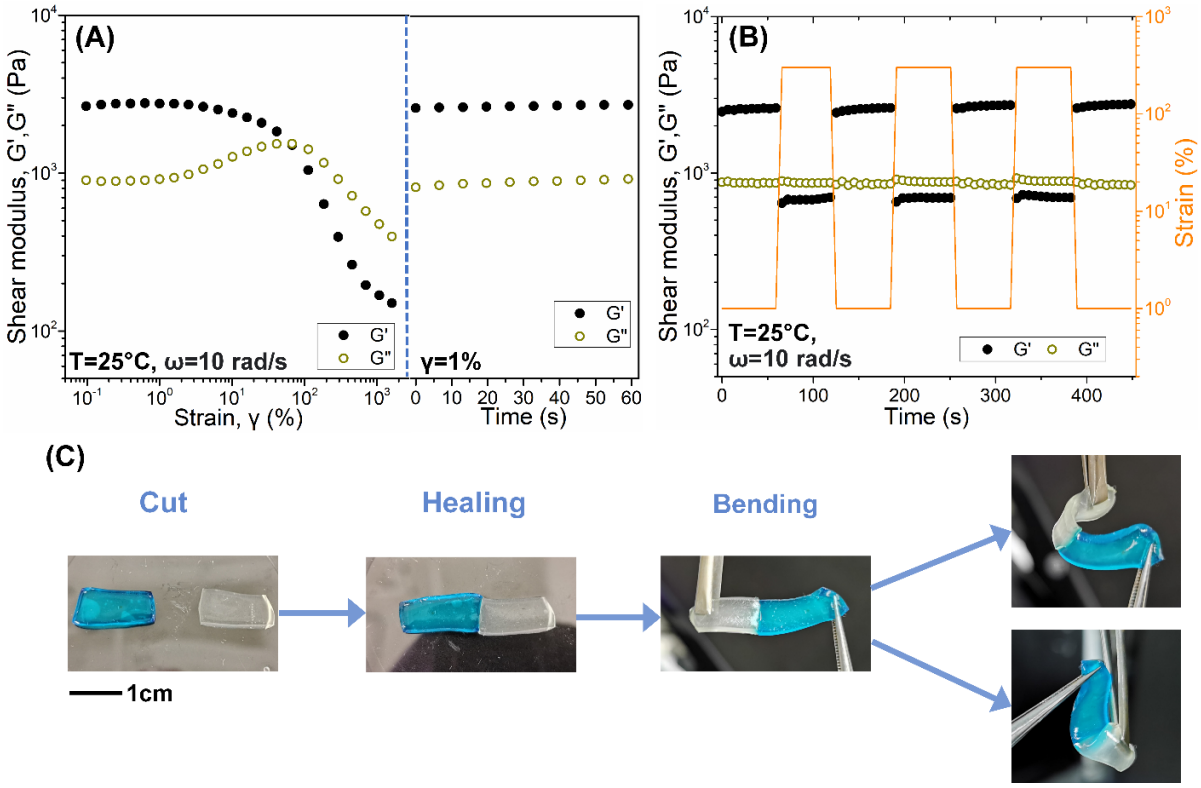

Figure 5.4 Self-healing properties of the P(AM-Hb3/CM0.5) hydrogel. (A) Oscillatory strain sweep of the hydrogel (left) followed by a time sweep recovery from 1200 % to 1% strain (right); (B) G' and G" of the cyclic steps with shear strain shifting between 1% and 300%; (C) Optical images of the hydrogel after cutting and healing for 10 min.

Strain sweep and cyclic step strain measurements were then conducted to evaluate the self-healing performances of the P(AM-Hb3/CM0.5). As shown in Figure 5.4A, the storage modulus surpassed the loss modulus in a broad oscillatory strain range from 0.1% to 113%. The crossover of G′ and G″ occurred at the oscillatory strain of 113%, which manifested the hydrogel network started to rupture. Further increasing shear strains resulted in higher G″ than G′, indicating severe damage of the hydrogel network. However, when the strain switched back to 1% at the frequency of 10 rad/s, both G′and G″ recovered to the initial values within 40 s. Meanwhile, the

repeatability of the self-healing properties of the PCM hydrogel was then analyzed via the cyclic step strain experiment by switching between small and large amplitude of 1 and 300 % strain with the step time of 60 s, respectively. As shown in Figure 5.4B, when a continuous shift between 1 and 300 % strain was applied, the G′and G″ of the hydrogel could repeatedly recover to their initial value within a 60 s step time, exhibiting a good recycling ability of its mechanical strength towards large strain. The quick restoration of the shear modulus as well as the exceptional cycling performance of the hydrogel indicate its capability of the network reconstruction after deformation, which could be ascribed to the dynamic non-covalent interactions of the hydrogel that undergoes reversible dissociation/association process. Moreover, the rectangular hydrogel samples were cut into pieces and the freshly generated surfaces were brought back into contact to enable healing process. After a 10 min contact, the two adhered pieces could withstand stretching and bending, as shown in Figure 5.4C. The mechanical strengths of the healed hydrogels were also measured by the tensile tests (Figure 5.S3), where the self-healed hydrogel reached the elongations of 126 and 357% after 30 min and 12 h of healing, respectively. Besides the self-healing property, the self-recovery and antifatigue performances of the developed P(AM-Hb3/CM0.5) hydrogel were also characterized by cyclic tensile tests without resting time [43]. As shown in Figure 5.S4, the hysteresis loop in the 1st cycle indicated that the hydrogel could dissipate energy under the loading-unloading process of tensile tests. However, the maximum tensile stress of the hydrogel decreased after the 1st cycle and tended to be stable after 3rd cycle. This could be ascribed to the dynamic feature of the micelle-crosslinked network with multiple non-covalent interactions. The hydrogel network is partially destroyed during the stretching of first cycle and leads to the decrease of tensile strength in the subsequent cycles. The stable cycling performance from 3rd to 10th cycles is originated from the dynamic

non-covalent interactions preserved in the hydrogel network that undergoes reversible dissociation/association process [44]. The reversible network structure endowed the hydrogels with excellent fatigue resistance property.

5.3.3 Adhesive Property of the Hydrogels

With the assistance of bridging polymers, P(AM-Hb3/CM0.5) hydrogel exhibited an excellent adhesive performance to various substrates and demonstrated temperature- or pH-modulated adhesion capabilities. As shown in Figure 5.5A, the F-127-coated P(AM-Hb3/CM0.5) hydrogel can tightly attach to the human skin and resist the flow of warm water (around 37 ºC close to body temperature). Meanwhile, the wood and porcine skin connected by Alginate-coated P(AM-Hb3/CM0.5) hydrogel at acidic pH of 3 could lift a weight of 100 g. The wet adhesive strength of the developed hydrogels was measured by lap-shear tests with water spread at the attached interfaces, as shown in Figure 5.S5. Figure 5.5B shows the measured adhesion strength-extension curves of pure and Alginate-coated P(AM-Hb3/CM0.5) hydrogel at pH 3 and 9 placed between porcine skin under wet conditions. Incorporation of Alginate on the surface of P(AM-Hb3/CM0.5) hydrogel significantly increased the adhesion strength from 6 kPa for pure P(AM-Hb3/CM0.5) hydrogel to around 30 kPa for Alginate-coated hydrogel at pH 3. Meanwhile, the adhesion strength decreased to ~ 8 kPa for Alginate-coated hydrogel at pH 9, which is within the range of soluble pH for Alginate (pKa around 4). The basic pH leads to the increase of solubility of alginate, thus inducing the instability of its connection with the hydrogel and porcine skin. The adhesion property of pH-responsive polymers Alginate and PAA was further investigated. Figure 5.5C shows the effect of environmental pH on the adhesion strength, ranging from pH 3 to 9. Both the Alginate and PAA exhibited a higher adhesion strength at acidic pH of 3 and 4

while a significant decrease was observed for pH over 5. This phenomenon could be correlated to the protonation/deprotonation of carboxyl groups of Alginate/PAA with the pKa ~ 4. At lower pH, most of the carboxyl groups of the Alginate/PAA are protonated, which induces their decreased solubility from water and the formation of intra- and inter-molecular hydrogen bonds, thus rendering the topological connection with the hydrogel and substrates. At higher pH over 5, most of the carboxyl groups of the Alginate/PAA are deprotonated, resulting in their increased solubility and decreased adhesion strength to realize the controllable detachment [32]. Figure 5.5E shows the effect of environmental temperature on the thermo-responsive polymers of F-127/F-68, ranging from 20 to 37 ºC. There is no obvious enhancement of the adhesion strength of F-127/F-68-coated P(AM-Hb3/CM0.5) at low temperatures of 20 and 25 ºC. At 37 ºC, a significant increase in adhesion strength of both F-127 and F-68 was detected. This is correlated to the critical solution temperature (LCST) of Pluronic F-127 and F-68 around or slightly below the physiological temperatures. At elevated temperatures around 37 ºC, the thermo-responsive F-127 and F-68 form a more stable hydrophobic association due to the dehydration of PEO heads of F-127/F-68 that reduce their steric repulsions [28]. Figure 5.5D and 5F show the effect of polymer concentration on the adhesion strength. The adhesion strength of both Alginate/PAA and F-127/F-68 increased with their polymer concentration, at pH 3 and 37 ºC, respectively. Generally, the adhesion strength of Alginate is higher than that of PAA, which is attributed to the higher molecular weight and viscosity of Alginate to PAA. Similarly, the adhesion strength of F-127 is higher than F-68, due to the higher molecular weight forming a more stable hydrophobic association at the contact interface of hydrogel with porcine skin. Figure 5.5G shows the adhesion strength of Alginate/PAA-coated P(AM-Hb3/CM0.5) hydrogel at pH 3 and pH 9 and F-127/F-68-coated P(AM-Hb3/CM0.5) hydrogel at 25 and 37 ºC to various substrates including

glass, wood, porcine skin and heart. The Alginate/PAA-coated or F-127/F68-coated P(AM-Hb3/CM0.5) hydrogel exhibited a relatively high adhesion strength to various substrates at pH 3 or 37 ºC, respectively, while the decline of adhesion occurred for both the cases at pH 9 or 25 ºC, respectively, realizing the transition of attachment/detachment in response to the external stimuli. Figure 5.5H demonstrates the stability of P(AM-Hb3/CM0.5) hydrogel (dyed by Basic blue) attached to the porcine skin with the assistance of Alginate at pH 3, withstanding the stretch and bend. The above results indicated that the developed hydrogel-polymer system possesses a universal adhesive property to various substrates with controllable removability, which holds great potential as the adhesive motion sensor in an on-demand manner under practical conditions.

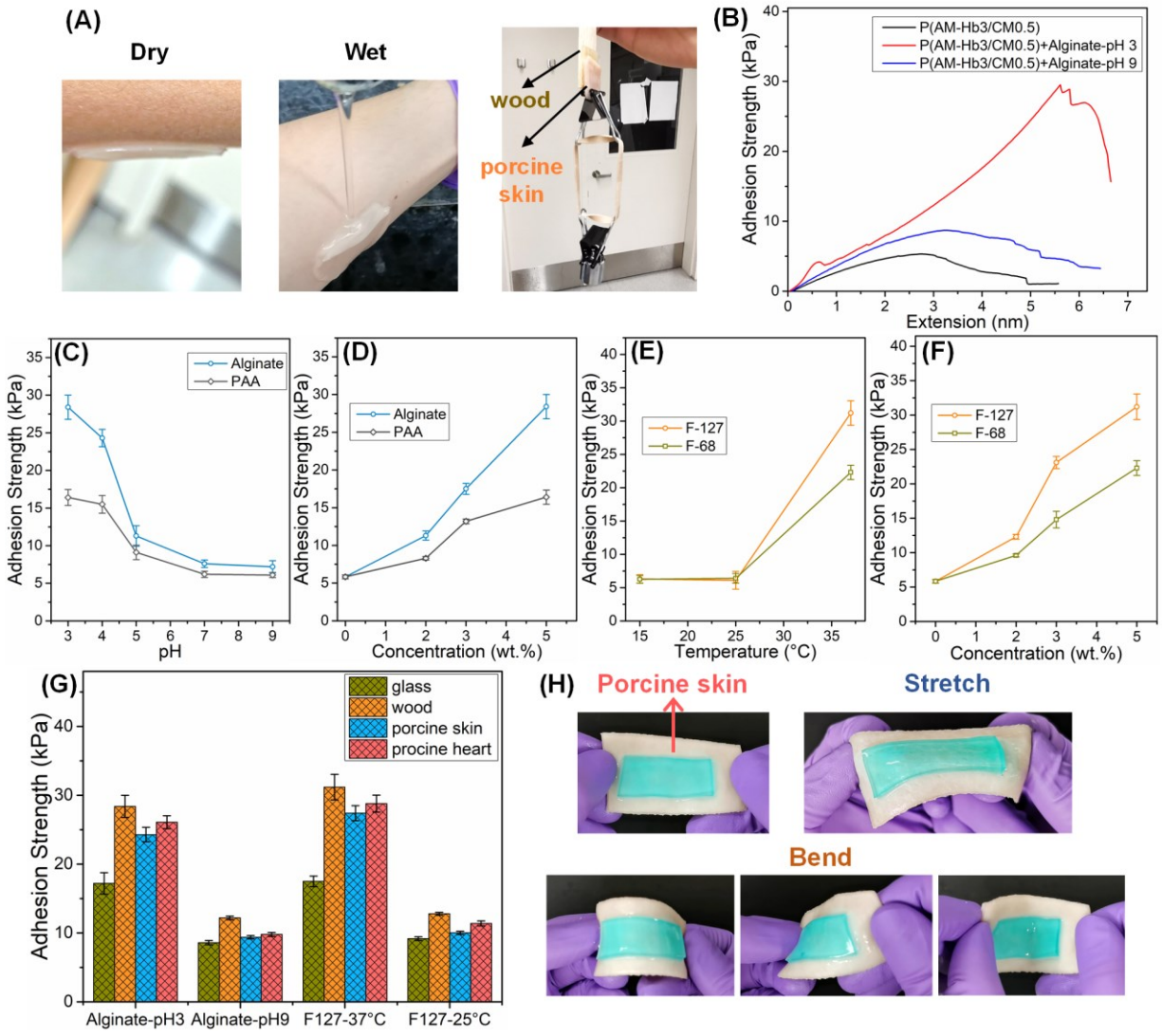

Figure 5.5 Adhesive properties of the P(AM-Hb3/CM0.5) hydrogel. (A) Optical images of hydrogel attached to human body, wood, and porcine skin; (B) Typical adhesion strength-extension curves of the hydrogel with 5 wt.% alginate at different pH conditions measured by lap shear tests using porcine skin as the substrate; Adhesion strength of the hydrogel with PAA/alginate at various (C) pH and (D) alginate concentrations as well as with F-68/F-127 at various (E) pH and (F) alginate concentrations (data reported as means ± SD for n = 3 samples per group); (G) Adhesion strength of the hydrogel with different target substrates (data reported

as means ± SD for n = 3 samples per group); (H) Optical images of the adhered hydrogel remains intact after stretching and bending.

5.3.4. Electrical Properties and Sensing Performance of the Hydrogels

The conductivities of the hydrogels were determined by the electrochemical impedance spectra measured using an electrochemical workstation (CHI920, CH Instruments). Figure 5.6A shows the conductivities of pure PAM and P(AM-Hb3/CM0.5) hydrogels with varying salinity. The conductivity of pure PAM is relatively low with the value of ~ 0.08 S/m, due to the insufficient ions in the hydrogel. In contrast, the conductivity of P(AM-Hb3/CM0.5) hydrogels is greatly increased with the increasing salinity (from 0.2 to 0.8 M NaCl) and reaches 2.72 S/m for P(AM-Hb3/CM0.5) hydrogel containing 0.8 M NaCl, which is comparable to the previously reported conductive hydrogels (conductivity 1.5-10 S/m) used for the efficient motion sensing [2, 4, 10, 28]. Figure 5.S6 shows the relative variation of resistance ($\Delta R/R_0$) of the PCM hydrogel with 0.8 M salinity in response to 300 % tensile strain. The $\Delta R/R_0$-strain curve exhibits a linear relationship with the slope of the curve referred as the gauge factor from 0-200 %. The gauge factor of P(AM-Hb3/CM0.5) hydrogel is determined to be 0.9 and 3.2 within the tensile strain of 0-110 % and 110-200 %, respectively, representing the sensitivity of the hydrogel in response to the stretching.

The repeatability of the strain-sensitive electrical performance of P(AM-Hb3/CM0.5) hydrogel was investigated by the cyclic loading/unloading tests between 0 and 100 % tensile strain. As shown in Figure 5.6B and 5.S7, the $\Delta R/R_0$ of P(AM-Hb3/CM0.5) hydrogel in response to a 100 % strain remained almost unchanged after 50 cycles, indicating its potential to provide stable and reliable sensing signals in long-term use. Figure 5.6C shows the $\Delta R/R_0$-time curve of P(AM-Hb3/CM0.5) hydrogel when applied to monitor the finger bending. At the bending angle

of 15º, 30º, and 45º, the sensing was conducted for least 10 times and the obtained signals of resistance variation are highly repeatable. In addition to the tensile tests, the response of the P(AM-Hb3/CM0.5) hydrogel to the compression was also investigated. Figure 5.6D shows the $\Delta R/R_0$-time curve P(AM-Hb3/CM0.5) hydrogel with compressive strain range from 20 to 70 %. Contrary to the tensile strain, the resistance variation turns to be negative value under compression and the obtained signals are highly stable and repeatable under all the compressive strains. The effect of the self-healing ability of the P(AM-Hb3/CM0.5) hydrogel on its electrical performance was also investigated by recording the current change during the cut/healing process. The P(AM-Hb3/CM0.5) hydrogel is connected in the series circuit with a LED lamp. The LED light extinguished when the hydrogel in the circuit was cut into two pieces and lightened up immediately as the separated pieces were brought into contact (Figure 5.6E). It could also be observed from the current change of the cut/healing process (Figure 5.6F) that the cut of the hydrogel resulted in a sudden drop of the current while the healing of the hydrogel led to a slight fluctuation of the current but stabilized after ~ 3 s. The cut-healing process was conducted for 3 times at different locations, and the rapid restoration of electrical performance was observed in all the cut-healing steps, indicating the repeatable self-healing of the conductivity of the P(AM-Hb3/CM0.5) hydrogel. In addition to the motion-sensing tests, the P(AM-Hb3/CM0.5) hydrogel was also applied on the broken substrate (porcine skin) to test its potential in sealing the breakage and monitoring the local hydraulic pressure, as shown in Figure 5.6G. The experiment setup is illustrated in Figure 5.S8. Figure 5.6H shows the measured relative resistance change ($\Delta R/R_0$) of the P(AM-Hb3/CM0.5) hydrogel in response to different hydraulic pressures. The P(AM-Hb3/CM0.5) hydrogel could resist the hydraulic pressure up to ~ 85 mmHg (comparable to human blood pressure of ~ 60-120 mmHg). The relative resistance

change of the P(AM-Hb3/CM0.5) hydrogel is attributed to its deformation in response to the varied hydraulic pressure, which provides an alternative method of non-invasive hydraulic pressure monitoring by transducing the variation of pressure to electrical signals for the more applicable measurement [45, 46].

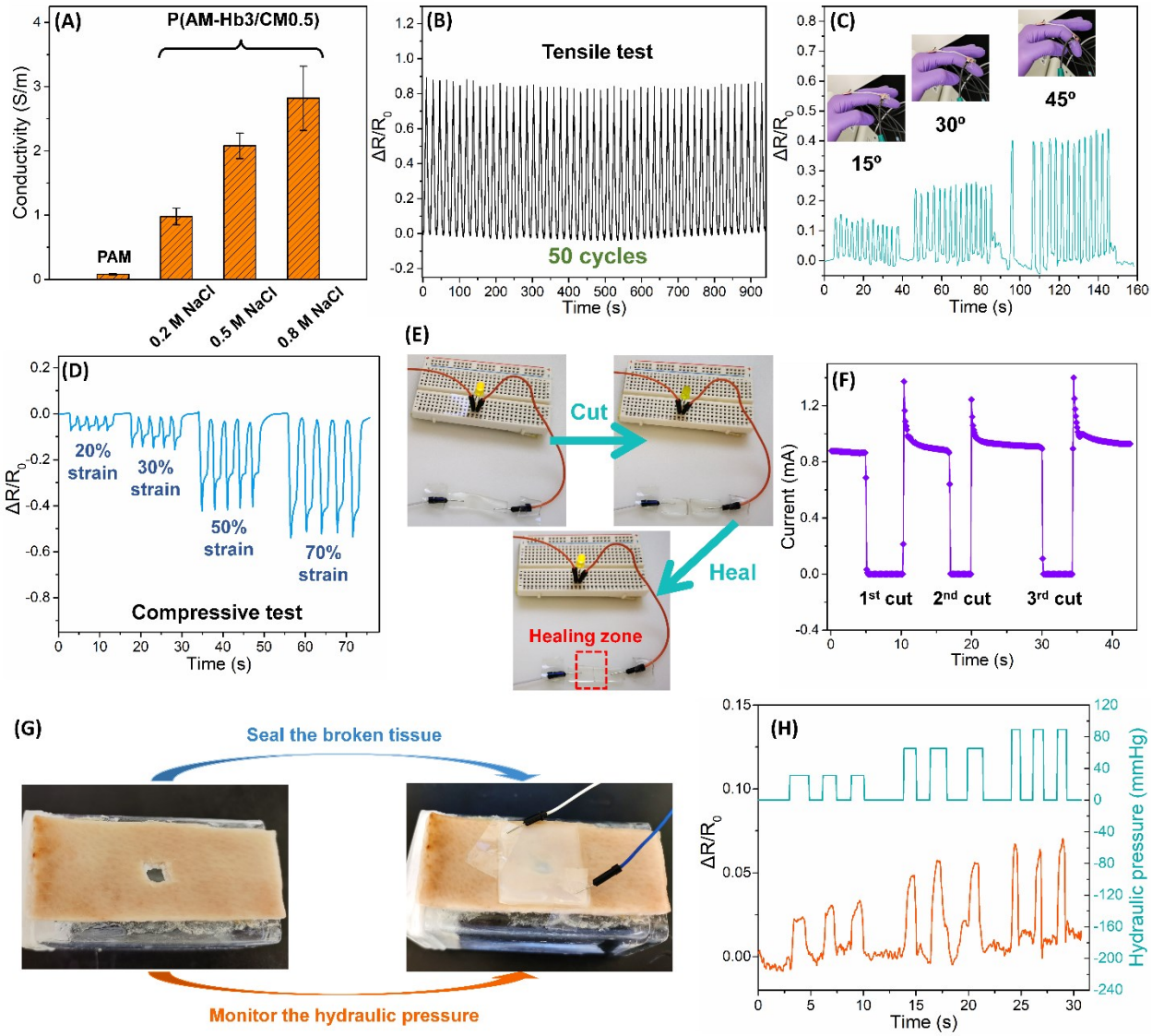

Figure 5.6 Electrical properties of the P(AM-Hb/CM) hydrogels. (A) Conductivities of hydrogels with different salt conditions (data reported as means ± SD for n = 3 samples per group); (B) Relative resistance change ($\Delta R/R_0$) of the P(AM-Hb3/CM0.5) hydrogel during 50 stretching−releasing cycles between 0 and 100% strain; (C) Demonstration of the P(AM-

Hb3/CM0.5) hydrogel as the motion sensor for detecting finger bending; (D) $\Delta R/R_0$ of P(AM-Hb3/CM0.5) hydrogel during compressive tests under different strain; (E) Demonstration of electrical self-healing ability of the P(AM-Hb3/CM0.5) hydrogel with a LED lamp in the series circuit with the monitoring of (F) current change of the hydrogel with three cut and healing processes; (G) Optical images of hydrogel applied to seal the seal the puncture area on porcine skin with the monitoring of (H) the hydraulic pressure.

5.3.5 Antimicrobial Property of the Hydrogels

The antimicrobial capability is highly desirable for wearable hydrogel electronics to avoid microbial accumulation that might impair the sensing performances [47, 48]. The antimicrobial property of the developed hydrogel was evaluated by the microbial growth inhibition assay employing *E. coli*. Figure 5.7A is a representative picture showing inhibition of *E. coli* growth by the P(AM-Hb3/CM0.5) but not pure PAM hydrogel. We think that the inhibition would be attributed to the interaction of quaternary ammonium moiety with a long alky chain belonging to BAC/CTAC micelles with bacterial cell walls [49].

The spread plate method was further used to quantitatively evaluate the antimicrobial property of the PCM hydrogel. In a typical experiment, both PAM and P(AM-Hb3/CM0.5) hydrogels were first immersed in *E. coli* in suspension, followed by a mild shaking for 4 h. The suspension was then transferred and spread on LB agar plates, followed by another incubation for 14 h. As shown in Figure 5.7B, 5.S9A, and S9B, the number of colonies in agar plates treated with the P(AM-Hb3/CM0.5) hydrogel is 91 ± 0.019 % lower than that with PAM hydrogel. A proposed mechanism of the P(AM-Hb3/CM0.5) hydrogel-mediated inhibition is illustrated in Figure 5.7C. These results demonstrated that the P(AM-Hb3/CM0.5) hydrogel containing

quaternary ammonium micelles exhibits significant inhibitory effect on the *E. coli* growth, indicating a reduced probability of microbial accumulation on the hydrogel surface.

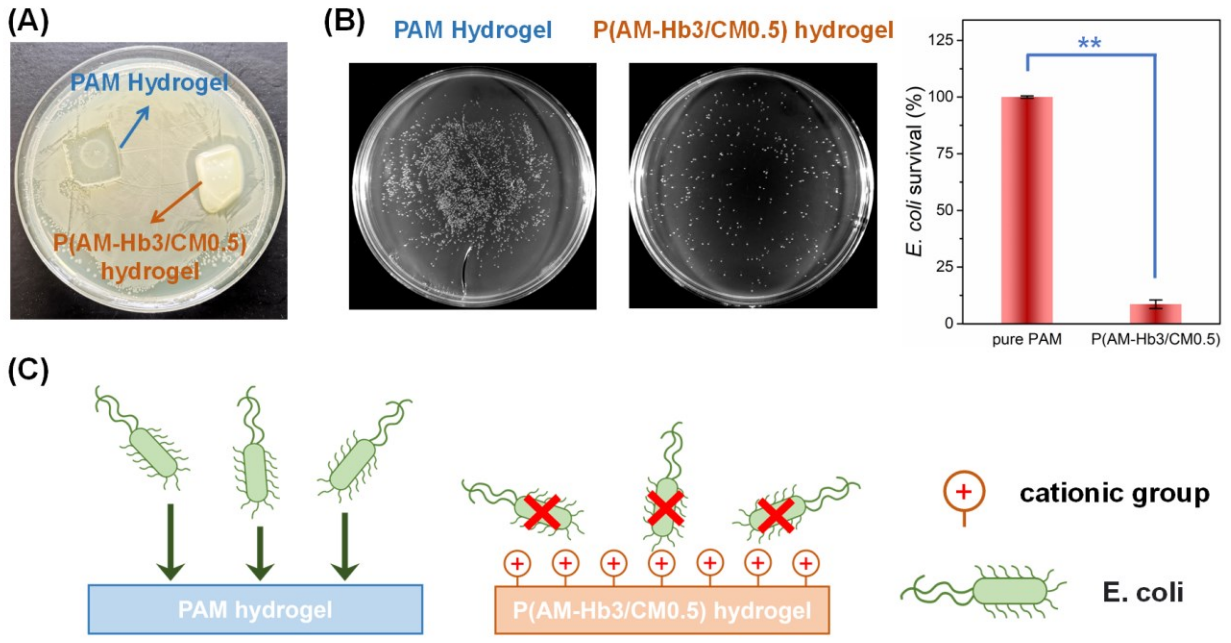

Figure 5.7 Antibacterial properties of hydrogel P(AM-Hb3/CM0.5). (A) Representative optical image showing an inhibition zone; (B) Representative *E. coli* colonies and averaged survival rate after incubation with PAM or P(AM-Hb3/CM0.5) hydrogel (n=3, ** represents $p < 0.01$); (C) Proposed antibacterial mechanism.

5.4 Conclusions

In this work, we have developed a highly stretchable, elastic, self-healing, and antimicrobial hydrogel ionic conductor. The as-developed (AM-Hb3/CM0.5) hydrogel is composed of a covalent PAM network with crosslinked BAC/CTAC/C_{18} micelles containing multiple dynamic and reversible non-covalent interactions (e.g., hydrogen bonding, hydrophobic, π-π, and cation-π interactions). The resulting hydrogel exhibits excellent stretchability (over 1100% strain), elasticity (over 83% recovery from 1000% tensile strain), and reliable electrical

and sensing performances. Moreover, the hydrogel ionic conductor was integrated with stimuli-responsive polymers to enable triggerable adhesion and on-demand removability for various substrates. Compared to inherently adhesive hydrogels, the P(AM-Hb3/CM0.5) possesses an environment-adaptive adhesive property with the assistance of pH-responsive polymers of Alginate or PAA as well as thermo-responsive polymers of F-127 or F-68 to achieve the stable attachment to and controllable detachment from the target substrates, which benefits the repositioning of fixed hydrogel sensors without causing damage to either the hydrogels or the attached surfaces. This work offers a promising strategy in constructing smart soft sensors, which holds great promises for the reliable, reproducible, and effective detection of body motion signals, which is critical for human health monitoring devices.

5.5 Supporting Infromation

5.5.1 Elastic modulus and recovery of the hydrogel

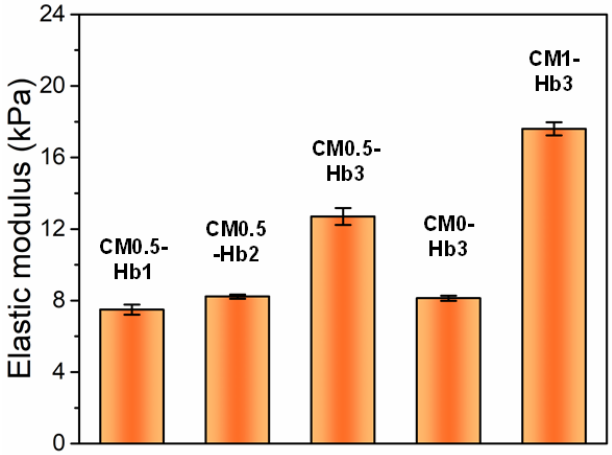

Figure 5.S4 Elastic moduli of the obtained P(AM-Hb/CM) hydrogels (data reported as means ± standard deviation (SD) for n = 3 samples per group).

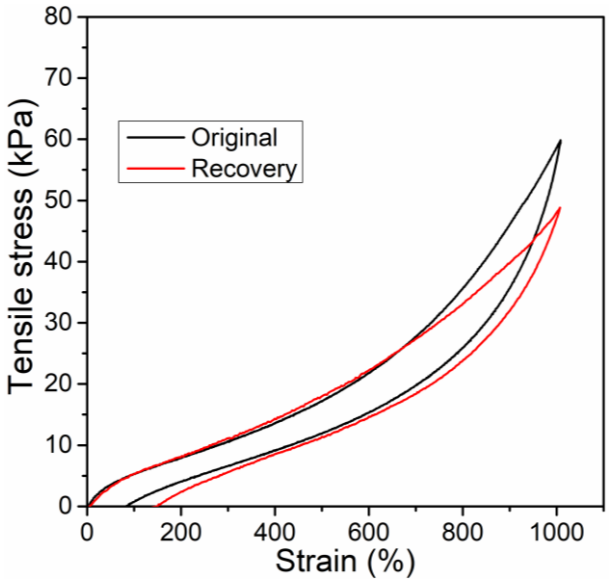

Figure 5.S2 Tensile loading/unloading cycles of 1000% strain for P(AM-Hb3/CM0.5) hydrogel.

5.5.2 Self-healing of PCM hydrogel

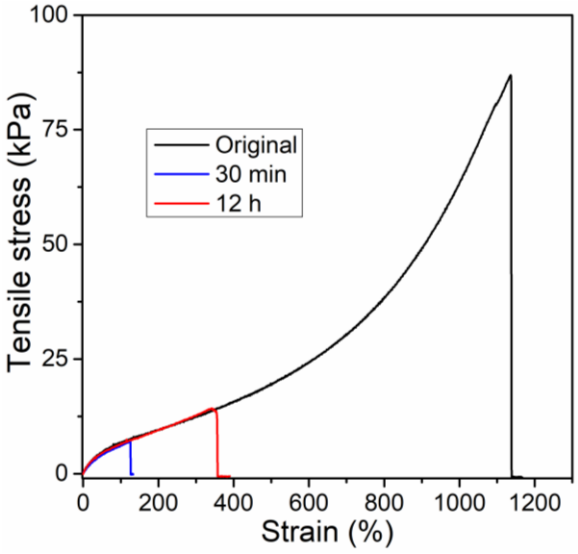

Figure 5.S2 Stress-strains curves of P(AM-Hb3/CM0.5) hydrogel hydrogels healed at different contact time of 30 min and 12 h.

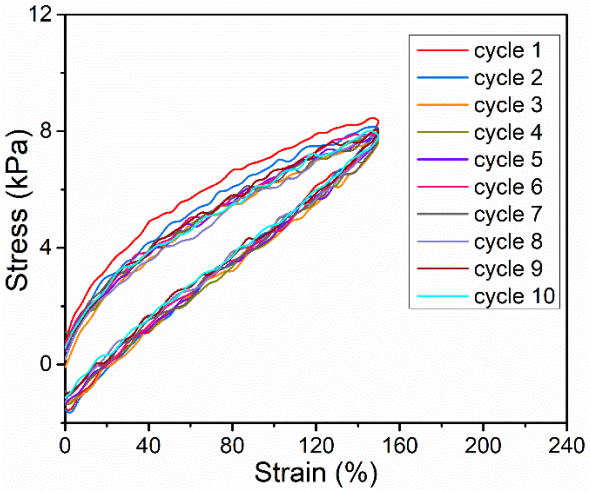

Figure 5.S5 10 successive cyclic tensile loading−unloading curves of P(AM-Hb3/CM0.5) hydrogel at a strain of 150% without resting between each cycle.

5.5.3 lap shear tests

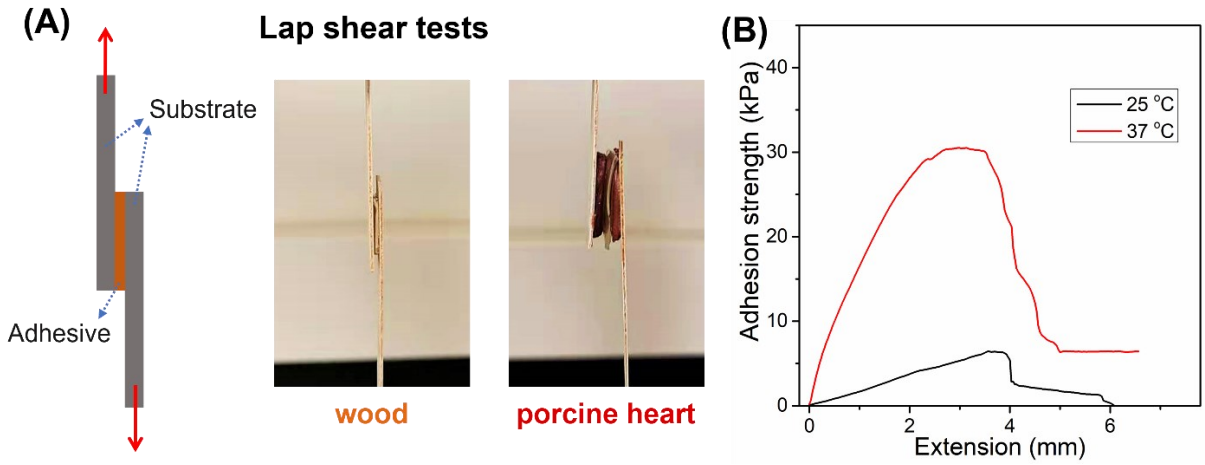

Figure 5.S5 (A) Schematic and optical images of lap shear tests using different substrates; (B) adhesion strength-extension curve of P(AM-Hb3/CM0.5) hydrogel measured using porcine skin as the substrate with the assistance of F-127 at 25 and 37 ˚C, respectively.

5.5.4 Sensitivity of P(AM-Hb3/CM0.5) hydrogel

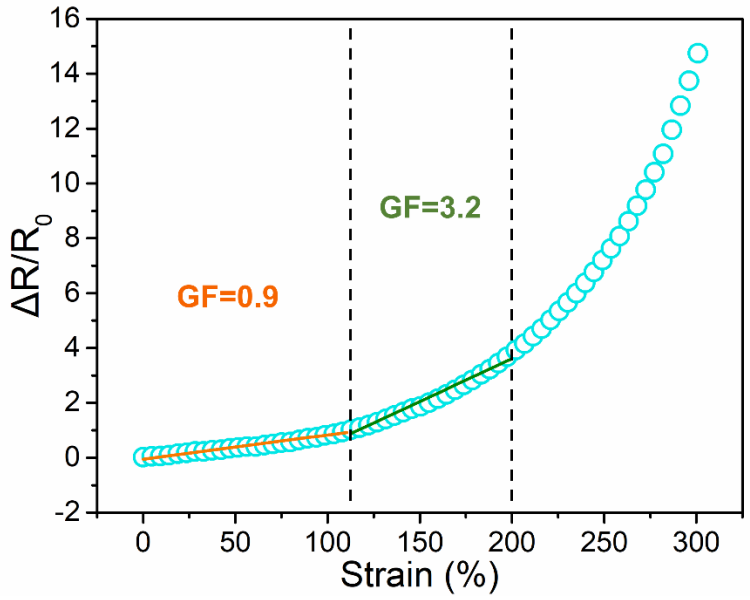

Figure 5.S6 Relative resistance change ($\Delta R/R_0$) of P(AM-Hb3/CM0.5) hydrogel with the applied strain from 0-300 %.

5.5.5 Cycling tests for conductivity

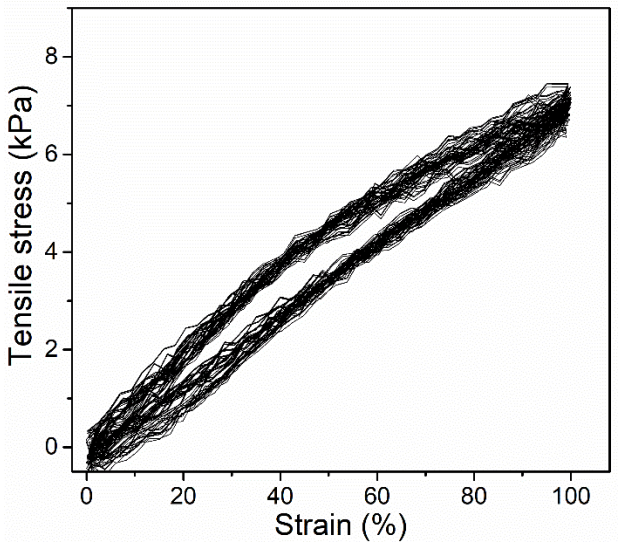

Figure 5.S7 50 tensile loading/unloading cycles of 100% strain for P(AM-Hb3/CM0.5) hydrogel.

5.5.6 Experiment setup for hydraulic pressure monitoring

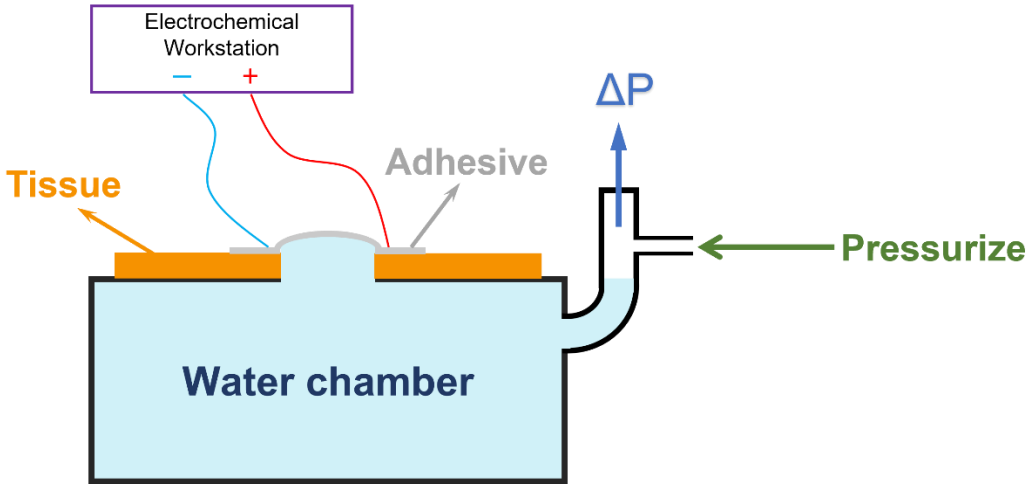

Figure 5.S8 Experiment setup for hydraulic pressure monitoring.

5.5.7 Antibacterial tests

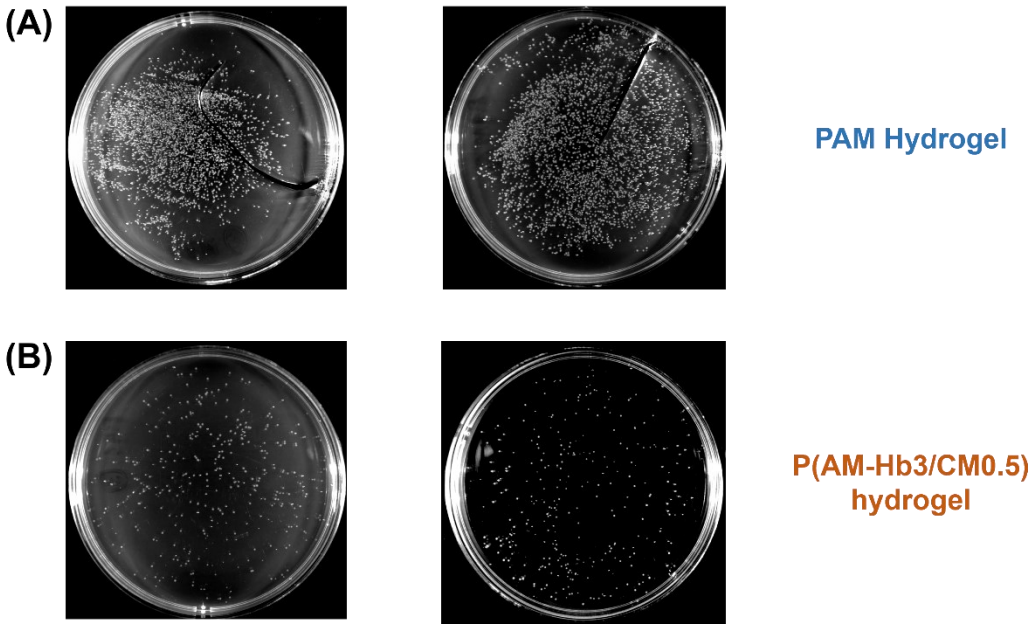

Figure 5.S9 E coli colonies after incubation with pure PAM and P(AM-Hb3/CM0.5) hydrogel.

References

[1] N. Alegret, A. Dominguez-Alfaro, D. Mecerreyes, 3D scaffolds based on conductive polymers for biomedical applications, Biomacromolecules, 20 (2018) 73-89.
[2] J. Chen, Q. Peng, T. Thundat, H. Zeng, Stretchable, injectable, and self-healing conductive hydrogel enabled by multiple hydrogen bonding toward wearable electronics, Chemistry of Materials, 31 (2019) 4553-4563.
[3] Z. Rao, F. Ershad, A. Almasri, L. Gonzalez, X. Wu, C. Yu, Soft electronics for the skin: from health monitors to human–machine interfaces, Advanced Materials Technologies, 5 (2020) 2000233.
[4] Y. Niu, H. Liu, R. He, Z. Li, H. Ren, B. Gao, H. Guo, G.M. Genin, F. Xu, The new generation of soft and wearable electronics for health monitoring in varying environment: From normal to extreme conditions, Materials Today, (2020).
[5] Q. Gui, Y. He, Y. Wang, Soft Electronics Based on Liquid Conductors, Advanced Electronic Materials, 7 (2021) 2000780.
[6] C. Chen, Y. Wang, T. Zhou, Z. Wan, Q. Yang, Z. Xu, D. Li, Y. Jin, Toward Strong and Tough Wood-Based Hydrogels for Sensors, Biomacromolecules, (2021).
[7] K. Ouyang, J. Zhuang, C. Chen, X. Wang, M. Xu, Z. Xu, Gradient Diffusion Anisotropic Carboxymethyl Cellulose Hydrogels for Strain Sensors, Biomacromolecules, (2021).
[8] S. De, T.M. Higgins, P.E. Lyons, E.M. Doherty, P.N. Nirmalraj, W.J. Blau, J.J. Boland, J.N. Coleman, Silver nanowire networks as flexible, transparent, conducting films: extremely high DC to optical conductivity ratios, ACS nano, 3 (2009) 1767-1774.
[9] S.H. Chae, Y.H. Lee, Carbon nanotubes and graphene towards soft electronics, Nano Convergence, 1 (2014) 1-26.
[10] Y. Zhou, C. Wan, Y. Yang, H. Yang, S. Wang, Z. Dai, K. Ji, H. Jiang, X. Chen, Y. Long, Highly stretchable, elastic, and ionic conductive hydrogel for artificial soft electronics, Advanced Functional Materials, 29 (2019) 1806220.
[11] J. Deng, H. Yuk, J. Wu, C.E. Varela, X. Chen, E.T. Roche, C.F. Guo, X. Zhao, Electrical bioadhesive interface for bioelectronics, Nature Materials, 20 (2021) 229-236.
[12] K.G. Cho, S. An, D.H. Cho, J.H. Kim, J. Nam, M. Kim, K.H. Lee, Block Copolymer‐Based Supramolecular Ionogels for Accurate On‐Skin Motion Monitoring, Advanced Functional Materials, (2021) 2102386.
[13] J. Yang, R. Bai, B. Chen, Z. Suo, Hydrogel adhesion: A supramolecular synergy of chemistry, topology, and mechanics, Advanced Functional Materials, 30 (2020) 1901693.
[14] H. Zeng, D.S. Hwang, J.N. Israelachvili, J.H. Waite, Strong reversible Fe3+-mediated bridging between dopa-containing protein films in water, Proceedings of the National Academy of Sciences, 107 (2010) 12850-12853.
[15] C.E. Brubaker, P.B. Messersmith, Enzymatically degradable mussel-inspired adhesive hydrogel, Biomacromolecules, 12 (2011) 4326-4334.
[16] Q. Lu, D.S. Hwang, Y. Liu, H. Zeng, Molecular interactions of mussel protective coating protein, mcfp-1, from Mytilus californianus, Biomaterials, 33 (2012) 1903-1911.
[17] Q. Lu, D.X. Oh, Y. Lee, Y. Jho, D.S. Hwang, H. Zeng, Nanomechanics of cation–π interactions in aqueous solution, Angewandte Chemie, 125 (2013) 4036-4040.

[18] G.P. Maier, M.V. Rapp, J.H. Waite, J.N. Israelachvili, A. Butler, Adaptive synergy between catechol and lysine promotes wet adhesion by surface salt displacement, Science, 349 (2015) 628-632.
[19] J. Zhang, L. Xiang, B. Yan, H. Zeng, Nanomechanics of Anion− Π Interaction in Aqueous Solution, Journal of the American Chemical Society, 142 (2020) 1710-1714.
[20] M. Pan, L. Gong, L. Xiang, W. Yang, W. Wang, L. Zhang, W. Hu, L. Han, H. Zeng, Modulating surface interactions for regenerable separation of oil-in-water emulsions, Journal of Membrane Science, 625 (2021) 119140.
[21] Y. Zhao, Y. Wu, L. Wang, M. Zhang, X. Chen, M. Liu, J. Fan, J. Liu, F. Zhou, Z. Wang, Bio-inspired reversible underwater adhesive, Nature communications, 8 (2017) 1-8.
[22] X. Deng, R. Attalla, L.P. Sadowski, M. Chen, M.J. Majcher, I. Urosev, D.-C. Yin, P.R. Selvaganapathy, C.D. Filipe, T. Hoare, Autonomously self-adhesive hydrogels as building blocks for additive manufacturing, Biomacromolecules, 19 (2018) 62-70.
[23] X. Chen, H. Yuk, J. Wu, C.S. Nabzdyk, X. Zhao, Instant tough bioadhesive with triggerable benign detachment, Proceedings of the National Academy of Sciences, 117 (2020) 15497-15503.
[24] J. Li, A. Celiz, J. Yang, Q. Yang, I. Wamala, W. Whyte, B. Seo, N. Vasilyev, J. Vlassak, Z. Suo, Tough adhesives for diverse wet surfaces, Science, 357 (2017) 378-381.
[25] E.A. Appel, J. del Barrio, X.J. Loh, O.A. Scherman, Supramolecular polymeric hydrogels, Chemical Society Reviews, 41 (2012) 6195-6214.
[26] J.L. Mann, C.Y. Anthony, G. Agmon, E.A. Appel, Supramolecular polymeric biomaterials, Biomaterials science, 6 (2018) 10-37.
[27] W. Wang, Z. Zeng, L. Xiang, C. Liu, D. Diaz-Dussan, Z. Du, A.B. Asha, W. Yang, Y.-Y. Peng, M. Pan, Injectable Self-Healing Hydrogel via Biological Environment-Adaptive Supramolecular Assembly for Gastric Perforation Healing, ACS nano, (2021).
[28] M. Wu, J. Chen, Y. Ma, B. Yan, M. Pan, Q. Peng, W. Wang, L. Han, J. Liu, H. Zeng, Ultra elastic, stretchable, self-healing conductive hydrogels with tunable optical properties for highly sensitive soft electronic sensors, Journal of Materials Chemistry A, 8 (2020) 24718-24733.
[29] S. Li, S. Dong, W. Xu, S. Tu, L. Yan, C. Zhao, J. Ding, X. Chen, Antibacterial hydrogels, Advanced science, 5 (2018) 1700527.
[30] W. Yang, W. Hu, J. Zhang, W. Wang, R. Cai, M. Pan, C. Huang, X. Chen, B. Yan, H. Zeng, Tannic acid/Fe3+ functionalized magnetic graphene oxide nanocomposite with high loading of silver nanoparticles as ultra-efficient catalyst and disinfectant for wastewater treatment, Chemical Engineering Journal, 405 (2021) 126629.
[31] H.H. Tuson, L.D. Renner, D.B. Weibel, Polyacrylamide hydrogels as substrates for studying bacteria, Chemical Communications, 48 (2012) 1595-1597.
[32] J. Yang, R. Bai, Z. Suo, Topological adhesion of wet materials, Advanced Materials, 30 (2018) 1800671.
[33] B.R. Freedman, O. Uzun, N.M.M. Luna, A. Rock, C. Clifford, E. Stoler, G. Östlund‐Sholars, C. Johnson, D.J. Mooney, Degradable and Removable Tough Adhesive Hydrogels, Advanced Materials, 33 (2021) 2008553.
[34] X. Di, J. Li, M. Yang, Q. Zhao, G. Wu, P. Sun, Bioinspired, nucleobase-driven, highly resilient, and fast-responsive antifreeze ionic conductive hydrogels for durable pressure and strain sensors, Journal of Materials Chemistry A, 9 (2021) 20703-20713.
[35] Y. Li, D. Wang, J. Wen, J. Liu, D. Zhang, J. Li, H. Chu, Ultra‐Stretchable, Variable Modulus, Shape Memory Multi‐Purpose Low Hysteresis Hydrogel Derived from Solvent‐

Induced Dynamic Micelle Sea‐Island Structure, Advanced Functional Materials, (2021) 2011259.
[36] D.C. Tuncaboylu, M. Sari, W. Oppermann, O. Okay, Tough and self-healing hydrogels formed via hydrophobic interactions, Macromolecules, 44 (2011) 4997-5005.
[37] J. Tie, H. Chai, Z. Mao, L. Zhang, Y. Zhong, X. Sui, H. Xu, Nanocellulose-mediated transparent high strength conductive hydrogel based on in-situ formed polypyrrole nanofibrils as a multimodal sensor, Carbohydrate Polymers, 273 (2021) 118600.
[38] H. Fan, J. Wang, Z. Tao, J. Huang, P. Rao, T. Kurokawa, J.P. Gong, Adjacent cationic–aromatic sequences yield strong electrostatic adhesion of hydrogels in seawater, Nature communications, 10 (2019) 1-8.
[39] J.D. Anastassopoulou, Mass and FT-IR spectra of quaternary ammonium surfactants, in: Chemistry and Properties of Biomolecular Systems, Springer, 1991, pp. 1-9.
[40] L. Wang, Z. Li, P. Huang, W. Ding, Synthesis of an acrylamide copolymer containing nano-SiO2 by ex situ Cu (0)-mediated SET-LRP, International Journal of Polymer Science, 2019 (2019).
[41] T. Liu, X. Guo, W. Liu, C. Hao, L. Wang, W.C. Hiscox, C. Liu, C. Jin, J. Xin, J. Zhang, Selective cleavage of ester linkages of anhydride-cured epoxy using a benign method and reuse of the decomposed polymer in new epoxy preparation, Green Chemistry, 19 (2017) 4364-4372.
[42] L. Han, M. Wang, L.O. Prieto‐López, X. Deng, J. Cui, Self‐hydrophobization in a dynamic hydrogel for creating nonspecific repeatable underwater adhesion, Advanced Functional Materials, 30 (2020) 1907064.
[43] Y. Lu, Y. Yue, Q. Ding, C. Mei, X. Xu, Q. Wu, H. Xiao, J. Han, Self-Recovery, Fatigue-Resistant, and Multifunctional Sensor Assembled by a Nanocellulose/Carbon Nanotube Nanocomplex-Mediated Hydrogel, ACS Applied Materials & Interfaces, 13 (2021) 50281-50297.
[44] Y. Lu, J. Han, Q. Ding, Y. Yue, C. Xia, S. Ge, Q. Van Le, X. Dou, C. Sonne, S.S. Lam, TEMPO-oxidized cellulose nanofibers/polyacrylamide hybrid hydrogel with intrinsic self-recovery and shape memory properties, Cellulose, 28 (2021) 1469-1488.
[45] L. Zhang, M. Liu, Y. Zhang, R. Pei, Recent progress of highly adhesive hydrogels as wound dressings, Biomacromolecules, 21 (2020) 3966-3983.
[46] Y. Zhong, F. Seidi, C. Li, Z. Wan, Y. Jin, J. Song, H. Xiao, Antimicrobial/Biocompatible Hydrogels Dual-Reinforced by Cellulose as Ultrastretchable and Rapid Self-Healing Wound Dressing, Biomacromolecules, 22 (2021) 1654-1663.
[47] A. Gupta, S.M. Briffa, S. Swingler, H. Gibson, V. Kannappan, G. Adamus, M. Kowalczuk, C. Martin, I. Radecka, Synthesis of silver nanoparticles using curcumin-cyclodextrins loaded into bacterial cellulose-based hydrogels for wound dressing applications, Biomacromolecules, 21 (2020) 1802-1811.
[48] P. Squinca, L. Berglund, K. Hanna, J. Rakar, J. Junker, H. Khalaf, C.S. Farinas, K. Oksman, Multifunctional Ginger Nanofiber Hydrogels with Tunable Absorption: The Potential for Advanced Wound Dressing Applications, Biomacromolecules, 22 (2021) 3202-3215.
[49] C.H. Kim, J.W. Choi, H.J. Chun, K.S. Choi, Synthesis of chitosan derivatives with quaternary ammonium salt and their antibacterial activity, Polymer Bulletin, 38 (1997) 387-393.

CHAPTER 6 Conclusions and Future Work

6.1 Major Conclusions and Contributions

In this thesis work, different types of inter- and intra-molecular interactions inspired by the marine mussel biological system have been studied and orchestrated to functionalize protective coatings and adhesive hydrogels for environmental and biomedical applications. The correlated interaction mechanisms regarding the working function of the developed coating and hydrogel materials have been investigated by the surface force measurement using the drop and colloidal probe AFM techniques. The major conclusions and original contributions are listed below:

(I) A facile and scalable PDA-PAA-PMTAC coating was successfully fabricated and applied for membrane filtration of O/W emulsions protected with different surfactants via a tunable surface force-based strategy. The surface charge of the PDA-PAA-PMTAC coating could be adjusted by the solution pH mainly due to the protonation/deprotonation of carboxylic groups on the coating surface. The results from the surface force measurements indicate that altering the solution pH leads to the positively or negatively charged coating surface, and strong electrostatic repulsion was measured between the CTAB or SDS-stabilized toluene droplets and the polymer coating, respectively. Hence, the attachment behavior of the toluene droplets was prevented on the coating surface, suggesting good antifouling performance. The oil/water separation performance tests using the PDA-PAA-PMTAC-coated membrane demonstrate that the water permeability was significantly influenced by solution pH. An exceptional separation performance was achieved with the filtration water flux over 3000 L m^{-2} h^{-1} bar^{-1} for both the CTAB-stabilized emulsions at pH 4 and SDS-stabilized emulsion at pH 10 with the separation efficiency > 99.8 %. Moreover, the functionalized membrane contaminated by emulsion drops

could be readily regenerated through immersion in 1 mM NaCl solution of suitable pH, indicating a superior reusability. This work improves the fundamental understanding of the surface interaction mechanisms associated with the fouling and antifouling issues in emulsion-related water treatment, and provides useful insights into the development of regenerable functional membrane surfaces with tunable surface interactions for various environmental applications such as oil/water separation.

(II) A novel underwater adhesive hydrogel was developed by mimicking the structure of mussel byssus cuticle. The hydrogel is engineered with a soft armour-like hydrophobic adhesive layer outside the hydrophilic hydrogel matrix by modulating iron-chelation of polydopamine (PDA) and sodium dodecyl sulfate (SDS). By leveraging this unique soft armour-like architecture, the developed hydrogels exhibited instant and robust adhesion to various biological tissues via hydrophobic shell-induced rapid drainage as well as on-demand detachment via UV curing to trigger the transition of Fe^{3+}/Fe^{2+}. When applied as the sealant materials to the broken tissue, the developed DISC-40 exhibited a great resistance to the water penetration, even under high hydraulic pressure of ~ 975 mmHg. Meanwhile, the underwater adhesive hydrogel with high water content of 86.7 wt.% and exceptional biocompatibility could perform as the tissue couplant for ultrasound imaging, showing great impedance match with biological tissues and superior imaging quality for diagnosis in the wet intraoral environment. Taken together, the results demonstrated the remarkable merits of the as-prepared underwater adhesive hydrogel for practical applications as the bridging interface connecting human and medical apparatuses to support the in-vivo diagnosis and related clinical applications.

(III) An ultra stretchable, elastic, self-healing, and antimicrobial hydrogel ionic conductor was developed. The as-developed (AM-Hb3/CM0.5) hydrogel is composed of a covalent PAM

network with crosslinked BAC/CTAC/C_{18} micelles containing multiple dynamic and reversible non-covalent interactions (e.g., hydrogen bonding, hydrophobic, π-π, and cation-π interactions). The resulting hydrogel exhibits excellent stretchability (over 1100% strain), elasticity (over 83% recovery from 1000% tensile strain), and reliable electrical and sensing performances. Moreover, the hydrogel ionic conductor was integrated with stimuli-responsive polymers to enable triggerable adhesion and on-demand removability for various substrates. Compared to inherently adhesive hydrogels, the P(AM-Hb3/CM0.5) possesses an environment-adaptive adhesive property with the assistance of pH-responsive polymers of Alginate or PAA as well as thermo-responsive polymers of F-127 or F-68 to achieve the stable attachment to and controllable detachment from the target substrates, which benefits the repositioning of fixed hydrogel sensors without causing damage to either the hydrogels or the attached surfaces. This work offers a promising strategy in constructing smart soft sensors, which holds great promises for the reliable, reproducible, and effective detection of body motion signals, which is critical for human health monitoring devices.

6.2 Future Work

(I) Although great antifouling performances of the superhydrophilic surfaces with tunable electrical properties have been achieved via the synergy of short-range hydration force and long-range electrostatic interactions. In practical applications, the unsatisfying mechanical strength of the soft polymer coating still limits the durability of the antifouling coating materials. One of the possible solutions is to incorporate solid support materials into the polymer coating to form a protective composite matrix which can greatly improve its resistance to the external forces. Another viable strategy is to design self-healing functions with the controllable release healing agent embedded in the coating layer and exposed to help the repair of the coating in response to

the external stimuli. These two strategies could be promising directions to improve the durability of antifouling coatings in practical applications.

(II) Although constructing hydrophobic surface over the hydrogel matrix significantly improves the wet adhesion capability of adhesive hydrogels. However, in this case, the cohesion failure always occurred during the detachment of the adhesives mainly due to the surface layer having a denser structure and catechol moieties being concentrated at the contact interface of adhesive and substrates. One of the viable solutions is to incorporate another type of dynamic bond that would not be affected by the metal coordination chemistry and support the cohesion strength of the hydrogel to dissipate energy and further improve the adhesion strength of the hydrogel. Precise design of the materials chemistry and the investigation of the corresponding intramolecular interactions are required to advance this soft armour-like layer-protected hydrogel system.

(III) Although great mechanical and sensing performances were achieved by incorporating multiple dynamic and reversible non-covalent interactions (hydrogen bonding, hydrophobic, π-π, and cation-π interactions) into the conductive hydrogels. The sensitivity within the range of 0-100% strain is not sufficient enough to deliver the signal of some subtle body signals such as sound waves and pulses. One of the potential solutions is to add electronic conductive materials into the ionic conductive polymer matrix. By combing electronic and ionic conductive materials in the hydrogel system, the conductivity and sensitivity could be further improved.

Bibliography

[1] A. Mahdavi, L. Ferreira, C. Sundback, J.W. Nichol, E.P. Chan, D.J. Carter, C.J. Bettinger, S. Patanavanich, L. Chignozha, E. Ben-Joseph, A biodegradable and biocompatible gecko-inspired tissue adhesive, Proceedings of the National Academy of Sciences, 105 (2008) 2307-2312.
[2] M.P. Murphy, B. Aksak, M. Sitti, Gecko - inspired directional and controllable adhesion, Small, 5 (2009) 170-175.
[3] H. Zhao, Q. Sun, X. Deng, J. Cui, Earthworm - Inspired Rough Polymer Coatings with Self - Replenishing Lubrication for Adaptive Friction - Reduction and Antifouling Surfaces, Advanced Materials, 30 (2018) 1802141.
[4] Y.-T. Cheng, D.E. Rodak, Is the lotus leaf superhydrophobic?, Applied physics letters, 86 (2005) 144101.
[5] H.J. Ensikat, P. Ditsche-Kuru, C. Neinhuis, W. Barthlott, Superhydrophobicity in perfection: the outstanding properties of the lotus leaf, Beilstein journal of nanotechnology, 2 (2011) 152-161.
[6] S.S. Latthe, C. Terashima, K. Nakata, A. Fujishima, Superhydrophobic surfaces developed by mimicking hierarchical surface morphology of lotus leaf, Molecules, 19 (2014) 4256-4283.
[7] T. Lefèvre, M. Auger, Spider silk inspired materials and sustainability: perspective, Materials Technology, 31 (2016) 384-399.
[8] J.H. Waiter, Reverse engineering of bioadhesion in marine mussels, Annals of the New York Academy of Sciences, 875 (1999) 301-309.
[9] L. Li, H. Zeng, Marine mussel adhesion and bio-inspired wet adhesives, Biotribology, 5 (2016) 44-51.
[10] B.P. Lee, P.B. Messersmith, J.N. Israelachvili, J.H. Waite, Mussel-inspired adhesives and coatings, Annual review of materials research, 41 (2011) 99-132.
[11] M. Yu, J. Hwang, T.J. Deming, Role of L-3, 4-dihydroxyphenylalanine in mussel adhesive proteins, Journal of the American Chemical Society, 121 (1999) 5825-5826.
[12] J. Yu, Y. Kan, M. Rapp, E. Danner, W. Wei, S. Das, D.R. Miller, Y. Chen, J.H. Waite, J.N. Israelachvili, Adaptive hydrophobic and hydrophilic interactions of mussel foot proteins with organic thin films, Proceedings of the National Academy of Sciences, 110 (2013) 15680-15685.
[13] H. Zeng, D.S. Hwang, J.N. Israelachvili, J.H. Waite, Strong reversible Fe3+-mediated bridging between dopa-containing protein films in water, Proceedings of the National Academy of Sciences, 107 (2010) 12850-12853.
[14] H.C. Yang, M.B. Wu, Y.J. Li, Y.F. Chen, L.S. Wan, Z.K. Xu, Effects of polyethyleneimine molecular weight and proportion on the membrane hydrophilization by codepositing with dopamine, Journal of Applied Polymer Science, 133 (2016).
[15] W.-Z. Qiu, H.-C. Yang, Z.-K. Xu, Dopamine-assisted co-deposition: an emerging and promising strategy for surface modification, Advances in colloid and interface science, 256 (2018) 111-125.
[16] Q. Lu, D.X. Oh, Y. Lee, Y. Jho, D.S. Hwang, H. Zeng, Nanomechanics of cation–π interactions in aqueous solution, Angewandte Chemie, 125 (2013) 4036-4040.
[17] L. Xiang, J. Zhang, W. Wang, L. Gong, L. Zhang, B. Yan, H. Zeng, Nanomechanics of π-cation-π interaction with implications for bio-inspired wet adhesion, Acta Biomaterialia, 117 (2020) 294-301.

[18] H. Lee, S.M. Dellatore, W.M. Miller, P.B. Messersmith, Mussel-inspired surface chemistry for multifunctional coatings, science, 318 (2007) 426-430.
[19] J. Jiang, L. Zhu, L. Zhu, H. Zhang, B. Zhu, Y. Xu, Antifouling and antimicrobial polymer membranes based on bioinspired polydopamine and strong hydrogen-bonded poly (N-vinyl pyrrolidone), ACS applied materials & interfaces, 5 (2013) 12895-12904.
[20] C. Zhao, F. Zuo, Z. Liao, Z. Qin, S. Du, Z. Zhao, Mussel-Inspired One-Pot Synthesis of a Fluorescent and Water-Soluble Polydopamine–Polyethyleneimine Copolymer, Macromolecular rapid communications, 36 (2015) 909-915.
[21] W.-Z. Qiu, H.-C. Yang, L.-S. Wan, Z.-K. Xu, Co-deposition of catechol/polyethyleneimine on porous membranes for efficient decolorization of dye water, Journal of Materials Chemistry A, 3 (2015) 14438-14444.
[22] C. Zhang, M.-Q. Ma, T.-T. Chen, H. Zhang, D.-F. Hu, B.-H. Wu, J. Ji, Z.-K. Xu, Dopamine-Triggered One-Step Polymerization and Codeposition of Acrylate Monomers for Functional Coatings, ACS applied materials & interfaces, 9 (2017) 34356-34366.
[23] M. Pan, L. Gong, L. Xiang, W. Yang, W. Wang, L. Zhang, W. Hu, L. Han, H. Zeng, Modulating surface interactions for regenerable separation of oil-in-water emulsions, Journal of Membrane Science, 625 (2021) 119140.
[24] W. Yang, W. Hu, J. Zhang, W. Wang, R. Cai, M. Pan, C. Huang, X. Chen, B. Yan, H. Zeng, Tannic acid/Fe3+ functionalized magnetic graphene oxide nanocomposite with high loading of silver nanoparticles as ultra-efficient catalyst and disinfectant for wastewater treatment, Chemical Engineering Journal, 405 (2021) 126629.
[25] G.P. Maier, M.V. Rapp, J.H. Waite, J.N. Israelachvili, A. Butler, Adaptive synergy between catechol and lysine promotes wet adhesion by surface salt displacement, Science, 349 (2015) 628-632.
[26] M. Pan, K.-C.T. Nguyen, W. Yang, X. Liu, X.-Z. Chen, P.W. Major, L.H. Le, H. Zeng, Soft armour-like layer-protected hydrogels for wet tissue adhesion and biological imaging, Chemical Engineering Journal, 434 (2022) 134418.
[27] L. Han, X. Lu, K. Liu, K. Wang, L. Fang, L.-T. Weng, H. Zhang, Y. Tang, F. Ren, C. Zhao, Mussel-inspired adhesive and tough hydrogel based on nanoclay confined dopamine polymerization, ACS nano, 11 (2017) 2561-2574.
[28] M.S. Kang, B. Chun, S.S. Kim, Surface modification of polypropylene membrane by low-temperature plasma treatment, Journal of applied polymer science, 81 (2001) 1555-1566.
[29] U. König, M. Nitschke, A. Menning, G. Eberth, M. Pilz, C. Arnhold, F. Simon, G. Adam, C. Werner, Durable surface modification of poly (tetrafluoroethylene) by low pressure H2O plasma treatment followed by acrylic acid graft polymerization, Colloids and Surfaces B: Biointerfaces, 24 (2002) 63-71.
[30] P. Luan, V.S.K. Kondeti, A.J. Knoll, P.J. Bruggeman, G.S. Oehrlein, Effect of water vapor on plasma processing at atmospheric pressure: Polymer etching and surface modification by an Ar/H2O plasma jet, Journal of Vacuum Science & Technology A: Vacuum, Surfaces, and Films, 37 (2019) 031305.
[31] M. Gupta, K.K. Gleason, Surface modification of high aspect ratio structures with fluoropolymer coatings using chemical vapor deposition, Thin Solid Films, 517 (2009) 3547-3550.
[32] N. Chen, D.H. Kim, P. Kovacik, H. Sojoudi, M. Wang, K.K. Gleason, Polymer thin films and surface modification by chemical vapor deposition: Recent progress, Annual review of chemical and biomolecular engineering, 7 (2016) 373-393.

[33] D. Lee, S. Yang, Surface modification of PDMS by atmospheric-pressure plasma-enhanced chemical vapor deposition and analysis of long-lasting surface hydrophilicity, Sensors and Actuators B: Chemical, 162 (2012) 425-434.
[34] C. Haensch, S. Hoeppener, U.S. Schubert, Chemical modification of self-assembled silane based monolayers by surface reactions, Chemical Society Reviews, 39 (2010) 2323-2334.
[35] C. Zhang, Y. Ou, W.X. Lei, L.S. Wan, J. Ji, Z.K. Xu, CuSO4/H2O2 - induced rapid deposition of polydopamine coatings with high uniformity and enhanced stability, Angewandte Chemie International Edition, 55 (2016) 3054-3057.
[36] A. Aliano, G. Cicero, H. Nili, N.G. Green, P. Garcıa-Sánchez, A. Ramos, A. Lenshof, T. Laurell, A. Qi, P. Chan, AFM, tapping mode, Encyclopedia of Nanotechnology, 99-99.
[37] Bruker, Bruker ICON3 AFM (Tapping Mode) Instruction, 2015.
[38] L. Gong, X. Qiu, L. Zhang, J. Huang, W. Hu, L. Xiang, D. Zhu, R. Sabbagh, M. Mahmoudi, V. Fattahpour, Probing the Interaction Mechanism between Oil-in-Water Emulsions and Electroless Nickel–Phosphorus Coating with Implications for Antifouling in Oil Production, Energy & Fuels, (2018).
[39] L. Zhang, L. Xie, C. Shi, J. Huang, Q. Liu, H. Zeng, Mechanistic Understanding of Asphaltene Surface Interactions in Aqueous Media, Energy & Fuels, 31 (2016) 3348-3357.
[40] C. Shi, L. Zhang, L. Xie, X. Lu, Q. Liu, J. He, C.A. Mantilla, F.G. Van den Berg, H. Zeng, Surface interaction of water-in-oil emulsion droplets with interfacially active asphaltenes, Langmuir, 33 (2017) 1265-1274.
[41] L. Xie, C. Shi, X. Cui, H. Zeng, Surface forces and interaction mechanisms of emulsion drops and gas bubbles in complex fluids, Langmuir, 33 (2017) 3911-3925.
[42] J. Bibette, F. Leal-Calderon, Surfactant-stabilized emulsions, Current Opinion in Colloid & Interface Science, 1 (1996) 746-751.
[43] X. Zhu, A. Dudchenko, X. Gu, D. Jassby, Surfactant-stabilized oil separation from water using ultrafiltration and nanofiltration, Journal of membrane science, 529 (2017) 159-169.
[44] X. Su, H. Li, X. Lai, L. Zhang, X. Liao, J. Wang, Z. Chen, J. He, X. Zeng, Dual-functional superhydrophobic textiles with asymmetric roll-down/pinned states for water droplet transportation and oil–water separation, ACS applied materials & interfaces, 10 (2018) 4213-4221.
[45] L. Li, Z. Xu, W. Sun, J. Chen, C. Dai, B. Yan, H. Zeng, Bio-inspired membrane with adaptable wettability for smart oil/water separation, Journal of Membrane Science, 598 (2020) 117661.
[46] Y. Zhu, D. Wang, L. Jiang, J. Jin, Recent progress in developing advanced membranes for emulsified oil/water separation, NPG Asia materials, 6 (2014) e101.
[47] Z. Chu, Y. Feng, S. Seeger, Oil/water separation with selective superantiwetting/superwetting surface materials, Angewandte Chemie International Edition, 54 (2015) 2328-2338.
[48] C. Charcosset, Ultrafiltration, Microfiltration, Nanofiltration and Reverse Osmosis in Integrated Membrane Processes, Integrated Membrane Systems and Processes, (2015) 1.
[49] T. Jin, J. Song, J. Zhu, L.D. Nghiem, B. Zhao, X.-M. Li, T. He, The role of the surfactant sodium dodecyl sulfate to dynamically reduce mass transfer resistance of SPEEK coated membrane for oil-in-water emulsion treatment, Journal of Membrane Science, 541 (2017) 9-18.
[50] Z. Yin, R.J.E. Yeow, Y. Ma, J.W. Chew, Link between interfacial interaction and membrane fouling during organic solvent ultrafiltration of colloidal foulants, Journal of Membrane Science, 611 (2020) 118369.

[51] K. Wang, X. Liu, Y. Tan, W. Zhang, S. Zhang, J. Li, Two-dimensional membrane and three-dimensional bulk aerogel materials via top-down wood nanotechnology for multibehavioral and reusable oil/water separation, Chemical Engineering Journal, 371 (2019) 769-780.
[52] M. Ge, C. Cao, J. Huang, X. Zhang, Y. Tang, X. Zhou, K. Zhang, Z. Chen, Y. Lai, Rational design of materials interface at nanoscale towards intelligent oil–water separation, Nanoscale Horizons, 3 (2018) 235-260.
[53] L. Tan, N. Han, Y. Qian, H. Zhang, H. Gao, L. Zhang, X. Zhang, Superhydrophilic and underwater superoleophobic poly (acrylonitrile-co-methyl acrylate) membrane for highly efficient separation of oil-in-water emulsions, Journal of Membrane Science, 564 (2018) 712-721.
[54] N. Shahkaramipour, A. Jafari, T. Tran, C.M. Stafford, C. Cheng, H. Lin, Maximizing the grafting of zwitterions onto the surface of ultrafiltration membranes to improve antifouling properties, Journal of Membrane Science, 601 (2020) 117909.
[55] Y.-M. Lin, G.C. Rutledge, Separation of oil-in-water emulsions stabilized by different types of surfactants using electrospun fiber membranes, Journal of membrane science, 563 (2018) 247-258.
[56] M.B. Tanis-Kanbur, S. Velioğlu, H.J. Tanudjaja, X. Hu, J.W. Chew, Understanding membrane fouling by oil-in-water emulsion via experiments and molecular dynamics simulations, Journal of Membrane Science, 566 (2018) 140-150.
[57] L. Gong, X. Qiu, L. Zhang, J. Huang, W. Hu, L. Xiang, D. Zhu, R. Sabbagh, M. Mahmoudi, V. Fattahpour, Probing the Interaction Mechanism between Oil-in-Water Emulsions and Electroless Nickel–Phosphorus Coating with Implications for Antifouling in Oil Production, Energy & Fuels, 33 (2018) 3764-3775.
[58] W. Zhang, Y. Zhu, X. Liu, D. Wang, J. Li, L. Jiang, J. Jin, Salt‐induced fabrication of superhydrophilic and underwater superoleophobic PAA‐g‐PVDF membranes for effective separation of oil‐in‐water emulsions, Angewandte Chemie International Edition, 53 (2014) 856-860.
[59] C. Shi, B. Yan, L. Xie, L. Zhang, J. Wang, A. Takahara, H. Zeng, Long‐Range Hydrophilic Attraction between Water and Polyelectrolyte Surfaces in Oil, Angewandte Chemie International Edition, 55 (2016) 15017-15021.
[60] T. Wang, Y.-Q. Wang, Y.-L. Su, Z.-Y. Jiang, Antifouling ultrafiltration membrane composed of polyethersulfone and sulfobetaine copolymer, Journal of membrane science, 280 (2006) 343-350.
[61] J. Wu, W. Wei, S. Li, Q. Zhong, F. Liu, J. Zheng, J. Wang, The effect of membrane surface charges on demulsification and fouling resistance during emulsion separation, Journal of membrane science, 563 (2018) 126-133.
[62] J. Gu, P. Xiao, J. Chen, J. Zhang, Y. Huang, T. Chen, Janus polymer/carbon nanotube hybrid membranes for oil/water separation, ACS applied materials & interfaces, 6 (2014) 16204-16209.
[63] X. Chen, L. Hong, Y. Xu, Z.W. Ong, Ceramic pore channels with inducted carbon nanotubes for removing oil from water, ACS applied materials & interfaces, 4 (2012) 1909-1918.
[64] Y. Zhu, F. Zhang, D. Wang, X.F. Pei, W. Zhang, J. Jin, A novel zwitterionic polyelectrolyte grafted PVDF membrane for thoroughly separating oil from water with ultrahigh efficiency, Journal of Materials Chemistry A, 1 (2013) 5758-5765.

[65] J. Zhang, L. Zhang, X. Cui, L. Gong, L. Xiang, C. Shi, W. Hu, H. Zeng, Scalable polyzwitterion–polydopamine coating for regenerable oil/water separation and underwater self-cleaning of stubborn heavy oil fouling without pre-hydration, Chemical communications, 54 (2018) 9734-9737.
[66] Y. Bie, J. Yang, X. Liu, J. Wang, Y. Nuli, W. Lu, Polydopamine wrapping silicon cross-linked with polyacrylic acid as high-performance anode for lithium-ion batteries, ACS applied materials & interfaces, 8 (2016) 2899-2904.
[67] J.-J. Li, Y.-N. Zhou, Z.-H. Luo, Mussel-inspired V-shaped copolymer coating for intelligent oil/water separation, Chemical Engineering Journal, 322 (2017) 693-701.
[68] Y. Chen, Y. Qiu, Q. Wang, D. Li, T. Hussain, H. Ke, Q. Wei, Mussel-inspired sandwich-like nanofibers/hydrogel composite with super adhesive, sustained drug release and anti-infection capacity, Chemical Engineering Journal, (2020) 125668.
[69] H.-M. Song, C. Chen, X.-X. Shui, H. Yang, L.-J. Zhu, Z.-X. Zeng, Q.-J. Xue, Asymmetric Janus membranes based on in situ mussel-inspired chemistry for efficient oil/water separation, Journal of Membrane Science, 573 (2019) 126-134.
[70] L. Zhang, M. Zhang, J. Lu, A. Tang, L. Zhu, Highly permeable thin-film nanocomposite membranes embedded with PDA/PEG nanocapsules as water transport channels, Journal of Membrane Science, 586 (2019) 115-121.
[71] L. Han, L. Xiang, J. Zhang, J. Chen, J. Liu, B. Yan, H. Zeng, Biomimetic Lubrication and Surface Interactions of Dopamine-Assisted Zwitterionic Polyelectrolyte Coatings, Langmuir, 34 (2018) 11593-11601.
[72] L. Han, L. Gong, J. Chen, J. Zhang, L. Xiang, L. Zhang, Q. Wang, B. Yan, H. Zeng, Universal Mussel-Inspired Ultrastable Surface-Anchoring Strategy via Adaptive Synergy of Catechol and Cations, ACS applied materials & interfaces, 10 (2018) 2166-2173.
[73] Y. Zhao, X. Yang, L. Yan, Y. Bai, S. Li, P. Sorokin, L. Shao, Biomimetic nanoparticle-engineered superwettable membranes for efficient oil/water separation, Journal of Membrane Science, 618 118525.
[74] J.-H. Jiang, L.-P. Zhu, X.-L. Li, Y.-Y. Xu, B.-K. Zhu, Surface modification of PE porous membranes based on the strong adhesion of polydopamine and covalent immobilization of heparin, Journal of Membrane Science, 364 (2010) 194-202.
[75] C. Shi, L. Xie, L. Zhang, X. Lu, H. Zeng, Probing the interaction mechanism between oil droplets with asphaltenes and solid surfaces using AFM, Journal of colloid and interface science, 558 (2019) 173-181.
[76] L. Zhang, L. Xie, X. Cui, J. Chen, H. Zeng, Intermolecular and surface forces at solid/oil/water/gas interfaces in petroleum production, Journal of colloid and interface science, 537 (2019) 505-519.
[77] J.L. Hutter, J. Bechhoefer, Calibration of atomic - force microscope tips, Review of Scientific Instruments, 64 (1993) 1868-1873.
[78] D.Y. Chan, E. Klaseboer, R. Manica, Theory of non-equilibrium force measurements involving deformable drops and bubbles, Advances in colloid and interface science, 165 (2011) 70-90.
[79] W.J. Yang, D. Pranantyo, K.-G. Neoh, E.-T. Kang, S.L.-M. Teo, D. Rittschof, Layer-by-layer click deposition of functional polymer coatings for combating marine biofouling, Biomacromolecules, 13 (2012) 2769-2780.

[80] H. Luo, C. Gu, W. Zheng, F. Dai, X. Wang, Z. Zheng, Facile synthesis of novel size-controlled antibacterial hybrid spheres using silver nanoparticles loaded with poly-dopamine spheres, RSC Advances, 5 (2015) 13470-13477.
[81] J.D. Anastassopoulou, Mass and FT-IR spectra of quaternary ammonium surfactants, in: Chemistry and Properties of Biomolecular Systems, Springer, 1991, pp. 1-9.
[82] Y. Maréchal, IR spectra of carboxylic acids in the gas phase: A quantitative reinvestigation, The Journal of chemical physics, 87 (1987) 6344-6353.
[83] M. Schmitt, H. Stark, Active Brownian motion of emulsion droplets: Coarsening dynamics at the interface and rotational diffusion, The European Physical Journal E, 39 (2016) 80.
[84] J. Ge, D. Zong, Q. Jin, J. Yu, B. Ding, Biomimetic and Superwettable Nanofibrous Skins for Highly Efficient Separation of Oil - in - Water Emulsions, Advanced Functional Materials, 28 (2018) 1705051.
[85] H. Shi, Y. He, Y. Pan, H. Di, G. Zeng, L. Zhang, C. Zhang, A modified mussel-inspired method to fabricate TiO2 decorated superhydrophilic PVDF membrane for oil/water separation, Journal of membrane science, 506 (2016) 60-70.
[86] Y. Zhu, J. Wang, F. Zhang, S. Gao, A. Wang, W. Fang, J. Jin, Zwitterionic Nanohydrogel Grafted PVDF Membranes with Comprehensive Antifouling Property and Superior Cycle Stability for Oil - in - Water Emulsion Separation, Advanced Functional Materials, 28 (2018) 1804121.
[87] R.B. Viana, A.B. da Silva, A.S. Pimentel, Infrared spectroscopy of anionic, cationic, and zwitterionic surfactants, Advances in physical chemistry, 2012 (2012).
[88] L. Li, B. Yan, J. Yang, L. Chen, H. Zeng, Novel mussel - inspired injectable self - healing hydrogel with anti - biofouling property, Advanced Materials, 27 (2015) 1294-1299.
[89] C. Wang, C. Lin, R. Ming, X. Li, P. Jonkheijm, M. Cheng, F. Shi, Macroscopic Supramolecular Assembly Strategy to Construct 3D Biocompatible Microenvironments with Site-Selective Cell Adhesion, ACS Applied Materials & Interfaces, (2021).
[90] Y. Gao, K. Peng, S. Mitragotri, Covalently Crosslinked Hydrogels via Step - Growth Reactions: Crosslinking Chemistries, Polymers, and Clinical Impact, Advanced Materials, (2021) 2006362.
[91] X. Yu, X. Wang, D. Li, R. Sheng, Y. Qian, R. Zhu, X. Wang, K. Lin, Mechanically reinforced injectable bioactive nanocomposite hydrogels for in-situ bone regeneration, Chemical Engineering Journal, (2021) 132799.
[92] X. Zhang, Y. Li, D. He, Z. Ma, K. Liu, K. Xue, H. Li, An effective strategy for preparing macroporous and self-healing bioactive hydrogels for cell delivery and wound healing, Chemical Engineering Journal, (2021) 130677.
[93] B. Kong, L. Sun, R. Liu, Y. Chen, Y. Shang, H. Tan, Y. Zhao, L. Sun, Recombinant human collagen hydrogels with hierarchically ordered microstructures for corneal stroma regeneration, Chemical Engineering Journal, 428 (2022) 131012.
[94] Y. Liu, R. Guo, T. Wu, Y. Lyu, M. Xiao, B. He, G. Fan, J. Yang, W. Liu, One zwitterionic injectable hydrogel with ion conductivity enables efficient restoration of cardiac function after myocardial infarction, Chemical Engineering Journal, 418 (2021) 129352.
[95] L. Zhang, L. Chen, Y. Xiang, Z. Liu, X. Mao, L. Zhang, L. Deng, Y. Zhang, L. Cheng, X. Sun, Multifunctional integrally-medicalized hydrogel system with internal synergy for efficient tissue regeneration, Chemical Engineering Journal, 406 (2021) 126839.
[96] P. Liu, Y. Xiong, L. Chen, C. Lin, Y. Yang, Z. Lin, Y. Yu, B. Mi, G. Liu, X. Xiao, Angiogenesis-Based Diabetic Skin Reconstruction through Multifunctional Hydrogel with

Sustained Releasing of M2 Macrophage-derived Exosome, Chemical Engineering Journal, (2021) 132413.
[97] J. Zhang, W. Xin, Y. Qin, Y. Hong, Z. Xiahou, K. Zhang, P. Fu, J. Yin, "All-in-one" Zwitterionic Granular Hydrogel Bioink for Stem Cell Spheroids Production and 3D Bioprinting, Chemical Engineering Journal, (2021) 132713.
[98] F. Xu, A. Lam, Z. Pan, G. Randhawa, M. Lamb, H. Sheardown, T. Hoare, Fast Thermoresponsive Poly (oligoethylene glycol methacrylate)(POEGMA)-Based Nanostructured Hydrogels for Reversible Tuning of Cell Interactions, ACS Biomaterials Science & Engineering, (2021).
[99] K. Yamagishi, I. Kirino, I. Takahashi, H. Amano, S. Takeoka, Y. Morimoto, T. Fujie, Tissue-adhesive wirelessly powered optoelectronic device for metronomic photodynamic cancer therapy, Nature biomedical engineering, 3 (2019) 27-36.
[100] S. Zhu, Y. Ying, Q. Wu, Z. Ni, Z. Huang, P. Cai, Y. Tu, W. Ying, J. Ye, R. Zhang, Alginate self-adhesive hydrogel combined with dental pulp stem cells and FGF21 repairs hemisection spinal cord injury via apoptosis and autophagy mechanisms, Chemical Engineering Journal, (2021) 130827.
[101] J.S. Lee, Y.S. Choi, J.S. Lee, E.J. Jeon, S. An, M.S. Lee, H.S. Yang, S.-W. Cho, Mechanically-reinforced and highly adhesive decellularized tissue-derived hydrogel for efficient tissue repair, Chemical Engineering Journal, 427 (2022) 130926.
[102] M. Li, Y. Liang, Y. Liang, G. Pan, B. Guo, Injectable stretchable self-healing dual dynamic network hydrogel as adhesive anti-oxidant wound dressing for photothermal clearance of bacteria and promoting wound healing of MRSA infected motion wounds, Chemical Engineering Journal, 427 (2022) 132039.
[103] K.-a. Johnson, N. Muzzin, S. Toufanian, R.A. Slick, M.W. Lawlor, B. Seifried, P. Moquin, D. Latulippe, T. Hoare, Drug-impregnated, pressurized gas expanded liquid-processed alginate hydrogel scaffolds for accelerated burn wound healing, Acta Biomaterialia, 112 (2020) 101-111.
[104] J. Liu, H. Wang, R. Ou, X. Yi, T. Liu, Z. Liu, Q. Wang, Anti-bacterial silk-based hydrogels for multifunctional electrical skin with mechanical-thermal dual sensitive integration, Chemical Engineering Journal, (2021) 130722.
[105] X. Zhang, Y. Zhang, W. Zhang, Y. Dai, F. Xia, Gold nanoparticles-deranged double network for Janus adhesive-tough hydrogel as strain sensor, Chemical Engineering Journal, (2021) 130447.
[106] J. Li, D.J. Mooney, Designing hydrogels for controlled drug delivery, Nature Reviews Materials, 1 (2016) 1-17.
[107] G. Zhang, Y. Chen, Y. Deng, T. Ngai, C. Wang, Dynamic supramolecular hydrogels: regulating hydrogel properties through self-complementary quadruple hydrogen bonds and thermo-switch, ACS Macro Letters, 6 (2017) 641-646.
[108] A. Yu, Y. Hu, X. Ma, L. Mo, M. Pan, X. Bi, Y. Wu, J. Wang, X. Li, Sequential drug release of co-assembled supramolecular hydrogel as synergistic therapy against Staphylococcus aureus endophthalmitis, Chemical Engineering Journal, 427 (2022) 130979.
[109] Y. Gao, Y. Hao, W. Zhang, Y. Wei, Y. Shu, J. Wang, Microwave-triggered ionic liquid-based hydrogel dressing with excellent hyperthermia and transdermal drug delivery performance, Chemical Engineering Journal, 429 (2022) 131590.
[110] J. Yang, R. Bai, Z. Suo, Topological adhesion of wet materials, Advanced Materials, 30 (2018) 1800671.

[111] H. Cui, W. Wang, L. Shi, W. Song, S. Wang, Superwettable Surface Engineering in Controlling Cell Adhesion for Emerging Bioapplications, Small Methods, 4 (2020) 2000573.
[112] S.H. Hong, M. Shin, E. Park, J.H. Ryu, J.A. Burdick, H. Lee, Alginate‐boronic acid: pH‐triggered bioinspired glue for hydrogel assembly, Advanced Functional Materials, 30 (2020) 1908497.
[113] S.-H. Lin, C.M. Papadakis, J.-J. Kang, J.-M. Lin, S.-h. Hsu, Injectable Phenolic-Chitosan Self-Healing Hydrogel with Hierarchical Micelle Architectures and Fast Adhesiveness, Chemistry of Materials, (2021).
[114] J. Li, A. Celiz, J. Yang, Q. Yang, I. Wamala, W. Whyte, B. Seo, N. Vasilyev, J. Vlassak, Z. Suo, Tough adhesives for diverse wet surfaces, Science, 357 (2017) 378-381.
[115] X. Wan, Z. Gu, F. Zhang, D. Hao, X. Liu, B. Dai, Y. Song, S. Wang, Asymmetric Janus adhesive tape prepared by interfacial hydrosilylation for wet/dry amphibious adhesion, NPG Asia Materials, 11 (2019) 1-9.
[116] D.H. Sierra, Fibrin sealant adhesive systems: a review of their chemistry, material properties and clinical applications, Journal of biomaterials applications, 7 (1993) 309-352.
[117] J. Jiao, F. Zhang, T. Jiao, Z. Gu, S. Wang, Bioinspired Superdurable Pestle‐Loop Mechanical Interlocker with Tunable Peeling Force, Strong Shear Adhesion, and Low Noise, Advanced Science, 5 (2018) 1700787.
[118] X. Chen, H. Yuk, J. Wu, C.S. Nabzdyk, X. Zhao, Instant tough bioadhesive with triggerable benign detachment, Proceedings of the National Academy of Sciences, 117 (2020) 15497-15503.
[119] Y. Chen, J. Meng, Z. Gu, X. Wan, L. Jiang, S. Wang, Bioinspired multiscale wet adhesive surfaces: structures and controlled adhesion, Advanced Functional Materials, 30 (2020) 1905287.
[120] Y. Zhang, S. Ma, B. Li, B. Yu, H. Lee, M. Cai, S.N. Gorb, F. Zhou, W. Liu, Gecko's Feet-Inspired Self-Peeling Switchable Dry/Wet Adhesive, Chemistry of Materials, 33 (2021) 2785-2795.
[121] B.K. Ahn, S. Das, R. Linstadt, Y. Kaufman, N.R. Martinez-Rodriguez, R. Mirshafian, E. Kesselman, Y. Talmon, B.H. Lipshutz, J.N. Israelachvili, High-performance mussel-inspired adhesives of reduced complexity, Nature communications, 6 (2015) 1-7.
[122] M.A. Gebbie, W. Wei, A.M. Schrader, T.R. Cristiani, H.A. Dobbs, M. Idso, B.F. Chmelka, J.H. Waite, J.N. Israelachvili, Tuning underwater adhesion with cation–π interactions, Nature chemistry, 9 (2017) 473-479.
[123] J. Zhang, L. Xiang, B. Yan, H. Zeng, Nanomechanics of Anion− Π Interaction in Aqueous Solution, Journal of the American Chemical Society, 142 (2020) 1710-1714.
[124] S. Lu, X. Zhang, Z. Tang, H. Xiao, M. Zhang, K. Liu, L. Chen, L. Huang, Y. Ni, H. Wu, Mussel-inspired blue-light-activated cellulose-based adhesive hydrogel with fast gelation, rapid haemostasis and antibacterial property for wound healing, Chemical Engineering Journal, 417 (2021) 129329.
[125] M. Suneetha, O.S. Moo, S.M. Choi, S. Zo, K.M. Rao, S.S. Han, Tissue-adhesive, stretchable, and self-healable hydrogels based on carboxymethyl cellulose-dopamine/PEDOT: PSS via mussel-inspired chemistry for bioelectronic applications, Chemical Engineering Journal, (2021) 130847.
[126] Q. Lu, D.S. Hwang, Y. Liu, H. Zeng, Molecular interactions of mussel protective coating protein, mcfp-1, from Mytilus californianus, Biomaterials, 33 (2012) 1903-1911.

[127] S. Kim, J. Huang, Y. Lee, S. Dutta, H.Y. Yoo, Y.M. Jung, Y. Jho, H. Zeng, D.S. Hwang, Complexation and coacervation of like-charged polyelectrolytes inspired by mussels, Proceedings of the National Academy of Sciences, 113 (2016) E847-E853.
[128] B. Yan, J. Huang, L. Han, L. Gong, L. Li, J.N. Israelachvili, H. Zeng, Duplicating dynamic strain-stiffening behavior and nanomechanics of biological tissues in a synthetic self-healing flexible network hydrogel, ACS nano, 11 (2017) 11074-11081.
[129] W. Zhang, R. Wang, Z. Sun, X. Zhu, Q. Zhao, T. Zhang, A. Cholewinski, F.K. Yang, B. Zhao, R. Pinnaratip, Catechol-functionalized hydrogels: biomimetic design, adhesion mechanism, and biomedical applications, Chemical Society Reviews, 49 (2020) 433-464.
[130] R. Xu, Y. Wu, Y. Ma, Y. Zhang, S. Ma, M. Cai, F. Zhou, W. Liu, Synthesis of novel copolymer/Mn+ biomimetic adhesives based on temperature strengthened coacervation effect, Chemical Engineering Journal, 425 (2021) 127249.
[131] Y. Ma, B. Zhang, I. Frenkel, Z. Zhang, X. Pei, F. Zhou, X. He, Mussel-Inspired Underwater Adhesives-from Adhesion Mechanisms to Engineering Applications: A Critical Review, Reviews of Adhesion and Adhesives, 9 (2021) 167-188.
[132] M. Shan, C. Gong, B. Li, G. Wu, A pH, glucose, and dopamine triple-responsive, self-healable adhesive hydrogel formed by phenylborate–catechol complexation, Polymer Chemistry, 8 (2017) 2997-3005.
[133] P. Zhu, M. Hu, Y. Deng, C. Wang, One - pot fabrication of a novel agar - polyacrylamide/graphene oxide nanocomposite double network hydrogel with high mechanical properties, Advanced Engineering Materials, 18 (2016) 1799-1807.
[134] Y. Wang, K. Jia, C. Xiang, J. Yang, X. Yao, Z. Suo, Instant, tough, noncovalent adhesion, ACS applied materials & interfaces, 11 (2019) 40749-40757.
[135] J. Steck, J. Kim, J. Yang, S. Hassan, Z. Suo, Topological adhesion. I. Rapid and strong topohesives, Extreme Mechanics Letters, 39 (2020) 100803.
[136] J. Yang, R. Bai, B. Chen, Z. Suo, Hydrogel adhesion: A supramolecular synergy of chemistry, topology, and mechanics, Advanced Functional Materials, 30 (2020) 1901693.
[137] Z. Wang, L. Guo, H. Xiao, H. Cong, S. Wang, A reversible underwater glue based on photo-and thermo-responsive dynamic covalent bonds, Materials Horizons, 7 (2020) 282-288.
[138] H. Yuk, C.E. Varela, C.S. Nabzdyk, X. Mao, R.F. Padera, E.T. Roche, X. Zhao, Dry double-sided tape for adhesion of wet tissues and devices, Nature, 575 (2019) 169-174.
[139] H. Yuk, J. Wu, T.L. Sarrafian, X. Mao, C.E. Varela, E.T. Roche, L.G. Griffiths, C.S. Nabzdyk, X. Zhao, Rapid and coagulation-independent haemostatic sealing by a paste inspired by barnacle glue, Nature biomedical engineering, 5 (2021) 1131-+.
[140] Q. Liu, X. Lu, L. Li, H. Zhang, G. Liu, H. Zhong, H. Zeng, Probing the reversible Fe3+–DOPA-mediated bridging interaction in mussel foot protein-1, The Journal of Physical Chemistry C, 120 (2016) 21670-21677.
[141] F. Jehle, E. Macías-Sánchez, S. Sviben, P. Fratzl, L. Bertinetti, M.J. Harrington, Hierarchically-structured metalloprotein composite coatings biofabricated from co-existing condensed liquid phases, Nature communications, 11 (2020) 1-9.
[142] S. Hu, X. Pei, L. Duan, Z. Zhu, Y. Liu, J. Chen, T. Chen, P. Ji, Q. Wan, J. Wang, A mussel-inspired film for adhesion to wet buccal tissue and efficient buccal drug delivery, Nature communications, 12 (2021) 1-17.
[143] S.-H. Kim, K. Kim, B.S. Kim, Y.-H. An, U.-J. Lee, S.-H. Lee, S.L. Kim, B.-G. Kim, N.S. Hwang, Fabrication of polyphenol-incorporated anti-inflammatory hydrogel via high-affinity enzymatic crosslinking for wet tissue adhesion, Biomaterials, 242 (2020) 119905.

[144] L. Chen, G. Zeng, D. Guo, J. Liu, X. Zhang, S. Lin, K. Zhang, Soft elastic hydrogel couplants for ultrasonography, Materials Science and Engineering: C, 119 (2021) 111609.
[145] J. Yi, K.-C.T. Nguyen, W. Wang, W. Yang, M. Pan, E. Lou, P.W. Major, L.H. Le, H. Zeng, Polyacrylamide/Alginate double-network tough hydrogels for intraoral ultrasound imaging, Journal of colloid and interface science, 578 (2020) 598-607.
[146] S. Mitragotri, Sonophoresis: ultrasound-mediated transdermal drug delivery, in: Percutaneous Penetration Enhancers Physical Methods in Penetration Enhancement, Springer, 2017, pp. 3-14.
[147] K. Wu, N. Shardt, L. Laouar, J.A. Elliott, N.M. Jomha, Vitrification of particulated articular cartilage via calculated protocols, NPJ Regenerative medicine, 6 (2021) 1-13.
[148] L.H. Le, An investigation of pulse-timing techniques for broadband ultrasonic velocity determination in cancellous bone: a simulation study, Physics in Medicine & Biology, 43 (1998) 2295.
[149] C. Zhang, L.H. Le, R. Zheng, D. Ta, E. Lou, Measurements of ultrasonic phase velocities and attenuation of slow waves in cellular aluminum foams as cancellous bone-mimicking phantoms, The Journal of the Acoustical Society of America, 129 (2011) 3317-3326.
[150] X. Zhang, R. Zhang, S. Wu, Y. Sun, H. Yang, B. Lin, Physically and chemically dual-crosslinked hydrogels with superior mechanical properties and self-healing behavior, New Journal of Chemistry, 44 (2020) 9903-9911.
[151] Z. Jing, X. Dai, X. Xian, X. Du, M. Liao, P. Hong, Y. Li, Tough, stretchable and compressive alginate-based hydrogels achieved by non-covalent interactions, RSC Advances, 10 (2020) 23592-23606.
[152] L. Burlamacchi, A. Lai, M. Monduzzi, G. Saba, NMR, EPR, and INDO Studies on the Complexes of Dopamine with Cu2+, Mn2+, and Fe3+ in Aqueous Solution, Journal of Magnetic Resonance (1969), 55 (1983) 39-50.
[153] F. Talens-Alesson, S. Hall, N. Hankins, B. Azzopardi, Flocculation of SDS micelles with Fe3+, Colloids and Surfaces A: Physicochemical and Engineering Aspects, 204 (2002) 85-91.
[154] N. Anitha, M. Palaniandavar, Mononuclear iron (III) complexes of 3N ligands in organized assemblies: spectral and redox properties and attainment of regioselective extradiol dioxygenase activity, Dalton Transactions, 40 (2011) 1888-1901.
[155] P.-G. De Gennes, Wetting: statics and dynamics, Reviews of modern physics, 57 (1985) 827.
[156] L. Gong, J. Wang, L. Zhang, V. Fattahpour, M. Mamoudi, M. Roostaei, B. Fermaniuk, J.-L. Luo, H. Zeng, Fouling mechanisms of asphaltenes and fine solids on bare and electroless nickel-phosphorus coated carbon steel, Fuel, 252 (2019) 188-199.
[157] L. Gong, J. Wang, L. Xiang, J. Huang, V. Fattahpour, M. Roostaei, M. Mamoudi, B. Fermaniuk, J.-L. Luo, H. Zeng, Characterizing foulants on slotted liner and probing the surface interaction mechanisms in organic media with implication for an antifouling strategy in oil production, Fuel, 290 (2021) 120008.
[158] Y. Murakami, K. Nakamura, The chelating behavior of catechol-4-sulfonate with iron (III) ion, Bulletin of the Chemical Society of Japan, 36 (1963) 1408-1411.
[159] J.S. Haynes, J.R. Sams, R.C. Thompson, Synthesis and structural studies of iron (II) and iron (III) sulfonates, Canadian Journal of Chemistry, 59 (1981) 669-678.
[160] Z. Khan, S.A. AL-Thabaiti, S. Hussain, Nanoscale water soluble self-assembled zero-valent iron: role of stabilizers in their morphology, RSC advances, 6 (2016) 7267-7278.

[161] S. Zhuo, Y. Guan, H. Li, J. Fang, P. Zhang, J. Du, C. Zhu, Facile fabrication of fluorescent Fe-doped carbon quantum dots for dopamine sensing and bioimaging application, Analyst, 144 (2019) 656-662.
[162] H. Fan, J. Wang, Z. Tao, J. Huang, P. Rao, T. Kurokawa, J.P. Gong, Adjacent cationic–aromatic sequences yield strong electrostatic adhesion of hydrogels in seawater, Nature communications, 10 (2019) 1-8.
[163] J.N. Israelachvili, Intermolecular and surface forces, Academic press, 2015.
[164] L. Han, K. Liu, M. Wang, K. Wang, L. Fang, H. Chen, J. Zhou, X. Lu, Mussel-inspired adhesive and conductive hydrogel with long-lasting moisture and extreme temperature tolerance, Advanced Functional Materials, 28 (2018) 1704195.
[165] D. Gan, W. Xing, L. Jiang, J. Fang, C. Zhao, F. Ren, L. Fang, K. Wang, X. Lu, Plant-inspired adhesive and tough hydrogel based on Ag-Lignin nanoparticles-triggered dynamic redox catechol chemistry, Nature communications, 10 (2019) 1-10.
[166] C. Xie, X. Wang, H. He, Y. Ding, X. Lu, Mussel-inspired hydrogels for self-adhesive bioelectronics, Advanced Functional Materials, 30 (2020) 1909954.
[167] Z. Jia, J. Gong, Y. Zeng, J. Ran, J. Liu, K. Wang, C. Xie, X. Lu, J. Wang, Bioinspired Conductive Silk Microfiber Integrated Bioelectronic for Diagnosis and Wound Healing in Diabetes, Advanced Functional Materials, 31 (2021) 2010461.
[168] J.-P. Laulhère, A.-M. Labouré, J. Briat, Photoreduction and incorporation of iron into ferritins, Biochemical Journal, 269 (1990) 79-84.
[169] A. De Luca, R.F. Dantas, S. Esplugas, Study of Fe (III)-NTA chelates stability for applicability in photo-Fenton at neutral pH, Applied Catalysis B: Environmental, 179 (2015) 372-379.
[170] J.L. Daristotle, S.T. Zaki, L.W. Lau, L. Torres Jr, A. Zografos, P. Srinivasan, O.B. Ayyub, A.D. Sandler, P. Kofinas, Improving the adhesion, flexibility, and hemostatic efficacy of a sprayable polymer blend surgical sealant by incorporating silica particles, Acta biomaterialia, 90 (2019) 205-216.
[171] A. Assmann, A. Vegh, M. Ghasemi-Rad, S. Bagherifard, G. Cheng, E.S. Sani, G.U. Ruiz-Esparza, I. Noshadi, A.D. Lassaletta, S. Gangadharan, A highly adhesive and naturally derived sealant, Biomaterials, 140 (2017) 115-127.
[172] Y. Liu, H. Meng, Z. Qian, N. Fan, W. Choi, F. Zhao, B.P. Lee, A moldable nanocomposite hydrogel composed of a Mussel-inspired polymer and a nanosilicate as a fit-to-shape tissue sealant, Angewandte Chemie International Edition, 56 (2017) 4224-4228.
[173] Y. Bu, L. Zhang, G. Sun, F. Sun, J. Liu, F. Yang, P. Tang, D. Wu, Tetra-PEG based hydrogel sealants for in vivo visceral hemostasis, Advanced Materials, 31 (2019) 1901580.
[174] N. Alegret, A. Dominguez-Alfaro, D. Mecerreyes, 3D scaffolds based on conductive polymers for biomedical applications, Biomacromolecules, 20 (2018) 73-89.
[175] J. Chen, Q. Peng, T. Thundat, H. Zeng, Stretchable, injectable, and self-healing conductive hydrogel enabled by multiple hydrogen bonding toward wearable electronics, Chemistry of Materials, 31 (2019) 4553-4563.
[176] Z. Rao, F. Ershad, A. Almasri, L. Gonzalez, X. Wu, C. Yu, Soft electronics for the skin: from health monitors to human–machine interfaces, Advanced Materials Technologies, 5 (2020) 2000233.
[177] Y. Niu, H. Liu, R. He, Z. Li, H. Ren, B. Gao, H. Guo, G.M. Genin, F. Xu, The new generation of soft and wearable electronics for health monitoring in varying environment: From normal to extreme conditions, Materials Today, (2020).

[178] Q. Gui, Y. He, Y. Wang, Soft Electronics Based on Liquid Conductors, Advanced Electronic Materials, 7 (2021) 2000780.
[179] C. Chen, Y. Wang, T. Zhou, Z. Wan, Q. Yang, Z. Xu, D. Li, Y. Jin, Toward Strong and Tough Wood-Based Hydrogels for Sensors, Biomacromolecules, (2021).
[180] K. Ouyang, J. Zhuang, C. Chen, X. Wang, M. Xu, Z. Xu, Gradient Diffusion Anisotropic Carboxymethyl Cellulose Hydrogels for Strain Sensors, Biomacromolecules, (2021).
[181] S. De, T.M. Higgins, P.E. Lyons, E.M. Doherty, P.N. Nirmalraj, W.J. Blau, J.J. Boland, J.N. Coleman, Silver nanowire networks as flexible, transparent, conducting films: extremely high DC to optical conductivity ratios, ACS nano, 3 (2009) 1767-1774.
[182] S.H. Chae, Y.H. Lee, Carbon nanotubes and graphene towards soft electronics, Nano Convergence, 1 (2014) 1-26.
[183] Y. Zhou, C. Wan, Y. Yang, H. Yang, S. Wang, Z. Dai, K. Ji, H. Jiang, X. Chen, Y. Long, Highly stretchable, elastic, and ionic conductive hydrogel for artificial soft electronics, Advanced Functional Materials, 29 (2019) 1806220.
[184] J. Deng, H. Yuk, J. Wu, C.E. Varela, X. Chen, E.T. Roche, C.F. Guo, X. Zhao, Electrical bioadhesive interface for bioelectronics, Nature Materials, 20 (2021) 229-236.
[185] K.G. Cho, S. An, D.H. Cho, J.H. Kim, J. Nam, M. Kim, K.H. Lee, Block Copolymer-Based Supramolecular Ionogels for Accurate On-Skin Motion Monitoring, Advanced Functional Materials, (2021) 2102386.
[186] C.E. Brubaker, P.B. Messersmith, Enzymatically degradable mussel-inspired adhesive hydrogel, Biomacromolecules, 12 (2011) 4326-4334.
[187] Y. Zhao, Y. Wu, L. Wang, M. Zhang, X. Chen, M. Liu, J. Fan, J. Liu, F. Zhou, Z. Wang, Bio-inspired reversible underwater adhesive, Nature communications, 8 (2017) 1-8.
[188] X. Deng, R. Attalla, L.P. Sadowski, M. Chen, M.J. Majcher, I. Urosev, D.-C. Yin, P.R. Selvaganapathy, C.D. Filipe, T. Hoare, Autonomously self-adhesive hydrogels as building blocks for additive manufacturing, Biomacromolecules, 19 (2018) 62-70.
[189] E.A. Appel, J. del Barrio, X.J. Loh, O.A. Scherman, Supramolecular polymeric hydrogels, Chemical Society Reviews, 41 (2012) 6195-6214.
[190] J.L. Mann, C.Y. Anthony, G. Agmon, E.A. Appel, Supramolecular polymeric biomaterials, Biomaterials science, 6 (2018) 10-37.
[191] W. Wang, Z. Zeng, L. Xiang, C. Liu, D. Diaz-Dussan, Z. Du, A.B. Asha, W. Yang, Y.-Y. Peng, M. Pan, Injectable Self-Healing Hydrogel via Biological Environment-Adaptive Supramolecular Assembly for Gastric Perforation Healing, ACS nano, (2021).
[192] M. Wu, J. Chen, Y. Ma, B. Yan, M. Pan, Q. Peng, W. Wang, L. Han, J. Liu, H. Zeng, Ultra elastic, stretchable, self-healing conductive hydrogels with tunable optical properties for highly sensitive soft electronic sensors, Journal of Materials Chemistry A, 8 (2020) 24718-24733.
[193] S. Li, S. Dong, W. Xu, S. Tu, L. Yan, C. Zhao, J. Ding, X. Chen, Antibacterial hydrogels, Advanced science, 5 (2018) 1700527.
[194] H.H. Tuson, L.D. Renner, D.B. Weibel, Polyacrylamide hydrogels as substrates for studying bacteria, Chemical Communications, 48 (2012) 1595-1597.
[195] B.R. Freedman, O. Uzun, N.M.M. Luna, A. Rock, C. Clifford, E. Stoler, G. Östlund-Sholars, C. Johnson, D.J. Mooney, Degradable and Removable Tough Adhesive Hydrogels, Advanced Materials, 33 (2021) 2008553.
[196] X. Di, J. Li, M. Yang, Q. Zhao, G. Wu, P. Sun, Bioinspired, nucleobase-driven, highly resilient, and fast-responsive antifreeze ionic conductive hydrogels for durable pressure and strain sensors, Journal of Materials Chemistry A, 9 (2021) 20703-20713.

[197] Y. Li, D. Wang, J. Wen, J. Liu, D. Zhang, J. Li, H. Chu, Ultra-Stretchable, Variable Modulus, Shape Memory Multi-Purpose Low Hysteresis Hydrogel Derived from Solvent-Induced Dynamic Micelle Sea-Island Structure, Advanced Functional Materials, (2021) 2011259.
[198] D.C. Tuncaboylu, M. Sari, W. Oppermann, O. Okay, Tough and self-healing hydrogels formed via hydrophobic interactions, Macromolecules, 44 (2011) 4997-5005.
[199] J. Tie, H. Chai, Z. Mao, L. Zhang, Y. Zhong, X. Sui, H. Xu, Nanocellulose-mediated transparent high strength conductive hydrogel based on in-situ formed polypyrrole nanofibrils as a multimodal sensor, Carbohydrate Polymers, 273 (2021) 118600.
[200] L. Wang, Z. Li, P. Huang, W. Ding, Synthesis of an acrylamide copolymer containing nano-SiO2 by ex situ Cu (0)-mediated SET-LRP, International Journal of Polymer Science, 2019 (2019).
[201] T. Liu, X. Guo, W. Liu, C. Hao, L. Wang, W.C. Hiscox, C. Liu, C. Jin, J. Xin, J. Zhang, Selective cleavage of ester linkages of anhydride-cured epoxy using a benign method and reuse of the decomposed polymer in new epoxy preparation, Green Chemistry, 19 (2017) 4364-4372.
[202] L. Han, M. Wang, L.O. Prieto-López, X. Deng, J. Cui, Self-hydrophobization in a dynamic hydrogel for creating nonspecific repeatable underwater adhesion, Advanced Functional Materials, 30 (2020) 1907064.
[203] Y. Lu, Y. Yue, Q. Ding, C. Mei, X. Xu, Q. Wu, H. Xiao, J. Han, Self-Recovery, Fatigue-Resistant, and Multifunctional Sensor Assembled by a Nanocellulose/Carbon Nanotube Nanocomplex-Mediated Hydrogel, ACS Applied Materials & Interfaces, 13 (2021) 50281-50297.
[204] Y. Lu, J. Han, Q. Ding, Y. Yue, C. Xia, S. Ge, Q. Van Le, X. Dou, C. Sonne, S.S. Lam, TEMPO-oxidized cellulose nanofibers/polyacrylamide hybrid hydrogel with intrinsic self-recovery and shape memory properties, Cellulose, 28 (2021) 1469-1488.
[205] L. Zhang, M. Liu, Y. Zhang, R. Pei, Recent progress of highly adhesive hydrogels as wound dressings, Biomacromolecules, 21 (2020) 3966-3983.
[206] Y. Zhong, F. Seidi, C. Li, Z. Wan, Y. Jin, J. Song, H. Xiao, Antimicrobial/Biocompatible Hydrogels Dual-Reinforced by Cellulose as Ultrastretchable and Rapid Self-Healing Wound Dressing, Biomacromolecules, 22 (2021) 1654-1663.
[207] A. Gupta, S.M. Briffa, S. Swingler, H. Gibson, V. Kannappan, G. Adamus, M. Kowalczuk, C. Martin, I. Radecka, Synthesis of silver nanoparticles using curcumin-cyclodextrins loaded into bacterial cellulose-based hydrogels for wound dressing applications, Biomacromolecules, 21 (2020) 1802-1811.
[208] P. Squinca, L. Berglund, K. Hanna, J. Rakar, J. Junker, H. Khalaf, C.S. Farinas, K. Oksman, Multifunctional Ginger Nanofiber Hydrogels with Tunable Absorption: The Potential for Advanced Wound Dressing Applications, Biomacromolecules, 22 (2021) 3202-3215.
[209] C.H. Kim, J.W. Choi, H.J. Chun, K.S. Choi, Synthesis of chitosan derivatives with quaternary ammonium salt and their antibacterial activity, Polymer Bulletin, 38 (1997) 387-393.